Low-Complexity Iterative Receiver Design for Multi-Carrier Faster-Than-Nyquist Signaling Over Frequency-Selective Fading Channel

by **Yunsi Ma**

Thesis submitted in fulfilment of the requirements for the degree of
Doctor of Philosophy
under the supervision of J. Andrew Zhang

School of Electrical and Data Engineering
Faculty of Engineering and IT
University of Technology Sydney
February 9, 2023

Certificate of Authorship / Originality

I, Yunsi Ma, declare that this thesis is submitted in fulfilment of the requirements for the award of Doctor of Philosophy, in the School of Electrical and Data Engineering at the University of Technology Sydney.

This thesis is wholly my own work unless otherwise referenced or acknowledged. In addition, I certify that all information sources and literature used are indicated in the thesis.

I certify that the work in this thesis has not previously been submitted for a degree nor has it been submitted as part of the requirements for a degree at any other academic institution except as fully acknowledged within the text. This thesis is the result of a Collaborative Doctoral Research Degree program with Beijing Institute of Technology.

This research is supported by the Australian Government Research Training Program.

Signature:	Production Note: Signature removed prior to publication.
Date:	February 9, 2023

Abstract

To meet the urgent requirements of future intelligent connection of all things and global coverage, the key to dealing with the contradiction between massive data and scarce spectrum resources is to improve the spectral efficiency of wireless communication systems. Multi-carrier faster-than-Nyquist (MFTN) signaling reduces the symbol period satisfying the Nyquist criterion in the time domain and the minimum spacing of orthogonal subcarriers in the frequency domain for remarkably improving the spectral efficiency, which still occupies the same frequency bandwidth. However, time-frequency compression introduces severe inter-symbol interference and inter-carrier interference simultaneously, which makes the receiver design of MFTN signaling quite challenging. Especially in multipath fading channels, the coupling of channel interference and self-interference imposed by MFTN signaling further increases the complexity of symbol detection and channel estimation in non-orthogonal transmission systems.

Based on statistical signal processing and parameter estimation theory, this dissertation studies the design of a low-complexity iterative receiver for MFTN signaling over a frequency-selective fading channel. Moreover, this thesis makes contributions to iterative equalization, joint channel estimation and equalization algorithms. The main contributions of this thesis are summarized as follows:

1. A low-complexity iterative receiver based on hybrid message passing is proposed for spectrally efficient frequency division multiplexing (SEFDM) signaling combined with index modulation (IM), which solves the problem of joint symbol detection and channel estimation for frequency-domain one-dimensional non-orthogonal multi-carrier signaling in unknown channel scenarios. Numerical results show that compared to its Nyquist-based counterpart, SEFDM-IM signaling can achieve a similar bit error rate (BER) performance and significantly improve the spectral efficiency.

2. A parametric bilinear generalized approximate message passing (PBiGAMP)-based frequency-domain joint channel estimation and equalization (FDJCEE) algorithm is proposed for MFTN signaling, which solves the problem of joint symbol detection and channel estimation for time-frequency two-dimensional non-orthogonal multi-carrier signaling in unknown channel scenarios. Simulation results demonstrate that, compared to the MMSE-based algorithm, both of the proposed algorithms achieve better BER performance and significantly reduce the computational complexity in time-varying channels.

3. A novel non-orthogonal transmission scheme of joint MFTN and IM is developed, which effectively improves the BER performance of MFTN signaling. A pair of iterative equalization algorithms based on vector approximate message passing (VAMP) are proposed for solving the symbol detection issue in known channel scenarios. Numerical results verify that the VAMP-TDE algorithm is superior in terms of BER performance, while the VAMP-FDE algorithm is able to compromise between BER performance and computational complexity.

Acknowledgements

As my doctoral dissertation is about to be completed, I would like to express my sincere gratitude to my supervisors, family, research collaborators, and friends for their care and help.

First of all, I would like to express my heartfelt thanks to my supervisor Andrew Zhang. His rigorous academic style and innovative scientific research attitude have deeply influenced me. Meanwhile, His broad academic vision and good guidance have cultivated my scientific research ability and enabled me to successfully complete my doctoral program.

I am also deeply indebted to my co-supervisor Kai Wu. My research benefits so much from his professional guidance.

I would like to thank Professor Nan Wu of Beijing Institute of Technology and Professor Lajos Hanzo of University of Southampton for their academic guidance and great help during my doctoral study.

Special thanks should go to my research collaborators and friends who fought alongside me. Thank you for every discussion with me and solving difficult problems together.

Last my thanks would go to my parents and boyfriend for their constant care, company, support and encouragement. Because of you, I am always full of love and confidence.

Yunsi Ma
February 9, 2023
Sydney, Australia

Publications

Publications Related to This Thesis

Journal Papers

J-1. **Y. Ma**, N. Wu, J. A. Zhang, B. Li and L. Hanzo, "Generalized Approximate Message Passing Equalization for Multi-Carrier Faster-Than-Nyquist Signaling," in **IEEE Transactions on Vehicular Technology**, vol. 71, no. 3, pp. 3309-3314, March 2022.

J-2. **Y. Ma**, N. Wu, J. A. Zhang, B. Li and L. Hanzo, "Parametric Bilinear Iterative Generalized Approximate Message Passing Reception of FTN Multi-Carrier Signaling," in **IEEE Transactions on Communications**, vol. 69, no. 12, pp. 8443-8458, Dec. 2021.

J-3. **Y. Ma**, N. Wu, W. Yuan, D. W. K. Ng and L. Hanzo, "Joint Channel Estimation and Equalization for Index-Modulated Spectrally Efficient Frequency Division Multiplexing Systems," in **IEEE Transactions on Communications**, vol. 68, no. 10, pp. 6230-6244, Oct. 2020.

J-4. **Y. Ma**, F. Tian, N. Wu, B. Li and X. Ma, "A Low-Complexity Receiver for Multicarrier Faster-Than-Nyquist Signaling Over Frequency Selective Channels," in **IEEE Communications Letters**, vol. 24, no. 1, pp. 81-85, Jan. 2020.

J-5. **Y. Ma**, N. Wu, K. Wu and J. A. Zhang, "VAMP-Based Iterative Equalization for Index-Modulated Multicarrier FTN Signaling," in **IEEE Transactions on Communications**, Accepted.

Conference Papers

C-1. **Y. Ma**, N. Wu, B. Li and H. Wang, "Low-Complexity Factor Graph-Based Joint Channel Estimation and Equalization for SEFDM Signaling," 2020 IEEE 92nd Vehicular Technology Conference (VTC2020-Fall), 2020, pp. 1-5.

C-2. **Y. Ma**, N. Wu, W. Yuan and H. Wang, "Hybrid BP-EP Based Iterative Receiver for Faster-Than-Nyquist with Index Modulation," 2019 IEEE 90th Vehicular Technology Conference (VTC2019-Fall), 2019, pp. 1-5.

C-3. **Y. Ma**, W. Yuan, N. Wu and Y. Li, "Message Passing Receiver for SEFDM Signaling Over Multipath Channels," 2019 IEEE VTS Asia Pacific Wireless Communications Symposium (APWCS), 2019, pp. 1-5.

List of Acronyms

AMP	Approximate Message Passing
AWGN	Additive White Gaussian Noise
BER	Bit Error Rate
BML	Block Maximum Likelihood
BP	Belief Propagation
CAR	Complex Auto-Regressive
CFR	Channel's Frequency Response
CIR	Channel Impulse Response
CSI	Channel State Information
EM	Expectation Maximization
EP	Expectation Propagation
FCE	Full Channel Estimator
FD	Frequency-Domain
FFT	Fast Fourier Transform
FTN	Faster-Than-Nyquist
GAMP	Generalized Approximate Message Passing
GMP	Gaussian Message Passing
ICI	Inter-Carrier Interference
IFFT	Inverse Fast Fourier Transform
IM	Index Modulation
ISI	Inter-Symbol Interference
JCEE	Joint Channel Estimation and Equalization
KLD	Kullback-Leibler Divergence
LDPC	Low Density Parity Check
LMMSE	Linear Minimum Mean Square Error
LLR	Log-Likelihood Ratio
LS	Least Squares
MAP	Maximum *A Posteriori*
MED	Minimum Euclidean Distance
MFTN	Multicarrier Faster-Than-Nyquist
ML	Maximum Likelihood

MMSE	Minimum Mean Square Error
MPSK	M-ary Phase Shift Keying
MQAM	M-ary Quadrature Amplitude Modulation
NMSE	Normalized Mean Square Error
OFDM	Orthogonal Frequency Division Multiplexing
PAPR	Peak to Average Power Ratio
PBiGAMP	Parametric Bilinear Generalized Approximate Message Passing
PCE	Partial Channel Estimator
PDF	Probability Distribution Function
PDP	Power Delay Profile
QAM	Quadrature Amplitude Modulation
QPSK	Quadrature Phase Shift Keying
SEFDM	Spectrally Efficient Frequency Division Multiplexing
SIC	Successive Interference Canceller
SPA	Sum Product Algorithm
VAMP	Vector Approximate Message Passing
VMP	Variational Message Passing
ZF	Zero Forcing

Contents

1 Introduction **2**

1.1 Background . . . 2
1.2 Motivations and Objectives . . . 4
1.3 Approaches and Contributions . . . 6
1.4 Thesis Organization . . . 7
1.5 Additional Research Contributions . . . 10

2 Literature Review **11**

2.1 Introduction . . . 11
2.2 Faster-Than-Nyquist Signaling . . . 13
2.2.1 Time-Domain Equalization . . . 13
2.2.2 Frequency-Domain Equalization . . . 15
2.2.3 Message Passing Algorithms . . . 16
2.2.4 Channel Estimation . . . 18
2.3 Spectrally Efficient Frequency Division Multiplexing Signaling . . . 20
2.3.1 Time-Domain Equalization . . . 20
2.3.2 Frequency-Domain Equalization . . . 21
2.3.3 Channel Estimation . . . 21
2.4 Multi-Carrier Faster-Than-Nyquist Signaling . . . 23
2.5 Index Modulation . . . 24
2.6 Conclusion . . . 26

3 Joint Channel Estimation and Equalization for Index-Modulated SEFDM Signaling **27**

3.1 Introduction . . . 27
3.2 System Model . . . 29
3.3 Iterative Equalization Based on GMP-EP . . . 31
3.3.1 The Colored Noise Approximation Using CAR Model . . . 31
3.3.2 Factor Graph Representation . . . 31
3.3.3 Message Updating for Hybrid GMP-EP Equalization . . . 32
3.4 Joint Channel Estimation and Equalization Based on Hybrid Message Passing . . . 39

3.4.1 Factor Graph Representation . . . 39
3.4.2 VMP-based Channel Estimation . . . 39
3.5 Complexity Analysis and Simulation Results . . . 44
3.5.1 Complexity Analysis . . . 44
3.5.2 Simulation Results . . . 46
3.6 Conclusion . . . 51

4 Joint Channel Estimation and Equalization for MFTN Signaling 53
4.1 Introduction . . . 53
4.2 Segment-Based Frequency-Domain Received Signal Model . . . 56
4.3 PBiGAMP-Based Frequency-Domain Joint Channel Estimation and Equalization 61
4.3.1 Factor Graph Representation . . . 61
4.3.2 PBiGAMP-Based Frequency-Domain Iterative Receiver . . . 62
4.3.3 Refined PBiGAMP-Based Frequency-Domain Iterative Receiver . . . 65
4.4 GAMP-Based Frequency-Domain Equalization With Known CSI . . . 67
4.5 Complexity Analysis and Simulation Results . . . 68
4.5.1 Complexity Analysis . . . 68
4.5.2 Simulation Results . . . 70
4.6 Conclusion . . . 76

5 Iterative Equalization for Index-Modulated MFTN Signaling 78
5.1 Introduction . . . 78
5.2 System Model . . . 80
5.3 Time-Domain Equalization Based on VAMP . . . 82
5.3.1 Factor Graph Representation . . . 82
5.3.2 Message Updating of VAMP-TDE . . . 83
5.4 Frequency-Domain Equalization Based on Interference Mitigation and VAMP . . 86
5.4.1 Frequency-Domain Received Signal Model . . . 86
5.4.2 Factor Graph Representation . . . 88
5.4.3 Message Updating of VAMP-FDE . . . 89
5.5 Complexity Analysis and Simulation Results . . . 92
5.5.1 Complexity Analysis . . . 92
5.5.2 Simulation Results . . . 92
5.6 Conclusion . . . 97

6 Conclusions and Future Work 98
6.1 Summary of Outcomes . . . 98
6.2 Recommendations & Future Work . . . 99
6.3 Concluding Remarks . . . 101

A Derivations of (3.41) and (3.42) 114

B Derivations of (4.12) **116**

C Derivations of the distribution of the equivalent noise in (4.14) **117**

D Derivations of the distribution of the frequency-domain equivalent noise in (5.28) **119**

List of Figures

2.1 The inherent ISI of single-carrier FTN signaling with $\tau = 0.8$. 13
2.2 Comparison of OFDM and SEFDM signaling. 20
2.3 Comparison of Nyquist and MFTN signaling. 23
2.4 Comparison of OFDM and OFDM-IM signaling. 25

3.1 Block diagram of an LDPC-coded SEFDM-IM tranceiver. 29
3.2 Factor graph for equalization of SEFDM-IM signaling with known CSI. 33
3.3 Factor graph for JCEE of SEFDM-IM signaling with unknown CSI. 40
3.4 BER performance of different equalizers for SEFDM-IM systems with known CSI, $(K_{\mathrm{g}}, K_{\mathrm{a}}) = (4, 1)$. 47
3.5 BER performance of different equalizers for SEFDM-IM systems with known CSI, $(N, K) = (4, 3)$. 47
3.6 BER performance of different JCEE algorithms for SEFDM-IM systems. 48
3.7 NMSE performance of different JCEE algorithms for SEFDM-IM systems. . . . 49
3.8 Impact of different combinations of K_{I} and I on BER performance. 49
3.9 Impact of different combinations of I_{c} and I on BER performance. 50
3.10 Impact of different combinations of ν and R_{c} on BER performance. 51

4.1 Block diagram of an LDPC-coded MFTN transceiver. 56
4.2 The condition number of the interference matrices in different received signal models. 60
4.3 Factor graph representation of the segment-based frequency-domain received signal model. 62
4.4 BER performance of different equalization algorithms for MFTN systems in the case of perfectly known CSI. 70
4.5 BER performance of the proposed R-GAMP-FDE algorithm for MFTN systems in the case of perfectly known CSI. 71
4.6 Interference energy and spectral efficiency of MFTN systems with various pulse shaping filters and packing factors. 73
4.7 BER performance of different algorithms for MFTN systems in the absence of CSI. 74

4.8 NMSE performance of different algorithms for MFTN systems in the absence of CSI. 75
4.9 Impact of various length of segment on BER performance of the proposed R-PBiGAMP-FDJCEE algorithm. 75
4.10 Impact of various combinations of I_c and I_e on BER performance of the proposed R-PBiGAMP-FDJCEE algorithm. 76

5.1 The transceiver structure of MFTN-IM signaling. 80
5.2 Vector factor graph of TDE for MFTN-IM signaling 83
5.3 Factor graph model of FDE for MFTN-IM signaling 88
5.4 Vector factor graph model of FDE combined with interference mitigation for MFTN-IM signaling 89
5.5 BER performance of different waveforms. 93
5.6 BER performance of different equalization algorithms for MFTN-IM signaling with $(K_g, K_a) = (4, 2)$. 94
5.7 BER performance of different equalization algorithms for MFTN-IM signaling with $(K_g, K_a) = (4, 3)$. 95
5.8 Impact of the packing factors on BER performance of MFTN-IM signaling. . . . 96
5.9 Impact of various combinations of packing factors and code rate on BER performance of MFTN-IM signaling. 97

List of Tables

3.1 Complexity Analysis of Equalization of SEFDM-IM Signaling 45
3.2 Complexity Analysis of Channel Estimation and Equalization of SEFDM-IM Signaling 46

4.1 Complexity Analysis of Channel Estimation and Equalization of MFTN Signaling 69

5.1 Complexity Analysis of Equalization of MFTN-IM Signaling 92

Chapter 1

Introduction

1.1 Background

Intelligent connection of everything and seamless global coverage are important characteristics of future information communication networks [1], [2]. After more than 40 years of development, supported by massive multiple input multiple output (MIMO) [3]–[5], polar code [6]–[8], orthogonal frequency division multiplexing (OFDM) [9]–[11] and other technologies, the fifth generation (5G) has reached Gbps level of transmission rate, millisecond level of transmission delay and million level of network capacity [12]–[16]. All of these provide the essential ability to intelligent connection of everything.

However, the deployment cost of the ground mobile communication network is exceptionally high, and its coverage is limited. It is challenging to meet the communication requirements of mountainous areas, forests, deserts, aviation, navigation, and other scenarios. By contrast, satellite communication network has the advantages of comprehensive coverage, long transmission distance, large communication capacity, and flexible networking mode. These features can fully compensate for the shortcomings of the ground mobile communication network. Therefore, satellite communication network is able to provide more economical, stable, flexible, and ubiquitous communication services in harsh terrain conditions or sparsely populated areas [17].

The sixth generation (6G) mobile communication system will establish an integrated network of air, ground, and sea for realizing the vision of intelligent connection of everything and seamless global coverage [18]–[20]. It is seen that the integration of ground mobile communication and satellite communication networks is a significant development trend for future information communication networks [21]. The integrated network will be based on the ground communication network and expanded by the satellite communication network. The synergistic development of them will promote the construction of the integration network. Since the birth of the first generation of mobile communication system in 1978, the ground mobile communication network has entered a phase of rapid development. With the gradual completion of the entire

commercial deployment of 5G, the formulation of the 6G standard is being actively promoted worldwide. However, the development of the satellite communication network has lagged.

The construction of broadband satellite-ground transmission link is the key to developing the integrated network. To meet the requirements of high-speed data transmission, Terahertz communication [22], [23], visible light communication, and other technologies have been conceived to acquire more available spectrum resources. However, with the increasing frequency band, Terahertz communications suffer from the increasing non-line-of-sight propagation loss caused by scattering, diffraction, and shadow fading. Moreover, Terahertz communications are sensitive to phase noise [24]. For satellite-ground transmission link, the Terahertz wave may be further attenuated by weather due to the atmospheric effect of the propagation medium. Regards to visible light communication technology, the laser satellite communication network has the advantages of high transmission rate, long transmission distance, strong anti-electromagnetic interference ability and confidentiality. However, when the laser propagates through an atmospheric channel, it may produce atmospheric attenuation and turbulence effects. Both may lead to bending propagation of the light wave, beam drift, transmission loss, coherence degradation, and other phenomena, seriously destroying the communication quality of satellite-ground transmission link.

Another efficient solution to solve the contradiction between broadband communication demand and scarce spectrum resources in satellite-ground transmission link is improving spectrum utilization. For a limited bandwidth, the typical communication systems employ high-order modulation for enhancing the transmission rate, such as 256 quadrature amplitude modulation (QAM) in 802.11ac standard [25]. However, high-order modulations are very sensitive to channel impairments, such as phase noise distortion, timing error, and multipath fading, easily resulting in severe bit error rate (BER) performance degradation. To this end, non-orthogonal waveforms represented by faster-than-Nyquist (FTN) have been extensively investigated for enhancing spectral efficiency.

FTN signaling is able to significantly enhance transmission rate within the same bandwidth via compressing the symbol period of Nyquist signals (i.e., satisfying the first Nyquist criteria) [26]–[28]. By relaxing the orthogonality constraint, FTN signaling employing low-order modulation can obtain the same transmission rate as Nyquist signaling with high-order modulation. Since the non-orthogonal signaling exploits low-order modulation, it is more robust to various channel impairments. Through configuring the packing factor value, FTN signal can continuously enhance the transmission rate, providing a more flexible and efficient transmission scheme for high-speed wireless communications.

The concept of FTN has been extended to multi-carrier systems to further improve the spectral efficiency, including one-dimensional frequency-domain packing spectrally efficient frequency division multiplexing (SEFDM) signaling [29] and two-dimensional time-frequency packing multicarrier faster-than-Nyquist (MFTN) signaling [30], [31]. By packing the time interval between adjacent symbols and frequency spacing between adjacent subcarriers, MFTN signaling can

remarkably enhance spectral efficiency than Nyquist signaling without additional BER performance erosion [32]. It has been demonstrated that non-orthogonal multi-carrier signaling has the potential to achieve higher capacity limits compared to orthogonal signaling [33]. However, the cost of improving spectral efficiency is that non-orthogonal multi-carrier signaling inevitably introduces inter-symbol interference (ISI) and inter-carrier interferences (ICI), both of which challenge its receiver design [34], [35].

Index modulation (IM) has been widely discussed as a novel digital modulation scheme, which utilizes the activated or inactivated indications of antennas, subcarriers, spreading codes, and time slots to implicitly transmit additional information [36]–[38]. The flexible extension of IM in multiple domains can provide an efficient modulation scheme in terms of spectral efficiency, energy efficiency[1], implementation complexity, anti-interference capability, and transmission reliability [39], [40]. The implicit transmission of additional information requires little or even zero extra power consumption, resulting in high energy efficiency for IM. The flexible structure of IM also enables more bits to be transmitted within the same physical resource by optimizing its mapping rules, thus improving the spectral efficiency. With these advantages, IM has become a very competitive modulation scheme for 5G and beyond communications [41]–[43].

Furthermore, non-orthogonal signaling of FTN family can be combined with IM [36], [40], [44]. Unlike typical modulation techniques, IM employs both the transmit entities and their activation patterns for carrying information bits [44]. Through implicitly transmitting partial information bits, IM can not only enhance the spectral efficiency but also improve the performance, especially in frequency-selective fading channel [36]. For the index-modulated non-orthogonal signaling, the self-interferences imposed by the breakthrough of Nyquist constraint can be mitigated via utilizing the implicit transmission characteristics of IM technology. Hence, the appropriate fusion transmission scheme is able to further improve the reliable transmission capacity of non-orthogonal waveform, for satisfying the different service requirements of satellite-ground communication.

Against this background, this work aims to design a novel non-orthogonal waveform with high spectral and energy efficiency and then study the low-complexity demodulation algorithms of non-orthogonal multi-carrier signaling. Based on statistical signal processing and parameter estimation theory, a series of parametric iterative channel estimation and equalization algorithms are derived under the assumption of frequency-selective fading channels, providing technical support for the application of non-orthogonal multi-carrier signaling in satellite-ground high-speed transmission link.

1.2 Motivations and Objectives

The spectrally efficient non-orthogonal multi-carrier signaling provides an efficient and robust solution for enhancing transmission rate and resisting channel impairments. Through packing

[1]The energy efficiency refers to the efficiency of the transmission power, which is independent of the receiver.

the orthogonal intervals between symbols or subcarriers, non-orthogonal signaling of FTN family can significantly improve spectral efficiency, at the expense of introducing the interferences depending on the packing factors and shaping pulses. After passing through frequency-selective fading channels, the received non-orthogonal signaling is further destroyed by the unknown interferences imposed by channels. At the receiver side, how to design a low-complexity receiver of non-orthogonal signaling for eliminating the one-dimensional or even two-dimensional coupling interferences is crucial but challenging.

However, in terms of demodulation, most of the existing studies relevant to non-orthogonal signaling have devoted to designing receivers for non-orthogonal single-carrier signaling, i.e., one-dimensional time-domain packing FTN signaling. Only a few literatures discuss the symbol detection or interference elimination algorithms of one-dimensional frequency-domain packing SEFDM signaling in additive white Gaussian noise (AWGN) or perfectly known multipath channels. This limits the application of SEFDM signaling in unknown channel scenarios. Moreover, regards to two-dimensional time-frequency packing MFTN signaling, few researches discuss its receiver design due to the intractable two-dimensional self-interferences.

Against this background, this work aims to design low-complexity iterative receivers for non-orthogonal multi-carrier signaling over frequency-selective fading channels. The design goal of these receivers is to balance the computational complexity and the demodulation performance of non-orthogonal multi-carrier transmission waveforms. The research results are not only to solve the current technical bottleneck, but also to provide a valuable research foundation for future high-speed wireless communications. Specifically, the research objectives of this thesis are:

1. To solve the symbol detection problem of one-dimensional frequency-domain packing multi-carrier signaling in unknown channel scenarios, objective 1 is to design a low-complexity joint channel estimation and equalization (JCEE) algorithm for index-modulated SEFDM signaling.

2. To solve the efficient reception problem of two-dimensional time-frequency packing multi-carrier signaling over frequency-selective fading channels, objective 2 is to design a parametric iterative message passing receiver for MFTN signaling, including JCEE algorithm in the case of unknown channel state information (CSI) and iterative equalization under the assumption of known CSI.

3. To further develop a novel non-orthogonal transmission scheme with high spectral and energy efficiency, objective 3 is to investigate the index-modulated MFTN signaling and then design its low-complexity equalization algorithms under the assumption of perfectly known CSI.

1.3 Approaches and Contributions

To achieve the above-mentioned research objectives, this work resorts to probabilistic graphical model to design low-complexity receivers for non-orthogonal multi-carrier waveforms. Factor graph provides a unified framework for a series of issues, including statistics, coding, statistical physics, signal processing and machine learning [45]–[47]. According to a factorization of joint *a posteriori* probability density function, a bipartite graph can be constructed for characterizing the dependency between variables, where the dependency is represented as a factor node. The *a posteriori* distributions of the target variables can be deduced via gleaning the message passing on factor graph. Furthermore, the message passing between variables obeys specific rules, such as sum-product or max-sum algorithm.

The computational complexity of the factor graph-based algorithms varies greatly depending on the message passing rules. To simplify the computational complexity, several signal processing approaches based on factor graph have been developed. A typical example is Gaussian message passing (GMP) in linear state space models, which forms a series of tabulated message passing rules. It can deal with linear minimum mean square error (LMMSE) estimation, recursive least squares, and Kalman filtering [47]. Through reformulating the received signal model as a linear state space model, a Forney-style factor graph can be constructed and then the GMP rules can be used to derive a parametric symbol detection or channel estimation algorithm.

As an alternative solution, the approximate message passing (AMP)-based algorithms provide an efficient approximation of max-sum or sum-product loopy belief propagation (BP) for the computations of maximum *a posteriori* (MAP) or minimum mean square error (MMSE) estimates. Based on the central limit theorem (CLT) and Taylor series expansion, generalized approximate message passing (GAMP) algorithm decouple the high-dimensional random linear mixing estimation problem into a series of scalar computations [48]. However, GAMP algorithm guarantees its convergence only if the linear transition matrix satisfies a large independent identically distributed zero-mean Gaussian assumption. In this case, the asymptotic behavior of GAMP algorithm can be analytically characterized by a series of state-evolution equations.

There are lots of modified AMP-based algorithms developed for improving the convergence of GAMP algorithms in [49]–[52]. The damped AMP algorithms introduce several damping factors to slow down the updates of intermediate variables and facilitate the convergence of AMP. Since the values of damping factors could only be chosen empirically, the performance improvements of these damped AMP algorithms are limited. In [50], a unitary transformation-based generalized approximate message passing (UTAMP) algorithm employing singular value decomposition (SVD) was proved to converge for any system transform matrix under the assumption of Gaussian inputs. Then, an orthogonal approximate message passing (OAMP) algorithm relying on general unitarily-invariant matrices also relaxes the divergence-free constraint of original GAMP algorithm [51]. However, their inevitable SVD operations lead to an excessive computational complexity. By contrast, a vector approximate message passing

(VAMP) algorithm only performs an initial SVD operation, which can be applied to a class of right-orthogonally invariant random matrices [52]. However, due to the ill-conditioning problem of non-orthogonal multi-carrier signaling, the simple extensions of the above-mentioned AMP-based algorithms still suffer from a severe BER performance loss. This is one of the technical bottlenecks to be addressed in this work.

The main contributions of this thesis are summarized below:

1. Based on hybrid message passing rules, a JCEE algorithm is proposed for SEFDM-IM signaling, which solves the low-complexity symbol detection and channel estimation problem of one-dimensional non-orthogonal multi-carrier signaling over unknown frequency-selective fading channels.

2. Inspired by PBiGAMP algorithm, an efficient frequency-domain iterative message passing receiver is developed for MFTN signaling, which solves the low-complexity symbol detection and channel estimation problem of two-dimensional non-orthogonal multi-carrier signaling over unknown frequency-selective fading channels.

3. A novel non-orthogonal waveform with high spectral efficiency and energy efficiency is designed via combining MFTN signaling and IM. Then, the corresponding VAMP-based time-domain equalization (TDE) and frequency-domain equalization (FDE) algorithms are derived for balancing the computational complexity and demodulation performance.

1.4 Thesis Organization

This thesis studies a series of low-complexity iterative receivers for multi-carrier non-orthogonal signaling over frequency-selective fading channels. First of all, one-dimensional frequency-domain packing SEFDM signaling is combined with IM and its JCEE algorithm is developed based on hybrid message passing rules. Then, two-dimensional time-frequency packing MFTN signaling is considered for achieving higher spectral efficiency. To tackle its challenging symbol detection and channel estimation problem, a pair of frequency-domain JCEE algorithms are derived under the framework of AMP. Finally, a novel non-orthogonal waveform with high spectral efficiency and energy efficiency is proposed by combining MFTN signaling and IM. Moreover, both time-domain and frequency-domain equalization algorithms are designed for the novel MFTN-IM signaling for balancing computational complexity and BER performance.

Chapter 2 provides a comprehensive review of literatures, which is relevant to the overall aim. This includes one-dimensional time-domain packing FTN signaling, one-dimensional frequency-domain packing SEFDM signaling, two-dimensional time-frequency packing MFTN signaling, and index modulated non-orthogonal signaling. The literature review focuses on the receiver design of these non-orthogonal waveforms, including interference elimination or symbol detection under the assumption of perfectly known CSI and channel estimation in unknown channels.

Chapter 3 aims to solve the JCEE problem of SEFDM signaling relying on IM. By approximat-

ing the interferences in the frequency domain, this work reformulates the problem to obey a linear state space model and constructs a multi-layer factor graph. To support a reconfigurable architecture, non-orthogonal demodulation is adopted and the colored noise encountered is approximated by a complex auto-regressive (CAR) model. For deriving a low-complexity parametric Gaussian message passing (GMP)-based method, an expectation propagation (EP)-based technique is exploited for approximating the discrete *a posteriori* distributions of the transmitted symbols in a Gaussian form. To further simplify the message updating, variational message passing (VMP) is applied to an equivalent soft node to obtain a Gaussian form. Compared to its Nyquist-based counterpart, SEFDM-IM signaling relying on the proposed algorithm exhibits up to 25% higher bandwidth efficiency without any BER performance degradation.

This chapter resulted in the following publications:

- **Y. Ma**, N. Wu, W. Yuan, D. W. K. Ng and L. Hanzo, "Joint Channel Estimation and Equalization for Index-Modulated Spectrally Efficient Frequency Division Multiplexing Systems," in **IEEE Transactions on Communications**, vol. 68, no. 10, pp. 6230-6244, Oct. 2020.
- **Y. Ma**, N. Wu, B. Li and H. Wang, "Low-Complexity Factor Graph-Based Joint Channel Estimation and Equalization for SEFDM Signaling," 2020 IEEE 92nd Vehicular Technology Conference (VTC2020-Fall), 2020, pp. 1-5.
- **Y. Ma**, W. Yuan, N. Wu and Y. Li, "Message Passing Receiver for SEFDM Signaling Over Multipath Channels," 2019 IEEE VTS Asia Pacific Wireless Communications Symposium (APWCS), 2019, pp. 1-5.

Chapter 4 aims to design a low-complexity iterative receiver for two-dimensional time-frequency packing MFTN signaling over frequency-selective fading channel. To mitigate the inherent ill-conditioning problem of MFTN signaling, this work constructs a segment-based frequency-domain received signal model in the form of a block circulant linear transition matrix, which can be efficiently calculated by applying a two-dimensional fast Fourier transform (FFT). Based on the eigenvalue decomposition of the block circulant matrices, the covariance matrix of the complex-valued colored noise process imposed by the associated two-dimensional non-orthogonal matched filtering can be diagonalized in the frequency domain. Building on this model, a parametric frequency-domain JCEE algorithm based on parametric bilinear generalized approximate message passing (PBiGAMP) is derived for MFTN signaling. This algorithm introduces a pair of additive terms for characterizing the interferences arising from adjacent segments and employs the exact discrete *a priori* probabilities of the transmitted symbols for improving the BER performance. To further enhance the system's robustness in the presence of ill-conditioned matrices, a refined PBiGAMP-based JCEE algorithm is developed by introducing a series of scaled identity matrices. Moreover, the proposed PBiGAMP-based frequency-domain JCEE algorithms may be readily decomposed into GAMP-based FDE algorithms under the assumption of perfectly known CSI. The overall complexity only increases logarithmically

with the total number of transmitted symbols. The simulation results demonstrate the benefits of the proposed PBiGAMP-based iterative message passing receiver conceived for MFTN signaling.

This chapter resulted in the following publications:

- **Y. Ma**, N. Wu, J. A. Zhang, B. Li and L. Hanzo, "Generalized Approximate Message Passing Equalization for Multi-Carrier Faster-Than-Nyquist Signaling," in **IEEE Transactions on Vehicular Technology**, vol. 71, no. 3, pp. 3309-3314, March 2022.
- **Y. Ma**, N. Wu, J. A. Zhang, B. Li and L. Hanzo, "Parametric Bilinear Iterative Generalized Approximate Message Passing Reception of FTN Multi-Carrier Signaling," in **IEEE Transactions on Communications**, vol. 69, no. 12, pp. 8443-8458, Dec. 2021.
- **Y. Ma**, F. Tian, N. Wu, B. Li and X. Ma, "A Low-Complexity Receiver for multicarrier Faster-Than-Nyquist Signaling Over Frequency Selective Channels," in **IEEE Communications Letters**, vol. 24, no. 1, pp. 81-85, Jan. 2020.

Chapter 5 aims to develop an evolutionary non-orthogonal physical waveform and then solve its low-complexity demodulation problem in frequency-selective fading channel. The novel waveform simultaneously achieves high spectral and energy efficiency via combining MFTN signaling with IM. Exploiting the implicit transmission of IM, the inactivated subcarriers alleviate the inherent two-dimensional interferences imposed by time-frequency packing. Then, a pair of iterative equalization algorithms are developed based on vector approximate message passing (VAMP). For the VAMP-based TDE algorithm, an extended constellation set is constructed for uniformly characterizing the activated and inactivated subcarriers. To further reduce the computational complexity, a subcarrier-based segment-wise frequency-domain received signal model is established. Accordingly, a low-complexity VAMP-based FDE algorithm is developed via combining interference elimination. Corroborated by simulations, the novel MFTN-IM waveform achieves superior BER performance over benchmark waveforms in the high signal noise ratio (SNR) regions. Interestingly, while VAMP-TDE outperforms VAMP-FDE in BER performance, the latter is more competitive in balancing demodulation performance and computational complexity.

This chapter resulted in the following publications:

- **Y. Ma**, N. Wu, W. Yuan and H. Wang, "Hybrid BP-EP Based Iterative Receiver for Faster-Than-Nyquist with Index Modulation," 2019 IEEE 90th Vehicular Technology Conference (VTC2019-Fall), 2019, pp. 1-5.
- **Y. Ma**, N. Wu, K. Wu and J. A. Zhang, "VAMP-Based Iterative Equalization for Index-Modulated multicarrier FTN Signaling," in **IEEE Transactions on Communications**, submitted.

Finally, Chapter 6 provides the main conclusions of this work and several recommended direc-

tions for future research.

1.5 Additional Research Contributions

A number of co-authored research publications are listed below:

- Vector Approximate Message Passing Based Iterative Receiver for OTFS System[C]. IEEE/CIC International Conference on Communications in China (ICCC Workshops), pp. 422-426, 2021.
- A Parallel Carrier Recovery Scheme for an 8Gbps Terahertz Communication System[C]. IEEE/CIC International Conference on Communications in China (ICCC), pp. 1308-1313, 2020.
- Low-Complexity Implementation of Parallel Receiver for Terahertz Communication System[C]. IET International Radar Conference (IRC), pp. 84-89, 2020.
- Low-Complexity Factor Graph-Based Iterative Detection for RRC-SEFDM Signals[C]. 10th International Conference on Wireless Communications and Signal Processing (WCSP), pp. 1-5, 2018.
- Gaussian Message Passing based Receiver for multicarrier Faster-Than-Nyquist Signaling[C]. 10th International Conference on Wireless Communications and Signal Processing (WCSP), pp. 1-5, 2018.

Chapter 2

Literature Review

2.1 Introduction

According to the Nyquist criterion, the maximum transmission rate of an ISI-free transmission system cannot exceed twice the channel bandwidth in AWGN channel. Traditional Nyquist signaling inevitably sacrifices its spectral efficiency to satisfy its orthogonality constraint. In 1975, a study by Bell Labs illustrated that FTN signaling using sinc pulses could improve the transmission rate of 25% in the same bandwidth than Nyquist signaling without suffering any loss in minimum Euclidean distance, thus achieving the same BER performance as Nyquist signaling [26]. By giving up the orthogonality condition in terms of the time interval of adjacent symbols imposed by the Nyquist criterion, FTN signaling significantly improves spectral efficiency [28], [53]. Specifically, the interval of the shaping pulses T is less than that of the Nyquist criterion T_0, i.e., $T = \tau T_0$, where $\tau \in (0, 1]$ denotes the time-domain packing factor[1]. From the perspective of channel capacity, the constrained capacity of FTN signaling is higher than those of the orthogonal waveforms employing all shaping pulses except the sinc pulse [54]. In recent years, as a promising non-orthogonal technique, FTN signaling has attracted substantial attention in satellite communications [55]–[57], ground mobile communications [58]–[61] and optical communications [62]–[65].

To improve the spectral efficiency of multi-carrier systems, the concept of time-domain single-carrier FTN has been extended to multi-carrier systems. In 2003, SEFDM signaling was proposed by Darwazeh et al., University College London [29]. Different from OFDM used in the fourth generation ground mobile communications [66], SEFDM signaling reduces the minimum frequency spacing of orthogonal subcarriers for enhancing its transmission rate with the same bandwidth [67], [68]. Specifically, the subcarrier spacing of SEFDM signaling is expressed as $F = \nu F_0$, where F_0 is the minimum orthogonal subcarrier spacing of OFDM signaling, and $\nu \in (0, 1]$ denotes the frequency-domain packing factor. It is obvious that SEFDM signaling deliberately induces ICIs due to the loss of orthogonality between subcarriers. Similar to

[1]The generic value of τ is larger than 0.8.

OFDM signaling, conventional SEFDM signaling employing rectangular shaping pulses leads to high out-of-band power leakage, which profoundly influences other users in adjacent frequency bands. To tackle this problem, a root raised cosine pulse (RRC) shaped SEFDM system was investigated in [69] for reducing the out-of-band power leakage of SEFDM signaling. More importantly, the ICIs imposed by frequency-domain compression of RRC-SEFDM signaling are dominated only by the impact of adjacent subcarriers. It not only simplifies the receiver design, but also improves the BER performance compared to rectangular pulse-shaped SEFDM signaling [70]. Moreover, as an efficient non-orthogonal multi-carrier scheme employing one-dimensional frequency-domain packing [67], [68], SEFDM signaling has been investigated in optical communications [71], visible-light communication (VLC) [72], and in satellite systems [73].

Based on the extensive research of single-carrier FTN signaling in the time domain and one-dimensional frequency-domain packing, the concept of FTN has been extended to multi-carrier systems to further improve the spectral efficiency [30], [31], [33], [34]. MFTN signaling was firstly proposed by Rusek and Anderson in 2005 [30]. It is no longer a simple one-dimensional compression in the time or frequency domain but a two-dimensional packing waveform. The time-domain interval and frequency-domain subcarrier spacing of MFTN signaling are $T = \tau T_0$ and $F = \nu F_0$, respectively, where T_0 is the Nyquist interval of orthogonal shaping pulse, F_0 is the minimum orthogonal subcarrier spacing, $\tau, \nu \in (0, 1]$ denote the time-domain and frequency-domain packing factors. By packing the time interval between adjacent symbols and frequency spacing between adjacent subcarriers, MFTN signaling can significantly improve the spectral efficiency than Nyquist-based transmission schemes [31], [34]. Furthermore, the largest achievable spectral efficiency can be achieved by jointly optimizing the time interval and frequency spacing. It has been shown that compared with Nyquist signaling, MFTN signaling can obtain higher channel capacity [33].

According to the discussions mentioned above, non-orthogonal signaling of FTN family can significantly improve spectral efficiency by compressing the orthogonal intervals between symbols or subcarriers, at the cost of introducing the inherent ISIs or ICIs only depending on the packing factors and shaping pulses. After passing through frequency-selective fading channels, the known inherent interferences of FTN signaling are further coupled with the unknown interferences imposed by channels. This dramatically increases the complexity of the receiver of non-orthogonal multi-carrier signaling. Most existing studies have discussed the symbol detection or interference elimination of single-carrier FTN signaling. In contrast, only a few works have considered the receiver of multi-carrier FTN signaling in AWGN or known multipath channels. Hence, this work aims to design low-complexity iterative receivers for non-orthogonal multi-carrier signaling over frequency-selective fading channels.

This chapter will briefly overview the existing studies related to interference elimination, symbol detection, and channel estimation for non-orthogonal signaling of FTN family. Section 2.2 discusses channel estimation and interference elimination of single-carrier FTN signaling.

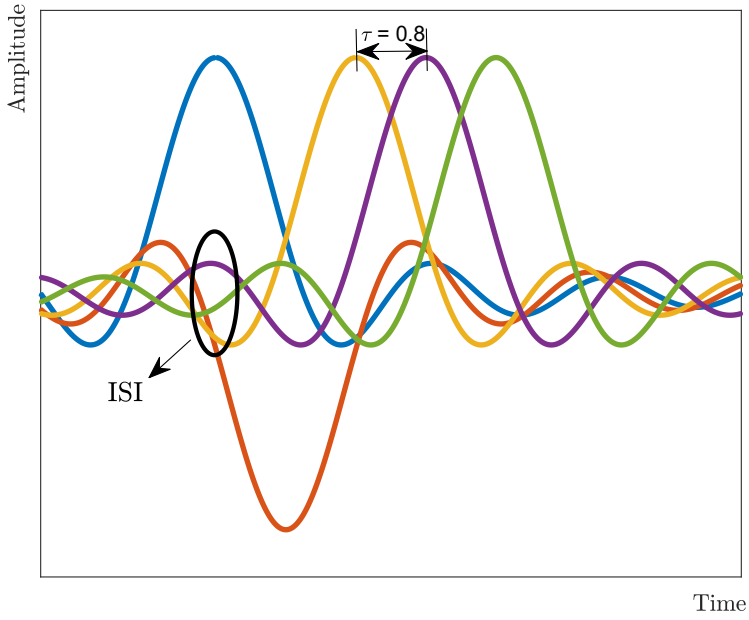


Figure 2.1: The inherent ISI of single-carrier FTN signaling with $\tau = 0.8$.

Section 2.3 discusses equalization and channel estimation of one-dimensional frequency-domain packing SEFDM signaling. Section 2.4 discusses few relevant studies of two-dimensional time-frequency packing MFTN signaling. Section 2.5 discusses index modulation and some fusion schemes relying on non-orthogonal signaling.

2.2 Faster-Than-Nyquist Signaling

Fig. 2.1 depicts a diagram of single-carrier FTN signaling with the packing factor $\tau = 0.8$. FTN signaling can significantly improve spectral efficiency without additional physical resources by packing the Nyquist interval of shaping pulses in the time domain. Then, it inevitably introduces ISIs even in AWGN or frequency-flat channels owing to relaxing the modulation orthogonality, complicating its receiver. Numerous studies have discussed the receiver design for single-carrier FTN signaling to balance computational complexity and demodulation performance. This section reviews them from the following aspects: time-domain equalization [53], [74]–[80], frequency-domain equalization [81]–[84], and message passing algorithms [59], [85]–[90], and channel estimation [59], [88], [91]. It has been demonstrated that the time-domain equalization outperforms the frequency-domain equalization for FTN signaling, while the latter may be attractive in low-complexity scenarios [35].

2.2.1 Time-Domain Equalization

The optimal equalization algorithm for overcoming the inherent interferences of single-carrier FTN signaling is maximum-likelihood sequence estimation, which can be implemented by the

Viterbi algorithm [92], [93]. The advantage of the optimal equalizer is a constant sampling rate even for various transmission rates. At the same time, its disadvantages contain the infeasible computational complexity and the performance loss due to non-ideal interpolation. In [53], the authors proposed a suboptimal joint equalization and decoding scheme based on the modified Viterbi algorithm for coded FTN signaling. For the FTN signaling employing an RRC shaping pulse with the roll-off factor of $\beta = 0.1$ and a time-domain packing factor of $\tau = 5/6$, the suboptimal turbo equalization could approach the optimum BER performance of Nyquist signaling. This conclusion is consistent with the Mazo limit of FTN signaling relying on the RRC shaping filter.

In [74], both serial and parallel concatenated coding schemes have been discussed for FTN signaling. In the serial concatenation scheme, FTN signaling can be regarded as the inner encoder combined with an outer convolutional code. Furthermore, the parallel scheme can be considered as FTN modulation combined with the bit interleaved coded modulation using an external rate-1/2 repetition code and an inner unity-rate convolutional code. It has been verified that the FTN systems employing the parallel-concatenated channel-encoded scheme and iterative turbo equalizer could achieve better BER performance than the coded FTN systems discussed in [53].

In [75], the concept of FTN was extended to nonbinary signal constellations, i.e., pulse amplitude modulation, which could outperform the binary-based counterpart in terms of spectral efficiency. The minimum distance for nonbinary FTN signaling was derived, and then the precoding scheme of the input date sequence was utilized to increase the minimum distance. Different from the typical precoding scheme for reducing the decoding burden at the cost of the BER performance loss [94], the precoding scheme of [75] aimed to improve the BER performance of nonbinary FTN signaling by sacrificing a little decoding complexity. Finally, a simple M-algorithm was employed to mitigate the inherent interferences of nonbinary FTN signaling, where only M most promising paths at each level in the trellis could be reserved, and the rest was released. It has been shown that the BER performance could approach the benchmark in the high SNR region.

A finite and discrete-time received signal model of FTN signaling was firstly developed in [76]. Then, a whitening filter was introduced to deal with the colored noise imposed by the non-orthogonal matched filter, whose output could be fed into the Viterbi algorithm. The authors also investigated the relationship between the minimum Euclidean distance and the truncated Viterbi algorithm. For example, a truncated Viterbi algorithm with about 32 states could approach the Mazo limit when the time-domain pack factor is $\tau = 0.5$. Then, a channel-coded FTN system employing both M-algorithm and Bahl, Cocke, Jelinek, and Raviv (BCJR)-based decoding algorithm was evaluated in terms of BER. The simulation results verified that, for an RRC shaping pulse, the BER performance of FTN signaling could improve with the increasing roll-off factor β. Note that FTN signaling with a more prominent roll-off factor β is easier to be implemented in practical applications.

The above-mentioned TDEs of single-carrier FTN signaling can efficiently eliminate the inherent ISIs in the low packing factor scenarios. However, the computational complexity induced by the trellis-based TDEs is still unacceptable, especially for a considerable truncated ISI length or constellation size. To this end, lots of reduced-state trellis-based FTN receivers were designed in [77]–[80]. Since the inherent interferences imposed by non-orthogonal modulation are similar to the ISIs imposed by a multipath channel, some efficient equalization techniques could be extended to demodulation of FTN signaling. In [77], [78], several truncated BCJR algorithms were developed for ISI channels, where the states used by the BCJR algorithm were divided into a main and an offset state. Among them, the proposed M-BCJR algorithm in [78] extended the main idea of the M-algorithm to calculate *a priori* information. When the ISIs are moderate and intense, the M-BCJR algorithm with the minimum phase input can significantly reduce the computational complexity.

In [79], the authors developed novel M-BCJR algorithms based on Forney observation model for low-complexity turbo TDEs and then exploited them to mitigate the severe ISIs induced by FTN signaling. Considering that calculating the accurate log-likelihood ratio (LLR) is essential for turbo equalization of FTN signaling, one of the main contributions of [79] is to add a third, low-complexity recursion for producing a backup LLR magnitude. Furthermore, to improve the BER performance of FTN signaling, a smoothed backup M-BCJR algorithm was also designed, where a moving average filter was used to grind the backup LLR values in the early iterations of a turbo decoder. In contrast, a pair of reduced-complexity M-BCJR algorithms based on Ungerboeck observation model were proposed for FTN signaling in [80]. By entirely using some "future" symbols, the proposed algorithms could select the M best states according to the MAP rules. Moreover, the authors have demonstrated that the proposed algorithms could guarantee correct path-loss-free performance.

In [95], a code-based channel shortening (CCS) algorithm was proposed for FTN signaling. By integrating a special type of convolutional code, i.e., output-retainable convolutional code (ORCC), joint detection and decoding of the CCS algorithm was only performed on code trellis, and then the channel memory could be absorbed. Moreover, an error performance bound of the proposed CCS algorithm relying on the ORCC structure was derived using the effective Euclidean distance between coded FTN symbols. The numerical results showed that FTN signaling employing the self-concatenated convolutional code could achieve a near-capacity performance. There is only 0.75 dB between the BER performance of the CCS algorithm and the Shannon limit of the shaping pulse.

2.2.2 Frequency-Domain Equalization

A series of FDE-aided algorithms have been presented for FTN signaling in [81]–[83]. All of them employed the characterizations of the circulant matrices to design frequency-domain MMSE equalizers, whose complexity could grow linearly with the block length of the transmitted symbols. Specifically, the authors constructed a circulant equivalent interference matrix by

inserting a few cyclic prefixes and resort to its eigenvalue decomposition relying on FFT to derive the frequency-domain received signal model with a diagonal equivalent channel matrix. After that, the intrinsic time-domain colored noise process was decoupled as an equivalent white noise process in the frequency domain. Through diagonalizing the covariance matrix of the frequency-domain noise, the weights of the MMSE-based FDE could be readily obtained without the matrix inversion of an MMSE-based TDE.

In [81], an FDE scheme combined with hard decision was conceived for uncoded FTN signaling in AWGN and frequency-selective channels. Furthermore, a three-stage-concatenated FDE scheme with soft decision (SoD) was developed for FTN signaling. The three-stage-concatenated structure comprises the MMSE-based FDE, convolutional decoder and unity-rate convolutional (URC) decoder at the receiver side. Among them, the convolutional decoder was regarded as the outer decoder and then exchanged the messages with the inner decoder (including the MMSE-based FDE and the URC decoder). Note that there was also the message interaction between the MMSE-based FDE and the URC decoder. Moreover, the extrinsic information transfer (EXIT) chart was used to investigate the convergence behavior of the FDE algorithm and the maximum achievable rate of FTN signaling. Considering that the overall complexity of the SoD-assisted FDE algorithm only depends on the block length of the transmitted symbols, the MMSE-based FDE algorithm is particularly beneficial for practical long-dispersion channels. Both of the above-mentioned FDE algorithms of FTN signaling employed the approximation of the covariance matrix of the frequency-domain noise, resulting in a considerable performance loss. In [83], a multi-stage turbo FDE-based FTN receiver combined with a noise whitening filter was further developed for improving the BER performance.

2.2.3 Message Passing Algorithms

With respect to advanced signaling processing, factor graphs provide a unified framework for a series of issues, including statistics, coding, statistical physics, signal processing and machine learning [45]–[47]. According to a factorization of a joint posterior probability density function, we can construct the corresponding bipartite graph and then calculate the marginal posterior distribution of the target variable using a sum-product or max-sum algorithm. To simplify the computational complexity, several signal processing approaches based on factor graph have been developed, mainly focusing on GMP in linear state space models. These methods can deal with linear MMSE estimation, the recursive least squares and Kalman filtering algorithms [47]. Then, we can resort to these tabulated message passing rules for the building blocks of linear models to compose a variety of such algorithms without additional computations and derivations. There have been some efficient factor graph-based equalization algorithms designed for FTN signaling [84]–[87], [89], [90].

In [85], an LMMSE equalizer based on factor graph was proposed for FTN signaling to deal with both the inherent ISIs and the colored noise owing to the non-orthogonal matched filter. Two kinds of factor graph models were constructed, i.e., iterative LMMSE equalizer and its

reduced version. Since the equalization structure is independent of the constellation sizes, the LMMSE-based algorithms are suitable for FTN signaling with a large alphabet. Based on the Gaussian approximation to the *a priori* messages from the channel decoder, the authors derived the message passing expressions on factor graph. Moreover, the colored noise process was approximated as an auto-regressive (AR) model, where the relevant parameters could be computed using the Yule-Walker equations.

To meet the increasing requirements of high-mobility wide-band applications, several low-complexity FDE algorithms based on various message passing rules were studied for FTN signaling over doubly selective fading channels [86], [87]. Through inserting a few cyclic prefixes, the inherent interference matrix could be constructed as a circulant matrix. According to the eigenvalue decomposition of the circulant matrix, the inherent interference matrix was rewritten as the product of the normalized discrete Fourier transform (DFT) matrix $\mathbf{F}$ and a diagonal matrix $\mathbf{\Lambda}$ composed of its eigenvalues. Then, the frequency-domain equivalent channel matrix was reformulated as the product of a matrix $\mathbf{C} = \mathbf{FHF}^H$ and a diagonal matrix $\mathbf{\Lambda}$, where $\mathbf{H}$ contains the channel coefficients. For frequency-selective fading channels, the matrix $\mathbf{C}$ is simplified as a diagonal matrix and then the FDE can be implemented as a single-tap equalizer. In contrast, for doubly selective fading channels, the matrix $\mathbf{C}$ is no longer a diagonal matrix. The matrix inversion of $\mathbf{C}$ results in a large computational complexity. Hence, several low-complexity equalization algorithms were further derived based on different message passing rules [86], [87]. In [86], a pair of iterative message passing receivers were designed for FTN signaling in the framework of variational Baysian. Specifically, the authors derived two FDEs based on mean field (MF) [96] and Bethe [97] approximations by minimizing the corresponding variational free energy (VFE) [98], respectively. In terms of computational complexity, they only linearly increase with the block length of the received FTN symbols. Using different message passing rules, a GMP-based FDE algorithm was presented for FTN signaling in doubly selective fading channels in [87]. The frequency-domain received signal model was rewritten as a linear state space model and then a Forney-style factor graph was constructed. Then, the authors derived the forward and backward message passing on factor graph. Moreover, the imperfect frequency-domain channel information was further considered for FTN signaling.

In [89], a serial-schedule belief propagation (FG-SS-BP)-based equalizer-based TDE algorithm was developed for FTN signaling employing various modulation orders in multipath fading channels. To derive a parametric message passing receiver, Gaussian approximation was exploited for simplifying the message updating expressions based on BP rules. Then, the FG-SS-BP algorithm was extended to MFTN signaling. When the typical cyclic prefix insertion scheme of OFDM signaling was employed, the phase continuity was still destroyed due to the subcarrier spacing compression for MFTN signaling. Hence, a continuous phase CP insertion scheme was designed for guaranteeing the properties of continuous phase and circular convolution. The numerical results demonstrated that, when the packing factor is 0.8, the FG-SS-BP-based TDE algorithm could approach the BER performance of the Nyquist-based counterpart. However,

the FG-SS-BP-based algorithm neglected the colored noise induced by non-orthogonal matched filters. Moreover, it also suffered from a considerable performance loss due to the Gaussian approximation of the *a priori* probabilities of the transmitted symbols.

The above-mentioned studies of FTN signaling only discuss the receiver design in linear channels. A novel iterative message passing receiver was designed for FTN signaling in nonlinear channels in [90]. By introducing the Taylor expansion, the nonlinear channel modeled by the three-order Volterra series was linearized. Then, the received signal model could be reformulated into a linear state space model. Considering that the non-orthogonal matched filter resulted in the colored noise in the received signal model, an AR process was exploited to approximate the colored noise. Based on this signal modeling, the corresponding vector-form factor graph was constructed and then the Gaussian message updating expressions were derived between different variables. Similarly, the discrete *a priori* probabilities were also approximated as Gaussian *a priori* probabilities using the EP algorithm, instead of the simple moment matching method.

2.2.4 Channel Estimation

The aforementioned receivers of single-carrier FTN signaling are only discussed in the case of known CSI. However, it is usually challenging to obtain accurate CSI in practice. Note that this is also the most significant difference between CSI and the inherent interferences imposed by FTN signaling. The former is hard to obtain accurately, while the latter is generally assumed to be known, only depending on the packing factor and the shaping pulse. Hence, channel estimation is essential to the receiver design of FTN signaling. Different from the channel estimation of Nyquist signaling, the unknown interferences imposed by the channels are coupled with the interferences induced by non-orthogonal compression. This means that the typical channel estimation methods of Nyquist systems cannot be directly extended for solving the channel estimation problem of non-orthogonal signaling. A few studies have focused on channel estimation of FTN signaling [59], [88], [91].

Inspired by the studies in [85], a joint channel estimation and decoding algorithm based on hybrid message passing rules was further designed for FTN signaling communicating over frequency-selective fading channels in [88]. Firstly, the unknown ISIs imposed by frequency-selective fading channels and the known ISIs induced by time-domain packing were separated. The known structure of the inherent ISIs was used to simplify the factor graph model, thus improving the demodulation performance. Then, the colored noise was also approximately modeled by an AR process, instead of introducing a whitening filter. Through reformulating the received signal model into a linear state space model, a Forney-style factor graph was constructed for joint channel estimation and decoding of single-carrier FTN signaling.n The message passing expressions were derived using BP rules and the approximated Gaussian *a priori* probabilities of the transmitted symbols were computed based on EP rules. To deal with the message updating on the inner product node connecting the channel coefficients and the transmitted symbols, the inner product node was grouped with the noisy measurements

to form a 'soft' factor node. Building on this, parametric message passing was derived using the VMP algorithm. The overall complexity of the proposed BP-EP-VMP algorithm increases linearly with the number of the transmitted symbols and grows cubically with the number of truncated ISI taps.

In [84], a semi-blind frequency-domain JCEE algorithm was designed for FTN signaling. Through inserting a few pilots, the channel coefficients could be estimated using the frequency-domain MMSE filter. Among them, the calculations of the MMSE weights were similar to those in [81], [82]. To improve the accuracy of channel estimation and data detection, a noise whitening algorithm similar to [83] was utilized to update the frequency-domain MMSE weights. Finally, a joint channel estimation and SoD FDE-assisted equalization method was developed for FTN signaling, where the estimated transmitted symbols in the previous iterations could be used as a long pilot block for further improving the performance of channel estimation.

In [59], a novel frequency-domain joint channel estimation and decoding was developed for FTN signaling in frequency-selective fading channels. Instead of the typical AR approximation of the colored noise, the authors constructed a circulant channel equivalent matrix by partitioning the received signals into several short segments and then introduced its eigenvalue decomposition relying on FFT operation to decouple the noise in the frequency domain. Note that the frequency-domain received signal model does not exploit cyclic prefixes, which further improves the spectral efficiency of FTN signaling employing a frequency-domain receiver. Moreover, the specific partition of the received FTN symbols could also enhance the accuracy of channel estimation and data detection. Most of the parametric message passing receivers employed the approximated Gaussian *a priori* probabilities of the transmitted symbols via matching the first and the second order moments, resulting in an additional performance loss. To this end, the GAMP algorithm [48], [99] was employed to design low-complexity equalization of FTN signaling and then embedded in the iteration between the channel estimator and decoder. Moreover, the exact discrete *a priori* probabilities of the transmitted symbols could be used to update the messages between different variables. The overall complexity of the frequency-domain joint channel estimation and decoding algorithm only grows logarithmically with the number of the transmitted symbols. The simulation results showed that FTN signaling employing the aforementioned algorithm could achieve 67% higher transmission rate with a negligible BER performance loss when the roll-off factor of the RRC shaping pulse is $\beta = 0.5$.

Recently, FTN signaling has been combined with the sparse code multiple access (SCMA) to provide a promising bandwidth-efficient scheme for future wireless communication systems [91]. To derive a parametric message passing receiver, a Gaussian message passing algorithm was designed for joint channel estimation and detection of FTN-SCMA signaling. The colored noise imposed by the non-orthogonal matched filter was approximated by an AR model. Furthermore, two active user detection algorithms were developed for FTN-SCMA signaling. The active probability could be derived as not only a weighting factor on the specific edge, but also an unknown variable on factor graph. Moreover, the EP method was exploited to approximate the

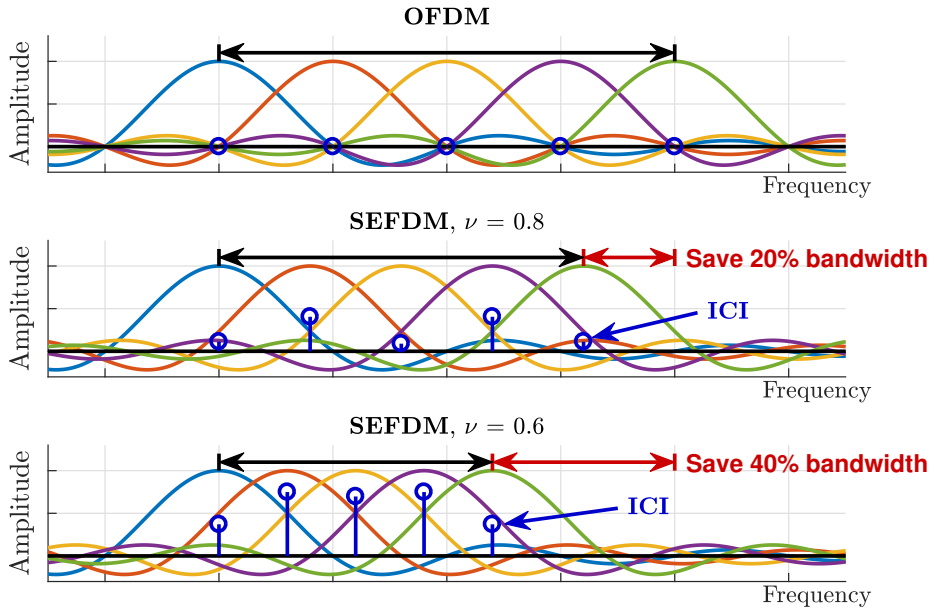


Figure 2.2: Comparison of OFDM and SEFDM signaling.

exact discrete *a priori* messages as Gaussian form by minimizing a specified relative entropy related to the trail distribution and the actual distribution.

2.3 Spectrally Efficient Frequency Division Multiplexing Signaling

Fig. 2.2 shows OFDM signaling and SEFDM signaling with various frequency-domain packing factors. For a fixed transmission rate, SEFDM signaling can effectively reduce the occupied bandwidth through transmitting partially overlapping subcarriers. For a fixed bandwidth, SEFDM signaling can transmit more subcarriers, thus increasing the transmission rate. Since the subcarriers no longer maintain orthogonality, SEFDM signaling inevitably introduces the inherent ICIs. With the decreasing frequency-domain packing factor, the transmission rate of SEFDM signaling increases, at the expense of increasing ICIs. This greatly increases the detection complexity of SEFDM signaling. Numerous existing works considered data detection and channel estimation for SEFDM systems, which are also grouped as TDEs [100]–[104], FDEs [105]–[107] and channel estimation [108]–[110].

2.3.1 Time-Domain Equalization

In [100], a maximum likelihood sequence detector was investigated as the optimal data detection algorithm, which suffered from an excessive computational complexity. Most existing studies focus on reducing the computational complexity of data detection of SEFDM signaling, whilst the demodulation performance can still approach that of the optimal detector [101]–[103], [105],

[107]. The sub-optimal linear detectors based on ZF and MMSE were discussed in [101], which could only perform well in high SNR regions. In [102], a hybrid truncated singular value decomposition (TSVD) and fixed-complexity sphere decoding (FSD) scheme was conceived for data detection of SEFDM signaling, where the TSVD estimates were used as the initializations of the FSD algorithm. Moreover, TSVD was replaced by iterative detector (ID) in [103] and then the ID-FSD algorithm could make a trade-off between the computational complexity and detection performance of SEFDM systems. However, both are only applicable to SEFDM systems having a low number of subcarriers owing to computation complexity. In [104], a low-complexity iterative message passing receiver was firstly proposed for RRC-shaped SEFDM signaling in AWGN channels. To reduce the computational complexity, the authors only considered the dominant interferences from the adjacent subcarriers. Then, the received signal model could be reformulated as a linear state space model. Building on this, a cycle-free Forney-style factor graph was constructed for equalization of RRC-SEFDM signaling. According to GMP rules, a parametric message passing algorithm was derived, whose complexity grows linearly with the number of subcarriers.

2.3.2 Frequency-Domain Equalization

Regarding FDEs of SEFDM signaling, a successive interference cancellation (SIC) scheme based on FFT operations combined with soft decision was conceived for coded SEFDM signaling using a large number of subcarriers [105]. However, soft message interaction between the frequency-domain and time-domain still leads to a prohibitively high computational complexity. In [106], the authors proposed an iterative interference estimation and compensation scheme in the frequency-domain for channel-coded SEFDM signaling, which could outperform the FFT-based detector of [105] in terms of BER performance. To effectively eliminate the ICIs induced by the non-orthogonal waveform, a separate frequency-domain equalizer based on ZF rules and a sequential decoding scheme based on MAP rules were proposed for zero-padding (ZP)-assisted SEFDM signaling in [107], which still results in a relatively high complexity in practice.

2.3.3 Channel Estimation

SEFDM signaling can be regarded as a particular case of MFTN signaling with the Nyquist interval in the time domain, which has also been widely studied in the literature [68], [111], [112]. Experimental SEFDM systems with considerable SE gains have been verified to serve various applications, such as 2.25 Gb/s transmission over the 60 GHz frequency band for future cellular networks, 10 Gb/s optical transmission and 24 Gb/s coherent optical transmission over single-mode fiber. Since SEFDM signaling suffers from an ill-conditioning problem, there are two main obstacles hindered its practicability, i.e., channel estimation and interference cancellation. To this end, several detectors based on sphere decoder were developed to mitigate the inherent ICIs and pilot-based channel estimators have been designed in both time and frequency domains. The above-mentioned data detection methods only consider the demodula-

tion of SEFDM signaling in the perfectly known channels. Due to the negative effect of severe inherent interferences and the ill-conditioning problem imposed by non-orthogonal packing, few published papers have presented channel estimation methods for SEFDM systems over a dispersive fading channel.

Only a few published studies considered pilot-based channel estimation methods of SEFDM signaling. In [108], a time-domain full channel estimator (FCE) based on ZF was designed for SEFDM signaling, which suffered from the ill-conditioning problem due to frequency-domain compression. To tackle this issue, a time-domain partial channel estimator (PCE) based on ZF was conceived for SEFDM signaling in [109]. For the PCE scheme, the pilots are only transmitted on mutually orthogonal subcarriers and the remaining subcarriers transmit zeros. In [110], three frequency-domain channel estimation schemes based on pilots were proposed for SEFDM. Specifically, interpolation-based partial channel estimation, OFDM pilots relying on interpolation and OFDM pilots dispelling with interpolation were considered. The first method, i.e., the interpolation-based partial channel estimation method, employed the observations within the subsets of mutually orthogonal SEFDM subcarriers. It has been stated in [109] that there are at least two mutually orthogonal subcarriers in an SEFDM system having a packing factor of $\alpha = a/b$, where $a, b \in \mathbb{N}$, $a < b$, $N > b$, and N is the number of subcarriers[2]. Hence, the channel's frequency response (CFR) could be obtained over the $(\lceil N/b \rceil)$ pilot subcarriers using the least squares (LS) method. Then, the CFRs of the remaining $(N - \lceil N/b \rceil)$ subcarriers could be interpolated using the estimated CFRs, where linear interpolation was used in [110] for simplicity. To mitigate the ill-conditioning problem of SEFDM signaling, the second method employs an OFDM pilot occupying the same bandwidth as SEFDM signaling. Since SEFDM signaling packs more subcarriers in a fixed bandwidth, the transmitted OFDM pilot only has $(\lceil \alpha \times N \rceil)$ subcarriers. For an SEFDM system with $\alpha = a/b$ where $a, b \in \mathbb{N}$, $a < b$, $N > b$, there are $(\lceil N/b \rceil)$ subcarriers out of N_p with an integer multiple of $(\alpha \Delta f_s)$, where Δf_s is the spacing of subcarriers. Hence, the corresponding CFRs could be found directly by LS estimation. Similarly, the CFRs over the remaining $(N - \lceil N/b \rceil)$ subcarriers were obtained by interpolation. To avoid the drawbacks of the interpolation algorithms, the third method employed an orthogonal pilot symbol that occupied the identical bandwidth as the non-orthogonal symbols, for a fixed number of subcarriers and frequency spacing. Under this configuration, channel estimates could be obtained directly via the LS method without interpolation. However, this method needs extra samples to compensate for the $(1 - \alpha)/(\alpha \Delta f_s)$ overhead, resulting in an extended pilot symbol period. Compared to the other two methods, the redundancy introduced by this scheme is determined by the sending frequency of the pilot data. For example, if the pilot is transmitted every K information symbols, the redundancy is calculated as $[(1 - \alpha)/(K + 1)] \times 100\%$. However, the aforementioned channel estimation methods of SEFDM signaling still cannot achieve an acceptable performance.

[2]The variable b represents the subcarrier spacing before frequency-domain compression, while a denotes the subcarrier spacing after frequency-domain compression.

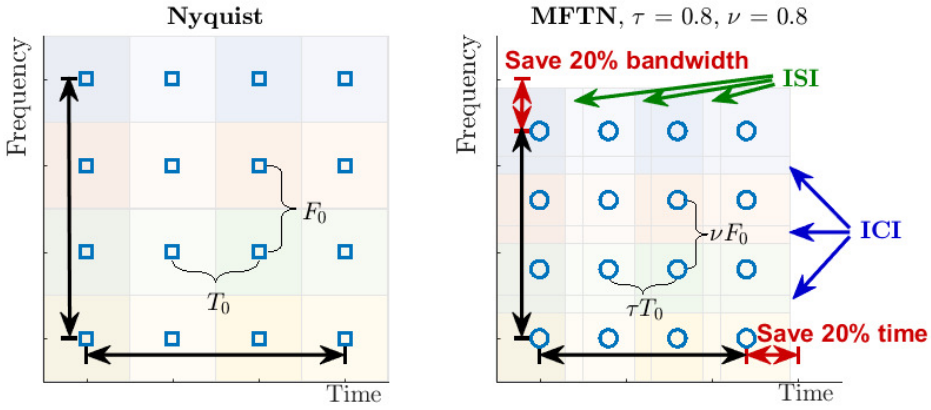


Figure 2.3: Comparison of Nyquist and MFTN signaling.

2.4 Multi-Carrier Faster-Than-Nyquist Signaling

Single-carrier FTN signaling or multi-carrier SEFDM signaling only employs the one-dimensional time-domain or frequency-domain packing. To further improve the spectral efficiency of non-orthogonal waveforms, Rusek and Anderson proposed a two-dimensional time-frequency packing MFTN signaling [30]. By relaxing the constraints on the orthogonality of the signaling pulse and subcarriers concerning the symbol interval and frequency spacing, MFTN signaling can provide a higher bandwidth efficiency than one-dimensional non-orthogonal signaling [31], [34]. Fig. 2.3 provides a comparison of Nyquist signaling and MFTN signaling. Observe that two-dimensional time-frequency packing MFTN signaling can effectively save time and frequency band resources. However, MFTN signaling inevitably inflicts severe ISIs and ICIs, which result in prohibitively high receiver complexity. Accordingly, conceiving low-complexity equalization is critical, but challenging for MFTN systems.

A popular class of MFTN signaling employs transmit precoding [113], [114]. Specifically, in [113], a linear precoding scheme combined with receiver-side turbo ICI cancellation was developed for MFTN systems. To circumvent the potential transmission contamination caused by small eigenvalues of the interference matrix, a Tomlinson–Harashima precoding (THP) method was designed for one-dimensional frequency-packed MFTN systems using high-order modulation in [114].

The other techniques employ advanced equalization at the receiver [31], [34], [65], [115]–[117]. In [115], the optimal MAP method was derived by harnessing the BCJR algorithm, which however imposed an exponentially escalating complexity. In [31], a suboptimal reduced-state BCJR detector based on SIC was proposed. However, its complexity still increases exponentially with the length of the truncated interferences. As a further advance, a memoryless turbo receiver having linearly increasing complexity was designed for MFTN systems in [34]. Hence, this less complex but less powerful receiver results in a BER performance loss in aggressive time-frequency packing scenarios. To strike a BER performance versus complexity trade-off, a pair of MMSE-based equalizers were developed for MFTN signaling in [116]. Unfortunately,

the two-dimensional MMSE-based equalizer suffers from a significant performance loss in severe ICI scenarios. By contrast, the one-dimensional version of [116] combined with SIC can asymptotically approach the MAP performance. However, the complexity of both methods is still dominated by the associated matrix inversion calculations. For longhaul optical transmission scenarios, turbo parallel interference cancellation schemes combined with BCJR-based ISI cancellation were proposed for time-frequency packed wavelength-division-multiplexed systems [65], [117].

Most of the above-mentioned equalizers were proposed for AWGN channels. Hence they cannot deal with the colored noise imposed by non-orthogonal matched filtering. It has been demonstrated that mitigating the effect of colored noise improves the BER performance [84]. Hence, it is necessary to tackle the inherent colored noise problem to design an efficient MFTN receiver. In [32], the authors proposed a GMP-based TDE relying on a vector-form trellis interference structure for MFTN systems operating in multipath channels. The truncated non-diagonal covariance matrix of the colored noise was exploited for improving the accuracy of message updating. To develop a parametric message passing receiver, the discrete *a priori* probabilities of the transmitted symbols are approximated by Gaussian distributions in [32], which results in an additional BER performance degradation.

When the packing factors are significantly reduced, MFTN signaling tends to suffer from a severe ill-conditioning problem, which may lead to the divergence of the equalization algorithms. However, there is a paucity of studies on tackling the ill-conditioning problem of MFTN signaling and all MFTN receivers mentioned above were investigated in the perfectly known CSI scenarios. For practical applications, channel coefficients are usually unavailable and need to be estimated. The JCEE techniques are efficient solutions to approach the accurate channel coefficients. Nevertheless, very few published works are related to JCEE of MFTN signaling. Since severe the two-dimensional interferences of MFTN signaling are tightly coupled with the Doppler spreads and frequency selectivity induced by frequency-selective fading channels, the published JCEE solutions of single-carrier FTN signaling [59], [88], [91], [118] to MFTN signaling. In addition, these JCEE algorithms of single-carrier FTN systems can only tackle the one-dimensional interferences imposed by non-orthogonal compression and cannot alleviate the ill-conditioning problem induced by time-frequency packing.

2.5 Index Modulation

In multi-carrier systems, IM can be combined with OFDM signaling, resulting in OFDM-IM signaling [44]. Compared to the typical OFDM signaling, OFDM-IM outperforms in terms of spectral efficiency, energy efficiency and peak to average power ratio (PAPR) [119]. For OFDM-IM signaling, the input bits are divided into two parts for selecting indices and constellation mapping, respectively. According to the first parts of the input bits, a portion of subcarriers is activated for transmitting the modulated symbols after constellation mapping, while the rest

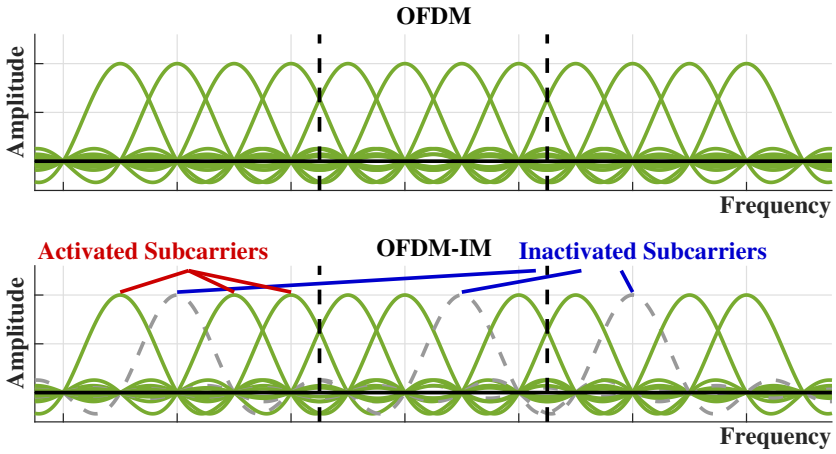


Figure 2.4: Comparison of OFDM and OFDM-IM signaling.

of the subcarriers are set to zeros. Fig. 2.4 depicts the comparisons of OFDM and OFDM-IM schemes with twelve subcarriers. Each IM subblock contains four subcarriers, comprising three activated subcarriers and one inactivated subcarrier. The activated subcarriers explicitly transmit the constellation symbols, while the inactivated subcarriers implicitly carry the IM bits. Note that OFDM-IM signaling has the same spectral efficiency as OFDM signaling in Fig. 2.4. Since the former has a certain number of inactivated subcarriers, it can effectively reduce the PAPRs of multi-carrier systems, and is more robust in frequency-selective fading channels.

Due to its high spectral efficiency and energy efficiency, IM has been combined with non-orthogonal waveforms. In [120]–[122], one-dimensional packing FTN signaling has been combined with IM for developing more attractive physical waveforms, with both high spectral efficiency and energy efficiency. It has been demonstrated that a multi-carrier system with IM is beneficial in terms of minimum Euclidean distance in low transmission rate scenarios [43]. However, the demodulation of non-orthogonal signaling becomes extremely complex due to the additional index domain.

In [120], IM was firstly introduced in single subcarrier FTN systems, where the inactivated subcarriers of zeros were exploited for mitigating the inherent ISIs. At the receiver side, the ISIs of FTN signaling were eliminated by the MMSE-based FDE [84] and then an ML-based detector was used for demapping the index and data bits. The computational complexity of ML detection increases exponentially with the number of bits in each IM subblock. In [121], a precoding method based on eigenvalue decomposition replaces the MMSE-based FDE of [120], which improves the BER performance in the case of small packing factors. However, these methods separate interference elimination from IM detection, inevitably resulting in an additional BER performance loss. Moreover, a complex fusion of FTN and space-time multiple-mode IM was studied in [122], where the FTN-IM signaling was shown to approach the spatial

diversity gain of multi-antenna systems.

Unlike single-carrier scenarios, only a few studies have discussed index-modulated multi-carrier non-orthogonal signaling [123], [124]. In [123], SEFDM signaling has been combined with IM for mitigating inherent ICIs. The corresponding receiver only considers the ICIs imposed by the adjacent subcarriers in the same IM subblock and then employs the IM detection. Consequently, the design suffers from additional BER performance degradation and excessive computational complexity. To reduce the complexity of IM detection, a two-stage demodulation structure was designed for SEFDM-IM signaling in [124], employing an MMSE-based equalization and a LLR-based IM detection combined with ML. Since only part of the activation patterns with the most significant LLR values are retained for the subsequent ML detection, there is a performance penalty. Moreover, to avoid the colored noise imposed by the non-orthogonal demodulation, the Gram-Schmidt orthogonalization was used to compute the orthogonal basis of matched filter in [124]. Once the packing factor varies, the orthogonal basis has to be recalculated, which makes it inflexible in practice.

2.6 Conclusion

This section has overviewed the existing studies on the receiver design of single-carrier FTN signaling, one-dimensional packing SEFDM signaling, two-dimensional packing MFTN signaling and index-modulated non-orthogonal waveforms. Numerous works deal with channel estimation and symbol detection of single-carrier FTN signaling in AWGN and complex channels. In contrast, there are only a few studies discussing the receiver design of multi-carrier non-orthogonal signaling, including SEFDM signaling and MFTN signaling, especially in frequency-selective fading channels. This significantly limits the application of non-orthogonal signaling. Against this background, designing low-complexity and efficient receivers for multi-carrier non-orthogonal signaling over frequency-selective fading channel is an important, but very challenging research work.

Chapter 3

Joint Channel Estimation and Equalization for Index-Modulated SEFDM Signaling

3.1 Introduction

To meet the demand for high-speed data transmission of the future wireless communications under the scarce spectrum resources, non-orthogonal transmission schemes having high spectral efficiency have been gained more and more attentions in recent years [125]–[129]. By allowing the overlapping of the originally orthogonal subcarriers, SEFDM signaling becomes capable of significantly improving the spectral efficiency, at the cost of deliberately introducing ICIs. However, the inherent ICIs increase the complexity of non-orthogonal demodulation at the receiver side.

Numerous literatures have studied the receiving methods of SEFDM signaling for effectively eliminating ICIs introduced by non-orthogonal transmission. Unfortunately, its optimal MLS detection suffers from an excessive computational complexity [130]. To reduce the complexity, whilst still performing close to the optimal detector, numerous contributions have been focused on receiver design for SEFDM signaling [102], [103], [105], [107]–[110]. The FSD based equalizer combined with TSVD [102] and the ID of [103] have been shown to be applicable to systems having a low number of subcarriers. By contrast, the FFT-based SIC of [105] was conceived for SEFDM systems having a large number of subcarriers. However, soft information exchanging between the time- and frequency-domains still results in prohibitively high computational complexity. For effectively mitigating the ICI imposed by the non-orthogonality of SEFDM signaling, a separate frequency-domain ZF-based equalizer and a MAP sequential decoders were developed in [107] for ZP-aided SEFDM systems. The above SEFDM receivers have assumed the availability of perfectly known CSI, which limits the application of these algorithms in practice.

Due to the effect of strong inherent interference and owing to the ill-conditioning nature of SEFDM systems, only a few contributions have proposed channel estimators for SEFDM signaling over dispersive fading channels. In [108], a time-domain FCE based on ZF was proposed for SEFDM systems, which suffers from an ill-conditioning problem imposed by compressing the spacing of subcarriers. To eliminate this problem, a time-domain PCE was developed in [109], which transmits pilots only on mutually orthogonal subcarriers. Moreover, in [110] three pilot-based frequency-domain channel estimation methods were designed for SEFDM systems at the cost of an additional interpolation operation or at the expense of introducing extra pilot symbol periods. By contrast, JCEE schemes can make full use of the recovered symbols for improving the accuracy of channel estimation. This not only effectively reduces the number of pilot frequencies, but also significantly improves the demodulation performance of SEFDM signaling in multipath channels. Therefore, it is urgent to design a low-complexity JCEE method for SEFDM signaling.

To further improve spectral efficiency and energy efficiency, SEFDM signaling is combined with IM. Since the inactivated subcarriers can be used to mitigate the inherent ICIs of non-orthogonal multi-carrier system, SEFDM-IM signaling improves the BER performance for a fixed spectral efficiency. Against this background, a novel iterative receiver is designed for SEFDM-IM systems communicating over frequency-selective fading channels, including a parametric iterative equalization algorithm based on GMP-EP in known CSI scenarios and a JCEE algorithm based on GMP-EP-VMP in unknown CSI scenarios.

In the case of perfectly known CSI, a reconfigurable non-orthogonal demodulation architecture is designed for maintaining compatible with typical multi-carrier systems, where a CAR model to deal with the resultant colored noise. Taking into account the dependencies between the SEFDM-IM subcarriers, an extended constellation including the deactivated symbols of zeros is introduced for exploring the potential performance gain of joint ICI mitigation and IM detection. By truncating the interferences, a Forney-style factor graph having two subgraphs with scalar input is constructed based on the linear state space model of SEFDM-IM equalization. Accordingly, a series of parametric message updating expressions constructed the FFGs are derived according to GMP rules, where the discrete distribution of the transmitted symbols can be approximated by a Gaussian form using EP rules by minimizing the Kullback–Leibler divergence (KLD) [131].

For unknown CSI scenarios, a low-complexity frequency-domain JCEE algorithm is proposed for SEFDM-IM systems communicating over frequency-selective fading channels. To alleviate the potential error propagations imposed by channel estimation due to the deactivated subcarriers of zeros and improve the accuracy of channel estimates, this work constructs a multi-layer factor graph connected via channel variables on the subcarriers having the same indices between the different SEFDM-IM symbols. Since applying BP to the inner product node of channel estimation and equalization leads to excessive computational complexity, the VMP rules defined on an equivalent soft node are used to simplify the message updating expressions between the

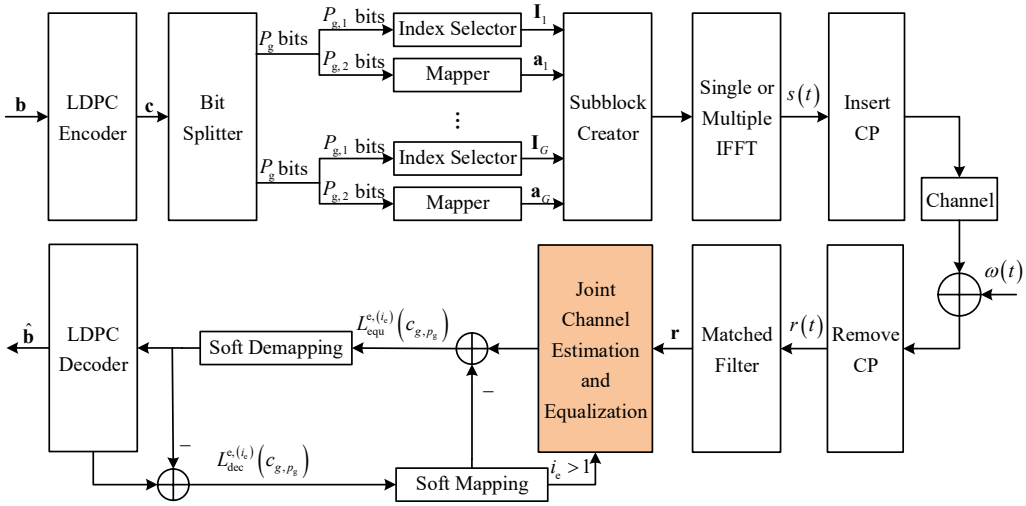


Figure 3.1: Block diagram of an LDPC-coded SEFDM-IM tranceiver.

channel estimator and the equalizer into a Gaussian form. Combined with other diagonalized approximations and FFT operations, a parametric algorithm can be derived on factor graph.

Finally, the proposed iterative algorithms have been evaluated via MATLAB simulations in terms of BER and NMSE performance. Compared to its Nyquist signaling based counterpart, SEFDM-IM signaling relying on the proposed algorithm exhibits up to 25% higher bandwidth efficiency without any BER performance degradation.

The rest of this chapter is organized as follows. The system model of SEFDM-IM signaling over frequency-selective fading channels is given in Section 3.2. In Section 3.3, GMP-EP equalization is developed for SEFDM-IM systems under the assumption of having perfectly known CSI. In Section 3.4, the proposed GMP-EP-VMP JCEE is derived. The performance of the proposed algorithms is evaluated by Monte Carlo simulations in Section 3.5. Finally, the conclusions are drawn in Section 3.6.

3.2 System Model

The block diagram of a low-density parity-check (LDPC)-coded[1] SEFDM-IM transceiver is depicted in Fig. 3.1. At the transmitter side, N_b information bits $\mathbf{b} = [b_0, \cdots, b_{N_\text{b}-1}]^T$ are encoded and then N_c coded bits $\mathbf{c} = [c_0, \cdots, c_{N_\text{c}-1}]^T$ are equally partitioned into G groups, each containing $P_\text{g} = N_\text{c}/G$ bits, i.e., $\mathbf{c}_g = [c_{g,0}, \cdots, c_{g,p_\text{g}}, \cdots, c_{g,P_\text{g}-1}]^T$, where c_{g,p_g} is equal to the $(gP_\text{g} + p_\text{g} + 1)$-th element of $\mathbf{c}$. Each group of P_g coded bits is mapped to an SEFDM-IM subblock of length $K_\text{g} = K/G$, where K is the number of SEFDM-IM subcarriers. For each SEFDM-IM subblock, only K_a out of K_g subcarriers are activated to transmit M-ary symbols, where the first $P_{\text{g},1} = \log_2\lfloor\binom{K_\text{g}}{K_\text{a}}\rfloor$ of P bits are used for determining K_a indices of the activated

[1]As a widely-used channel code, the LDPC code is employed only as a paradigm in the thesis. The type of channel code is independent of the following derivations of the demodulation algorithms. That means the proposed receivers of this thesis can also employ other channel codes.

subcarriers, while the remaining $P_{\mathrm{g},2} = K_{\mathrm{a}} \log_2 M$ bits are mapped onto the constellation points $\boldsymbol{\mathcal{S}}$. The activated indices and modulated M-ary symbols of the g-th subblock are denoted as $\mathbf{I}_g = \{I_{g,0}, I_{g,1}, \cdots, I_{g,K_{\mathrm{a}}-1}\}, I_{g,k_{\mathrm{a}}} \in \{0, \cdots, K_{\mathrm{g}}-1\}$ and $\mathbf{a}_g = [a_{g,0}, a_{g,1}, \cdots, a_{g,K_{\mathrm{a}}-1}]^T, a_{g,k_{\mathrm{a}}} \in \boldsymbol{\mathcal{S}}$. The power of the signal constellation is normalized to unit average power, i.e., $\mathbb{E}\{\mathbf{a}_g^H \mathbf{a}_g\} = K$. The vector of the modulated SEFDM symbols in the g-th subblock is $\mathbf{x}_g = [x_{g,0}, \cdots, x_{g,K_{\mathrm{g}}-1}]^T$, where $x_{g,k_{\mathrm{g}}} = a_{g,k_{\mathrm{a}}}$ for $k_{\mathrm{g}} = I_{g,k_{\mathrm{a}}} \in \mathbf{I}_g$ and $x_{g,k_{\mathrm{g}}} = 0$ for $k_{\mathrm{g}} \notin \mathbf{I}_g$. Then, G subblocks are concatenated to generate the K transmitted SEFDM-IM symbols, i.e., $\mathbf{x} = [\mathbf{x}_0^T, \cdots, \mathbf{x}_{G-1}^T]^T$. To enhance the spectral efficiency, the complex-valued symbols $\mathbf{x}$ are mapped to K non-orthogonal subcarriers relying on the bandwidth packing factor of ν. The IFFT can be used for modulation in the SEFDM-IM systems [132]. Consequently, the equivalent baseband signal is expressed as

$$s(t) = \sqrt{\frac{K_{\mathrm{g}}}{K_{\mathrm{a}} T_0}} \sum_{k=0}^{K-1} x_k e^{\frac{j2\pi\nu k t}{T_0}}, \tag{3.1}$$

where x_k is the k-th modulated symbol, $\sqrt{K_{\mathrm{g}}/K_{\mathrm{a}}}$ is the signal power normalization factor, T_0 denotes the duration of the time-domain symbols.

Without loss of generality, the length of cyclic prefix is assumed to be sufficient for ISI-free transmission over an L-tap frequency-selective fading channel. The received SEFDM-IM signal is given by

$$r(t) = \sum_{l=0}^{L-1} h_l s(t - \tau_l) + \omega(t), \tag{3.2}$$

where h_l and τ_l are channel impulse response (CIR) and delay of the l-th path, respectively, and $\omega(t)$ is the AWGN process with zero mean and variance σ_0^2.

To support reconfigurable architectures and facilitate compatibility with the receivers of the existing systems, instead of introducing additional orthonormalization operation, a non-orthogonal matched filtering [133] is adopted. The k_{r}-th output of the non-orthogonal matched filter is

$$\begin{aligned} r_{k_{\mathrm{r}}} &= \sqrt{\frac{K_{\mathrm{a}}}{K_{\mathrm{g}} T_0}} \int_0^{T_0} r(t) e^{-\frac{j2\pi\nu k_{\mathrm{r}} t}{T_0}} dt \\ &= \frac{1}{T_0} \sum_{k_{\mathrm{t}}=0}^{K-1} x_{k_{\mathrm{t}}} \sum_{l=0}^{L-1} h_l e^{-\frac{j2\pi\nu k_{\mathrm{t}} \tau_l}{T_0}} \int_0^{T_0} e^{-\frac{j2\pi\nu(k_{\mathrm{r}}-k_{\mathrm{t}})t}{T_0}} dt + \omega_{k_{\mathrm{r}}} \\ &= \sum_{k_{\mathrm{t}}=0}^{K-1} \phi_{k_{\mathrm{r}},k_{\mathrm{t}}} \breve{h}_{k_{\mathrm{t}}} x_{k_{\mathrm{t}}} + \omega_{k_{\mathrm{r}}}, \end{aligned} \tag{3.3}$$

where $\breve{h}_{k_{\mathrm{t}}} = \sum_{l=0}^{L-1} h_l e^{-\frac{j2\pi\nu k_{\mathrm{t}} \tau_l}{T_0}}$ is the CFR of the k_{t}-th subcarrier, $\omega_{k_{\mathrm{r}}} = \sqrt{\frac{K_{\mathrm{a}}}{K_{\mathrm{g}} T_0}} \int_0^{T_0} \omega(t)$ $e^{-\frac{j2\pi\nu k_{\mathrm{r}} t}{T_0}} dt$ is the colored noise sample of the k_{t}-th subcarrier, the complex-valued autocorrelation matrix of the colored noise process is $\mathbb{E}\{\boldsymbol{\omega}\boldsymbol{\omega}^H\} = K_{\mathrm{a}}/K_{\mathrm{g}} \sigma_0^2 \boldsymbol{\Phi}$, $\boldsymbol{\omega} = [\omega_0, \cdots, \omega_{K-1}]^T$,

and $\mathbf{\Phi}$ denotes the interference matrix with elements $\mathbf{\Phi}_{[m,n]} = \phi_{m,n} = e^{-j\pi\nu(m-n)}\text{sinc}[\nu(m-n)]$.

3.3 Iterative Equalization Based on GMP-EP

In this section, a joint interference mitigation and detection scheme is developed for SEFDM-IM systems under the assumption of perfectly known CSI in this section. By introducing the extended constellation containing deactivated subcarriers and reformulating the SEFDM-IM equalization design via a linear state space model, the factor graph having two subgraphs corresponding to the symbol-based interference mitigation and the colored noise approximation is constructed. Besides, discrete input messages are parameterized by a Gaussian form based on EP, hence all messages on factor graph are derived using GMP rules. This work independently solves the known interference elimination problem of SEFDM-IM systems, whilst additionally providing a valuable research basis for JCEE techniques for SEFDM-IM signaling in Section 3.4.

3.3.1 The Colored Noise Approximation Using CAR Model

For single-carrier FTN signaling, auto-regressive model has been widely used for approximating the time-domain colored noise process [85], [88]. However, the autocorrelation matrix of the frequency-domain colored noise is a complex-valued Toeplitz matrix, which cannot be effectively characterized via an real-valued auto-regressive model. To this end, this work employs the P_0-th order CAR model [134] for characterizing the colored noise as

$$\xi_k = \sum_{p_0=1}^{P_0} \lambda_{p_0}\xi_{k-p_0} + \tilde{\xi}_k = \boldsymbol{\lambda}^T\boldsymbol{\xi}_{k-1} + \tilde{\xi}_k, \tag{3.4}$$

where $\boldsymbol{\lambda}_\omega = [\lambda_0, \cdots, \lambda_{P_0-1}]^T$ denotes the complex-valued coefficient vector, $\boldsymbol{\xi}_{k-1} = [\xi_{k-1}, \cdots, \xi_{k-P_0}]^T$ is defined as the state vector, while $\tilde{\xi}_k$ is a complex-valued AWGN sample with zero mean and variance $\sigma_{\tilde{\xi}}^2 = \phi_{0,0} - \boldsymbol{\phi}_{P_0}^H\boldsymbol{\lambda}_\omega$. By minimizing the mean squared error, i.e., $\mathbb{E}\{|\tilde{\xi}_k|^2\}$, the optimal CAR coefficients are given by $\boldsymbol{\lambda}_\omega = \mathbf{R}_{P_0}^{-1}\boldsymbol{\phi}_{P_0}$, where $\mathbf{R}_{P_0} = \frac{K_\text{a}\sigma_0^2}{K_\text{g}}[\phi_{0,0}, \phi_{0,1}, \cdots, \phi_{0,P_0-1}; \cdots; \phi_{P_0-1,0}, \phi_{P_0-1,1}, \cdots, \phi_{P_0-1,P_0-1}]$ and $\boldsymbol{\phi}_{P_0} = [\phi_{0,0}, \cdots, \phi_{0,P_0-1}]^T$.

3.3.2 Factor Graph Representation

Due to the inter-dependence of the SEFDM-IM subcarriers in a subblock, conventional receivers typically rely on a multistage demodulation strategy [124], i.e., the interferences are eliminated in the first stage and then ML detection is employed for recovering the index bits and the symbol bits in the second stage. To develop a low-complexity joint interference mitigation and IM detection algorithm for SEFDM-IM signaling, an extended constellation $\{0, \boldsymbol{\mathcal{S}}\}$ is intentionally introduced for incorporating the deactivated subcarriers of zeros. Accordingly, activated pattern constraints can be included as the *a priori* probability distribution of each transmitted symbol.

Owing to the fact that the ICI introduced by packing the non-orthogonal subcarriers decreases as the subcarrier spacing increases, only the interferences from the immediately adjacent subcarriers are considered for reducing the complexity. Assuming that the truncated length is K_{I}, only the interferences imposed by the neighboring $2K_{\mathrm{I}}$ subcarriers are considered for symbol detection on the current subcarrier. Accordingly, the received signal of (3.3) is rewritten as

$$r_k = \boldsymbol{\phi}_k^T \mathbf{s}_k + \omega_k, \tag{3.5}$$

where $\boldsymbol{\phi}_k = [\phi_{k,k-K_{\mathrm{I}}}, \cdots, \phi_{k,k}, \cdots, \phi_{k,k+K_{\mathrm{I}}}]^T$ represents the truncated interference vector of the k-th subcarrier, $\mathbf{s}_k = [s_{k-K_{\mathrm{I}}}, \cdots, s_k, \cdots, s_{k+K_{\mathrm{I}}}]^T$ denotes the state vector with $s_k = \breve{h}_k x_k$, x_k belongs to the extended constellation $\{0, \boldsymbol{\mathcal{S}}\}$. The state vector $\mathbf{s}_{k-1}$ and $\mathbf{s}_k$ satisfy the following linear state transition model of

$$\mathbf{s}_k = \boldsymbol{\Xi}_{\dot{K}_{\mathrm{I}}} \mathbf{s}_{k-1} + \boldsymbol{\zeta}_{\dot{K}_{\mathrm{I}}} s_{k+K_{\mathrm{I}}}, \tag{3.6}$$

where $\boldsymbol{\Xi}_{\dot{K}_{\mathrm{I}}} = [\mathbf{0}_{\dot{K}_{\mathrm{I}}-1}, \mathbf{I}_{\dot{K}_{\mathrm{I}}-1}; \mathbf{0}_{\dot{K}_{\mathrm{I}}}^T]$, $\boldsymbol{\zeta}_{\dot{K}_{\mathrm{I}}} = [\mathbf{0}_{\dot{K}_{\mathrm{I}}-1}; 1]$, and $\dot{K}_{\mathrm{I}} = 2K_{\mathrm{I}} + 1$. According to the colored noise approximation in (3.4), (3.5) can be rewritten as

$$r_k = \boldsymbol{\phi}_k^T \mathbf{s}_k + \xi_k, \tag{3.7}$$

where $\xi_k = \boldsymbol{\zeta}_\xi^T \boldsymbol{\xi}_k$ with $\boldsymbol{\zeta}_\xi = [1; \mathbf{0}_{P_0-1}]$. The linear transition constraint between $\boldsymbol{\xi}_k$ and $\boldsymbol{\xi}_{k-1}$ is

$$\boldsymbol{\xi}_k = \boldsymbol{\Xi}_\xi \boldsymbol{\xi}_{k-1} + \boldsymbol{\zeta}_\xi \tilde{\xi}_k, \tag{3.8}$$

where $\boldsymbol{\Xi}_\xi = [\boldsymbol{\lambda}_\omega^T; \mathbf{I}_{P_0-1}, \mathbf{0}_{P_0-1}]$.

Based on (3.6)-(3.8), the factor graph of the SEFDM-IM system with known CSI is constructed in Fig. 3.2. Subgraph ① and Subgraph ② correspond to the symbol-wise interference mitigation and the colored noise approximation, respectively. The edges denote variables and the factor nodes represent local functions. The natural schedule for the message computations on factor graph consists of two independent recursions, namely, forward message passing along the direction of the arrow and backward message passing opposite the direction of the arrow. In the following, the messages on the factor graph will be derived in details.

3.3.3 Message Updating for Hybrid GMP-EP Equalization

To design a parametric iterative equalization algorithm for SEFDM-IM signaling, the GMP algorithm [47], [135] is employed to derive the message updating expressions between variables on factor graph in Fig. 3.2. The forward and backward messages are characterized by the mean vector $\overrightarrow{\mathbf{m}}$ and the covariance matrix $\overrightarrow{\mathbf{V}}$ or the transformed mean vector $\overleftarrow{\mathbf{W}}\overleftarrow{\mathbf{m}}$ and the weight matrix $\overleftarrow{\mathbf{W}} = \overrightarrow{\mathbf{V}}^{-1}$, respectively.

• *Gaussian Message Updating for Interference Mitigation in Subgraph ①*

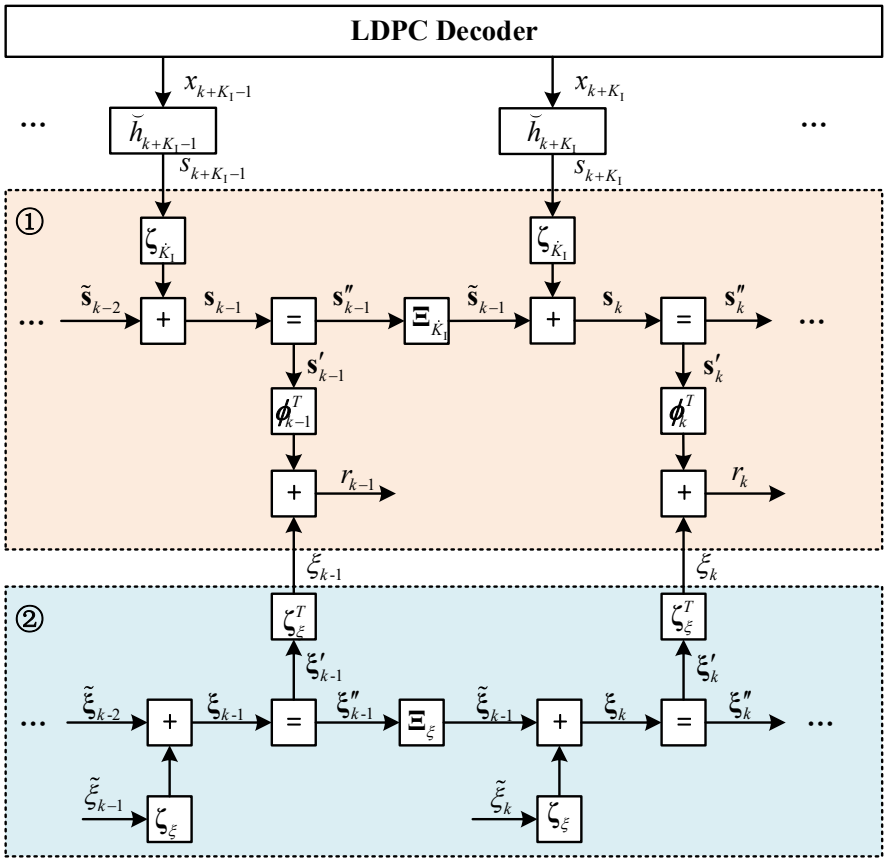


Figure 3.2: Factor graph for equalization of SEFDM-IM signaling with known CSI.

In the i-th iteration, the mean vector $\overrightarrow{\mathbf{m}}_{\mathbf{s}_{k-1}}(i)$ and covariance matrix $\overrightarrow{\mathbf{V}}_{\mathbf{s}_{k-1}}(i)$ of the state vector $\mathbf{s}_{k-1}$ are assumed to be available. According to the forward message passing rules for the composite block of multiplication and equality (as listed in TABLE 4 of [47]), the forward messages of the variables $\mathbf{s}''_{k-1}$ are given by

$$\overrightarrow{\mathbf{m}}_{\mathbf{s}''_{k-1}}(i) = \overrightarrow{\mathbf{m}}_{\mathbf{s}_{k-1}}(i) + \frac{\overrightarrow{\mathbf{V}}_{\mathbf{s}_{k-1}}(i)\left(\boldsymbol{\phi}^T_{k-1}\right)^H\left(r_{k-1} - \boldsymbol{\phi}^T_{k-1}\overrightarrow{\mathbf{m}}_{\mathbf{s}_{k-1}}(i)\right)}{\overrightarrow{V}_{\xi_{k-1}}(i-1) + \boldsymbol{\phi}^T_{k-1}\overrightarrow{\mathbf{V}}_{\mathbf{s}_{k-1}}(i)\left(\boldsymbol{\phi}^T_{k-1}\right)^H}, \tag{3.9}$$

$$\overrightarrow{\mathbf{V}}_{\mathbf{s}''_{k-1}}(i) = \overrightarrow{\mathbf{V}}_{\mathbf{s}_{k-1}}(i)\frac{\overrightarrow{\mathbf{V}}_{\mathbf{s}_{k-1}}(i)\left(\boldsymbol{\phi}^T_{k-1}\right)^H\boldsymbol{\phi}^T_{k-1}\overrightarrow{\mathbf{V}}_{\mathbf{s}_{k-1}}(i)}{\overrightarrow{V}_{\xi_{k-1}}(i-1) + \boldsymbol{\phi}^T_{k-1}\overrightarrow{\mathbf{V}}_{\mathbf{s}_{k-1}}(i)\left(\boldsymbol{\phi}^T_{k-1}\right)^H}, \tag{3.10}$$

where r_{k-1} is the k-th sample of the received SEFDM-IM signal and $\overrightarrow{V}_{\xi_{k-1}}(i-1)$ is the forward variance of the approximate noise ξ_{k-1} in the $(i-1)$-th inner iteration. Based on the forward updating rules of the matrix multiplication node (as listed in TABLE 3 of [47]), the forward mean vector and covariance matrix of $\tilde{\mathbf{s}}_{k-1}$ are obtained, respectively, as

$$\overrightarrow{\mathbf{m}}_{\tilde{\mathbf{s}}_{k-1}}(i) = \boldsymbol{\Xi}_{\dot{K}_\mathrm{I}}\overrightarrow{\mathbf{m}}_{\mathbf{s}''_{k-1}}(i), \tag{3.11}$$

$$\overrightarrow{\mathbf{V}}_{\tilde{\mathbf{s}}_{k-1}}(i) = \boldsymbol{\Xi}_{\dot{K}_\mathrm{I}}\overrightarrow{\mathbf{V}}_{\mathbf{s}''_{k-1}}(i)\boldsymbol{\Xi}^H_{\dot{K}_\mathrm{I}}. \tag{3.12}$$

Based on the forward messages in (3.9)-(3.12), relying to the forward message passing rules for the composite block of multiplication and addition (as listed in TABLE 4 of [47]), the forward messages of $\mathbf{s}_k$ can be updated as

$$\overrightarrow{\mathbf{m}}_{\mathbf{s}_k}(i) = \overrightarrow{\mathbf{m}}_{\tilde{\mathbf{s}}_{k-1}}(i) + \breve{h}_{k+K_\mathrm{I}} \overrightarrow{m}_{x_{k+K_\mathrm{I}}}(i-1)\boldsymbol{\zeta}_{\dot{K}_\mathrm{I}}, \tag{3.13}$$

$$\overrightarrow{\mathbf{V}}_{\mathbf{s}_k}(i) = \overrightarrow{\mathbf{V}}_{\tilde{\mathbf{s}}_{k-1}}(i) + \left|\breve{h}_{k+K_\mathrm{I}}\right|^2 \overrightarrow{V}_{x_{k+K_\mathrm{I}}}(i-1)\boldsymbol{\zeta}_{\dot{K}_\mathrm{I}}\boldsymbol{\zeta}_{\dot{K}_\mathrm{I}}^H, \tag{3.14}$$

where $\breve{h}_{k+K_\mathrm{I}}$ is the CFR of the $(k+K_\mathrm{I})$-th subcarrier, $\overrightarrow{m}_{x_{k+K_\mathrm{I}}}(i-1)$ and $\overrightarrow{V}_{x_{k+K_\mathrm{I}}}(i-1)$ are the *a priori* mean and variance of the $(k+K_\mathrm{I})$-th transmitted symbol, which will be elaborated on later.

Similar to the derivations of forward messages, assuming that the weight matrix $\overleftarrow{\mathbf{W}}_{\mathbf{s}_k}(i)$ and the transformed mean vector $\overleftarrow{\mathbf{W}}_{\mathbf{s}_k}(i)\overleftarrow{\mathbf{m}}_{\mathbf{s}_k}(i)$ are available, relying to the backward message passing rules for the composite block of multiplication and addition (as listed in TABLE 4 of [47]), the backward messages of $\tilde{\mathbf{s}}_{k-1}$ are expressed as

$$\overleftarrow{\mathbf{W}}_{\tilde{\mathbf{s}}_{k-1}}(i) = \overleftarrow{\mathbf{W}}_{\mathbf{s}_k}(i) - \frac{\left|\breve{h}_{k+K_\mathrm{I}}\right|^2 \overrightarrow{V}_{x_{k+K_\mathrm{I}}}(i-1)\overleftarrow{\mathbf{W}}_{\mathbf{s}_k}(i)\boldsymbol{\zeta}_{\dot{K}_\mathrm{I}}\boldsymbol{\zeta}_{\dot{K}_\mathrm{I}}^H\overleftarrow{\mathbf{W}}_{\mathbf{s}_k}(i)}{1+\left|\breve{h}_{k+K_\mathrm{I}}\right|^2 \overrightarrow{V}_{x_{k+K_\mathrm{I}}}(i-1)\boldsymbol{\zeta}_{\dot{K}_\mathrm{I}}^H\overleftarrow{\mathbf{W}}_{\mathbf{s}_k}(i)\boldsymbol{\zeta}_{\dot{K}_\mathrm{I}}}, \tag{3.15}$$

$$\begin{aligned}\overleftarrow{\mathbf{W}}_{\tilde{\mathbf{s}}_{k-1}}(i)\overleftarrow{\mathbf{m}}_{\tilde{\mathbf{s}}_{k-1}}(i) = &\left(\mathbf{I}_{\dot{K}_\mathrm{I}} - \frac{\left|\breve{h}_{k+K_\mathrm{I}}\right|^2 \overrightarrow{V}_{x_{k+K_\mathrm{I}}}(i-1)\overleftarrow{\mathbf{W}}_{\mathbf{s}_k}(i)\boldsymbol{\zeta}_{\dot{K}_\mathrm{I}}\boldsymbol{\zeta}_{\dot{K}_\mathrm{I}}^H}{1+\left|\breve{h}_{k+K_\mathrm{I}}\right|^2 \overrightarrow{V}_{x_{k+K_\mathrm{I}}}(i-1)\boldsymbol{\zeta}_{\dot{K}_\mathrm{I}}^H\overleftarrow{\mathbf{W}}_{\mathbf{s}_k}(i)\boldsymbol{\zeta}_{\dot{K}_\mathrm{I}}}\right)\\ &\times\left(\overleftarrow{\mathbf{W}}_{\mathbf{s}_k}(i)\overleftarrow{\mathbf{m}}_{\mathbf{s}_k}(i) - \breve{h}_{k+K_\mathrm{I}}\overrightarrow{m}_{x_{k+K_\mathrm{I}}}(i-1)\overleftarrow{\mathbf{W}}_{\mathbf{s}_k}(i)\boldsymbol{\zeta}_{\dot{K}_\mathrm{I}}\right).\end{aligned} \tag{3.16}$$

Then, according to the backward message passing rules for the multiplication factor node (as listed in TABLE 3 of [47]), the backward messages of $\mathbf{s}''_{k-1}$ are given by

$$\overleftarrow{\mathbf{W}}_{\mathbf{s}''_{k-1}}(i) = \boldsymbol{\Xi}_{\dot{K}_\mathrm{I}}^H \overleftarrow{\mathbf{W}}_{\tilde{\mathbf{s}}_{k-1}}(i)\boldsymbol{\Xi}_{\dot{K}_\mathrm{I}}, \tag{3.17}$$

$$\overleftarrow{\mathbf{W}}_{\mathbf{s}''_{k-1}}(i)\overleftarrow{\mathbf{m}}_{\mathbf{s}''_{k-1}}(i) = \boldsymbol{\Xi}_{\dot{K}_\mathrm{I}}^H \overleftarrow{\mathbf{W}}_{\tilde{\mathbf{s}}_{k-1}}(i)\overleftarrow{\mathbf{m}}_{\tilde{\mathbf{s}}_{k-1}}(i). \tag{3.18}$$

Based on (3.15)-(3.18), according to the backward message passing rules for the composite block of multiplication and equality (as listed in TABLE 4 of [47]), the backward messages of the state variables $\mathbf{s}_{k-1}$ can be updated as

$$\overleftarrow{\mathbf{W}}_{\mathbf{s}_{k-1}}(i) = \overleftarrow{\mathbf{W}}_{\mathbf{s}''_{k-1}}(i) + \frac{\left(\boldsymbol{\phi}_{k-1}^T\right)^H\boldsymbol{\phi}_{k-1}^T}{\overrightarrow{V}_{\xi_{k-1}}(i-1)}, \tag{3.19}$$

$$\overleftarrow{\mathbf{W}}_{\mathbf{s}_{k-1}}(i)\overleftarrow{\mathbf{m}}_{\mathbf{s}_{k-1}}(i) = \overleftarrow{\mathbf{W}}_{\mathbf{s}''_{k-1}}(i)\overleftarrow{\mathbf{m}}_{\mathbf{s}''_{k-1}}(i) + \frac{\left(\boldsymbol{\phi}_{k-1}^T\right)^H r_{k-1}}{\overrightarrow{V}_{\xi_{k-1}}(i-1)}, \tag{3.20}$$

where $\overrightarrow{V}_{\xi_{k-1}}(i-1)$ is updated on Subgraph ② in the previous iteration.

From (3.14) and (3.19), the *a posteriori* variance of the state vector $\mathbf{s}_k$ is calculated as

$$\mathbf{V}_{\mathbf{s}_k}(i) = \big((\overrightarrow{\mathbf{V}}_{\mathbf{s}_k}(i))^{-1} + \overleftarrow{\mathbf{W}}_{\mathbf{s}_k}(i)\big)^{-1}. \tag{3.21}$$

Then, the *a posteriori* variance of the approximated noise ξ_k is given by

$$V_{\xi_k}(i) = \boldsymbol{\phi}_{k-1}^T \mathbf{V}_{\mathbf{s}_k}(i) \big(\boldsymbol{\phi}_{k-1}^T\big)^H. \tag{3.22}$$

Since the mean of the noise process is zero, only the covariance has to be exchanged between Subgraph ① and Subgraph ②. According to the *a posteriori* variance of (3.22) and the forward message $\overrightarrow{V}_{\xi_k}(i-1)$ of (3.29), the backward message $\overleftarrow{V}_{\xi_k}^{(i_t)}$ from Subgraph ① to Subgraph ② is derived as

$$\overleftarrow{V}_{\xi_k}(i) = \frac{V_{\xi_k}(i)\overrightarrow{V}_{\xi_k}(i-1)}{\overrightarrow{V}_{\xi_k}(i-1) - V_{\xi_k}(i)}. \tag{3.23}$$

• *Gaussian Message Updating for Colored Noise Approximation in Subgraph ②*

Similarly, the forward and backward messages on Subgraph ② are calculated based on GMP rules. Note that the mean vectors of the variables in Subgraph ② are zeros, only the backward weight matrices need to be updated. Assuming that the covariance matrix $\overrightarrow{\mathbf{V}}_{\boldsymbol{\xi}_{k-1}}(i)$ is available, the forward variance vector of $\boldsymbol{\xi}''_{k-1}$ is expressed as

$$\overrightarrow{\mathbf{V}}_{\boldsymbol{\xi}''_{k-1}}(i) = \overrightarrow{\mathbf{V}}_{\boldsymbol{\xi}_{k-1}}(i) - \frac{\overrightarrow{\mathbf{V}}_{\boldsymbol{\xi}_{k-1}}(i)\big(\boldsymbol{\zeta}_\xi^T\big)^H \boldsymbol{\zeta}_\xi^T \overrightarrow{\mathbf{V}}_{\boldsymbol{\xi}_{k-1}}(i)}{\overleftarrow{V}_{\xi_k} + \boldsymbol{\zeta}_\xi^T \overrightarrow{\mathbf{V}}_{\boldsymbol{\xi}_{k-1}} \big(\boldsymbol{\zeta}_\xi^T\big)^H}. \tag{3.24}$$

Similar to the derivations of (3.12) and (3.14), the forward covariance matrix $\overrightarrow{\mathbf{V}}_{\xi_k}(i)$ is represented as

$$\overrightarrow{\mathbf{V}}_{\boldsymbol{\xi}_k}(i) = \boldsymbol{\Xi}_\xi \overrightarrow{\mathbf{V}}_{\boldsymbol{\xi}''_{k-1}}(i) \boldsymbol{\Xi}_\xi^H + \sigma_{\tilde{\xi}}^2 \boldsymbol{\zeta}_\xi \boldsymbol{\zeta}_\xi^H. \tag{3.25}$$

Assuming that the weight matrix $\overleftarrow{\mathbf{W}}_{\boldsymbol{\xi}_k}(i)$ is available, the weight matrix of the variable $\tilde{\boldsymbol{\xi}}_{k-1}$ is given by

$$\overleftarrow{\mathbf{W}}_{\tilde{\boldsymbol{\xi}}_{k-1}}(i) = \overleftarrow{\mathbf{W}}_{\boldsymbol{\xi}_k}(i) - \frac{\sigma_{\tilde{\xi}}^2 \overleftarrow{\mathbf{W}}_{\boldsymbol{\xi}_k}(i) \boldsymbol{\zeta}_\xi \boldsymbol{\zeta}_\xi^H \overleftarrow{\mathbf{W}}_{\boldsymbol{\xi}_k}(i)}{1 + \sigma_{\tilde{\xi}}^2 \boldsymbol{\zeta}_\xi^H \overleftarrow{\mathbf{W}}_{\boldsymbol{\xi}_k}(i) \boldsymbol{\zeta}_\xi}. \tag{3.26}$$

Then, the backward weight matrix $\overleftarrow{\mathbf{W}}_{\boldsymbol{\xi}_{k-1}}(i)$ is updated as

$$\overleftarrow{\mathbf{W}}_{\boldsymbol{\xi}_{k-1}}(i) = \boldsymbol{\Xi}_\xi^H \overleftarrow{\mathbf{W}}_{\tilde{\boldsymbol{\xi}}_{k-1}}(i) \boldsymbol{\Xi}_\xi + \frac{\boldsymbol{\zeta}_\xi^H \boldsymbol{\zeta}_\xi}{\overleftarrow{V}_{\xi_k}(i-1)}, \tag{3.27}$$

where $\overleftarrow{V}_{\xi_k}(i)$ is obtained from Subgraph ①.

Based on (3.25) and (3.27), the *a posteriori* variance of the state vector $\boldsymbol{\xi}_k$ is computed as

$$\mathbf{V}_{\boldsymbol{\xi}_k}(i) = \big((\overrightarrow{\mathbf{V}}_{\boldsymbol{\xi}_k}(i))^{-1} + \overleftarrow{\mathbf{W}}_{\boldsymbol{\xi}_k}(i)\big)^{-1}. \tag{3.28}$$

Then, the forward message of the k-th element of vector $\boldsymbol{\xi}_k$ from Subgraph ② to Subgraph ① is derived as

$$\overrightarrow{V}_{\xi_k}(i) = \frac{\overleftarrow{V}_{\xi_k}(i)\boldsymbol{\zeta}_\xi \mathbf{V}_{\boldsymbol{\xi}_k}(i)\boldsymbol{\zeta}_\xi^H}{\overleftarrow{V}_{\xi_k}(i) - \boldsymbol{\zeta}_\xi \mathbf{V}_{\boldsymbol{\xi}_k}(i)\boldsymbol{\zeta}_\xi^H}. \tag{3.29}$$

• *The A Priori Message Approximation Based on EP*

In the turbo receiver, soft extrinsic information is exchanged between the channel decoder and the SEFDM-IM equalizer, as shown in Fig. 3.1. The message updating within the equalizer is regarded as the inner iteration, while the message passing between the equalizer and decoder is the extrinsic iteration. In each iteration, the *a priori* messages of the transmitted symbols are obtained using the extrinsic LLRs gleaned from the output of the channel decoder. Assuming that the p_{g}-th extrinsic LLR of the g-th SEFDM-IM subblock is $L_{\mathrm{dec}}^{\mathrm{e},(i_{\mathrm{e}})}(c_{g,p_{\mathrm{g}}})$ in the i_{e}-th extrinsic iteration, the *a priori* probability of the coded bit is $P^{(i_{\mathrm{e}})}(c_{g,p_{\mathrm{g}}}) = \frac{1}{2}\big[1 + (-1)^{c_{g,p_{\mathrm{g}}}} \tanh\big(\frac{1}{2}L_{\mathrm{dec}}^{\mathrm{e},(i_{\mathrm{e}})}(c_{g,p_{\mathrm{g}}})\big)\big]$, where $c_{g,p_{\mathrm{g}}} \in \{0,1\}$ and $p_{\mathrm{g}} \in \{0,\cdots,P_{\mathrm{g}}-1\}$.

According to the activation pattern constraints of IM and the mapping rules of M-ary modulation, the *a priori* probability of the transmitted symbol x_k can be computed using the *a priori* probabilities of the P_{g} coded bits in the corresponding subblock. Let us assume that K_{a} indices of the m_1-th activated pattern $\mathbf{I}_{m_1} = \{I_{m_1,0},\ldots,I_{m_1,K_{\mathrm{a}}-1}\}$ correspond to the coded index modulation bits $\mathbf{c}_{m_1} = [c_{m_1,0},\cdots,c_{m_1,P_{\mathrm{g},1}-1}]^T$ and the m_2-th constellation candidate $\mathbf{a}_{m_2} = [a_{m_2,0},\ldots,a_{m_2,K_{\mathrm{a}}-1}]$ corresponds to the coded modulated symbol bits $\mathbf{c}_{m_2} = [c_{m_2,0},\cdots,c_{m_2,P_{\mathrm{g},2}}-1]^T, m_2 \in \{0,\cdots,2^{P_{\mathrm{g},2}}-1\}$. The *a priori* probability of the transmitted symbol $x_{g,k_{\mathrm{g}}}$ in the g-th subblock is expressed as

$$P_{g,k_{\mathrm{g}},0}^{(i_{\mathrm{e}})} = \sum_{m_1,k_{\mathrm{g}}\notin\mathbf{I}_{m_1}} \left[\prod_{p_{\mathrm{g},1}=0}^{P_{\mathrm{g},1}-1} P^{(i_{\mathrm{e}})}(c_{g,p_{\mathrm{g},1}} = c_{m_1,p_{\mathrm{g},1}})\right], \tag{3.30}$$

$$P_{g,k_{\mathrm{g}},m}^{(i_{\mathrm{e}})} = \sum_{m_1,k_{\mathrm{g}}\in\mathbf{I}_{m_1}} \left[\prod_{p_{\mathrm{g},1}=0}^{P_{\mathrm{g},1}-1} P^{(i_{\mathrm{e}})}(c_{g,p_{\mathrm{g},1}} = c_{m_1,p_{\mathrm{g},1}}) \prod_{p_{\mathrm{g},2}=P_{\mathrm{g},1}}^{P_{\mathrm{g}-1}} P^{(i_{\mathrm{e}})}(c_{g,p_{\mathrm{g},2}} = c_{m_2,p_{\mathrm{g},2}-P_{\mathrm{g},1}})\right], \tag{3.31}$$

where $c_{g,p_{\mathrm{g},1}}$ denotes the index bits, while $c_{g,p_{\mathrm{g},2}}$ represents the classic modulated symbol bits.

Nevertheless, the discrete distribution of the incoming message imposes exponentially increased complexity. To circumvent this, this work resorts to approximating the distribution by a Gaussian form. Second-order moment matching is a fairly straightforward method, but suffers from an excessive approximation error. By contrast, EP is an efficient technique of approximating *a*

posteriori beliefs that belong to the exponential distribution families [136], [137]. The approximated Gaussian distribution is derived via minimizing the KLD between the true marginal distribution $b_{x_k}(i)$ and the trial distribution $\bar{b}_{x_k}(i)$, i.e.,

$$\bar{b}_{x_k}(i) = \arg\min_{\bar{b}_{x_k}(i)} D_{\mathrm{KL}}\big(b_{x_k}(i)\big|\big|\bar{b}_{x_k}(i)\big), \tag{3.32}$$

where the *a priori* probability of the transmitted symbol x_k depends on both $P^{(i_e)}_{g,k_g,0}$ and on $P^{(i_e)}_{g,k_g,m}$. The projection of a univariate distribution onto the Gaussian distribution in (3.32) is equivalent to matching the moments of the discrete *a posteriori* distribution and the Gaussian distribution [138]. Having the *a priori* distributions and the outgoing Gaussian messages at the i_t-th inner iteration, the first-order and second-order moment of the *a posteriori* distribution $b_{x_k}(i)$ are given by

$$m_{x_k}(i) \propto \sum_{m=0}^{M-1} \mathcal{S}_m P^{(i_e)}_{g,n,m} \zeta^m_{x_k}(i), \tag{3.33}$$

$$V_{x_k}(i) \propto P^{(i_e)}_{g,k_g,0} |m_{x_k}(i)|^2 \zeta^0_{x_k}(i) + \sum_{m=0}^{M-1} |\mathcal{S}_m - m_{x_k}(i)|^2 P^{(i_e)}_{g,n,m} \zeta^m_{x_k}(i), \tag{3.34}$$

where $\zeta^0_{x_k}(i) = \exp(-|\overleftarrow{m}_{x_k}(i)|^2/\overleftarrow{V}_{x_k}(i))$, $\zeta^m_{x_k}(i) = \exp(-|\mathcal{S}_m - \overleftarrow{m}_{x_k}(i)|^2/\overleftarrow{V}_{x_k}(i))$, $\overleftarrow{m}_{x_k}(i)$ and $\overleftarrow{V}_{x_k}(i)$ are the outgoing mean and variance. Based on (3.33) and (3.34), the forward messages arriving from the channel decoder are

$$\overrightarrow{m}_{x_k}(i) = \frac{m_{x_k}(i)\overleftarrow{V}_{x_k}(i) - \overleftarrow{m}_{x_k}(i) V_{x_k}(i)}{\overleftarrow{V}_{x_k}(i) - V_{x_k}(i)}, \tag{3.35}$$

$$\overrightarrow{V}_{x_k}(i) = \frac{\overleftarrow{V}_{x_k}(i) V_{x_k}(i)}{\overleftarrow{V}_{x_k}(i) - V_{x_k}(i)}. \tag{3.36}$$

• *Extrinsic LLR Calculation*

For expressing the extrinsic LLR gleaned from the equalizer for the processing of the channel decoder, the auxiliary quantity [47] of the state $\mathbf{s}_k$ is introduced as

$$\tilde{\mathbf{W}}_{\mathbf{s}_k}(i) = \big(\overrightarrow{\mathbf{V}}_{\mathbf{s}_k}(i) + \overleftarrow{\mathbf{V}}_{\mathbf{s}_k}(i)\big)^{-1}. \tag{3.37}$$

Thus, given the CSI, the backward mean and variance of the transmitted symbol at the i_t-th inner iteration are formulated as

$$\overleftarrow{m}_{x_{k+K_\mathrm{I}}}(i) = \frac{\breve{h}^*_{k+K_\mathrm{I}} \boldsymbol{\zeta}^H_{K_\mathrm{I}} \tilde{\mathbf{W}}_{\mathbf{s}_k}(i)\big(\overleftarrow{\mathbf{m}}_{\mathbf{s}_k}(i) - \overleftarrow{\mathbf{m}}_{\tilde{\mathbf{s}}_k}(i)\big)}{|\breve{h}_{k+K_\mathrm{I}}|^2 \boldsymbol{\zeta}^H_{K_\mathrm{I}} \tilde{\mathbf{W}}_{\mathbf{s}_k}(i) \boldsymbol{\zeta}_{K_\mathrm{I}}}, \tag{3.38}$$

$$\overleftarrow{V}_{x_{k+K_\mathrm{I}}}(i) = \frac{1 - \overrightarrow{V}_{s_{k+K_\mathrm{I}}}(i-1)}{|\breve{h}_{k+K_\mathrm{I}}|^2 \boldsymbol{\zeta}_\mathrm{s}^H \tilde{\mathbf{W}}_{\mathbf{s}_k}(i) \boldsymbol{\zeta}_{\dot{K}_\mathrm{I}}}. \tag{3.39}$$

Then, the extrinsic LLR output by the equalizer per subblock can be calculated by the corresponding expressions in [139], [140].

The proposed hybrid GMP-EP equalization algorithm for SEFDM-IM systems with known CSI is summarized in **Algorithm** 1, where I_in and I_out are the number of the inner and outer iterations, respectively.

Algorithm 1 Hybrid GMP-EP Equalization of SEFDM-IM Signaling with Known CSI

1: **Initialization**: The extrinsic LLR of the channel decoder is initialized as $L_\mathrm{dec}^{\mathrm{e},(1)}(c_{g,p_\mathrm{g}}) = 0$. Then, the *a priori* messages of the transmitted symbols are $\overrightarrow{m}_{x_k}(1) = 0$ and $\overrightarrow{V}_{x_k}(1) = +\infty$.
2: In Subgraph ①, the forward messages are initialized as $\overrightarrow{\mathbf{m}}_{\mathbf{s}_0}(1) = \mathbf{0}_{\dot{K}_\mathrm{I}}$ and $\overrightarrow{\mathbf{V}}_{\mathbf{s}_0}(1) = \mathbf{I}_{\dot{K}_\mathrm{I}}$, while the backward messages are initialized as $\overleftarrow{\mathbf{W}}_{\mathbf{s}_{K-1}}(1)\overleftarrow{\mathbf{m}}_{\mathbf{s}_{K-1}}(1) = \mathbf{0}_{\dot{K}_\mathrm{I}}$ and $\overleftarrow{\mathbf{W}}_{\mathbf{s}_{K-1}}(1) = \mathbf{I}_{\dot{K}_\mathrm{I}}$.
3: In Subgraph ②, the forward covariance matrix of $\boldsymbol{\xi}_0$ is initialized as $\overrightarrow{\mathbf{V}}_{\boldsymbol{\xi}_0}(1) = \mathbf{I}_{P_0}$ and the backward weight vector of $\boldsymbol{\xi}_{K-1}$ is initialized as $\overleftarrow{\mathbf{W}}_{\boldsymbol{\xi}_{K-1}}(1) = \mathbf{I}_{P_0}$.
4: **for** $i_\mathrm{e} = 1$ to I_e **do**
5: **for** $i = 1$ to I_in **do**
6: Compute the forward and backward messages in Subgraph ① according to (3.9)-(3.20);
7: Compute the backward messages passing from Subgraph ① to Subgraph ② according to (3.23);
8: Compute the forward and backward messages in Subgraph ② according to(3.24)-(3.27);
9: Compute the forward messages passing from Subgraph ② to Subgraph ① according to (3.29);
10: Compute the backward messages of the transmitted symbols according to (3.38) and (3.39);
11: Based on the discrete *a priori* probabilities and the backward messages of the transmitted symbols, compute their approximated *a priori* mean and variance vectors according to (3.33)-(3.36);
12: **end for**
13: Compute the extrinsic LLRs of the equalizer based on the backward messages and feed them to channel decoder;
14: Perform BCJR channel decoding and feed the extrinsic LLRs of channel decoder to equalizer.
15: Compute the discrete *a priori* probabilities of the transmitted symbols according to (3.30) and (3.31).
16: **end for**

3.4 Joint Channel Estimation and Equalization Based on Hybrid Message Passing

In contrast to OFDM-based systems, a typical linear MMSE channel estimator designed for SEFDM-IM signaling suffers from an excessive computational complexity due to the matrix inversion of the inherent interference matrix. In this section, a low-complexity joint frequency-domain channel estimation and equalization method is developed for SEFDM-IM systems. By appropriately grouping the elements of the channel's frequency responses, the channel estimator is reformulated via a linear state space model and connected with the equalizer described in Section 3.3 via an inner product node. To tackle error propagation during channel estimation on the deactivated subcarriers, the channel characteristics are exploited for constructing a multi-layer factor graph.

3.4.1 Factor Graph Representation

Consider a L-tap frequency-selective fading channel, where the number of subcarriers is $K = QL$, where Q is a positive integer. By grouping the elements of CFR, Q vectors are obtained as $\breve{\mathbf{h}}_q = [\breve{h}_q, \breve{h}_{Q+q}, \cdots, \breve{h}_{(L-1)Q+q}]^T, q \in \{0, \cdots, Q-1\}$. Each vector $\breve{\mathbf{h}}_q$ consists of Q CFR samples and can be obtained via non-orthogonal transformation of the CIR as $\breve{\mathbf{h}}_q = \breve{\mathbf{F}}_L(\mathbf{\Lambda}_0^q)^H\mathbf{h}$, where $\breve{\mathbf{F}}_L$ is a non-orthogonal transformation matrix with $(\breve{\mathbf{F}}_L)_{[m,n]} = e^{-\frac{j2\pi\nu mn}{L}}$, $\mathbf{\Lambda}_0 = \mathcal{D}(\boldsymbol{\lambda}_0)$ and $\boldsymbol{\lambda}_0 = [1, e^{\frac{j2\pi\nu}{K}}, \cdots, e^{\frac{j2\pi\nu(L-1)}{K}}]^T$. Thus, the state transition equation is given by

$$\breve{\mathbf{h}}_{q-1} = \breve{\mathbf{F}}_L\mathbf{\Lambda}_0\breve{\mathbf{F}}_L^{-1}\breve{\mathbf{h}}_q. \tag{3.40}$$

The vector $\breve{\mathbf{s}}_q^{\tilde{l}}$ of the $\tilde{l}$-th SEFDM-IM symbol is represented as $\breve{\mathbf{s}}_q^{\tilde{l}} = [s_q^{\tilde{l}}, s_{Q+q}^{\tilde{l}}, \cdots, s_{(L-1)Q+q}^{\tilde{l}}]^T$, where the element is $s_j^{\tilde{l}} = \boldsymbol{\upsilon}_j^T\breve{\mathbf{s}}_q^{\tilde{l}}$, and $\boldsymbol{\upsilon}_j$ denotes an indicator vector with the j-th element being one. Moreover, the transmitted SEFDM-IM symbols and CFR satisfy $\breve{\mathbf{s}}_q^{\tilde{l}} = \breve{\mathbf{h}}_q^{\tilde{l}} \odot \breve{\mathbf{x}}_q^{\tilde{l}}$.

With the assumption of an unknown CSI, channel factor node in Fig. 3.2 is replaced by the frequency-domain channel estimator feeding the equalizer. For quasi-static channels, different layers are connected via channel variable nodes on the same subcarrier positions of different symbols. Based on the above model, the $\tilde{L}$-sublayer factor graph representation of the joint channel estimation and SEFDM-IM equalization relying on unknown CSI is depicted in Fig. 3.3. The equalizer contains Subgraph ① and Subgraph ② in Fig. 3.2. Moreover, the inner product node represents the inner product constraint $\delta(\breve{\mathbf{s}}_q^{\tilde{l}} - \breve{\mathbf{h}}_q^{\tilde{l}} \odot \breve{\mathbf{x}}_q^{\tilde{l}})$.

3.4.2 VMP-based Channel Estimation

• *Forward Message Approximation of* $s_k^{\tilde{l}}$

The *a priori* information gleaned from channel decoder is computed as (3.33)-(3.36). The approximated Gaussian messages passed from the channel estimator to the equalizer are expressed

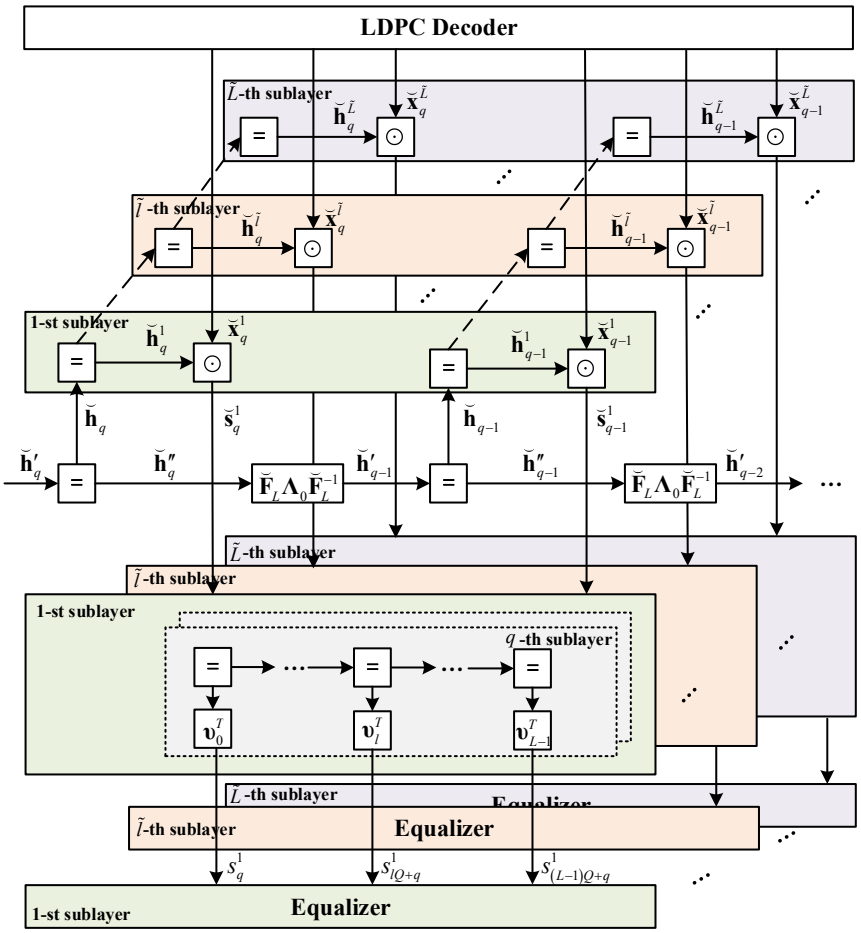


Figure 3.3: Factor graph for JCEE of SEFDM-IM signaling with unknown CSI.

as

$$\overrightarrow{m}_{s_k^{\tilde{l}}}(i) = \boldsymbol{v}_l^T\big(\overrightarrow{\mathbf{m}}_{\breve{\mathbf{x}}_q^{\tilde{l}}}(i) \odot \overrightarrow{\mathbf{m}}_{\breve{\mathbf{h}}_q^{\tilde{l}}}(i)\big), \tag{3.41}$$

$$\begin{aligned}\overrightarrow{v}_{s_k^{\tilde{l}}}(i) = \boldsymbol{v}_l^T\Big[&\mathcal{D}\big(\overrightarrow{\mathbf{m}}_{\breve{\mathbf{x}}_q^{\tilde{l}}}(i) \odot \overrightarrow{\mathbf{m}}_{\breve{\mathbf{x}}_q^{\tilde{l}}}(i)\big) + \overrightarrow{\mathbf{V}}_{\breve{\mathbf{x}}_q^{\tilde{l}}}(i)\Big] \\ &\times \Big[\mathcal{D}\big(\overrightarrow{\mathbf{m}}_{\breve{\mathbf{h}}_q^{\tilde{l}}}(i) \odot \overrightarrow{\mathbf{m}}_{\breve{\mathbf{h}}_q^{\tilde{l}}}(i)\big) + \overrightarrow{\mathbf{V}}_{\breve{\mathbf{h}}_q^{\tilde{l}}}(i)\Big]\big(\boldsymbol{v}_l^T\big)^H - \big(\overrightarrow{m}_{s_k^{\tilde{l}}}(i)\big)^2,\end{aligned} \tag{3.42}$$

where the forward messages $\overrightarrow{\mathbf{m}}_{\breve{\mathbf{h}}_q^{\tilde{l}}}(i)$ and $\overrightarrow{\mathbf{V}}_{\breve{\mathbf{h}}_q^{\tilde{l}}}(i)$ denote the forward mean vector and covariance matrix of the frequency-domain channel coefficients in the i-th iteration. The derivations of (3.41) and (3.42) are given in **Appendix** A

• *Backward Message Approximation of* $\breve{\mathbf{h}}_q^{\tilde{l}}$ *and* $\breve{\mathbf{x}}_q^{\tilde{l}}$

The backward messages of variables $\breve{\mathbf{s}}_q^{\tilde{l}}$ consist of the corresponding outgoing messages of the equalizer. For the inner product node, message updating using classical BP is intractable. To derive approximated Gaussian expressions, the backward message of $\breve{\mathbf{h}}_q^{\tilde{l}}$ from the inner product

node is updated according to the VMP rules of [141], [142] as

$$\overleftarrow{\mu}\left(\breve{\mathbf{h}}_q^{\tilde{l}}\right) \propto \exp\left(\int \ln \delta\left(\breve{\mathbf{s}}_q^{\tilde{l}} - \mathcal{D}\left(\breve{\mathbf{x}}_q^{\tilde{l}}\right)\breve{\mathbf{h}}_q^{\tilde{l}}\right) b\left(\breve{\mathbf{x}}_q^{\tilde{l}}\right) b\left(\breve{\mathbf{s}}_q^{\tilde{l}}\right) d\breve{\mathbf{x}}_q^{\tilde{l}} d\breve{\mathbf{s}}_q^{\tilde{l}}\right), \tag{3.43}$$

where $b\left(\breve{\mathbf{x}}_q^{\tilde{l}}\right)$ and $b\left(\breve{\mathbf{s}}_q^{\tilde{l}}\right)$ are the beliefs of the variables $\breve{\mathbf{x}}_q^{\tilde{l}}$ and $\breve{\mathbf{s}}_q^{\tilde{l}}$, respectively. Note that the logarithm of the delta function involved in the integration of (3.43) is pathological [139]. To this end, the inner product node is grouped with the state variables as an equivalent soft node, i.e.,

$$f_q^{\tilde{l}}\left(\breve{\mathbf{x}}_q^{\tilde{l}}, \breve{\mathbf{h}}_q^{\tilde{l}}\right) \propto \exp\left[-\left(\mathcal{D}\left(\breve{\mathbf{x}}_q^{\tilde{l}}\right)\breve{\mathbf{h}}_q^{\tilde{l}} - \overleftarrow{\mathbf{m}}_{\breve{\mathbf{s}}_q^{\tilde{l}}}(i)\right)^H \left(\overleftarrow{\mathbf{V}}_{\breve{\mathbf{s}}_q^{\tilde{l}}}(i)\right)^{-1} \left(\mathcal{D}\left(\breve{\mathbf{x}}_q^{\tilde{l}}\right)\breve{\mathbf{h}}_q^{\tilde{l}} - \overleftarrow{\mathbf{m}}_{\breve{\mathbf{s}}_q^{\tilde{l}}}(i)\right)\right]. \tag{3.44}$$

According to the VMP rules [142], the backward message of variables $\breve{\mathbf{h}}_q^{\tilde{l}}$ is rewritten as

$$\overleftarrow{\mu}\left(\breve{\mathbf{h}}_q^{\tilde{l}}\right) \propto \exp\left(\int \ln f_q^{\tilde{l}}\left(\breve{\mathbf{x}}_q^{\tilde{l}}, \breve{\mathbf{h}}_q^{\tilde{l}}\right) b\left(\breve{\mathbf{x}}_q^{\tilde{l}}\right) d\breve{\mathbf{x}}_q^{\tilde{l}}\right), \tag{3.45}$$

where the *a posteriori* belief obeys $b\left(\breve{\mathbf{x}}_q^{\tilde{l}}\right) \propto \mathcal{CN}\left(\breve{\mathbf{x}}_q^{\tilde{l}}; \mathbf{m}_{\breve{\mathbf{x}}_q^{\tilde{l}}}(i), \mathbf{V}_{\breve{\mathbf{x}}_q^{\tilde{l}}}(i)\right)$. Hence, (3.45) can be further derived as

$$\begin{aligned}
\overleftarrow{\mu}\left(\breve{\mathbf{h}}_q^{\tilde{l}}\right) \propto & \exp\Bigg\{-\int \left[\mathcal{D}\left(\breve{\mathbf{x}}_q^{\tilde{l}}\right)\breve{\mathbf{h}}_q^{\tilde{l}} - \overleftarrow{\mathbf{m}}_{\breve{\mathbf{s}}_q^{\tilde{l}}}(i)\right]^H \left(\overleftarrow{\mathbf{V}}_{\breve{\mathbf{s}}_q^{\tilde{l}}}(i)\right)^{-1} \left[\mathcal{D}\left(\breve{\mathbf{x}}_q^{\tilde{l}}\right)\breve{\mathbf{h}}_q^{\tilde{l}} - \overleftarrow{\mathbf{m}}_{\breve{\mathbf{s}}_q^{\tilde{l}}}(i)\right] \\
& \times \mathcal{CN}\left(\breve{\mathbf{x}}_q^{\tilde{l}}; \mathbf{m}_{\breve{\mathbf{x}}_q^{\tilde{l}}}(i), \mathbf{V}_{\breve{\mathbf{x}}_q^{\tilde{l}}}(i)\right) d\breve{\mathbf{x}}_q^{\tilde{l}}\Bigg\} \\
\propto & \exp\Bigg\{-\left(\breve{\mathbf{h}}_q^{\tilde{l}}\right)^H \left[\int \mathcal{D}\left(\breve{\mathbf{x}}_q^{\tilde{l}}\right)^H \left(\overleftarrow{\mathbf{V}}_{\breve{\mathbf{s}}_q^{\tilde{l}}}(i)\right)^{-1} \mathcal{D}\left(\breve{\mathbf{x}}_q^{\tilde{l}}\right) \mathcal{CN}\left(\breve{\mathbf{x}}_q^{\tilde{l}}; \mathbf{m}_{\breve{\mathbf{x}}_q^{\tilde{l}}}(i), \mathbf{V}_{\breve{\mathbf{x}}_q^{\tilde{l}}}(i)\right) d\breve{\mathbf{x}}_q^{\tilde{l}}\right] \breve{\mathbf{h}}_q^{\tilde{l}} \\
& + 2\mathrm{Re}\left\{\left(\breve{\mathbf{h}}_q^{\tilde{l}}\right)^H \left[\int \left(\mathcal{D}\left(\breve{\mathbf{x}}_q^{\tilde{l}}\right)\right)^H \mathcal{CN}\left(\breve{\mathbf{x}}_q^{\tilde{l}}; \mathbf{m}_{\breve{\mathbf{x}}_q^{\tilde{l}}}(i), \mathbf{V}_{\breve{\mathbf{x}}_q^{\tilde{l}}}(i)\right) d\breve{\mathbf{x}}_q^{\tilde{l}}\right] \left(\overleftarrow{\mathbf{V}}_{\breve{\mathbf{s}}_q^{\tilde{l}}}(i)\right)^{-1} \overleftarrow{\mathbf{m}}_{\breve{\mathbf{s}}_q^{\tilde{l}}}(i)\right\}\Bigg\} \\
\propto & \exp\Bigg\{-\left(\breve{\mathbf{h}}_q^{\tilde{l}}\right)^H \mathcal{D}\left[\mathbb{E}\left\{\left(\breve{\mathbf{x}}_q^{\tilde{l}}\right)^H \odot \breve{\mathbf{x}}_q^{\tilde{l}}\right\}\right] \left(\overleftarrow{\mathbf{V}}_{\breve{\mathbf{s}}_q^{\tilde{l}}}(i)\right)^{-1} \breve{\mathbf{h}}_q^{\tilde{l}} \\
& + 2\mathrm{Re}\left\{\left(\breve{\mathbf{h}}_q^{\tilde{l}}\right)^H \mathcal{D}\left[\mathbb{E}\left\{\left(\breve{\mathbf{x}}_q^{\tilde{l}}\right)^H\right\}\right] \left(\overleftarrow{\mathbf{V}}_{\breve{\mathbf{s}}_q^{\tilde{l}}}(i)\right)^{-1} \overleftarrow{\mathbf{m}}_{\breve{\mathbf{s}}_q^{\tilde{l}}}(i)\right\}\Bigg\} \\
\propto & \exp\Bigg\{-\left(\breve{\mathbf{h}}_q^{\tilde{l}}\right)^H \left[\mathbf{V}_{\breve{\mathbf{x}}_q^{\tilde{l}}}(i) + \mathcal{D}\left(\left(\mathbf{m}_{\breve{\mathbf{x}}_q^{\tilde{l}}}(i)\right)^H \odot \mathbf{m}_{\breve{\mathbf{x}}_q^{\tilde{l}}}(i)\right)\right] \left(\overleftarrow{\mathbf{V}}_{\breve{\mathbf{s}}_q^{\tilde{l}}}(i)\right)^{-1} \breve{\mathbf{h}}_q^{\tilde{l}} \\
& + 2\mathrm{Re}\left\{-\left(\breve{\mathbf{h}}_q^{\tilde{l}}\right)^H \mathcal{D}\left[\left(\mathbf{m}_{\breve{\mathbf{x}}_q^{\tilde{l}}}(i)\right)^H \odot \overleftarrow{\mathbf{m}}_{\breve{\mathbf{s}}_q^{\tilde{l}}}(i)\right] \left(\overleftarrow{\mathbf{V}}_{\breve{\mathbf{s}}_q^{\tilde{l}}}(i)\right)^{-1}\right\}\Bigg\}.
\end{aligned} \tag{3.46}$$

Based on the above derivations, the backward message of $\breve{\mathbf{h}}_q^{\tilde{l}}$ satisfies $\overleftarrow{\mu}\left(\breve{\mathbf{h}}_q^{\tilde{l}}\right) \propto \mathcal{CN}\left(\breve{\mathbf{h}}_q^{\tilde{l}}; \mathbf{m}_{\breve{\mathbf{h}}_q^{\tilde{l}}}(i), \mathbf{V}_{\breve{\mathbf{h}}_q^{\tilde{l}}}(i)\right)$.

The corresponding backward mean vector and covariance matrix are given by

$$\overleftarrow{\mathbf{m}}_{\breve{\mathbf{h}}_q^{\tilde{l}}}(i)=\mathcal{D}\left(\left(\mathbf{m}_{\breve{\mathbf{x}}_q^{\tilde{l}}}(i)\right)^H\odot\overleftarrow{\mathbf{m}}_{\breve{\mathbf{s}}_q^{\tilde{l}}}(i)\right)\left[\mathbf{V}_{\breve{\mathbf{x}}_q^{\tilde{l}}}(i)+\mathcal{D}\left(\left(\mathbf{m}_{\breve{\mathbf{x}}_q^{\tilde{l}}}(i)\right)^H\odot\mathbf{m}_{\breve{\mathbf{x}}_q^{\tilde{l}}}(i)\right)\right]^{-1} \tag{3.47}$$

$$\overleftarrow{\mathbf{V}}_{\breve{\mathbf{h}}_q^{\tilde{l}}}(i)=\overleftarrow{\mathbf{V}}_{\breve{\mathbf{s}}_q^{\tilde{l}}}(i)\left[\mathbf{V}_{\breve{\mathbf{x}}_q^{\tilde{l}}}(i)+\mathcal{D}\left(\left(\mathbf{m}_{\breve{\mathbf{x}}_q^{\tilde{l}}}(i)\right)^H\odot\mathbf{m}_{\breve{\mathbf{x}}_q^{\tilde{l}}}(i)\right)\right]^{-1}, \tag{3.48}$$

where both $\mathbf{V}_{\breve{\mathbf{x}}_q^{\tilde{l}}}(i)$ and $\overleftarrow{\mathbf{V}}_{\breve{\mathbf{s}}_q^{\tilde{l}}}(i)$ are diagonal matrices. The *a posteriori* mean vector and covariance matrix of $\breve{\mathbf{x}}_q^{\tilde{l}}$ are formulated as

$$\mathbf{m}_{\breve{\mathbf{x}}_q^{\tilde{l}}}(i)=\overrightarrow{\mathbf{V}}_{\breve{\mathbf{x}}_q^{\tilde{l}}}(i)\left[\left(\overrightarrow{\mathbf{V}}_{\breve{\mathbf{x}}_q^{\tilde{l}}}(i)\right)^{-1}\overrightarrow{\mathbf{m}}_{\breve{\mathbf{x}}_q^{\tilde{l}}}(i)+\left(\overleftarrow{\mathbf{V}}_{\breve{\mathbf{x}}_q^{\tilde{l}}}(i)\right)^{-1}\overleftarrow{\mathbf{m}}_{\breve{\mathbf{x}}_q^{\tilde{l}}}(i)\right], \tag{3.49}$$

$$\mathbf{V}_{\breve{\mathbf{x}}_q^{\tilde{l}}}(i)=\left[\left(\overrightarrow{\mathbf{V}}_{\breve{\mathbf{x}}_q^{\tilde{l}}}(i)\right)^{-1}+\left(\overleftarrow{\mathbf{V}}_{\breve{\mathbf{x}}_q^{\tilde{l}}}(i)\right)^{-1}\right]^{-1}. \tag{3.50}$$

Since the inner product constraint can also be represented as $\delta(\breve{\mathbf{s}}_q^{\tilde{l}}-\mathcal{D}(\breve{\mathbf{h}}_q^{\tilde{l}})\breve{\mathbf{x}}_q^{\tilde{l}})$, similar to the derivations of (3.47) and (3.48), the backward mean vector and covariance matrix of variables $\breve{\mathbf{x}}_q^{\tilde{l}}$ are derived as

$$\overleftarrow{\mathbf{m}}_{\breve{\mathbf{x}}_q^{\tilde{l}}}(i)=\mathcal{D}\left(\left(\mathbf{m}_{\breve{\mathbf{h}}_q^{\tilde{l}}}(i-1)\right)^H\odot\overleftarrow{\mathbf{m}}_{\breve{\mathbf{s}}_q^{\tilde{l}}}(i)\right)\left[\mathbf{V}_{\breve{\mathbf{h}}_q^{\tilde{l}}}(i-1)+\mathcal{D}\left(\left(\mathbf{m}_{\breve{\mathbf{h}}_q^{\tilde{l}}}(i-1)\right)^H\odot\mathbf{m}_{\breve{\mathbf{h}}_q^{\tilde{l}}}(i-1)\right)\right]^{-1}, \tag{3.51}$$

$$\overleftarrow{\mathbf{V}}_{\breve{\mathbf{x}}_q^{\tilde{l}}}(i)=\overleftarrow{\mathbf{V}}_{\breve{\mathbf{s}}_q^{\tilde{l}}}(i)\left[\mathbf{V}_{\breve{\mathbf{h}}_q^{\tilde{l}}}(i-1)+\mathcal{D}\left(\left(\mathbf{m}_{\breve{\mathbf{h}}_q^{\tilde{l}}}(i-1)\right)^H\odot\mathbf{m}_{\breve{\mathbf{h}}_q^{\tilde{l}}}(i-1)\right)\right]^{-1}, \tag{3.52}$$

where the *a posteriori* mean vector and covariance matrix of $\breve{\mathbf{h}}_q^{\tilde{l}}$ can be obtained similarly to those in (3.53) and (3.54), i.e.,

$$\mathbf{m}_{\breve{\mathbf{h}}_q^{\tilde{l}}}(i)=\overrightarrow{\mathbf{V}}_{\breve{\mathbf{h}}_q^{\tilde{l}}}(i)\left[\left(\overrightarrow{\mathbf{V}}_{\breve{\mathbf{h}}_q^{\tilde{l}}}(i)\right)^{-1}\overrightarrow{\mathbf{m}}_{\breve{\mathbf{h}}_q^{\tilde{l}}}(i)+\left(\overleftarrow{\mathbf{V}}_{\breve{\mathbf{h}}_q^{\tilde{l}}}(i)\right)^{-1}\overleftarrow{\mathbf{m}}_{\breve{\mathbf{h}}_q^{\tilde{l}}}(i)\right], \tag{3.53}$$

$$\mathbf{V}_{\breve{\mathbf{h}}_q^{\tilde{l}}}(i)=\left[\left(\overrightarrow{\mathbf{V}}_{\breve{\mathbf{h}}_q^{\tilde{l}}}(i)\right)^{-1}+\left(\overleftarrow{\mathbf{V}}_{\breve{\mathbf{h}}_q^{\tilde{l}}}(i)\right)^{-1}\right]^{-1}. \tag{3.54}$$

Therefore, the backward messages of $x_k^{\tilde{l}}$ are given by

$$\overleftarrow{m}_{x_k^{\tilde{l}}}(i)=\overleftarrow{m}_{x^{\tilde{l}}_{(l_0-1)Q+q}}(i)=\boldsymbol{\upsilon}_{\boldsymbol{l_0}}^T\overleftarrow{\mathbf{m}}_{\breve{\mathbf{x}}_q^{\tilde{l}}}(i), \tag{3.55}$$

$$\overleftarrow{V}_{x_k^{\tilde{l}}}(i)=\overleftarrow{V}_{x^{\tilde{l}}_{(l_0-1)Q+q}}(i)=\boldsymbol{\upsilon}_{\boldsymbol{l_0}}^T\overleftarrow{\mathbf{V}}_{\breve{\mathbf{x}}_q^{\tilde{l}}}(i)\boldsymbol{\upsilon}_{\boldsymbol{l_0}}, \tag{3.56}$$

where $x_k^{\tilde{l}}$ is the l_0 element of $\breve{\mathbf{x}}_q^{\tilde{l}}=[x_q^{\tilde{l}},x_{Q+q}^{\tilde{l}},\cdots,x_{(L-1)Q+q}^{\tilde{l}}]^T$ and the subscript k satisfies $k=(l_0-1)Q+q$.

• *Gaussian Message Passing of Channel Estimation*

Based on the backward messages of the variables $\breve{\mathbf{h}}_q^{\tilde{l}}$ in the $\tilde{l}$-th sublayer, the GMP rules concerning equality nodes are employed for determining the messages exchanged between different sublayers. The backward weight matrices and the transformed mean vectors related to the same subcarriers are added together to produce the backward messages of $\breve{\mathbf{h}}_q$, yielding,

$$\overleftarrow{\mathbf{m}}_{\breve{\mathbf{h}}_q}(i) = \overleftarrow{\mathbf{V}}_{\breve{\mathbf{h}}_q}(i) \sum_{\breve{l}=1}^{\breve{L}} \overleftarrow{\mathbf{W}}_{\breve{\mathbf{h}}_q^{\tilde{l}}}(i) \overleftarrow{\mathbf{m}}_{\breve{\mathbf{h}}_q^{\tilde{l}}}(i), \tag{3.57}$$

$$\overleftarrow{\mathbf{V}}_{\breve{\mathbf{h}}_q}(i) = \left(\sum_{\breve{l}=1}^{\breve{L}} \overleftarrow{\mathbf{W}}_{\breve{\mathbf{h}}_q^{\tilde{l}}}(i) \right)^{-1}, \tag{3.58}$$

where $\overleftarrow{\mathbf{W}}_{\breve{\mathbf{h}}_q^{\tilde{l}}}(i) = \big(\overleftarrow{\mathbf{V}}_{\breve{\mathbf{h}}_q^{\tilde{l}}}(i)\big)^{-1}$. Then, the forward messages of the state $\breve{\mathbf{h}}_q''$ are also computed as

$$\overrightarrow{\mathbf{m}}_{\breve{\mathbf{h}}_q''}(i) = \overrightarrow{\mathbf{V}}_{\breve{\mathbf{h}}_q''}(i) \Big[\big(\overrightarrow{\mathbf{V}}_{\breve{\mathbf{h}}_q'}(i)\big)^{-1} \overrightarrow{\mathbf{m}}_{\breve{\mathbf{h}}_q'}(i) + \big(\overleftarrow{\mathbf{V}}_{\breve{\mathbf{h}}_q}(i)\big)^{-1} \overleftarrow{\mathbf{m}}_{\breve{\mathbf{h}}_q}(i) \Big], \tag{3.59}$$

$$\overrightarrow{\mathbf{V}}_{\breve{\mathbf{h}}_q''}(i) = \Big[\big(\overrightarrow{\mathbf{V}}_{\breve{\mathbf{h}}_q'}(i)\big)^{-1} + \big(\overleftarrow{\mathbf{V}}_{\breve{\mathbf{h}}_q}(i)\big)^{-1} \Big]^{-1}. \tag{3.60}$$

Similarly, the backward message of $\breve{\mathbf{h}}_{q-1}'$ are computed as

$$\overrightarrow{\mathbf{m}}_{\breve{\mathbf{h}}_{q-1}'}(i) = \breve{\mathbf{F}}_L \mathbf{\Lambda}_0 \breve{\mathbf{F}}_L^{-1} \overrightarrow{\mathbf{m}}_{\breve{\mathbf{h}}_q''}(i), \tag{3.61}$$

$$\overrightarrow{\mathbf{V}}_{\breve{\mathbf{h}}_{q-1}'}(i) = \breve{\mathbf{F}}_L \mathbf{\Lambda}_0 \breve{\mathbf{F}}_L^{-1} \overrightarrow{\mathbf{V}}_{\breve{\mathbf{h}}_q''}(i) \big(\breve{\mathbf{F}}_L \mathbf{\Lambda}_0 \breve{\mathbf{F}}_L^{-1}\big)^H. \tag{3.62}$$

Moreover, the initial messages for the edge representing $\breve{\mathbf{h}}_{Q-1}'$ can be obtained by using pilots based on the time-domain channel estimation method [108].

Obviously, the covariance matrix $\overrightarrow{\mathbf{V}}_{\breve{\mathbf{h}}_{q-1}'}(i)$ is no longer diagonal in (3.62), which substantially increases the complexity of the proposed algorithm. To reduce the computation complexity, the covariance matrix of (3.62) is approximated as

$$\overrightarrow{\mathbf{V}}_{\breve{\mathbf{h}}_q'}(i) = \frac{1}{L} \mathrm{tr}\Big(\overrightarrow{\mathbf{V}}_{\breve{\mathbf{h}}_q''}(i) \Big) \mathbf{I}_L. \tag{3.63}$$

Based on (3.63), the forward messages of $\breve{\mathbf{h}}_0'$ can be expressed at the rightmost side of the factor graph. Upon combining with the backward messages in (3.47) and (3.48), the mean and variance vectors of $\breve{\mathbf{h}}_0'$ are given by

$$\mathbf{m}_{\breve{\mathbf{h}}_0}(i) = \mathbf{V}_{\breve{\mathbf{h}}_0}(i) \Big[\big(\overrightarrow{\mathbf{V}}_{\breve{\mathbf{h}}_0}(i)\big)^{-1} \overrightarrow{\mathbf{m}}_{\breve{\mathbf{h}}_0}(i) + \big(\overleftarrow{\mathbf{V}}_{\breve{\mathbf{h}}_0}(i)\big)^{-1} \overleftarrow{\mathbf{m}}_{\breve{\mathbf{h}}_0}(i) \Big], \tag{3.64}$$

$$\mathbf{V}_{\breve{\mathbf{h}}_0}(i) = \Big[\big(\overrightarrow{\mathbf{V}}_{\breve{\mathbf{h}}_0}(i)\big)^{-1} + \big(\overleftarrow{\mathbf{V}}_{\breve{\mathbf{h}}_0}(i)\big)^{-1} \Big]^{-1}. \tag{3.65}$$

Since the *a posteriori* messages are identical on the equation nodes, the channel estimates at the i-th inner iteration can be updated as

$$\mathbf{m}_{\breve{\mathbf{h}}_q^{\tilde{l}}}(i) = \mathbf{m}_{\breve{\mathbf{h}}_q}(i) = \breve{\mathbf{F}}_L \mathbf{\Lambda}_0^H \breve{\mathbf{F}}_L^{-1} \mathbf{m}_{\breve{\mathbf{h}}_{q-1}}(i), \tag{3.66}$$

$$\mathbf{V}_{\breve{\mathbf{h}}_q^{\tilde{l}}}(i) = \mathbf{V}_{\breve{\mathbf{h}}_q}(i) = \breve{\mathbf{F}}_L \mathbf{\Lambda}_0^H \breve{\mathbf{F}}_L^{-1} \mathbf{V}_{\breve{\mathbf{h}}_{q-1}}(i) \breve{\mathbf{F}}_L^{-H} \mathbf{\Lambda}_0 \breve{\mathbf{F}}_L^H. \tag{3.67}$$

Note that the product of $\breve{\mathbf{F}}_L$ (or $\breve{\mathbf{F}}_L^H$) with a vector in the above-mentioned equations can be efficiently implemented using IFFT operations. When L/ν is an integer, only a L/ν-point IFFT is needed. When L/ν is not an integer, several L/ν-point IFFT modules are employed [132].

The proposed hybrid GMP-EP-VMP JCEE algorithm for SEFDM-IM systems communicating over frequency-selective fading channels is summarized in **Algorithm** 2, where I_{in} and I_{e} are the number of the inner and outer iterations, respectively.

Algorithm 2 Hybrid GMP-EP-VMP JCEE of SEFDM-IM Signaling with Unknown CSI

1: **Initialization**: The initial values of channel coefficients are obtained by the pilot-based ZF method in [108].
2: Run the initialization steps in **Algorithm** 1.
3: **for** $i_o = 1$ to I_{e} **do**
4: **for** $i_t = 1$ to I_{in} **do**
5: Compute the forward mean vector and covariance matrix of $s_k^{\tilde{l}}$ according to (3.41) and (3.42);
6: Execute step 4-7 in **Algorithm** 1;
7: Compute the messages related to the inner product constraint node using (3.47)-(3.54);
8: Compute the backward messages of the transmitted symbols and channel coefficients related to the inner product node according to (3.47)-(3.54);
9: Compute the backward messages of $\breve{x}_k^{\tilde{l}}$ according to (3.55) and (3.56);
10: Based on the discrete *a priori* probabilities and the backward messages of the transmitted symbols, compute their approximated *a priori* mean and variance vectors according to (3.33)-(3.36);
11: Compute the backward mean vector and covariance matrix of $\breve{\mathbf{h}}_q$ using the backward messages of $\breve{\mathbf{h}}_q^{\tilde{l}}$ from different SEFDM-IM symbols according to (3.57) and (3.58);
12: Compute the forward messages of the channel estimator according to (3.59)-(3.63);
13: Compute the *a posteriori* messages of variables $\breve{\mathbf{h}}_q^{\tilde{l}}$ according to (3.64)-(3.67);
14: **end for**
15: Execute step 11-13 in **Algorithm** 1.
16: **end for**

3.5 Complexity Analysis and Simulation Results

3.5.1 Complexity Analysis

The complexity comparison of the proposed GMP-EP and GMP-EP-VMP algorithms to that of the existing methods is summarized in Table 3.1 and Table 3.2, respectively. Since the standard

Table 3.1: Complexity Analysis of Equalization of SEFDM-IM Signaling

ML	$\mathcal{O}(2^{P_{\mathrm{g}}G})$
BML	$\mathcal{O}(2^{P_{\mathrm{g}}\lceil L_{\mathrm{m}}/K_{\mathrm{g}}\rceil})$
MMSE-SBS	$\mathcal{O}(K^3)$
MMSE-LLR	$\mathcal{O}(K^3)+\mathcal{O}(GM^2)$
SIC-SBS	$\mathcal{O}(3cK\log_2 K)$
GMP-EP	$\mathcal{O}(K\dot{K}_{\mathrm{I}}^2)$ and $\dot{K}_{\mathrm{I}} \ll K$

soft information calculation and BCJR decoding are performed in all methods in the following, this work only discusses the complexity of the equalizer and channel estimator. The optimal ML equalizer suffers from an exponentially increased complexity order of $\mathcal{O}(2^{P_{\mathrm{g}}G})$, where P_{g} is the number of coded bits per subblock and G is the total number of subblocks. The complexity of the BML method approximately adopted from [123] exploits an ML detector having a reduced search space and a complexity order of $\mathcal{O}(2^{P_{\mathrm{g}}\lceil L_{\mathrm{m}}/K_{\mathrm{g}}\rceil})$, where L_{m} is the truncated length of the interferences for the exhaustive search and N is the number of SEFDM-IM subcarriers per subblock. The improved MMSE-LLR method suitably adopted from [124] consists of the MMSE equalizer and the LLR-based detector having an extended joint search space, a complexity order of $\mathcal{O}(K^3)$ and $\mathcal{O}(GM^2)$, respectively, where K is the total number of SEFDM-IM subcarriers and M represents the M-ary constellation mapping. When relying on IFFT/FFT-based modulation/demodulation, the complexity of the SIC-SBS equalizer extended from [105] and [34] grows logarithmically with the length of FFT. For the proposed GMP-EP equalizer, the complexity is dominated by the matrix inversion operation in (3.37) and (3.21), having a complexity order of $\mathcal{O}(\dot{K}_{\mathrm{I}}^3)$, where $\dot{K}_{\mathrm{I}} = 2K_{\mathrm{I}}+1$ is the total truncated length of interferences considered for ICI mitigation. Since it is computed $K/\dot{K}_{\mathrm{I}}$ times per iteration, the total complexity of the proposed GMP-EP equalizer is on the order of $\mathcal{O}(K\dot{K}_{\mathrm{I}}^2)$ per iteration. Compared to the existing methods, the proposed GMP-EP equalizer is preferable for SEFDM-IM systems having a large number of subcarriers and/or high-order modulation.

For the channel estimation, the classical time-domain pilot-based FCE [108] and PCE [109] channel estimators are derived based on the ZF criterion, having a complexity order of $\mathcal{O}(K^3)$. In [110], the frequency-domain PCE using SEFDM pilots is derived, which has a linearly increasing complexity vs the number of subcarriers, plus the additional interpolation complexity. The above channel estimator can be combined with an SIC equalizer for constructing an SEFDM-IM receiver. The variance matrices of the proposed hybrid GMP-EP-VMP algorithm are approximated by diagonal matrices using the trace operation in (3.62), which results in trivial complexity for the matrix inversion. The inversion operation of the non-diagonal matrix $\breve{\mathbf{F}}_L$ only has to be calculated once, which can be performed off-line. As a result, the complexity of the GMP-EP-VMP method is dominated by the matrix product operation related to $\breve{\mathbf{F}}_L$, which can be implemented by the IFFT/FFT operation. The complexity of the other matrix product operations depends on the number of subcarriers and on the length of the channel memory per iteration. Therefore, the total complexity of the proposed channel estimator is

Table 3.2: Complexity Analysis of Channel Estimation and Equalization of SEFDM-IM Signaling

Algorithm	Complexity	
	Channel Estimation	Equalization
T-FCE/PCE-SIC	$\mathcal{O}(K^3)$	$\mathcal{O}(3cK\log_2 K)$
F-PCE-SIC	$\mathcal{O}(K)$	$\mathcal{O}(3cK\log_2 K)$
GMP-EP-VMP	$\mathcal{O}(cK\log_2 L)+\mathcal{O}(KL)$	$\mathcal{O}(K\dot{K}_{\mathrm{I}}^2)$ and $\dot{K}_{\mathrm{I}} \ll K$

$\mathcal{O}(cK\log_2 L)+\mathcal{O}(KL)$ for $\nu = b/c$, $b, c \in \mathbb{N}$ per iteration.

3.5.2 Simulation Results

Both the BER and NMSE performance of the proposed methods are evaluated by Monte Carlo simulations. In all simulations, a LDPC code having code rate of $R_{\mathrm{c}} = 3312/4032$ and code length of 4032 bits is employed, unless otherwise specified. In [43], it is demonstrated that subcarrier-index modulation is beneficial for the scenario of a relatively low transmission rate below 2 bits/s/Hz. Hence, QPSK modulation using Gray mapping is employed. Each frame consists of $\tilde{L} = 32$ SEFDM-IM symbols and pilots are only transmitted on the first symbol. For notational simplicity, the SEFDM-IM scheme with K_{a} out of K_{g} subcarriers being active per subblock is referred as the $(K_{\mathrm{g}}, K_{\mathrm{a}})$ scheme. The order of CAR model is set to $P_0 = 1$. The truncated length of interferences is $K_{\mathrm{I}} = 5$, unless otherwise specified. A Rician fading channel having $L = 8$ paths and a Rician factor of $K_{\mathrm{h}} = 10\ dB$ is studied [143]. The coefficient h_l of the l-th path is independently generated according to the distribution $h_l \propto \mathcal{CN}(h_l; 0, \sigma_{h_l}^2)$ and $\sigma_{h_l}^2 = \exp(-0.1l)/(\sum_l \sigma_{h_l}^2)^2$. The total number of iterations and inner LDPC decoding iterations are $I = I_{\mathrm{in}} I_{\mathrm{e}} = 50$ and $I_{\mathrm{c}} = 50$, respectively.

The BER performance of the proposed equalizer ($I_{\mathrm{in}} = 1$) is evaluated and compared to that of other existing equalizers conceived for SEFDM-IM signaling using known CSI, as shown in Fig. 3.4. Due to the high complexity of some of the existing methods, the number of subcarriers is set to $K = 16$. The BML method ($L_{\mathrm{m}} = 4$) in [123] and the MMSE-LLR method in [124] are extended to coded SEFDM-IM systems by calculating soft information representing the index bits and symbol bits. The BER performance of OFDM-IM signaling is also included as a benchmark. Observe that the BML equalizer and the MMSE-LLR equalizer do not perform well. This is because the BML equalizer ignores interferences from other IM subblocks and the MMSE-LLR equalizer only reserves $K_{\mathrm{a}} + 1$ candidate active patterns. Compared to the OFDM-IM signaling, the MMSE-SBS equalizer suffers from 0.5 dB and 1.0 dB performance loss at BER $= 10^{-5}$ for $\nu = 0.9$ and $\nu = 0.8$, respectively. Due to joint interference cancellation and IM detection, the proposed hybrid GMP-EP equalizer attains a comparable BER performance at an 11% higher transmission rate than its orthogonal subcarrier based counterpart. When further decreasing the subcarrier packing factor, SEFDM-IM signaling improves the spectral

[2] A quasi-static frequency-selective channel model is considered. The channel coefficients are fixed for each Monte Carlo simulation, while they vary according to the channel model for different Monte Carlo simulations.

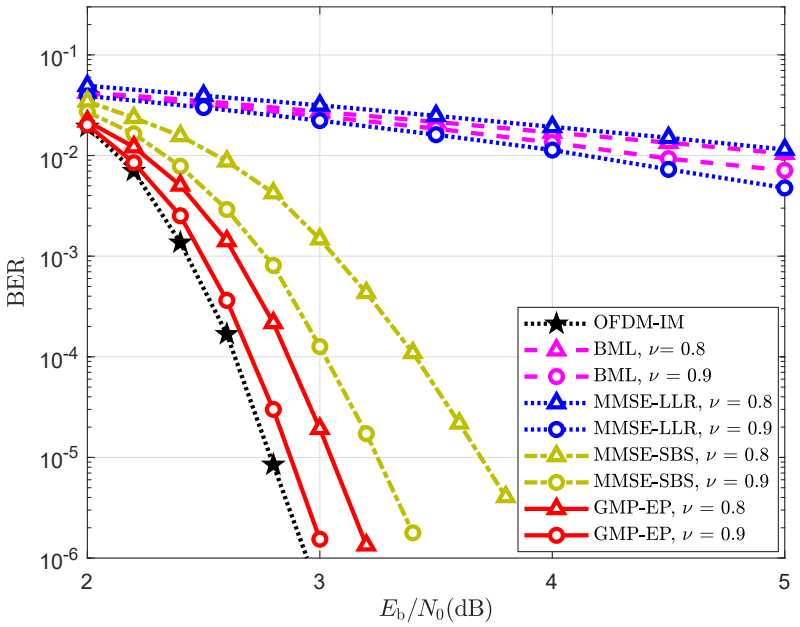


Figure 3.4: BER performance of different equalizers for SEFDM-IM systems with known CSI, $(K_g, K_a) = (4, 1)$.

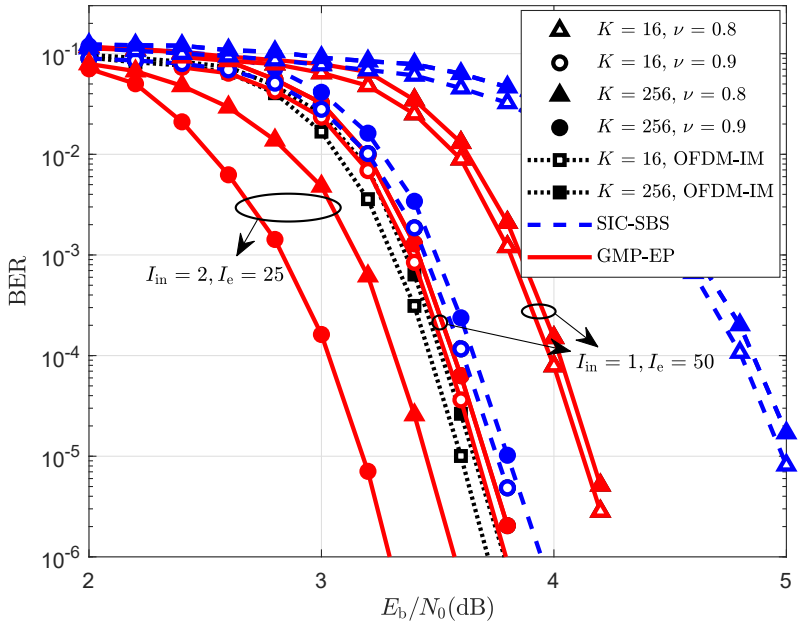


Figure 3.5: BER performance of different equalizers for SEFDM-IM systems with known CSI, $(N, K) = (4, 3)$.

efficiency by up to 25% at the cost of only 0.3 dB E_b/N_0 loss at BER = 10^{-5}.

In Fig. 3.5, the BER performance of the proposed equalizer $I_{in} = 50$ is evaluated and compared to the SIC-SBS equalizer (which becomes the MMSE-SBS equalizer when $I_{in} = 1$). In the following simulations, the IM parameters are set to $(K_g, K_a) = (4, 3)$. To illustrate the flexibility

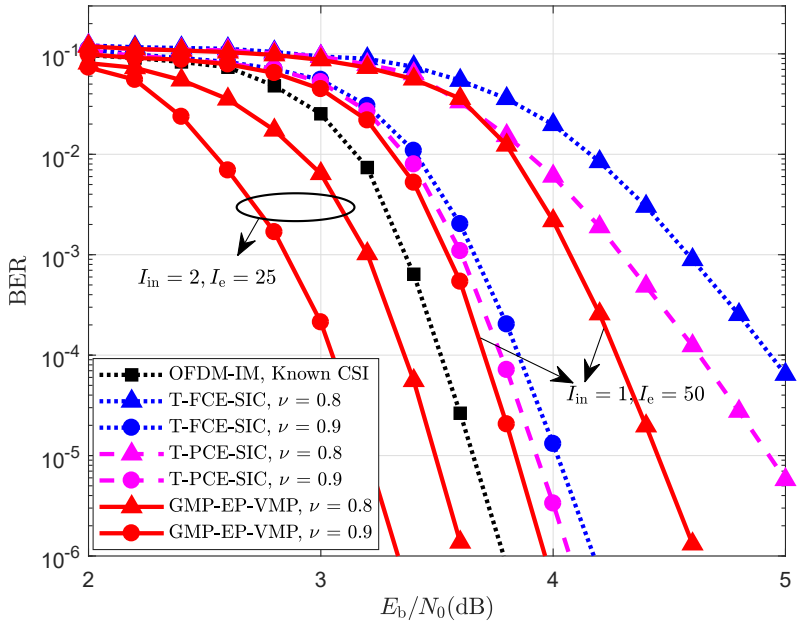


Figure 3.6: BER performance of different JCEE algorithms for SEFDM-IM systems.

of the proposed equalizer, the simulation results for SEFDM-IM systems having various number of subcarriers is provided, i.e., $K = 16$ and $K = 256$. It is observed that the BER of SEFDM-IM signaling only increases slightly upon increasing the number of subcarriers due to the ill-conditioning problem of SEFDM-IM signaling. Compared to its OFDM-IM counterpart, for $\nu = 0.8$, SEFDM-IM signaling based on the proposed GMP-EP equalizer achieves both 25% higher transmission rate and 0.2 dB $\mathrm{E_b/N_0}$ gain at BER $= 10^{-5}$ by judiciously selecting the values of I_{in} and I_{e}. By contrast, the SIC-SBS equalizer suffers from 1.4 dB performance loss for $\nu = 0.8$ due to the impact of severe equivalent interferences at the first iteration.

As shown in Fig. 3.6 and Fig. 3.7, the BER and NMSE performance of the proposed hybrid GMP-EP-VMP JCEE method are evaluated, respectively. The number of subcarriers is set to be $K = 256$. The corresponding curves of the time-domain FCE-SIC and PCE-SIC algorithms, i.e., T-FCE-SIC and T-PCE-SIC, are also plotted for comparison. The BER performance of Nyquist signaling with perfect CSI is also included as a reference. As seen, the BER and NMSE performance of the T-PCE-SIC method are superior to those of the T-FCE-SIC method because the former only transmits pilots on mutually orthogonal subcarriers to alleviate the effects of the ill-conditioning problem of SEFDM signaling. Note that the proposed channel estimator employs not only the pilots, but also the transmitted symbols recovered in the previous iterations. Hence, the proposed method relying on the most appropriate activation order of the receive components outperforms other schemes in terms of their BER and NMSE performance, especially for severe ICIs scenarios. Compared to that of OFDM-IM signaling, for $\nu = 0.9$, the $\mathrm{E_b/N_0}$ gain of the proposed GMP-EP-VMP method using $I_{\mathrm{in}} = 2, I_{\mathrm{e}} = 25$ is about 0.4 dB at BER $= 10^{-5}$. Even if the spacing of subcarriers is reduced to $\nu = 0.8$, coded SEFDM-IM signaling still has about 0.2 dB $\mathrm{E_b/N_0}$ gain. Compared to OFDM-IM signaling,

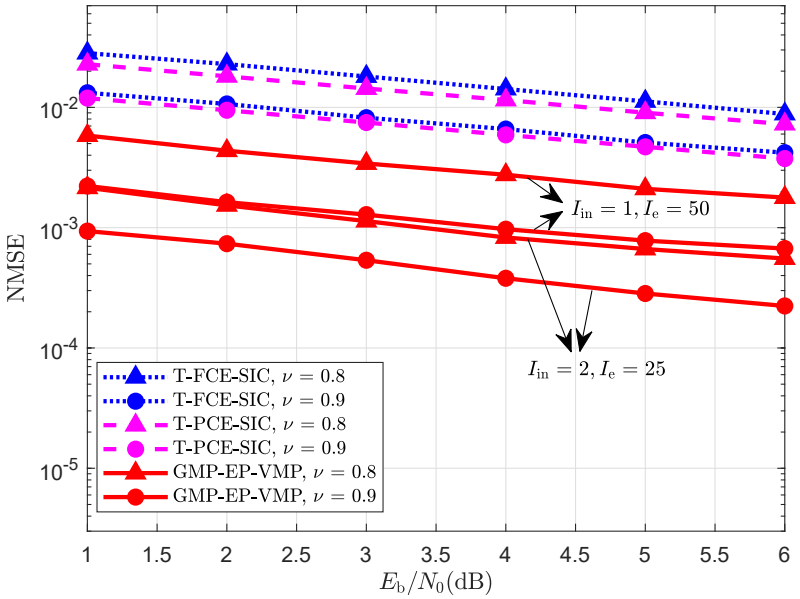
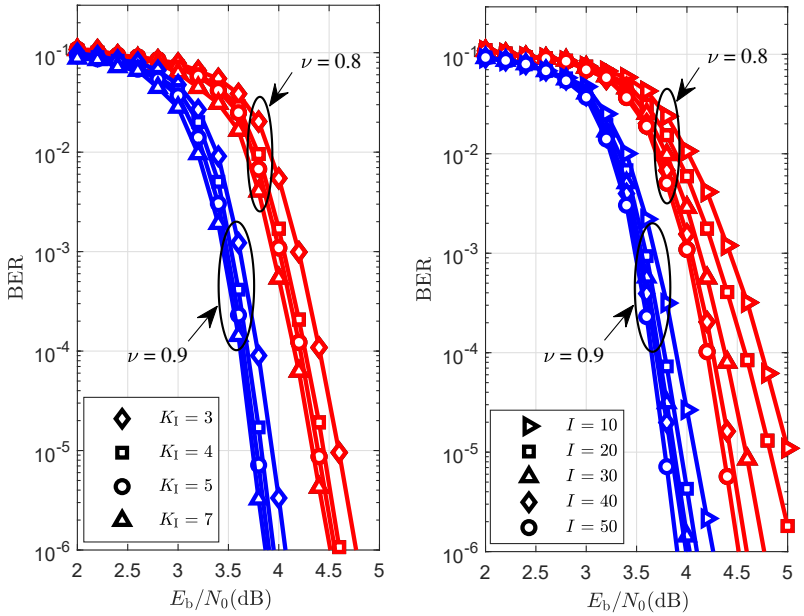


Figure 3.7: NMSE performance of different JCEE algorithms for SEFDM-IM systems.



(a) $K_I \in \{3, 4, 5, 7\}, I = 50$ (b) $K_I = 5, I \in \{10, 20, 30, 40, 50\}$

Figure 3.8: Impact of different combinations of K_I and I on BER performance.

the performance gain may result from the more robustness to the channel impairments due to the smaller subcarrier spacing of SEFDM-IM signaling. However, when the inner iteration of the equalizer runs only once, an additional 0.6 dB performance erosion may be encountered for $\nu = 0.8$ and $\nu = 0.9$. Hence, designing a judicious activation order is critical to the proposed methods.

The complexity of the proposed algorithm depends both on the length of the truncated interfer-

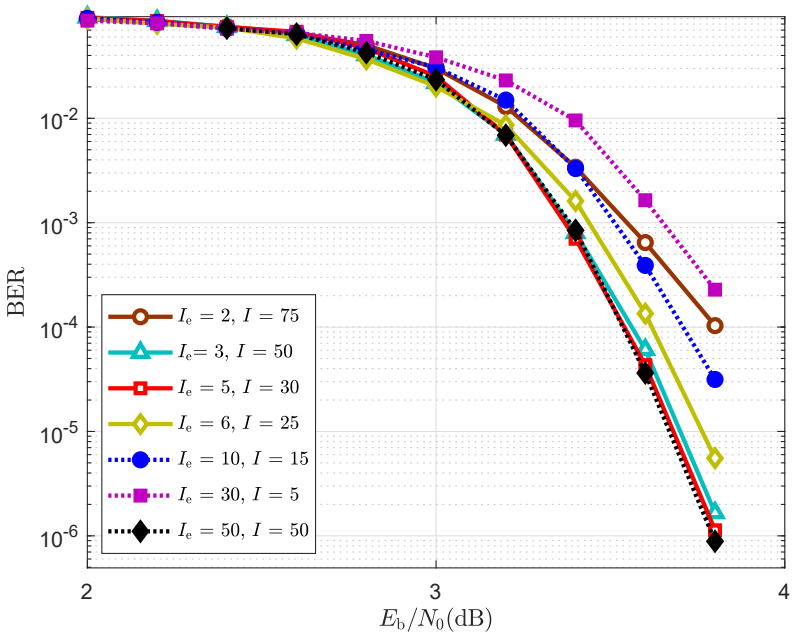


Figure 3.9: Impact of different combinations of I_c and I on BER performance.

ences and on the number of turbo iterations. The impact of K_I and I on the BER performance is illustrated in Fig. 3.8, where $I_{in} = 1$. For simplicity, the number of subcarriers is $K = 16$ in the following simulations. It is seen that the BER performance of SEFDM-IM signaling with various packing factors improves as the number K_I or I increases. When K_I or I is higher than a certain value, the performance gain becomes marginal, especially for dense subcarrier packing. In Fig. 3.8 (a), significant performance gaps is observed between $K_I = 3$ and $K_I = 7$, which is due to the underestimation of the interferences induced by non-orthogonal signaling. By contrast, $K_I \geq 4$ is a reasonable approximation for $\nu = 0.8, \nu = 0.9$ in this case. In Fig. 3.8 (b), the convergence speed of the proposed algorithm becomes slower upon reducing ν. The result coincides with the fact that a smaller ν imposes stronger interferences. To strike a performance vs complexity balance, $I \geq 20$ is a reasonable option for $\nu = 0.8, \nu = 0.9$.

The BER performance of the proposed method with different combinations of the number of LDPC decoding iterations I_c and turbo iterations I are evaluated in Fig. 3.9, where $\nu = 0.9$ and $I_{in} = 1$. Since the complexity of LDPC decoding dominates the complexity of turbo receiver, the total number of LDPC decoding is fixed, i.e., the product of I_c and I, to be constant. It can be observed that, at the beginning, the BER performance of the proposed method improves with the increasing of I_c. Specifically, when $I_c = 5, I = 30$, the BER performance is very close to the one with $I_c = 50, I = 50$. However, when further increasing I_c, the BER performance degrades. This may due to the fact that the proposed method cannot coverage with inadequate turbo iterations. Therefore, message scheduling between LDPC decoding as well as channel estimation and equalization can be optimized to reduce the computational complexity.

In Fig. 3.10, the BER performance of SEFDM-IM signaling is evaluated for a fixed spectral

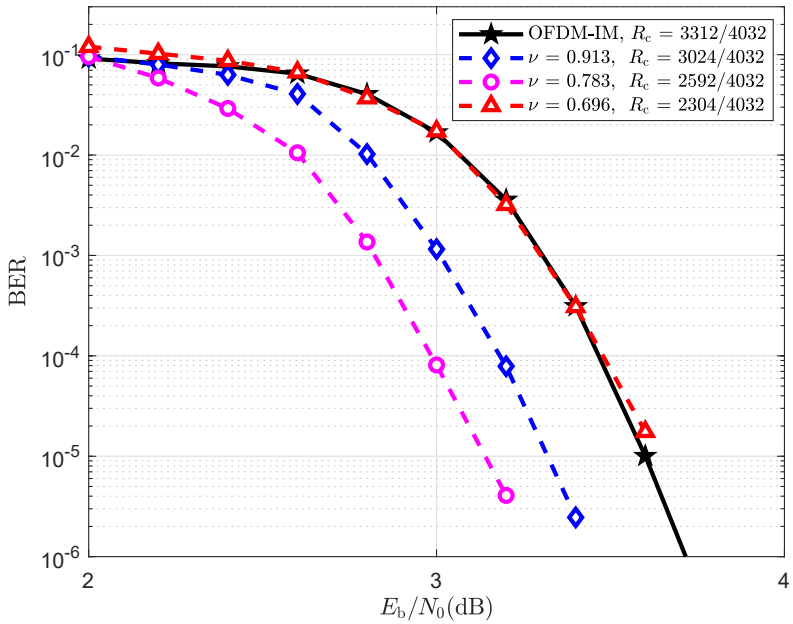


Figure 3.10: Impact of different combinations of ν and R_c on BER performance.

efficiency of $\eta = 1.64$ bits/s/Hz at different combinations of the subcarrier packing factor ν and code rate R_c, where $I_c = 50$, $I_{in} = 1$ and $I = 50$. The spectral efficiency of SEFDM-IM signaling is calculated as $\eta = R_c(\log_2\lfloor\binom{K_g}{K_a}\rfloor + K_a \log_2 M)/(\nu K_g)$ bits/s/Hz[128]. The scenario of OFDM-IM signaling with known CSI is plotted as the benchmark, where $\nu = 1$ and $R_c = 3312/4032$. Observe that the performance gain is about 0.3 dB for SEFDM-IM signaling associated with $\nu = 0.913, R_c = 3024/4032$. Upon reducing the coding rate and the packing factor simultaneously to $\nu = 0.783, R_c = 2592/4032$, the gain becomes 0.5 dB at the same bandwidth efficiency. Note that the performance gain cannot be increased by keep decreasing R_c for a fixed η. When further reducing ν and R_c, e.g., $\nu = 0.696, R_c = 2304/4032$, the BER performance is degraded. This is due to the fact that when the subcarrier packing factor is much smaller than the Mazo limit [26], the residual ICI degrades the decoding performance. Hence, in practical applications of SEFDM-IM systems, the proposed scheme can strike a compromise between the packing factor and code rate.

3.6 Conclusion

A low-complexity JCEE was conceived for SEFDM-IM signaling over frequency-selective fading channels. To extract the potential performance gain, the interference mitigation and IM detection were jointly performed for the scenario of perfectly known CSI. By introducing the extended constellation concept and further reformulating the design problem via a linear state space model, a Forney-style factor graph having two subgraphs was constructed. Based on Gaussian approximations of the discrete transmitted symbols via the EP method, a low-complexity parametric message passing algorithm was derived. For the scenario of unknown CSI, a multi-layer

factor graph was constructed to tackle the problem of error propagation in channel estimation induced by the deactivated subcarriers of SEFDM-IM signaling. To obtain Gaussian expressions for message passing between the channel estimator and equalizer, a soft node was built and the forward and backward messages were derived according to VMP rules. The simulation results shown that for a known CSI scenario, the proposed GMP-EP equalizer outperformed the extended non-iterative BML, MMSE-LLR, and MMSE-SBS methods. Furthermore, the performance of the proposed method was also superior to the iterative SIC-SBS method, especially for small packing factors. For an unknown CSI scenario, the proposed GMP-EP-VMP method performed very close to its known CSI counterpart. The complexity of the proposed GMP-EP equalizer increases linearly with the number of subcarriers, and that of the proposed GMP-EP-VMP channel estimation algorithm grows logarithmically with the length of the channel memory and linearly with the number of subcarriers.

Chapter 4

Joint Channel Estimation and Equalization for MFTN Signaling

4.1 Introduction

FTN signaling constitutes an innovative spectrally efficient non-orthogonal signaling solution for high-speed wireless communication systems [60], [95], [128]. By abandoning the orthogonality condition of different modulated waveforms, FTN signaling becomes capable of improving the transmission rate without requiring additional bandwidth. Hence, it achieves higher capacity than Nyquist signaling [54].

Given these benefits of FTN signaling, the concept of FTN has also been extended to multi-carrier transmission systems. In Chapter 3, the hybrid message passing algorithms have been developed for solving the low-complexity demodulation problem of one-dimensional frequency-domain packing signaling, i.e., SEFDM signaling. For further improving the spectral efficiency, the Nyquist interval of the signaling pulse in the time domain and the minimum orthogonal frequency spacing in the frequency domain can be 'squeezed' simultaneously, i.e., two-dimensional time-frequency packing MFTN signaling [31].

In this chapter, the receiver design of MFTN signaling will be discussed. For MFTN signaling, the two-dimensional distance between the signals can be optimized for maximizing the achievable spectral efficiency [34]. In recent years, MFTN signaling has been investigated both in satellite systems [144] and high-capacity optical systems [145], [146]. However, the severe ISIs and ICIs imposed by time-frequency packing lead to a potentially excessive detection complexity, which may limit the practical applications of MFTN systems.

Nonetheless, substantial research efforts have been dedicated to designing efficient receivers for MFTN systems. In [31], a MAP probability receiver based on the BCJR algorithm [115] was proposed for approaching the BER performance of Nyquist systems, albeit at the expense of an exponentially escalating complexity. An attraction two-dimensional MMSE-based equalizer was

designed for the interference mitigation of MFTN signaling in [116], where authors succeed in rendering the complexity independent of both the number of subcarriers and of the constellation size. However, its BER performance was significantly degraded in severe ICI scenarios. To tackle this problem, a one dimensional MMSE equalizer coupled with SIC was also designed in [116] for approaching the MAP-SIC equalizer's performance in the high SNR region. However, the scheme of [116] still exhibited a high computational complexity owing to the associated multiple matrix inversion operations. Note that the aforementioned equalizers cannot deal with the colored noise induced by the non-orthogonal matched filter of MFTN systems. Recently, a parametric Gaussian message passing receiver based on a novel truncated two-dimensional trellis structure was proposed for eliminating the severe two-dimensional interferences encountered by MFTN signaling in frequency-selective channels [32], where a realistic non-diagonal colored noise covariance matrix was used for updating the messages on the associated factor graph. Nevertheless, an inevitable BER performance loss is caused by the Gaussian approximation of the discrete *a priori* distributions of the transmitted symbols.

All of the above-mentioned MFTN receivers were investigated under the idealized simplifying assumption of perfectly known CSI. In practice, perfect CSI is unattainable, but it may be approached by JCEE techniques even in frequency-selective fading channels. Having said that, no JCEE solutions have been reported in the open literature for MFTN systems. Only a few studies discuss JCEE algorithms for one-dimensional packing FTN signaling in unknown channels [59], [88], [91], [118]. In [88], the authors developed a joint channel estimation and decoding (JCED) algorithm based on hybrid message passing. A multi-layer factor graph model was constructed by separating the known ISIs imposed by time-domain compression and the unknown ISIs imposed by multipath channels, where the colored noise process was approximated as an AR model. Then, both GMP and VMP were exploited for updating messages between variables. For the unknown time-varying channels, a frequency-domain JCED algorithm was designed for FTN systems in [59]. Different from the typical frequency-domain receivers [81], [82], [84], the JCED algorithm of [59] reformulated a frequency-domain system model without utilizing cyclic prefix. Furthermore, the GAMP algorithm was introduced for improving BER performance in the case of the discrete transmitted symbols. FTN signaling has been combined with SCMA and then the corresponding joint channel estimation, symbol detection, and user activity tracking was proposed in [91]. Note that the joint channel estimation and symbol detection method is similar to that of [88]. Moreover, a ZF-based channel estimation for single-carrier FTN signaling was studied and the optimal training sequence was designed via minimizing MSE.

These JCEE algorithms of single-carrier FTN systems cannot simply be extended to MFTN systems due to the intractable coupling of the Doppler spreads, frequency selectivity and severe two-dimensional interferences. Moreover, the existing JCEE algorithms of single-carrier FTN systems can only deal with the one dimensional interferences and cannot alleviate the ill-conditioning problem imposed by time-frequency packing. Motivated by tackling these chal-

lenges, this work appropriately adapts the PBiGAMP algorithm of [147] for solving the high-dimensional random bilinear mixing recovery problem. The associated ill-conditioning problem[1] caused by the non-orthogonal nature of MFTN signaling often prevents the PBiGAMP algorithm for readily converge, but still no solutions have been found for improving the convergence of the PBiGAMP algorithm. Hence, this work develops a low-complexity PBiGAMP-based frequency-domain iterative message passing receiver, which is robust to the above-mentioned impediments of MFTN systems operating in frequency-selective fading channels.

To improve the convergence of PBiGAMP-based receiver, a novel segment-based frequency-domain received signal model is derived through inserting a few cyclic postfixes in the frequency domain and truncating the inherent two-dimensional interferences. By reformulating the linear transition matrix into one having a block circulant structure, the proposed model can reduce the condition number of the equivalent channel matrix and then mitigate the ill-conditioning problem of MFTN signaling. Moreover, the covariance matrix of the equivalent colored noise process is reconstructed as a block circulant matrix. Building on this, the colored noise process induced by the non-orthogonal matched filter is whitened in the frequency domain based on the eigenvalue decompositions of the block circulant matrices.

Based on the proposed segment-based frequency-domain received signal model, a pair of PBiGAMP-based frequency-domain JCEE (FDJCEE) algorithms are developed for MFTN systems. With the aid of several average approximations, the refined version not only circumvents the strong sensitivity of the ill-conditioned matrices to small perturbations, but also reduces the computational complexity. Instead of using the typical Gaussian approximations of the transmitted symbols that rely on the moment matching method, the exact discrete *a priori* probabilities are used for improving the symbol detection performance. To eliminate the two-dimensional interferences engendered by the adjacent segments, two additive terms are inserted to improve the accuracy of the "pseudo" *a priori* mean vector of the noiseless measurements. In the case of known CSI, the proposed JCEE algorithms can be readily decomposed into two FDE algorithms.

The rest of this chapter is organized as follows. In Section 4.2, a segment-based frequency-domain received signal model is constructed and its effects on the ill-conditioning problem of MFTN signaling are further discussed. The proposed PBiGAMP-based iterative receiver is described in Section 4.3. The BER and NMSE performance results of the proposed algorithms are evaluated and compared to the state-of-the-art algorithms in Section 4.4. Finally, the conclusions are offered in Section 4.6.

[1] When the minimum eigenvalue of the interference matrix approaches zero, the linear system tends to become ill-conditioned [148]. As discussed in [149], their ill-conditioning cannot be completely overcome by any unbiased estimator. Hence, this work can only mitigate the effect of ill-conditioning on the BER performance, but cannot completely eliminate it.

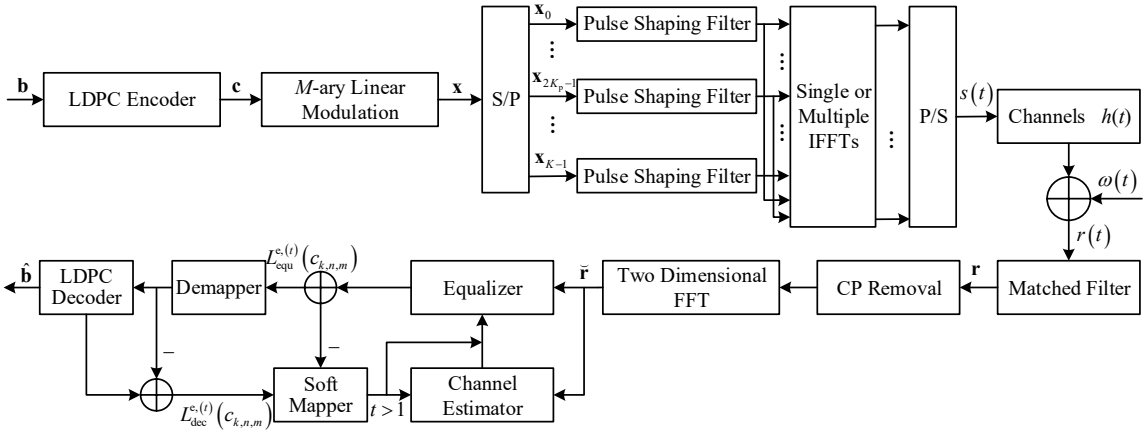


Figure 4.1: Block diagram of an LDPC-coded MFTN transceiver.

4.2 Segment-Based Frequency-Domain Received Signal Model

The general transceiver structure of LDPC-coded MFTN systems is illustrated in Fig. 4.1. The input bits $\mathbf{b} = [b_0, \cdots, b_{N_\mathrm{b}-1}]^T$ are encoded to obtain N_c LDPC-coded bits $\mathbf{c} = [c_0, \cdots, c_{N_\mathrm{c}-1}]^T$. Considering a MFTN system having K subcarriers and each subcarrier containing $N = N_\mathrm{s}/K$ symbols in the time domain, the coded bits are mapped onto M-ary linear modulation constellation points to generate the independently and identically distributed modulated symbols. Then, the serial modulated symbol sequence $\mathbf{x}$ is partitioned into K parallel subsequences, where $\mathbf{x} = [\mathbf{x}_0^T, \cdots, \mathbf{x}_{K-1}^T]^T$ and $\mathbf{x}_k = [x_{k,0}, \cdots, x_{k,N-1}]^T$ contains N modulated symbols of the k-th subcarrier. Furthermore, the modulated symbols are passed through a pulse shaping filter $p(t)$ associated with the symbol interval τT_0, where $\tau \in (0, 1]$ is the time packing factor and T_0 is the Nyquist time interval. After that, the symbols of the first $2K_\mathrm{p}$ subcarriers are concatenated to the original symbol sequence as cyclic postfixes in the frequency domain. To further improve the spectral efficiency, the modulated symbols are transmitted on K overlapped subcarriers with the frequency spacing νF_0, where $\nu \in (0, 1]$ is the frequency packing factor and F_0 is the minimum orthogonal frequency spacing. This operation can be efficiently implemented by single or multiple IFFT modules [132]. After the parallel to serial (P/S) conversion, the baseband transmitted MFTN signal is expressed as

$$s(t) = \sum_{k=0}^{\tilde{K}-1} \sum_{n=0}^{N-1} x_{k,n} p(t - n\tau T_0) e^{j2\pi k\nu F_0 t}, \tag{4.1}$$

where $\tilde{K} = K + 2K_\mathrm{p}$, the value of K_p depends on the truncated interference length K_I, k and n are the subcarrier index and the time index, respectively.

At the output of a frequency-selective fading channel having a CIR $h(t, \iota)$, the received signal

is given by

$$r(t) = \int_{-\infty}^{+\infty} h(t,\iota)s(t-\iota)d\iota + \omega(t), \tag{4.2}$$

where $h(t,\iota) = 0$ for $\iota < 0$ and $\iota > \iota_{\max}$, $\iota_{\max}$ is the maximum delay spread, and $\omega(t)$ is an AWGN process with zero mean and variance σ_0^2.

Assuming perfect synchronization between the transmitter and the receiver, the output of the non-orthogonal matched filter is derived as

$$\begin{aligned} r_{k_\mathrm{r},n_\mathrm{r}} &= \int_{-\infty}^{\infty} r(t)p(t-n_\mathrm{r}\tau T_0)e^{-j2\pi k_\mathrm{r}\nu F_0 t}dt \\ &= \sum_{l=0}^{L-1} h_{n_\mathrm{r},l} \sum_{k_\mathrm{t}=0}^{\tilde{K}-1}\sum_{n_\mathrm{t}=0}^{N-1} x_{k_\mathrm{t},n_\mathrm{t}} e^{-j2\pi k_\mathrm{t} l\nu F_0\tau T_0} \int_{-\infty}^{\infty} p(t-n_\mathrm{r}\tau T_0)p(t-(n_\mathrm{t}+l)\tau T_0)e^{-j2\pi(k_\mathrm{r}-k_\mathrm{t})\nu F_0 t}dt + \omega_{k_\mathrm{r},n_\mathrm{r}} \\ &= \sum_{l=0}^{L-1} h_{n_\mathrm{r},l} \sum_{k_\mathrm{t}=0}^{\tilde{K}-1}\sum_{n_\mathrm{t}=0}^{N-1} A_\mathrm{p}((n_\Delta+l)\tau T_0, k_\Delta\nu F_0)\psi_{k_\Delta,n_\mathrm{r}}^{k_\mathrm{t},l} x_{k_\mathrm{t},n_\mathrm{t}} + \omega_{k_\mathrm{r},n_\mathrm{r}}, \end{aligned} \tag{4.3}$$

where $n_\Delta = n_\mathrm{t} - n_\mathrm{r}$, $k_\Delta = k_\mathrm{t} - k_\mathrm{r}$, k_r and n_r are the indices of the received symbols, k_t and n_t are the indices of the transmitted symbols, $h_{n_\mathrm{r},l}$ is the l-th channel coefficient at the time index n_r, $A_\mathrm{p}(\tau T_0, \nu F_0) = \int_{-\infty}^{+\infty} p(t)p(t-\tau T_0)e^{j2\pi\nu F_0 t}\mathrm{d}t$ is the ambiguity function, $\psi_{k_\Delta,n_\mathrm{r}}^{k_\mathrm{t},l} = e^{j2\pi(k_\Delta n_\mathrm{r} - k_\mathrm{t} l)\nu F_0\tau T_0}$ and finally $\omega_{k_\mathrm{r},n_\mathrm{r}} = \int_{-\infty}^{\infty}\omega(t)p(t-n_\mathrm{r}\tau T_0)e^{-j2\pi k_\mathrm{r}\nu F_0 t}dt$ is the colored noise process having a covariance matrix $\mathbf{R}_\omega$ with the elements of $\mathbb{E}\{\omega_{k_1,n_1}\omega_{k_2,n_2}^*\} = \sigma_0^2 A_\mathrm{p}\big[(n_1 - n_2)\tau T_0, (k_1-k_2)\nu F_0\big]$.

According to (4.3), the time-domain received signal of MFTN system is represented as

$$\mathbf{r} = \sum_{l=0}^{L-1}(\mathbf{I}_K \otimes \dot{\mathbf{h}}_l)\mathbf{G}_l\mathbf{x} + \boldsymbol{\omega}, \tag{4.4}$$

where $\dot{\mathbf{h}}_l = [h_{0,l}, \cdots, h_{N-1,l}]^T$ denotes the channel coefficient of the l-tap, $\mathbf{G}_l$ denotes the time-domain interference matrix, and $\boldsymbol{\omega}$ denotes the time-domain colored noise process. Note that $\mathbf{G}_l$ is an ill-conditioned matrix, having a large condition number. Since the two-dimensional interference matrix of (4.3) suffers from potential ill-conditioning problem, the solutions of the bilinear JCEE problem are sensitive to small perturbations. The condition number can be regarded as an indicator of whether the linear transition matrix is ill-conditioned or well-conditioned. The condition number of the two-dimensional interference matrix in (4.3) increases with the reduction of the packing factors and hence the negative effects of the ill-conditioning become worse. In this section, a novel received signal model is constructed for assisting in mitigating the ill-conditioning of MFTN signaling.

According to the received signal model of (4.3), the inevitable ISIs and ICIs of MFTN signaling can be characterized by the ambiguity function $A_\mathrm{p}(\tau T_0, \nu F_0)$. The inherent two-dimensional

interferences imposed by time-frequency packing depend on both the shaping pulse and on the packing factors, but they reduce upon increasing the intervals of the symbols and subcarriers. In this work, a RRC pulse shaping filter having a roll-off factor β is employed. Considering that the ISIs and ICIs are dominated by the neighboring symbols and subcarriers, the demodulation complexity of MFTN systems can be reduced by employing a truncated two-dimensional interference model, i.e., $A_{\rm p}\big[(n_\Delta+l)\tau T_0, k_\Delta \nu F_0\big]=0$ for $|n_\Delta+l|>N_{\rm I}$ or $|k_\Delta|>K_{\rm I}$, where $N_{\rm I}$ and $K_{\rm I}$ are the truncated ISI and ICI intervals.

To develop an efficient MFTN receiver for frequency-selective fading channels, the transmitted symbols of the $k_{\rm t}$-th subcarriers $\mathbf{x}_{k_{\rm t}}$ are partitioned into $L_{\rm q}$ short segments of length $L_{\rm m}$ given by $\mathbf{x}_{k_{\rm t},q}=[x_{k_{\rm t},qL_{\rm m}},\cdots,x_{k_{\rm t},(q+1)L_{\rm m}-1}]^T$, where $q=0,\cdots,L_{\rm q}-1$, $N=L_{\rm q}L_{\rm m}$, $L_{\rm g}-1\leq L_{\rm m}\leq N$, and $L_{\rm g}=L+2N_{\rm I}$. For the time-invariant or quasi-static channels, $L_{\rm m}$ can be set to N. Without loss of generality, the CSI is assumed to be fixed for the duration of a single segment [59]. Based on the above-mentioned derivations of the time-domain received signal, the observation vector of the k-th subcarrier in the q-th segment, i.e., $\mathbf{r}_{k_{\rm r},q}=[r_{k_{\rm r},qL_{\rm m}},\cdots,r_{k_{\rm r},qL_{\rm m}+N_{\rm s}-1}]^T$, $N_{\rm s}=L_{\rm m}+L_{\rm g}-1$, can be expressed as

$$\mathbf{r}_{k_{\rm r},q}=\sum_{l=0}^{L-1}h_{q,l}\sum_{k_{\rm t}\in\mathcal{I}_{K_{\rm I}}^{k_{\rm r}}}\mathcal{D}(\boldsymbol{\psi}_{k_\Delta,q}^{k_{\rm t},l})(\mathbf{g}_{k_\Delta,l}*\mathbf{x}_{k_{\rm t},q})+\mathbf{z}_{k_{\rm r},q-1}^{\rm tail}+\mathbf{z}_{k_{\rm r},q+1}^{\rm head}+\boldsymbol{\omega}_{k_{\rm r},q},\tag{4.5}$$

where $h_{q,l}$ is the l-th channel coefficient in the q-th segment, $\mathcal{I}_{K_{\rm I}}^{k_{\rm r}}=\{k_{\rm r}-K_{\rm I},k_{\rm r}-K_{\rm I}+1,\cdots,k_{\rm r}+K_{\rm I}\}$, $\boldsymbol{\psi}_{k_\Delta,q}^{k_{\rm t},l}=[\psi_{k_\Delta,qL_{\rm m}}^{k_{\rm t},l},\cdots,\psi_{k_\Delta,qL_{\rm m}+L_{\rm s}-1}^{k_{\rm t},l}]^T$, $\mathbf{g}_{k_\Delta,l}=[\mathbf{0}_l^T\ \mathbf{g}_{k_\Delta}^T\ \mathbf{0}_{(L-1-l)}^T]^T$ represents the significant ISIs and ICIs within one segment, $\mathbf{g}_{k_\Delta}=[A_{\rm p}(N_{\rm I}\tau T_0,k_\Delta\nu F_0),\cdots,A_{\rm p}(-N_{\rm I}\tau T_0,k_\Delta\nu F_0)]^T$, and $\boldsymbol{\omega}_{k_{\rm r},q}=[\omega_{k_{\rm r},qL_{\rm m}},\cdots,\omega_{k_{\rm r},qL_{\rm m}+L_{\rm s}-1}]^T$ is the truncated colored noise vector. Moreover, $\mathbf{z}_{k_{\rm r},q-1}^{\rm tail}$ and $\mathbf{z}_{k_{\rm r},q+1}^{\rm head}$ characterize the two-dimensional interferences imposed by the tail of the $(q-1)$-th segment and by the head of the $(q+1)$-th segment, which are given by

$$\mathbf{z}_{k_{\rm r},q-1}^{\rm tail}=\boldsymbol{\Xi}_{\rm t}\bigg[\sum_{l=0}^{L-1}h_{q-1,l}\sum_{k_{\rm t}\in\mathcal{I}_{K_{\rm I}}^{k_{\rm r}}}\mathcal{D}(\boldsymbol{\psi}_{k_\Delta,q-1}^{k_{\rm t},l})(\mathbf{g}_{k_\Delta,l}*\mathbf{x}_{k_{\rm t},q-1})\bigg],\tag{4.6}$$

$$\mathbf{z}_{k_{\rm r},q+1}^{\rm head}=\boldsymbol{\Xi}_{\rm h}\bigg[\sum_{l=0}^{L-1}h_{q+1,l}\sum_{k_{\rm t}\in\mathcal{I}_{K_{\rm I}}^{k_{\rm r}}}\mathcal{D}(\boldsymbol{\psi}_{k_\Delta,q+1}^{k_{\rm t},l})(\mathbf{g}_{k_\Delta,l}*\mathbf{x}_{k_{\rm t},q+1})\bigg],\tag{4.7}$$

where $\boldsymbol{\Xi}_{\rm t}=[\mathbf{0}_{(L_{\rm g}-1)\times L_{\rm m}}\ \mathbf{I}_{L_{\rm g}-1};\ \mathbf{0}_{L_{\rm m}\times L_{\rm m}}\ \mathbf{0}_{L_{\rm m}\times(L_{\rm g}-1)}]$, $\boldsymbol{\Xi}_{\rm h}=[\mathbf{0}_{L_{\rm m}\times(L_{\rm g}-1)}\ \mathbf{0}_{L_{\rm m}\times L_{\rm m}};\ \mathbf{I}_{L_{\rm g}-1}\ \mathbf{0}_{(L_{\rm g}-1)\times L_{\rm m}}]$, $\mathbf{z}_{k_{\rm r},-1}^{\rm tail}=\mathbf{z}_{k_{\rm r},L_{\rm q}}^{\rm head}=\mathbf{0}_{L_{\rm s}}$.

By appending the required number of zeros to both the truncated interference vector $\mathbf{g}_{k_\Delta,l}$ and the transmitted symbol vector $\mathbf{x}_{k_{\rm t},q}$, the linear convolution in (4.5) can be converted to cyclic

convolution as

$$\mathbf{r}_{k_\mathrm{r},q} = \sum_{l=0}^{L-1} h_{q,l} \sum_{k_\mathrm{t}\in\mathcal{I}_{K_\mathrm{I}}^{k_\mathrm{r}}} \mathcal{D}(\boldsymbol{\psi}_{k_\Delta,q}^{k_\mathrm{t},l})(\boldsymbol{\Phi}_\mathrm{g}\mathbf{g}_{k_\Delta,l} \circledast \boldsymbol{\Phi}_\mathrm{m}\mathbf{x}_{k_\mathrm{t},q}) + \mathbf{z}_{k_\mathrm{r},q-1}^{\mathrm{tail}} + \mathbf{z}_{k_\mathrm{r},q+1}^{\mathrm{head}} + \boldsymbol{\omega}_{k_\mathrm{r},q}, \tag{4.8}$$

where $\boldsymbol{\Phi}_\mathrm{g} = [\mathbf{I}_{L_\mathrm{g}}\ \mathbf{0}_{L_\mathrm{g}\times(L_\mathrm{s}-L_\mathrm{g})}]^T$ is used for inserting $(L_\mathrm{s}-L_\mathrm{g})$ zeros into the truncated interference vector, $\boldsymbol{\Phi}_\mathrm{m} = [\mathbf{I}_{L_\mathrm{m}}\ \mathbf{0}_{L_\mathrm{m}\times(L_\mathrm{s}-L_\mathrm{m})}]^T$ is exploited for inserting $L_\mathrm{s}-L_\mathrm{m}$ zeros into the transmitted symbol vector $\mathbf{x}_{k_\mathrm{t},q}$.

According to the properties of cyclic convolution, the received signal in (4.8) is rewritten as

$$\begin{aligned}
\mathbf{r}_{k_\mathrm{r},q} &= \sum_{l=0}^{L-1} h_{q,l} \sum_{k_\mathrm{t}\in\mathcal{I}_{K_\mathrm{I}}^{k_\mathrm{r}}} \mathcal{D}(\boldsymbol{\psi}_{k_\Delta,q}^{k_\mathrm{t},l})\mathbf{F}_{L_\mathrm{s}}^H\mathcal{D}(\breve{\mathbf{g}}_{k_\Delta,l})\mathbf{F}_{L_\mathrm{s}}\boldsymbol{\Phi}_\mathrm{m}\mathbf{x}_{k_\mathrm{t},q} + \mathbf{z}_{k_\mathrm{r},q-1}^{\mathrm{tail}} + \mathbf{z}_{k_\mathrm{r},q+1}^{\mathrm{head}} + \boldsymbol{\omega}_{k_\mathrm{r},q} \\
&= \sum_{l=0}^{L-1} h_{q,l}\lambda_{k_\mathrm{r}}^l\mathbf{F}_{L_\mathrm{s}}^H\mathcal{D}(\breve{\mathbf{g}}_{0,l})\mathbf{F}_{L_\mathrm{s}}\boldsymbol{\Phi}_\mathrm{m}\mathbf{x}_{k_\mathrm{r},q} + \mathbf{z}_{k_\mathrm{r},q}^{\mathrm{ici}} + \mathbf{z}_{k_\mathrm{r},q-1}^{\mathrm{tail}} + \mathbf{z}_{k_\mathrm{r},q+1}^{\mathrm{head}} + \boldsymbol{\omega}_{k_\mathrm{r},q} \\
&= \sum_{l=0}^{L-1} h_{q,l}\lambda_{k_\mathrm{r}}^l\mathbf{F}_{L_\mathrm{s}}^H\mathcal{D}(\breve{\mathbf{g}}_{0,l})\mathbf{F}_{L_\mathrm{s}}\boldsymbol{\Phi}_\mathrm{m}\mathbf{x}_{k_\mathrm{r},q} + \boldsymbol{\kappa}_{k_\mathrm{r},q} + \boldsymbol{\omega}_{k_\mathrm{r},q},
\end{aligned} \tag{4.9}$$

and

$$\mathbf{z}_{k_\mathrm{r},q}^{\mathrm{ici}} = \sum_{l=0}^{L-1} h_{q,l} \sum_{k_\mathrm{t}\in\mathcal{I}_{K_\mathrm{I}\backslash k_\mathrm{r}}} \lambda_{k_\mathrm{t}}^l \mathcal{D}(\boldsymbol{\theta}_{k_\Delta,q})\mathbf{F}_{L_\mathrm{s}}^H\mathcal{D}(\breve{\mathbf{g}}_{k_\Delta,l})\mathbf{F}_{L_\mathrm{s}}\boldsymbol{\Phi}_\mathrm{m}\mathbf{x}_{k_\mathrm{t},q}, \tag{4.10}$$

where $\mathbf{F}_{L_\mathrm{s}}$ is an $L_\mathrm{s}\times L_\mathrm{s}$ normalized discrete Fourier transform matrix, $\breve{\mathbf{g}}_{k_\Delta,l} \triangleq \sqrt{L_\mathrm{s}}\mathbf{F}_{L_\mathrm{s}}\boldsymbol{\Phi}_\mathrm{g}\mathbf{g}_{k_\Delta,l}$, $\boldsymbol{\kappa}_{k_\mathrm{r},q} = \mathbf{z}_{k_\mathrm{r},q}^{\mathrm{ici}} + \mathbf{z}_{k_\mathrm{r},q-1}^{\mathrm{tail}} + \mathbf{z}_{k_\mathrm{r},q+1}^{\mathrm{head}}$ denotes the interference vector, $\mathcal{I}_{K_\mathrm{I}\backslash k_\mathrm{r}} = \{k_\mathrm{r}-K_\mathrm{I}, k_\mathrm{r}-K_\mathrm{I}+1, \cdots, k_\mathrm{r}-1, k_\mathrm{r}+1, \cdots, k_\mathrm{r}+K_\mathrm{I}\}$, and $\boldsymbol{\theta}_{k_\Delta,q} = [\theta_{k_\Delta}^{qL_\mathrm{m}}, \cdots, \theta_{k_\Delta}^{qL_\mathrm{m}+L_\mathrm{s}-1}]^T$.

Through removing the first and last K_p subcarriers, the received MFTN signal in the q-th segment is expressed as

$$\mathbf{r}_q = \sum_{l=0}^{L-1} h_{q,l}\big(\mathbf{I}_K\otimes\mathbf{F}_{L_\mathrm{s}}\big)^H\bar{\mathbf{G}}_{q,l}\big(\mathbf{I}_K\otimes\mathbf{F}_{L_\mathrm{s}}\big)\tilde{\boldsymbol{\Lambda}}_l\tilde{\boldsymbol{\Phi}}_\mathrm{m}\mathbf{x}_q + \boldsymbol{\varpi}_q, \tag{4.11}$$

where $\bar{\mathbf{G}}_{q,l}$ is an $L_\mathrm{s}\times L_\mathrm{s}$ block circulant matrix and composed of K^2 diagonal matrices with size L_s, $\tilde{\boldsymbol{\Lambda}}_l = \mathcal{D}(\boldsymbol{\lambda}_l)\otimes\mathbf{I}_{L_\mathrm{s}}$ and $\boldsymbol{\lambda}_l = [\lambda_0^l, \cdots, \lambda_{K-1}^l]^T$, $\tilde{\boldsymbol{\Phi}}_\mathrm{m} = (\mathbf{I}_K\otimes\boldsymbol{\Phi}_\mathrm{m})$, and $\boldsymbol{\varpi}_q = \boldsymbol{\kappa}_q + \boldsymbol{\omega}_q$ is the equivalent time-domain noise process. According to the properties of block circulant matrices, $\bar{\mathbf{G}}_{q,l}$ satisfies the decomposition of

$$\bar{\mathbf{G}}_{q,l} = (\mathbf{F}_K\otimes\mathbf{I}_{L_\mathrm{s}})^H\boldsymbol{\Lambda}_{q,l}(\mathbf{F}_K\otimes\mathbf{I}_{L_\mathrm{s}}), \tag{4.12}$$

where $\boldsymbol{\Lambda}_{q,l}$ is a diagonal matrix and the derivations are given in **Appendix** B. Hence, (4.11)

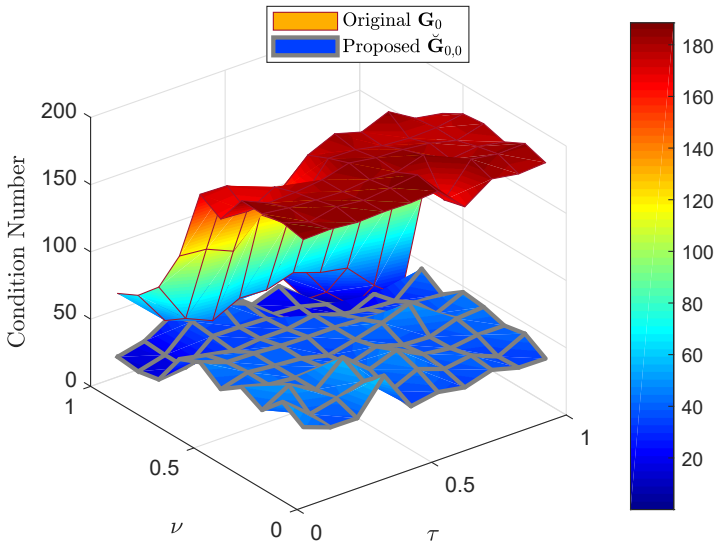


Figure 4.2: The condition number of the interference matrices in different received signal models.

is rewritten as

$$\mathbf{r}_q = \sum_{l=0}^{L-1} h_{q,l} \big(\mathbf{F}_K \otimes \mathbf{F}_{L_\mathrm{s}}\big)^H \mathbf{\Lambda}_{q,l} \big(\mathbf{F}_K \otimes \mathbf{F}_{L_\mathrm{s}}\big) \tilde{\mathbf{\Lambda}}_l \tilde{\mathbf{\Phi}}_\mathrm{m} \mathbf{x}_q + \boldsymbol{\varpi}_q, \tag{4.13}$$

where $(\mathbf{F}_K \otimes \mathbf{F}_{L_\mathrm{s}})$ is a unitary matrix.

The segment-based frequency-domain received model can be obtained by applying the two-dimensional Fourier transformation of the received signal in (4.13), which is given by

$$\begin{aligned} \breve{\mathbf{r}}_q &= \big(\mathbf{F}_K \otimes \mathbf{F}_{L_\mathrm{s}}\big)\mathbf{r}_q = \sum_{l=0}^{L-1} h_{q,l} \mathbf{\Lambda}_{q,l} \big(\mathbf{F}_K \otimes \mathbf{F}_{L_\mathrm{s}}\big) \tilde{\mathbf{\Lambda}}_l \tilde{\mathbf{\Phi}}_\mathrm{m} \mathbf{x}_q + \breve{\boldsymbol{\varpi}}_q \\ &= \sum_{l=0}^{L-1} h_{q,l} \mathbf{\Lambda}_{q,l} \ddot{\mathbf{F}}_{KL_\mathrm{s},l} \mathbf{x}_q + \breve{\boldsymbol{\varpi}}_q = \sum_{l=0}^{L-1} h_{q,l} \breve{\mathbf{G}}_{q,l} \mathbf{x}_q + \breve{\boldsymbol{\varpi}}_q, \end{aligned} \tag{4.14}$$

where $\breve{\mathbf{G}}_{q,l} \triangleq \mathbf{\Lambda}_{q,l} \ddot{\mathbf{F}}_{KL_\mathrm{s},l}$ is the segment-based frequency-domain equivalent channel matrix, $\mathbf{\Lambda}_{q,l}$ is a $KL_\mathrm{s} \times KL_\mathrm{s}$ diagonal matrix, $\ddot{\mathbf{F}}_{KL_\mathrm{s},l} \triangleq (\mathbf{F}_K \otimes \mathbf{F}_{L_\mathrm{s}}) \tilde{\mathbf{\Lambda}}_l \tilde{\mathbf{\Phi}}_\mathrm{m}$, $\breve{\boldsymbol{\varpi}}_q = (\mathbf{F}_K \otimes \mathbf{F}_{L_\mathrm{s}}) \boldsymbol{\varpi}_q$ denotes the frequency-domain equivalent noise process obeying Gaussian distribution. In the i-th iteration, the distribution of the frequency-domain equivalent noise process satisfies $\breve{\boldsymbol{\varpi}}_q \sim \mathcal{CN}\big[\breve{\boldsymbol{\varpi}}_q; \hat{\boldsymbol{\kappa}}_q(i), \mathcal{D}(\boldsymbol{\nu}_q^{\breve{\boldsymbol{\varpi}}}(i))\big]$, where the derivations are provided in **Appendix** C.

Fig. 4.2 compares the condition number of the interference matrices corresponding to the 0-th tap in the proposed segment-based frequency-domain received signal model and that in the time-domain received signal model of (4.3). The simulation parameters are as follows. The truncated ISI and ICI intervals are $N_\mathrm{I} = 12$ and $K_\mathrm{I} = 1$, respectively. The length of each segment is $L_\mathrm{m} = 42$ and the roll-off factor of the RRC shaping pulse is $\beta = 0.3$. Observe that

the proposed model can significantly reduce the condition number of the interference matrix. For a fixed spectral efficiency, the condition number can be minimized by jointly optimizing the combination of the packing factors. For the original model, the condition number of the interference matrix $\mathbf{G}_0$ significantly increases with the reduction of the frequency packing factor ν. By contrast, the condition number of the proposed model varies gently with the packing factors. Hence, the proposed segment-based frequency-domain received signal model is expected to significantly mitigate the inherent ill-conditioning problem of MFTN signaling.

4.3 PBiGAMP-Based Frequency-Domain Joint Channel Estimation and Equalization

4.3.1 Factor Graph Representation

Building on the above-mentioned segment-based frequency-domain received signal model, the received symbol vector in (4.14) is rewritten as

$$\breve{\mathbf{r}}_q = \breve{\mathbf{z}}_q + \mathbf{w}_q = \sum_{l=0}^{L-1} h_{q,l} \mathbf{\Lambda}_{q,l} \ddot{\mathbf{F}}_{KL_\mathrm{s},l} \mathbf{x}_q + \breve{\boldsymbol{\varpi}}_q, \tag{4.15}$$

where $\breve{\mathbf{z}}_q = \sum_{l=0}^{L-1} h_{q,l} \mathbf{\Lambda}_{q,l} \ddot{\mathbf{F}}_{KL_\mathrm{s},l} \mathbf{x}_q$ denotes the noiseless observation vector, $\breve{\boldsymbol{\varpi}}_q$ is a Gaussian equivalent noise process.

Assuming that the likelihood function is component-wise independent, the *a posteriori* probability of the channel coefficients and the transmitted symbols can be factorized as

$$\begin{aligned} p(\mathbf{x}_q, \mathbf{h}_q | \breve{\mathbf{r}}_q) &\propto p(\breve{\mathbf{r}}_q | \breve{\mathbf{z}}_q) p(\breve{\mathbf{z}}_q | \mathbf{h}_q, \mathbf{x}_q) p(\mathbf{h}_q) p(\mathbf{x}_q) \\ &\propto \prod_{k=0}^{K-1} \prod_{n=0}^{N-1} \prod_{n \in \mathcal{I}_N} p(\breve{r}_{k,n} | \breve{z}_{k,n}) p(\breve{z}_{k,n} | \mathbf{h}_q, \mathbf{x}_q) \prod_{l=0}^{L-1} p(h_{q,l}) \prod_{k'=0}^{K-1} \prod_{n' \in \mathcal{I}_q} p(x_{k',n'}), \end{aligned} \tag{4.16}$$

where $p(\breve{\mathbf{r}}_q | \breve{\mathbf{z}}_q)$ is the likelihood function, $p(h_{q,l})$ is the *a priori* probability of the l-th channel coefficient in the q-th segment, and $p(x_{k',n'})$ is the *a priori* probability of the n'-th time-domain transmitted symbol of the k'-th subcarrier, and $\mathcal{I}_q = \{qL_\mathrm{m}, \ \cdots, \ (q+1)L_\mathrm{m} - 1\}$.

According to the factorization of the *a posteriori* probability in (4.16), a factor graph is constructed to characterize the statistical relationships between variables shown in Fig. 4.3. Since the factor graph contains dense short loops, the typical loopy belief propagation (LBP) over the factor graph leads to an excessive computational complexity. Although Gaussian BP can be used for reducing the complexity of the LBP, the Gaussian approximations of the discrete *a priori* messages of the transmitted symbols may result in an additional performance loss. The goal is to simultaneously estimate the channel coefficients and the transmitted symbols from the noisy received observations. This is equivalent to solving the high-dimensional random

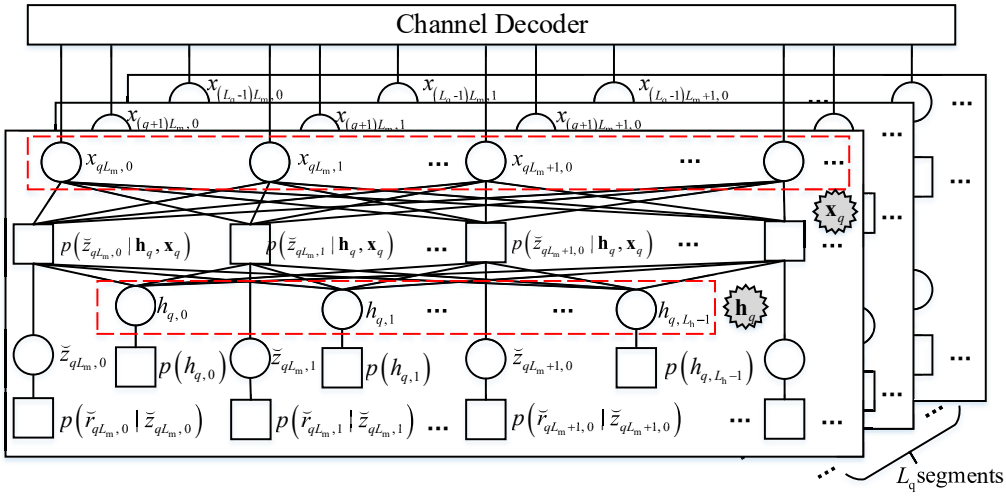


Figure 4.3: Factor graph representation of the segment-based frequency-domain received signal model.

bilinear mixing recovery problem. Hence, the computationally efficient PBiGAMP algorithm is utilized for decoupling the bilinear estimation problem into a series of scalar computations, where all messages can be characterized and updated by their mean and variance vectors.

4.3.2 PBiGAMP-Based Frequency-Domain Iterative Receiver

According to the SPA rules [46], [47], the *a posteriori* probability of the noiseless measurement $\breve{z}_{k,n}$ is proportional to the product of the message propagated from the factor node (FN) $p(\breve{z}_{k,n}|\mathbf{h}_q, \mathbf{x}_q)$ to the variable node (VN) $\breve{z}_{k,n}$ and the conditional probability density function $p(\breve{r}_{k,n}|\breve{z}_{k,n})$. Hence, the former can be regarded as the "pseudo" *a priori* probability of the noiseless measurement $\breve{z}_{k,n}$. As shown in Fig. 4.3, this message is calculated by integrating the product of the messages propagated from all VNs $\mathbf{x}_q$ and $\mathbf{h}_q$ to the FN $p(\breve{z}_{k,n}|\mathbf{h}_q, \mathbf{x}_q)$ and the function $p(\breve{z}_{k,n}|\mathbf{h}_q, \mathbf{x}_q)$ over all the VNs in $\mathbf{x}_q$ and $\mathbf{h}_q$. Applying central-limit-theorem (CLT) to the messages gleaned from the FNs $p(\breve{\mathbf{z}}_q|\mathbf{h}_q, \mathbf{x}_q)$ to the VNs $\breve{\mathbf{z}}_q$, the "pseudo" *a priori* probabilities of the noiseless measurements $\breve{\mathbf{z}}_q$ are approximated as independent Gaussian distributions $\mathcal{CN}\left[\breve{\mathbf{z}}_q; \hat{\mathbf{p}}_q(i), \mathcal{D}(\boldsymbol{\nu}_q^p(i))\right]$ [150]. Accordingly, the "pseudo" *a priori* mean of $\breve{\mathbf{z}}_q$ is given by

$$\hat{\mathbf{p}}_q(i) = \sum_{l=0}^{L-1} \hat{h}_{q,l}(i)\boldsymbol{\Lambda}_{q,l}\ddot{\mathbf{F}}_{KL_\mathrm{s},l}\hat{\mathbf{x}}_q(i) - \bar{\boldsymbol{\nu}}_q^p(i) \odot \hat{\mathbf{s}}_q(i-1) + \hat{\boldsymbol{\kappa}}_q(i). \tag{4.17}$$

Moreover, the "pseudo" *a priori* variance vector $\boldsymbol{\nu}_q^p(t)$ of the noiseless measurements $\breve{\mathbf{z}}_q$ in the t-th iteration is derived as

$$\boldsymbol{\nu}_q^p(i) = \bar{\boldsymbol{\nu}}_q^p(i) + \sum_{l=0}^{L-1} \nu_{q,l}^h(i)|\boldsymbol{\Lambda}_{q,l}\ddot{\mathbf{F}}_{KL_\mathrm{s},l}|^2\boldsymbol{\nu}_q^x(i), \tag{4.18}$$

and

$$\bar{\boldsymbol{\nu}}_q^p(i) = \sum_{l=0}^{L-1} \nu_{q,l}^h(i) |\boldsymbol{\Lambda}_{q,l} \ddot{\mathbf{F}}_{KL_\mathrm{s},l} \hat{\mathbf{x}}_q(i)|^2 + |\sum_{l=0}^{L-1} \hat{h}_{q,l}(i) \boldsymbol{\Lambda}_{q,l} \ddot{\mathbf{F}}_{KL_\mathrm{s},l}|^2 \boldsymbol{\nu}_q^x(i), \tag{4.19}$$

where $\hat{h}_{q,l}(t)$ and $\nu_{q,l}^h(t)$ are the *a posteriori* mean and variance of the l-th channel estimate in the q-th segment. Note that the noiseless measurement contains the colored noise process of (4.15) having non-zero mean. To improve the accuracy of the "pseudo" *a priori* mean vector of the noiseless measurement, this work introduces two additive terms characterizing the two-dimensional interferences arising from the adjacent segments for improving its updating expression.

By taking the product of the likelihood function $p(\breve{\mathbf{r}}_q|\breve{\mathbf{z}}_q) \propto \mathcal{CN}\big[\breve{\mathbf{z}}_q; \breve{\mathbf{r}}_q, \mathcal{D}(\boldsymbol{\nu}_q^{\breve{\boldsymbol{\varpi}}}(i))\big]$ and the "pseudo" *a priori* message $p(\breve{\mathbf{z}}_q) \propto \mathcal{CN}\big[\breve{\mathbf{z}}_q; \hat{\mathbf{p}}_q(i), \mathcal{D}(\boldsymbol{\nu}_q^p(i))\big]$, the *a posteriori* probability of $\breve{\mathbf{z}}_q$ is modelled by the Gaussian distribution as $p(\breve{\mathbf{z}}_q|\breve{\mathbf{r}}_q) \propto \mathcal{CN}\big[\breve{\mathbf{z}}_q; \hat{\breve{\mathbf{z}}}_q(i), \mathcal{D}(\boldsymbol{\nu}_q^{\breve{z}}(i))\big]$ with

$$\hat{\breve{\mathbf{z}}}_q(i) = [\breve{\mathbf{r}}_q \odot \boldsymbol{\nu}_q^p(i) + \boldsymbol{\nu}_q^{\breve{\boldsymbol{\varpi}}}(i) \odot \hat{\mathbf{p}}_q(i)] \oslash [\boldsymbol{\nu}_q^p(i) + \boldsymbol{\nu}_q^{\breve{\boldsymbol{\varpi}}}(i)], \tag{4.20}$$

$$\boldsymbol{\nu}_q^{\breve{z}}(i) = [\boldsymbol{\nu}_q^{\breve{\boldsymbol{\varpi}}}(i) \odot \boldsymbol{\nu}_q^p(i)] \oslash [\boldsymbol{\nu}_q^p(i) + \boldsymbol{\nu}_q^{\breve{\boldsymbol{\varpi}}}(i)]. \tag{4.21}$$

According to the derivations of PBiGAMP algorithm, the messages passed from the factor node $p(\breve{z}_{k,n}|\mathbf{h}_q, \mathbf{x}_q)$ to the variable node $\mathbf{x}_q$ or $\mathbf{h}_q$ can be expanded as a Taylor series, whose first derivative $\hat{\mathbf{s}}_q$ and second derivative $\boldsymbol{\nu}_q^s$ are updated as

$$\hat{\mathbf{s}}_q(i) = [\hat{\breve{\mathbf{z}}}_q(i) - \hat{\mathbf{p}}_q(i)] \oslash \boldsymbol{\nu}_q^p(i) = [\breve{\mathbf{r}}_q - \hat{\mathbf{p}}_q(i)] \oslash [\boldsymbol{\nu}_q^p(i) + \boldsymbol{\nu}_q^{\breve{\boldsymbol{\varpi}}}(i)], \tag{4.22}$$

$$\boldsymbol{\nu}_q^s(i) = [\boldsymbol{\nu}_q^p(i) - \boldsymbol{\nu}_q^{\breve{z}}(i)] \oslash [\boldsymbol{\nu}_q^p(i)]^2 = \mathbf{1}_{KL_\mathrm{s}} \oslash [\boldsymbol{\nu}_q^p(i) + \boldsymbol{\nu}_q^{\breve{\boldsymbol{\varpi}}}(i)]. \tag{4.23}$$

The variable $\boldsymbol{\gamma}_q$ is introduced to represent the product of all outgoing messages from the likelihood function nodes to the transmitted symbol VNs. The vector $\boldsymbol{\gamma}_q$ can be regarded as the noisy observation of the transmitted symbol $\mathbf{x}_q$ in an AWGN channel having the noise variance of $\boldsymbol{\nu}_q^\gamma$. The marginal *a posteriori* probability of the unknown transmitted symbols is given by

$$p(\mathbf{x}_q|\breve{\mathbf{r}}_q) = \frac{p(\mathbf{x}_q)\mathcal{CN}\big[\mathbf{x}_q; \hat{\boldsymbol{\gamma}}_q(t), \mathcal{D}(\boldsymbol{\nu}_q^\gamma(t))\big]}{\int_{\mathbf{x}_q} p(\mathbf{x}_q)\mathcal{CN}\big[\mathbf{x}_q; \hat{\boldsymbol{\gamma}}_q(t), \mathcal{D}(\boldsymbol{\nu}_q^\gamma(t))\big]}, \tag{4.24}$$

where the outgoing mean vector $\hat{\boldsymbol{\gamma}}_q(t)$ and variance vector $\boldsymbol{\nu}_q^\gamma(t)$ are updated as

$$\begin{aligned}\hat{\boldsymbol{\gamma}}_q(i) = \hat{\mathbf{x}}_q(i) &+ \boldsymbol{\nu}_q^\gamma(i) \odot \left[\sum_{l=0}^{L-1} \hat{h}_{q,l}(i) \boldsymbol{\Lambda}_{q,l} \ddot{\mathbf{F}}_{KL_\mathrm{s},l}\right]^H \hat{\mathbf{s}}_q(i) \\ &- \boldsymbol{\nu}_q^\gamma(i) \odot \hat{\mathbf{x}}_q(i) \odot \sum_{l=0}^{L-1} \nu_{q,l}^h(i) |\ddot{\mathbf{F}}_{KL_\mathrm{s},l}^H \boldsymbol{\Lambda}_{q,l}^H|^2 \boldsymbol{\nu}_q^s(i),\end{aligned} \tag{4.25}$$

$$\boldsymbol{\nu}_q^{\gamma}(i) = \mathbf{1}_{KL_{\mathrm{m}}} \oslash \left[\left| (\sum_{l=0}^{L-1} \hat{h}_{q,l}(i) \boldsymbol{\Lambda}_{q,l} \ddot{\mathbf{F}}_{KL_{\mathrm{s}},l})^H \right|^2 \boldsymbol{\nu}_q^{s}(i) \right]. \tag{4.26}$$

The *a priori* messages of the transmitted symbols are calculated based on soft extrinsic information gleaned from the channel decoder. Let us assume that the $\bar{m}$-th extrinsic LLR of $x_{k,n}$ acquired from the channel decoder output is $L_{\mathrm{dec}}^{\mathrm{e},(t)}(c_{k,n,\bar{m}})$, the *a priori* probability of the coded bit $c_{k,n,\bar{m}} \in \{0,1\}, m = 0, \cdots, \log_2 M - 1$ in the t-th iteration is $p(c_{k,n,\bar{m}}) = \frac{1}{2}\big[1+(-1)^{c_{k,n,\bar{m}}} \tanh\big(\frac{1}{2} L_{\mathrm{dec}}^{\mathrm{e},(t)}(c_{k,n,\bar{m}})\big)\big]$. Since each transmitted symbol belongs to the constellation set $\mathcal{S} \triangleq \{\mathcal{S}_1, \cdots, \mathcal{S}_M\}$, the discrete *a priori* probabilities $\{p(x_{k,n})\}$ can be computed according to the constellation mapping rules. Hence, the conditional *a posteriori* probability of each transmitted symbol $x_{k,n}$ in the q-th segment is $p(x_{k,n}|\breve{\mathbf{r}}_q) \propto p(x_{k,n}) \mathcal{CN}[x_{k,n}; \hat{\gamma}_{k,n}(t), \nu_q^{\gamma}(t)]$. The corresponding conditional *a posteriori* expectation and variance are given by

$$\hat{x}_{k,n}(i+1) = \mathbb{E}\{x_{k,n}|\gamma_{k,n} = \hat{\gamma}_{k,n}(i); \nu_q^{\gamma}(i)\} \propto \sum_m \mathcal{S}_m p(x_{k,n} = \mathcal{S}_m) \zeta_{k,n}^m(i), \tag{4.27}$$

$$\begin{aligned} \nu_{k,n}^x(i+1) &= \mathbb{V}\{x_{k,n}|\gamma_{k,n} = \hat{\gamma}_{k,n}(i); \nu_q^{\gamma}(i)\} \\ &\propto \sum_m |\hat{x}_{k,n}(i+1) - \mathcal{S}_m|^2 p(x_{k,n} = \mathcal{S}_m) \zeta_{k,n}^m(i), \end{aligned} \tag{4.28}$$

where $\zeta_{k,n}^m(i) \triangleq \exp(-|\mathcal{S}_m - \hat{\gamma}_{k,n}(i)|^2 / \nu_{k,n}^{\gamma}(i))$. Note that the *a posteriori* variance of $\nu_{k,n}^x(t+1)$ is used for characterizing the estimation accuracy of the transmitted symbol in the t-th iteration and then for updating the "pseudo" *a priori* variance of the noiseless measurement in the $(t+1)$-st iteration.

Similar to the above-mentioned characterization of the symbol detection, the outgoing messages of the unknown channel coefficients are approximated by the Gaussian distribution, i.e., $\mathcal{CN}(\mathbf{h}_q; \hat{\boldsymbol{\varrho}}_q, \boldsymbol{\nu}_q^{\varrho})$. Hence, the l-th element of the outgoing mean vector $\hat{\boldsymbol{\varrho}}_q$ and variance vector $\boldsymbol{\nu}_q^{\varrho}$ are expressed respectively as

$$\begin{aligned} \hat{\varrho}_{q,l}(i) &= \hat{h}_{q,l}(i) + \nu_{q,l}^{\varrho}(i) [\boldsymbol{\Lambda}_{q,l} \ddot{\mathbf{F}}_{KL_{\mathrm{s}},l} \hat{\mathbf{x}}_q(i)]^H \hat{\mathbf{s}}_q(i) \\ &\quad - \hat{h}_{q,l}(i) \nu_{q,l}^{\varrho}(i) \nu_q^x(i) \mathbf{1}_{KL_{\mathrm{s}}}^T |\ddot{\mathbf{F}}_{KL_{\mathrm{s}},l}^H \boldsymbol{\Lambda}_{q,l}^H|^2 \boldsymbol{\nu}_q^s(i), \end{aligned} \tag{4.29}$$

$$1/\nu_{q,l}^{\varrho}(i) = \left| \left(\boldsymbol{\Lambda}_{q,l} \ddot{\mathbf{F}}_{KL_{\mathrm{s}},l} \hat{\mathbf{x}}_q(i) \right)^H \right|^2 \boldsymbol{\nu}_q^s(i). \tag{4.30}$$

Under the assumption of the Gaussian *a priori* probability, the *a posteriori* distribution of $h_{q,l}$ is given by $p(h_{q,l}|\breve{\mathbf{z}}_q) \propto \mathcal{CN}\big[h_{q,l}; \hat{h}_{q,l}(i+1), \nu_{q,l}^h(i+1)\big]$ with

$$\hat{h}_{q,l}(i+1) = [\hat{\varrho}_{q,l}(i) \bar{\nu}_{q,l}^h + \bar{h}_{q,l} \nu_{q,l}^{\varrho}(i)] / [\bar{\nu}_{q,l}^h + \nu_{q,l}^{\varrho}(i)], \tag{4.31}$$

$$\nu_{q,l}^h(i+1) = \bar{\nu}_{q,l}^h \nu_{q,l}^{\varrho}(i) / [\bar{\nu}_{q,l}^h + \nu_{q,l}^{\varrho}(i)], \tag{4.32}$$

where the *a priori* probability $\mathcal{CN}\big(h_{q,l}; \bar{h}_{q,l}, \bar{\nu}_{q,l}^h\big)$ can be obtained by pilot-based least-squared estimation (LSE) [151]. Similarly, the *a posteriori* variance $\nu_{q,l}^h(t+1)$ is also utilized for quanti-

fying the accuracy of the channel estimate and then for updating the "pseudo" *a priori* variance of the noiseless measurement in the next iteration.

According to the aforementioned derivations, the PBiGAMP-based JCEE algorithm proposed for MFTN signaling is summarized in **Algorithm** 3.

Algorithm 3 PBiGAMP-Based Frequency-Domain JCEE Algorithm (PBiGAMP-FDJCEE)

1: **Initialization**: Set the *a posteriori* mean and variance of the transmitted symbols to be $\hat{x}_{k,n}(1) = 0$ and $\nu^x_{k,n}(1) = 1$, $k = 0, \cdots, K-1, n = 0, \cdots, N-1$. The initialized channel coefficients $\hat{\mathbf{h}}_q(1)$ and $\boldsymbol{\nu}^h_q(1)$ are obtained by a pilot-based LSE. Set $\hat{\mathbf{s}}_q(0) = \mathbf{0}_{N_\mathrm{s}}$ for $q = 0, \cdots, L_\mathrm{q} - 1$ as described in [147].
2: **for** $t = 1$ to I_e **do**
3: **for** $q = 0$ to $L_\mathrm{q} - 1$ **do**
4: The time-domain received symbols are transformed to frequency-domain via two-dimensional FFT in (4.14).
5: Compute $\hat{\mathbf{p}}_q(t)$ and $\boldsymbol{\nu}^p_q(t)$ using (4.17) and (4.18).
6: Compute $\hat{\mathbf{s}}_q(t)$ and $\boldsymbol{\nu}^s_q(t)$ using (4.22) and (4.23).
7: Compute the outgoing messages $\hat{\boldsymbol{\gamma}}_q(i)$ and $\boldsymbol{\nu}^\gamma_q(i)$ of the transmitted symbols using (4.25) and (4.26).
8: Compute each element of the *a posteriori* messages $\hat{\mathbf{x}}_q(i+1)$ and $\boldsymbol{\nu}^x_q(i+1)$ of the transmitted symbols using (4.27) and (4.28).
9: Compute each element of the outgoing messages $\hat{\boldsymbol{\varrho}}_q(i)$ and $\boldsymbol{\nu}^\varrho_q(i)$ of the channel coefficients using (4.29) and (4.30).
10: Compute each element of the *a posteriori* messages $\hat{\mathbf{h}}_q(i+1)$ and $\boldsymbol{\nu}^h_q(i+1)$ of the channel coefficients using (4.31) and (4.32).
11: **end for**
12: Compute the extrinsic LLRs of the equalizer based on the outgoing messages of the transmitted symbols and then feed them to the channel decoder.
13: Perform BCJR channel decoding and feed the soft extrinsic information to the equalizer.
14: **end for**

4.3.3 Refined PBiGAMP-Based Frequency-Domain Iterative Receiver

According to the derivations of the PBiGAMP-FDJCEE algorithm proposed in Section 4.3.2, the equations (4.18), (4.19), (4.26), (4.25), (4.30), and (4.29) contain the squared modulus of the frequency-domain equivalent channel matrix, which may increase the condition numbers. To solve this problem, a series of scaled identity matrices are invoked for approximating the variance vectors of the transmitted symbols in (4.28) and the second derivative term in (4.23). Moreover, the scaled identity matrix corresponding to $\boldsymbol{\nu}^s_q(t)$ is also harnessed for improving the accuracy of channel estimation. The detailed derivations are as follows.

The "pseudo" *a priori* variance of the noiseless measurement in (4.18) can be rewritten as

$$\boldsymbol{\nu}_q^p(i) = \bar{\boldsymbol{\nu}}_q^p(i) + \sum_{l=0}^{L-1} \nu_{q,l}^h(i)\mathcal{D}\big[\boldsymbol{\Lambda}_{q,l}\ddot{\mathbf{F}}_{KL_\mathrm{s},l}\mathcal{D}(\boldsymbol{\nu}_q^x(i))\ddot{\mathbf{F}}_{KL_\mathrm{s},l}^H\boldsymbol{\Lambda}_{q,l}^H\big]\mathbf{1}_{KL_\mathrm{s}}$$
$$= \bar{\boldsymbol{\nu}}_q^p(i) + \sum_{l=0}^{L-1} \nu_{q,l}^h(i)\mathcal{D}\big[\boldsymbol{\Lambda}_{q,l}(\mathbf{F}_K \otimes \mathbf{F}_{L_\mathrm{s}})\tilde{\boldsymbol{\Lambda}}_l\tilde{\boldsymbol{\Phi}}_\mathrm{m}\mathcal{D}(\boldsymbol{\nu}_q^x(i))\tilde{\boldsymbol{\Phi}}_\mathrm{m}^H\tilde{\boldsymbol{\Lambda}}_l^H(\mathbf{F}_K \otimes \mathbf{F}_{L_\mathrm{s}})^H\boldsymbol{\Lambda}_{q,l}^H\big]\mathbf{1}_{KL_\mathrm{s}}. \quad (4.33)$$

To simplify the second term in the above equation, a scaled identity matrix $\bar{\nu}_q^x(i)\mathbf{I}_{KL_\mathrm{s}}$ is exploited as the average approximation of the term $\tilde{\boldsymbol{\Phi}}_\mathrm{m}\mathcal{D}(\boldsymbol{\nu}_q^x(i))\tilde{\boldsymbol{\Phi}}_\mathrm{m}^H$, where $\bar{\nu}_q^x(i) = 1/(KL_\mathrm{s})\mathbf{1}_{KL_\mathrm{s}}^T\tilde{\boldsymbol{\Phi}}_\mathrm{m}\mathcal{D}(\boldsymbol{\nu}_q^x(i))\tilde{\boldsymbol{\Phi}}_\mathrm{m}^H\mathbf{1}_{KL_\mathrm{s}}$ is the average variance of the transmitted symbols in the q-th segment. Then, the "pseudo" *a priori* variance vector of the noiseless measurement vector in (4.33) is expressed as

$$\boldsymbol{\nu}_q^p(i) \approx \bar{\boldsymbol{\nu}}_q^p(i) + \sum_{l=0}^{L-1} \nu_{q,l}^h(i)\mathcal{D}\big[\boldsymbol{\Lambda}_{q,l}(\mathbf{F}_K \otimes \mathbf{F}_{L_\mathrm{s}})\bar{\nu}_q^x(i)\mathbf{I}_{KL_\mathrm{s}}(\mathbf{F}_K \otimes \mathbf{F}_{L_\mathrm{s}})^H\boldsymbol{\Lambda}_{q,l}^H\big]\mathbf{1}_{KL_\mathrm{s}}$$
$$= \bar{\boldsymbol{\nu}}_q^p(i) + \bar{\nu}_q^x(i)\sum_{l=0}^{L-1} \nu_{q,l}^h(i)\boldsymbol{\Lambda}_{q,l}\boldsymbol{\Lambda}_{q,l}^H\mathbf{1}_{KL_\mathrm{s}}. \quad (4.34)$$

Similarly, the second term of $\bar{\boldsymbol{\nu}}_q^p(i)$ in (4.19) can be also simplified using the scaled identity matrix $\bar{\nu}_{q,l,l'}^x(i)\mathbf{I}_{KL_\mathrm{s}}$. Accordingly, (4.19) is approximated as

$$\bar{\boldsymbol{\nu}}_q^p(i) = \sum_{l=0}^{L-1} \nu_{q,l}^h(i)|\boldsymbol{\Lambda}_{q,l}\ddot{\mathbf{F}}_{KL_\mathrm{s},l}\hat{\mathbf{x}}_q(i)|^2 + |\sum_{l=0}^{L-1} \hat{h}_{q,l}(i)\boldsymbol{\Lambda}_{q,l}\ddot{\mathbf{F}}_{KL_\mathrm{s},l}|^2\boldsymbol{\nu}_q^x(i)$$
$$= \sum_{l=0}^{L-1} \nu_{q,l}^h(i)|\boldsymbol{\Lambda}_{q,l}\ddot{\mathbf{F}}_{KL_\mathrm{s},l}\hat{\mathbf{x}}_q(i)|^2 + \mathcal{D}\left[\sum_{l,l'=0}^{L-1} \hat{h}_{q,l}(i)\hat{h}_{q,l'}^*(i)\boldsymbol{\Lambda}_{q,l}\ddot{\mathbf{F}}_{KL_\mathrm{s},l}\mathcal{D}(\boldsymbol{\nu}_q^x(i))\ddot{\mathbf{F}}_{KL_\mathrm{s},l'}^H\boldsymbol{\Lambda}_{q,l'}^H\right]\mathbf{1}_{KL_\mathrm{s}}$$
$$\approx \sum_{l=0}^{L-1} \nu_{q,l}^h(i)|\boldsymbol{\Lambda}_{q,l}\ddot{\mathbf{F}}_{KL_\mathrm{s},l}\hat{\mathbf{x}}_q(i)|^2 + \sum_{l,l'=0}^{L-1} \hat{h}_{q,l}(i)\hat{h}_{q,l'}^*(i)\bar{\nu}_{q,l,l'}^x(i)\boldsymbol{\Lambda}_{q,l}\boldsymbol{\Lambda}_{q,l'}^H\mathbf{1}_{KL_\mathrm{s}}, \quad (4.35)$$

where the weighting coefficient is $\bar{\nu}_{q,l,l'}^x(i) = 1/(KL_\mathrm{s})\mathbf{1}_{KL_\mathrm{s}}^T\tilde{\boldsymbol{\Lambda}}_l\tilde{\boldsymbol{\Phi}}_\mathrm{m}\mathcal{D}(\boldsymbol{\nu}_q^x(i))\tilde{\boldsymbol{\Phi}}_\mathrm{m}^H\tilde{\boldsymbol{\Lambda}}_{l'}^H\mathbf{1}_{KL_\mathrm{s}}$, and $\bar{\nu}_{q,l,l'}^x(i) = \bar{\nu}_q^x(i)$ for $l = l'$.

Based on (4.26), the outgoing variance vector of the transmitted symbols can be calculated as

$$\boldsymbol{\nu}_q^\gamma(i) = \mathbf{1}_{KL_\mathrm{m}} \oslash \left[\big|(\sum_{l=0}^{L-1} \hat{h}_{q,l}(i)\boldsymbol{\Lambda}_{q,l}\ddot{\mathbf{F}}_{KL_\mathrm{s},l})^H\big|^2\boldsymbol{\nu}_q^s(i)\right]$$
$$= \mathbf{1}_{KL_\mathrm{m}} \oslash \left\{\mathcal{D}\left[\sum_{l,l'=0}^{L-1} \hat{h}_{q,l}^*(i)\hat{h}_{q,l'}(i)\ddot{\mathbf{F}}_{KL_\mathrm{s},l}^H\boldsymbol{\Lambda}_{q,l}^H\mathcal{D}(\boldsymbol{\nu}_q^s(i))\boldsymbol{\Lambda}_{q,l'}\ddot{\mathbf{F}}_{KL_\mathrm{s},l'}\right]\mathbf{1}_{KL_\mathrm{s}}\right\}$$
$$= \mathbf{1}_{KL_\mathrm{m}} \oslash \Bigg\{\mathcal{D}\Bigg[\sum_{l,l'=0}^{L-1} \hat{h}_{q,l}^*(i)\hat{h}_{q,l'}(i)\tilde{\boldsymbol{\Phi}}_\mathrm{m}^H\tilde{\boldsymbol{\Lambda}}_l^H(\mathbf{F}_K \otimes \mathbf{F}_{L_\mathrm{s}})^H$$
$$\times \boldsymbol{\Lambda}_{q,l}^H\mathcal{D}(\boldsymbol{\nu}_q^s(i))\boldsymbol{\Lambda}_{q,l'}(\mathbf{F}_K \otimes \mathbf{F}_{L_\mathrm{s}})\tilde{\boldsymbol{\Lambda}}_{l'}\tilde{\boldsymbol{\Phi}}_\mathrm{m}\Bigg]\mathbf{1}_{KL_\mathrm{s}}\Bigg\}. \quad (4.36)$$

Through introducing a scaled identity matrix $\varsigma^s_{q,l,l'}(i)\mathbf{I}_{KL_\mathrm{s}}$ for replacing the middle term between the two-dimensional Fourier operations, the above equation is simplified as

$$\begin{aligned}\boldsymbol{\nu}^{\gamma}_{q}(i) &\approx \mathbf{1}_{KL_\mathrm{m}} \oslash \Bigg\{ \mathcal{D}\Bigg[\sum_{l,l'=0}^{L-1} \hat{h}^{*}_{q,l}(i)\hat{h}_{q,l'}(i)\tilde{\boldsymbol{\Phi}}^{H}_{\mathrm{m}}\tilde{\boldsymbol{\Lambda}}^{H}_{l}(\mathbf{F}_K \otimes \mathbf{F}_{L_\mathrm{s}})^{H} \\ &\qquad \times \varsigma^{s}_{q,l,l'}(i)\mathbf{I}_{KL_\mathrm{s}}(\mathbf{F}_K \otimes \mathbf{F}_{L_\mathrm{s}})\tilde{\boldsymbol{\Lambda}}_{l'}\tilde{\boldsymbol{\Phi}}_{\mathrm{m}} \Bigg] \mathbf{1}_{KL_\mathrm{s}} \Bigg\} \\ &= \mathbf{1}_{KL_\mathrm{m}} \oslash \Bigg\{ \mathcal{D}\Bigg[\sum_{l,l'=0}^{L-1} \hat{h}^{*}_{q,l}(i)\hat{h}_{q,l'}(i)\varsigma^{s}_{q,l,l'}(i)\tilde{\boldsymbol{\Phi}}^{H}_{\mathrm{m}}\tilde{\boldsymbol{\Lambda}}_{l'-l}\tilde{\boldsymbol{\Phi}}_{\mathrm{m}} \Bigg] \mathbf{1}_{KL_\mathrm{s}} \Bigg\}, \end{aligned} \tag{4.37}$$

where the weighting coefficient is $\varsigma^s_{q,l,l'}(i) = 1/(KL_\mathrm{s})\mathbf{1}^T_{KL_\mathrm{s}}\boldsymbol{\Lambda}^H_{q,l}\mathcal{D}(\boldsymbol{\nu}^s_q(i))\boldsymbol{\Lambda}_{q,l'}\mathbf{1}_{KL_\mathrm{s}}$. Accordingly, a scaled identity matrix $\varsigma^s_{q,l,l}(i)\mathbf{I}_{KL_\mathrm{s}}$ is employed for deriving the simplified outgoing mean vector $\hat{\boldsymbol{\gamma}}_q(t)$ as

$$\hat{\boldsymbol{\gamma}}_q(i) \approx \hat{\mathbf{x}}_q(i) + \boldsymbol{\nu}^{\gamma}_q(i) \odot \big[\sum_{l=0}^{L-1} \hat{h}_{q,l}(i)\boldsymbol{\Lambda}_{q,l}\ddot{\mathbf{F}}_{KL_\mathrm{s}}\big]^H \hat{\mathbf{s}}_q(i) - \sum_{l=0}^{L-1} \nu^h_{q,l}(i)\varsigma^s_{q,l,l}\boldsymbol{\nu}^{\gamma}_q(i) \odot \hat{\mathbf{x}}_q(i). \tag{4.38}$$

As for channel estimation, by introducing the scaled identity matrix $\varsigma^s_{q,l,l}(i)\mathbf{I}_{KL_\mathrm{s}}$, the outgoing variance of the l-th unknown channel coefficient in (4.30) can be simplified as

$$1/\nu^{\varrho}_{q,l}(i) = (\hat{\mathbf{x}}_q(i))^H \ddot{\mathbf{F}}^H_{KL_\mathrm{s}}\boldsymbol{\Lambda}^H_{q,l}\mathcal{D}(\boldsymbol{\nu}^s_q(i))\boldsymbol{\Lambda}_{q,l}\ddot{\mathbf{F}}_{KL_\mathrm{s}}\hat{\mathbf{x}}_q(i) \approx \varsigma^s_{q,l,l}||\hat{\mathbf{x}}_q(i)||^2. \tag{4.39}$$

Moreover, the outgoing mean of the l-th channel coefficient in (4.29) is approximated as

$$\hat{\varrho}_{q,l}(i) \approx \hat{h}_{q,l}(i) + \varsigma^s_{q,l,l}(\boldsymbol{\Lambda}_{q,l}\ddot{\mathbf{F}}_{KL_\mathrm{s}}\hat{\mathbf{x}}_q(i))^H\hat{\mathbf{s}}_q(i) - KL_\mathrm{s}\hat{h}_{q,l}(i)\nu^{\varrho}_{q,l}(i)\nu^x_q(i)\varsigma^s_{q,l,l}(i). \tag{4.40}$$

According to the above-mentioned approximations, the proposed refined PBiGAMP-based JCEE procedure of MFTN signaling is summarized in **Algorithm** 4.

4.4 GAMP-Based Frequency-Domain Equalization With Known CSI

In the special case of perfectly known CSI, the channel coefficients no longer have to be estimated. Hence, the channel estimates can be replaced by the exact channel coefficients. The proposed PBiGAMP-based receivers are readily simplified to the GAMP-FDE and R-GAMP-FDE algorithms, which are summarized in **Algorithm** 5 and **Algorithm** 6.

Algorithm 4 Refined PBiGAMP-Based Frequency-Domain JCEE Algorithm (R-PBiGAMP-FDJCEE)

1: Run the same initialization and calculation steps in **Algorithm** 3 except for the following three modifications:
2: **for** $t = 1$ to I_{e} **do**
3: **for** $q = 0$ to $L_{\mathrm{q}} - 1$ **do**
4: Compute the *a priori* variance vector $\boldsymbol{\nu}_q^p(i)$ of the noiseless measurements using (4.34) and (4.35).
5: Compute the outgoing messages $\hat{\boldsymbol{\gamma}}_q(i)$ and $\boldsymbol{\nu}_q^{\gamma}(i)$ of the transmitted symbols using (4.38) and (4.37).
6: Compute each element of the outgoing messages $\hat{\boldsymbol{\varrho}}_q(i)$ and $\boldsymbol{\nu}_q^{\varrho}(i)$ of the channel coefficients using (4.40) and (4.39).
7: **end for**
8: **end for**

Algorithm 5 The GAMP-Based FDE Algorithm (GAMP-FDE) For Perfectly Known CSI

1: **Initialization**: Set the *a posteriori* mean and variance of the transmitted symbols to be $\hat{x}_{k,n}(1) = 0$ and $\nu_{k,n}^{x}(1) = 1$, $k = 0, \cdots, K-1, n = 0, \cdots, N-1$. Set $\hat{\mathbf{s}}_q(0) = \mathbf{0}_{N_{\mathrm{s}}}$, $\hat{h}_{q,l}(t) = h_{q,l}$, and $\nu_{q,l}^{h}(t) = 0$ for $q = 0, \cdots, L_{\mathrm{q}} - 1$, $l = 0, \cdots, L-1$.
2: Run Step 2-14 in **Algorithm** 3 except Step 9 and 10.

4.5 Complexity Analysis and Simulation Results

4.5.1 Complexity Analysis

This section analyzes the computational complexity of the proposed PBiGAMP-based algorithms and compare them to that of the existing algorithms, as summarized in TABLE 4.1. Since all methods perform standard soft information calculations and BCJR decoding, only the computational complexity of the equalizer and channel estimator in a single iteration is discussed. Moreover, the complexity of FDE algorithms is dominated by the number of complex multiplications and two-dimensional FFT/IFFT operations, which are analyzed independently in TABLE 4.1.

Under the assumption of perfectly known CSI, the proposed GAMP-based algorithms are compared to three typical TDE algorithms: MMSE-TDE, GAMP-TDE, and UTAMP-TDE. The MMSE-TDE algorithm of [152] needs to calculate the inversion of the equivalent channel matrix, resulting in a complexity order of $\mathcal{O}(N_{\mathrm{s}}^3)$. As described in [48], the worst-case total complexity of GAMP per iteration is $\mathcal{O}(N_{\mathrm{s}}^2)$ when the size of the equivalent channel matrix is $N_{\mathrm{s}} \times N_{\mathrm{s}}$. As a modified version of AMP, UTAMP exploits SVD of the $N_{\mathrm{s}} \times N_{\mathrm{s}}$ equivalent channel matrix for improving the convergence of AMP [50]. The complexity of SVD is $\mathcal{O}(N_{\mathrm{s}}^3)$, while the complexity of message passing relying on the non-structured equivalent channel matrix is $\mathcal{O}(N_{\mathrm{s}}^2)$. For GAMP-FDE, $(2L+3)$ KN_{s}-point two-dimensional FFT/IFFT operations are needed for the calculations of (4.14), (4.17) and (4.25), having a complexity order of $\mathcal{O}((2L+3)L_{\mathrm{q}}KL_{\mathrm{s}}\log(KL_{\mathrm{s}}))$. Since (4.19) and (4.26) need to compute the complex multiplications of a squared matrix and

Algorithm 6 The Refined GAMP-Based FDE Algorithm (R-GAMP-FDE) For Perfectly Known CSI

1: Run the same initialization and calculation steps in **Algorithm** 5 except for the following two modifications:
2: **for** $q = 0$ to $L_{\mathrm{q}} - 1$ **do**
3: **for** $t = 1$ to I_{e} **do**
4: Compute the *a priori* variance vector of the noiseless measurements $\boldsymbol{\nu}_q^p(t)$ using (4.34) and (4.35).
5: Compute the outgoing messages $\boldsymbol{\nu}_q^{\gamma}(t)$ and $\hat{\boldsymbol{\gamma}}_q(t)$ using (4.37) and (4.38).
6: **end for**
7: **end for**

Table 4.1: Complexity Analysis of Channel Estimation and Equalization of MFTN Signaling

Algorithm	Equalization		Channel Estimation
	Complex MUL	FFT/IFFT	
MMSE-TDE	$\mathcal{O}(K^3N^3)$	-	-
GAMP-TDE	$\mathcal{O}(K^2N^2)$	-	-
UTAMP-TDE	$\mathcal{O}(K^3N^3)$	-	-
GAMP-FDE	$\mathcal{O}(L_{\mathrm{q}}K^2L_{\mathrm{s}}^2)$	$\mathcal{O}((2L+3)L_{\mathrm{q}}KL_{\mathrm{s}}\log(KL_{\mathrm{s}}))$	-
R-GAMP-FDE	$\mathcal{O}(L_{\mathrm{q}}KL_{\mathrm{s}})$	$\mathcal{O}((2L+3)L_{\mathrm{q}}KL_{\mathrm{s}}\log(KL_{\mathrm{s}}))$	-
LS-MMSE	$\mathcal{O}(L_{\mathrm{q}}K^3L_{\mathrm{s}}^3)$	-	$\mathcal{O}(L_{\mathrm{q}}LN_{\mathrm{p}})$
PBiGAMP-FDJCEE	$\mathcal{O}(L_{\mathrm{q}}K^2L_{\mathrm{s}}^2)$	$\mathcal{O}((2L+3)L_{\mathrm{q}}KL_{\mathrm{s}}\log(KL_{\mathrm{s}}))$	$\mathcal{O}(L_{\mathrm{q}}LKL_{\mathrm{s}})$
R-PBiGAMP-FDJCEE	$\mathcal{O}(L_{\mathrm{q}}KL_{\mathrm{s}})$	$\mathcal{O}((2L+3)L_{\mathrm{q}}KL_{\mathrm{s}}\log(KL_{\mathrm{s}}))$	$\mathcal{O}(L_{\mathrm{q}}LKL_{\mathrm{s}})$

a vector, the remaining complexity is $\mathcal{O}(L_{\mathrm{q}}K^2L_{\mathrm{s}}^2)$. By contrast, these complex multiplications are omitted by introducing a series of scaled identity matrices in its refined version, resulting in the complexity induced by the complex multiplications being $\mathcal{O}(L_{\mathrm{q}}KL_{\mathrm{s}})$.

For MFTN systems operating in the absence of CSI, both the LS-based channel estimator of [151] and the MMSE-based equalizer of [152] labeled as "LS-MMSE" are extended by conceiving the proposed segment-based frequency-domain received signal model for MFTN systems. Since the interferences of MFTN signaling only depend on the shaping pulse and packing factors, the weighted matrix of the LS-based channel estimator can be calculated off-line and stored in advance. This substantially reduces the computational complexity in practice. Hence, only the complexity associated with the complex multiplication of the weighted matrix and the received observations is considered. The complexity order of LS-based channel estimator is $\mathcal{O}(LN_{\mathrm{ls}})$ per segment, with N_{ls} being the number of pilots, while that of MMSE-based equalizer is $\mathcal{O}(L_{\mathrm{q}}K^3L_{\mathrm{s}}^3)$ per segment dominated by the matrix inversion of the non-diagonal covariance matrix of the frequency-domain transmitted symbols. For PBiGAMP-FDJCEE, $(2L+3)$ KN_{s}-point two-dimensional FFT/IFFT operations are needed for the calculations of (4.14), (4.17) and (4.25). Moreover, there are a series of complex multiplications in (4.18), (4.19), (4.25), (4.26) and (4.29). Note that the term $\ddot{\mathbf{F}}_{KL_{\mathrm{s}},l}\hat{\mathbf{x}}_q(i)$ of (4.29) has been obtained in (4.17), without an additional complexity. For the refined PBiGAMP-FDJCEE algorithm, there are only $(2L+3)$ KN_{s}-point two-dimensional FFT/IFFT operations, having a lower complexity.

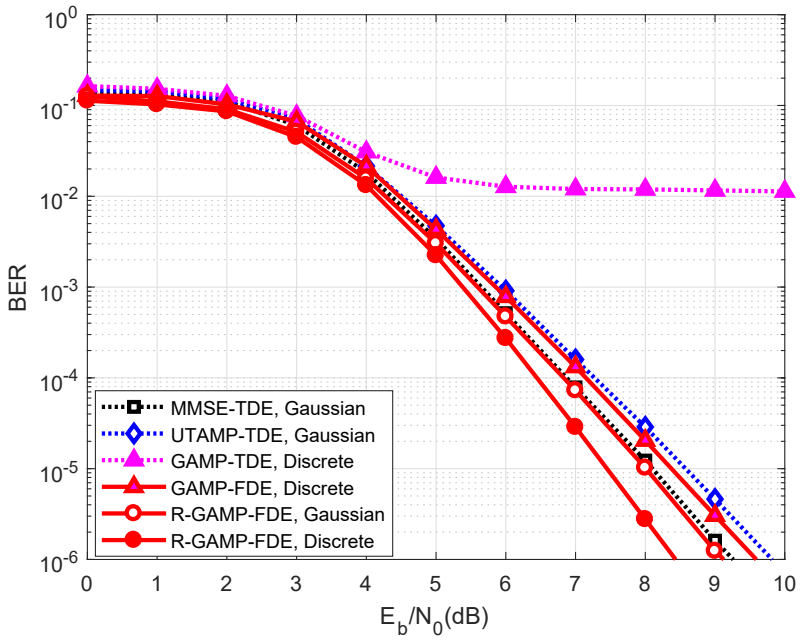


Figure 4.4: BER performance of different equalization algorithms for MFTN systems in the case of perfectly known CSI.

4.5.2 Simulation Results

This section provides both BER and NMSE performance of the proposed GAMP-FDE, R-GAMP-FDE, PBiGAMP-FDJCEE, and R-PBiGAMP-FDJCEE algorithms designed for MFTN signaling in frequency-selective fading channels. To verify their efficiency, the MMSE of [152], the UTAMP algorithm of [50], and the GAMP algorithm of [48] to TDE of MFTN systems are extended and then compared to the proposed algorithms.

The following simulations consider an LDPC code of rate $R_{\mathrm{c}} = 23/28$ and code length of $L_{\mathrm{c}} = 4032$ bits. The number of subcarriers is $K = 64$ and each subcarrier has $N = 512$ symbols employing QPSK modulation. The carrier frequency and symbol period are 2 GHz and 2 μs, respectively. The roll-off factor of the RRC shaping filter is $\beta = 0.3$ and the truncated lengths of the inherent two-dimensional interferences are $N_{\mathrm{I}} = 12$ and $K_{\mathrm{I}} = 1$, respectively. The fixed truncated lengths have been verified to be able to cover the dominant two-dimensional interferences in the following simulations. Moreover, the length of each segment is $L_{\mathrm{m}} = 42$. For frequency-selective fading channels, the number of taps is set to be $L_{\mathrm{h}} = 8$ and the l-th PDP satisfies $\sigma_{h_l}^2 = \exp(-0.1l)/(\sum_l \sigma_{h_l}^2)$. Consider a car traveling at 80 km/h and a high-speed trains at 270 km/h. The corresponding Doppler spreads are $f_d = 150$ Hz and $f_d = 500$ Hz, respectively, while the normalized fading rates are 0.0003 and 0.001. The number of external iterations between the equalizer and the channel decoder is $I_{\mathrm{e}} = 50$ and the number of internal LDPC decoding iterations is $I_{\mathrm{c}} = 5$.

In Fig. 4.4, the BER performance of the proposed GAMP-FDE and R-GAMP-FDE algorithms is compared to those of the existing equalization algorithms at a velocity of 80 km/h, where the

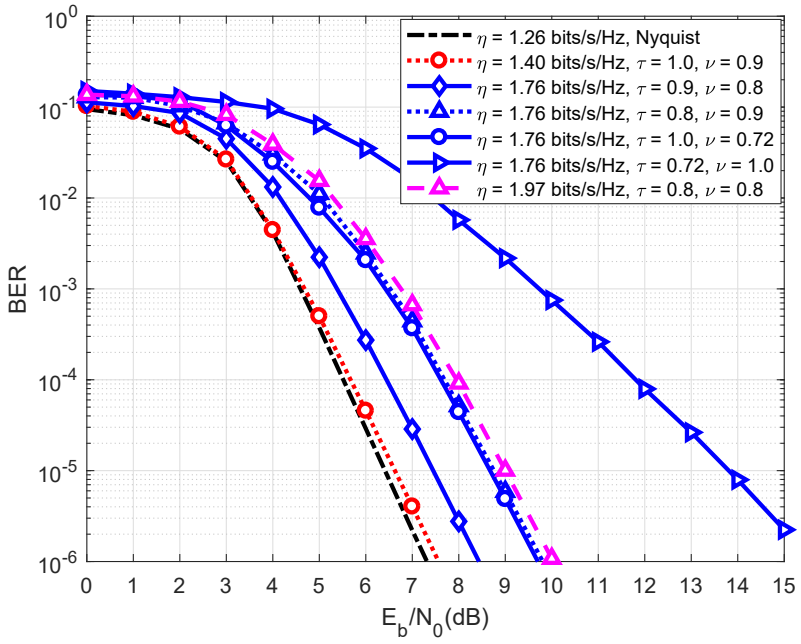


Figure 4.5: BER performance of the proposed R-GAMP-FDE algorithm for MFTN systems in the case of perfectly known CSI.

Doppler spread is $f_d = 150$ Hz and $\tau = 0.9, \nu = 0.8$. The GAMP-TDE algorithm has an error floor in the high $\mathrm{E_b/N_0}$ region due to the divergence of GAMP induced by the ill-conditioning problem of MFTN systems. Compared to GAMP-TDE, both UTAMP-TDE[2] and GAMP-FDE significantly improve the BER performance, where GAMP-FDE obtains an additional gain by exploiting the exact discrete *a priori* distributions of the transmitted symbols. Since GAMP-based algorithms rely on the MMSE approximations, the MMSE-TDE algorithm[3] outperforms both the UTAMP-TDE and GAMP-FDE. Moreover, the proposed R-GAMP-FDE algorithm is superior to the MMSE-TDE algorithm in terms of BER. The performance gain of R-GAMP-FDE can be attributed to the average approximations of $\boldsymbol{\nu}_q^x(t)$ and $\boldsymbol{\nu}_q^s(t)$, which circumvent the strong sensitivity of the ill-conditioned matrices to small perturbations. Moreover, compared to its counterpart using the exact discrete *a priori* probabilities, R-GAMP-FDE employing the Gaussian *a priori* distribution approximation suffers from an additional 0.7 dB $\mathrm{E_b/N_0}$ loss at BER $= 10^{-6}$.

In Fig. 4.5, the BER performance of MFTN systems employing R-GAMP-FDE is evaluated at different combinations of time and frequency packing factors, where the Doppler spread is $f_d = 150$ Hz. The BER performance of their Nyquist counterpart (i.e., $\tau = 1.0, \nu = 1.0$) with perfect CSI is also included as a benchmark. It is seen that at $\tau = 1.0, \nu = 0.9$, MFTN signaling improves the spectral efficiency[4] by up to 11% at a negligible BER performance degradation.

[2]Since the UTAMP algorithm is guaranteed to converge in case of Gaussian priors, the UTAMP-TDE algorithm only exploits the Gaussian approximations of the *a priori* probabilities of the transmitted symbols.

[3]To avoid an intractable computational complexity imposed by the discrete *a priori* distributions of the transmitted symbols, the MMSE-TDE algorithm only employ its Gaussian approximations.

[4]The spectral efficiency of MFTN signaling can be computed as $\eta = R_c \log_2 M/[\tau\nu(1+\beta)]$ bits/s/Hz [128].

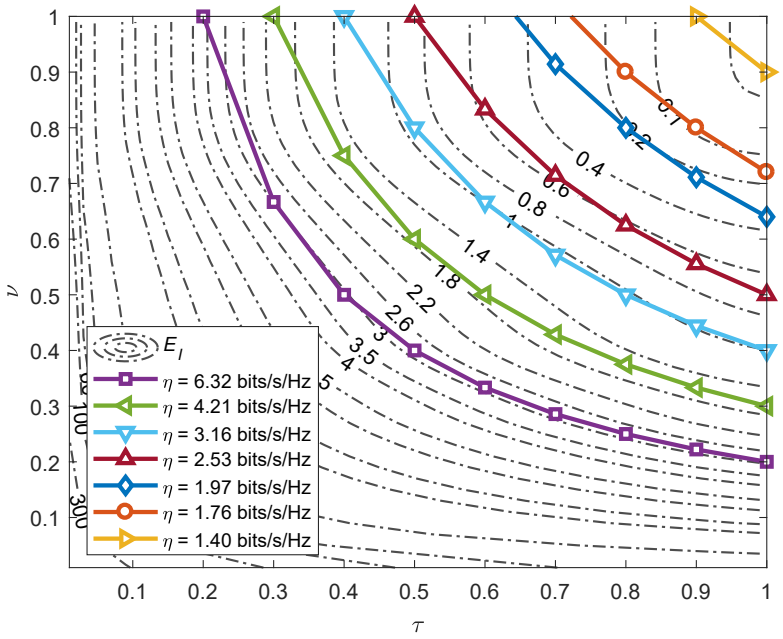
When further reducing τ and ν, the MFTN systems based on the proposed R-GAMP-FDE algorithm obtain about 39% and 56% higher transmission rates, for $\tau = 0.9, \nu = 0.8$ and $\tau = 0.8, \nu = 0.8$, respectively, albeit at the cost of about 1.1 dB and 2.6 dB E_b/N_0 losses at BER $= 10^{-6}$. Moreover, for a given pulse shaping filter and a fixed spectral efficiency, the BER performance of MFTN signaling can be significantly improved by optimizing τ and ν. Observe that MFTN systems having $\tau = 1.0, \nu = 0.72$, $\tau = 0.9, \nu = 0.8$, $\tau = 0.8, \nu = 0.9$ and $\tau = 0.72, \nu = 1.0$ achieve the same spectral efficiency, while with $\tau = 0.9, \nu = 0.8$ they achieve better BER than other packing factors. This is because MFTN systems having $\tau = 0.9, \nu = 0.8$ suffer from a lower inherent interference energy[5] than those of other cases, when an RRC shaping filter is employed, as shown in Fig. 4.6(a).

To clarify the relationship between the packing factor combinations and the pulse shaping filter in Fig. 4.6, the inherent interference energy E_I and spectral efficiency η of MFTN systems employing RRC and Gaussian pulses[6] are evaluated under different packing factor combinations. Observe that the effects of τ and ν on E_I depend on the choice pulse shaping filters for a fixed η. For an RRC pulse and a fixed spectral efficiency, the reduction of τ leads to higher interference energy than that of ν. For example, the MFTN systems having $\tau = 0.9, \nu = 0.8$ and $\tau = 0.72, \nu = 1.0$ have the same η, while the interference energy for $\tau = 0.72, \nu = 1.0$ is much higher than that for $\tau = 0.9, \nu = 0.8$. The corresponding BER performance is depicted in Fig. 4.5, where the MFTN system with $\tau = 0.72, \nu = 1.0$ suffers from an additional 6.5 dB E_b/N_0 erosion at BER $= 10^{-5}$ compared to its counterpart using $\tau = 0.9, \nu = 0.8$. However, for a Gaussian pulse, the negative influence of ν on E_I is more grave than that of τ. The interference energy remains nearly constant within a certain range of τ. Then, a higher η at a negligible BER performance degradation is obtained via reducing τ in the case of Gaussian pulses. It is concluded that the η can be improved by jointly optimizing τ and ν, instead of only reducing either τ or ν.

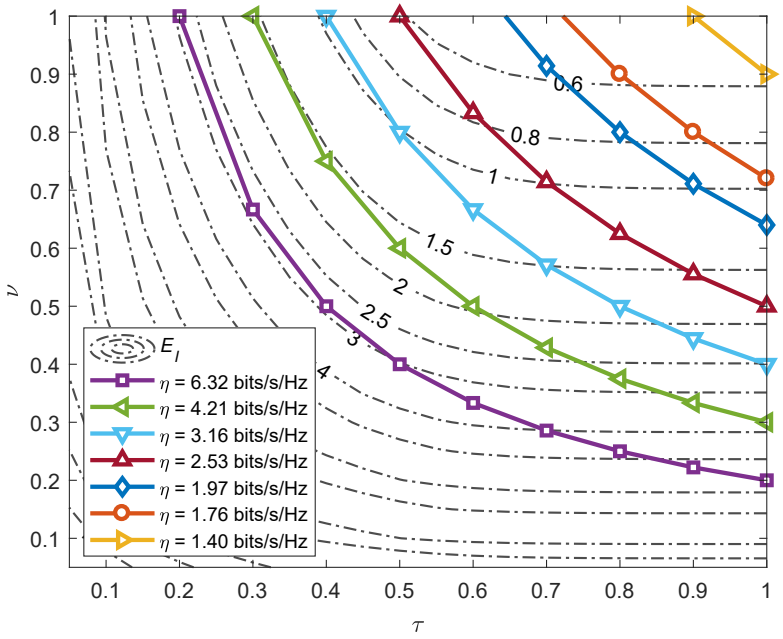
In Fig. 4.7 and Fig. 4.8, both the BER and NMSE performance of the proposed JCEE algorithms are compared to those of the LS-MMSE method, where $\tau = 0.9, \nu = 0.8$. The following simulations consider MFTN systems in frequency-selective fading channels at a velocity of 270 km/h, where the corresponding Doppler spread is $f_d = 500$ Hz. The BER and NMSE performance of their Nyquist-based counterpart with unknown CSI are also included as benchmarks. For channel estimation, the proposed PBiGAMP-based algorithms obtain more accurate channel estimates than LS-MMSE, since the former exploits both the pilots and the data symbols for improving the accuracy of channel estimation. However, superior channel estimation cannot always guarantee better BER performance, especially in severe inherent interference scenarios. Compared to the Nyquist-based counterpart, the MFTN systems employing the proposed algorithms obtain the similar NMSE performance, but still suffer from a non-negligible BER performance loss. For example, MFTN signaling employing the proposed R-PBiGAMP-FDJCEE

[5] In [153], the inherent interference energy of MFTN signaling is defined as $E_\mathrm{I} = E_\mathrm{s} \sum_n \sum_k |A_\mathrm{p}(n\tau T, k\nu F)|^2 - 1$, where E_s denotes the energy of the transmitted symbols.

[6] The Gaussian pulse is expressed as $p_\mathrm{G}(t) = (2/\rho)^{1/4} e^{-\pi t^2/\rho}$ with $\rho = 0.3$.



(a) RRC



(b) Gaussian

Figure 4.6: Interference energy and spectral efficiency of MFTN systems with various pulse shaping filters and packing factors.

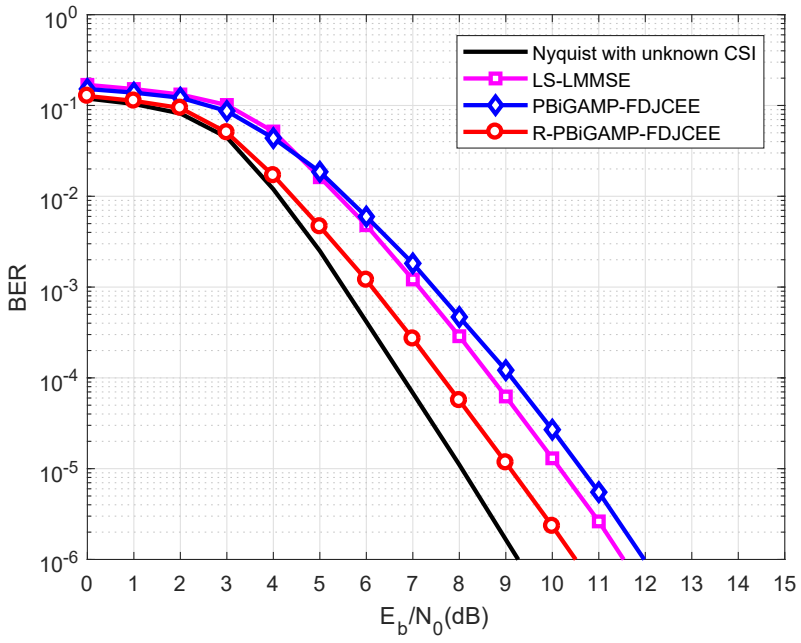


Figure 4.7: BER performance of different algorithms for MFTN systems in the absence of CSI.

algorithm can increase the transmission rate by up to 39%, at the cost of about 1.2 dB $\mathrm{E_b/N_0}$ loss at BER $= 10^{-6}$. That means that the inherent two-dimensional interferences induced by time-frequency packing are more crucial than those imposed by channels in this case. For equalization, as an efficient approximation of MMSE equalization [147], PBiGAMP-FDJCEE can only approach the LS-MMSE algorithm in terms of BER, while the complexity of PBiGAMP-FDJCEE is much smaller than that of LS-MMSE as shown in TABLE 4.1. Note that the proposed R-PBiGAMP-FDJCEE can still improve the BER performance, compared to LS-MMSE. In Fig. 4.7, about 1.0 dB $\mathrm{E_b/N_0}$ gain is observed at BER $= 10^{-5}$. The performance gain of R-PBiGAMP-FDJCEE arises from the efficient average approximations of $\boldsymbol{\nu}_q^x(t)$ and $\boldsymbol{\nu}_q^s(t)$, which improves the robustness of the ill-conditioned matrices to small perturbations. Moreover, as shown in Fig. 4.8, the NMSE performance of different algorithms tends to remain constant upon increasing $\mathrm{E_b/N_0}$.

Considering that the channel coefficients are assumed to be constant in each segment, the segment length of L_{m} is crucial for its performance versus computational complexity. The impact of L_{m} on the BER of the proposed R-PBiGAMP-FDJCEE algorithm is investigated in Fig. 4.9, where $\tau = 0.9, \nu = 0.8$. Observe that BER degrades upon increasing L_{m} for a fixed Doppler spread. When the segment length increases to $L_{\mathrm{m}} = 126$, a significant BER loss can be observed due to the inaccurate quasi-static channel assumption. By contrast, the BER of the proposed R-PBiGAMP-FDJCEE algorithm can be improved by reducing the segment length L_m, at the cost of increased computational complexity. Compared to the cases with $L_{\mathrm{m}} = 63$ and $L_{\mathrm{m}} = 84$, R-PBiGAMP-FDJCEE using $L_{\mathrm{m}} = 42$ obtains an additional 1.2 dB and 2.7 dB $\mathrm{E_b/N_0}$ gains at BER $= 10^{-6}$ in Fig. 4.9. When the segment length is further reduced, its BER performance gain becomes marginal, while the number of segments L_{q} significantly increases.

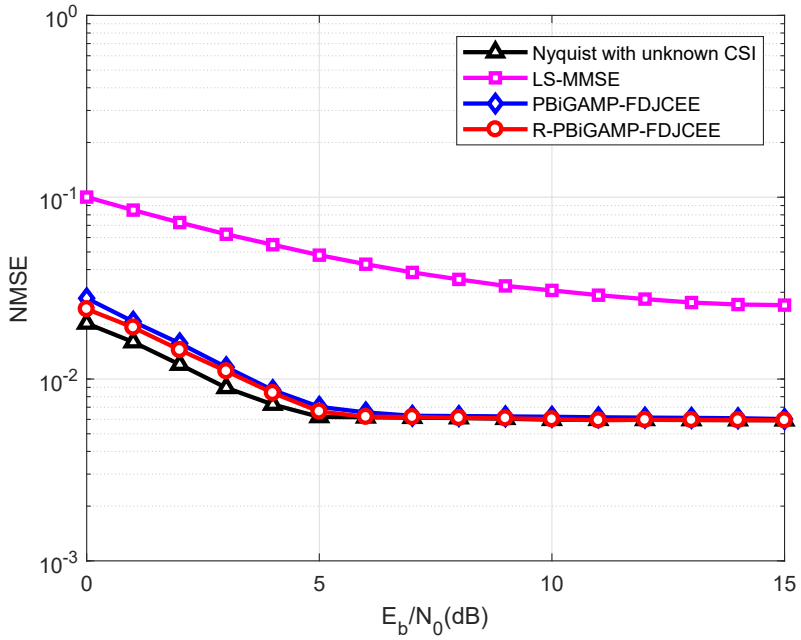


Figure 4.8: NMSE performance of different algorithms for MFTN systems in the absence of CSI.

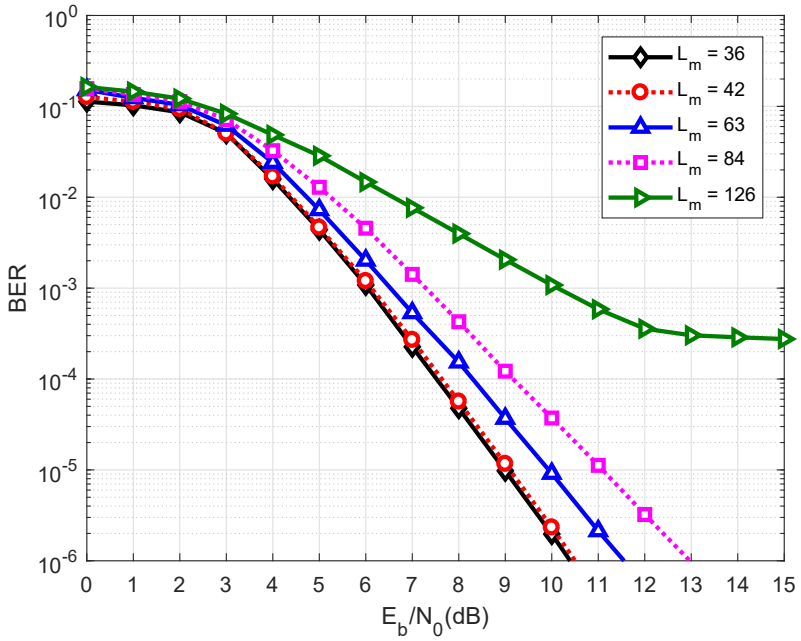


Figure 4.9: Impact of various length of segment on BER performance of the proposed R-PBiGAMP-FDJCEE algorithm.

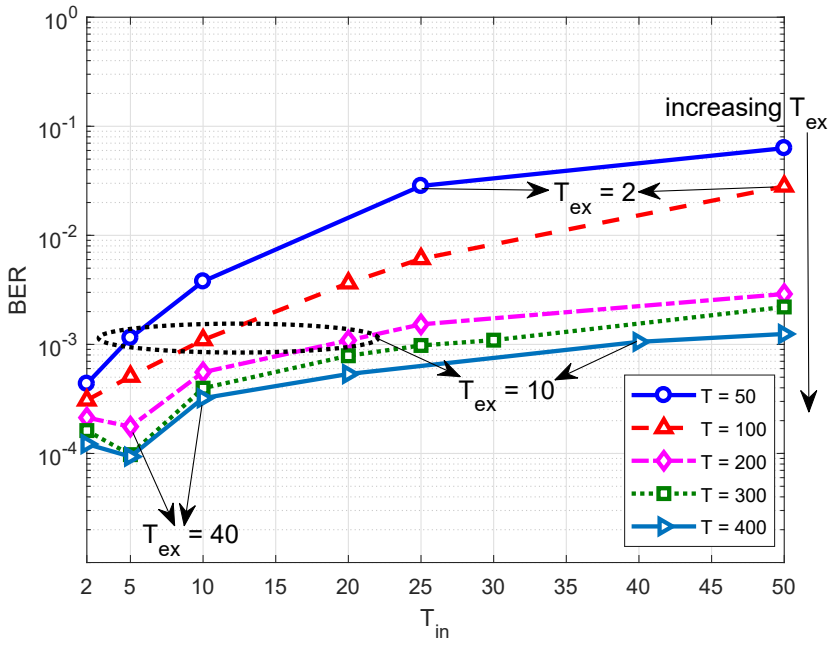


Figure 4.10: Impact of various combinations of I_c and I_e on BER performance of the proposed R-PBiGAMP-FDJCEE algorithm.

Hence, $L_m = 42$ is an appropriate option for R-PBiGAMP-FDJCEE in the MFTN system considered. In practice, we can adjust the segment length of L_m to strike a performance versus complexity trade-off.

In Fig. 4.10, the BER performance of the proposed R-PBiGAMP-FDJCEE algorithm is evaluated using various combinations of I_c and I_e at $E_b/N_0 = 7$ dB, where the total number of iterations $T = I_c \cdot I_e$ and $\tau = 0.9, \nu = 0.8$. It is seen that, given I_c, BER performance is improved with the increase of I_e. On the contrary, given I_e, e.g., $I_e = 2$ and $I_e = 10$, increasing I_c does not improve the BER performance. Moreover, when the total number of iterations T is fixed, for $I_c > 10$, increasing I_c (or decreasing I_e) deteriorates the BER performance. Hence, it is concluded that the external iterations between the equalizer and the channel decoder are much more crucial than the internal iterations of LDPC decoder. Observe that $I_c = 5$ is appropriate for the studied MFTN systems. In fact, increasing I_c may even worsen the BER performance. For $I_e = 40$, there is a significant BER loss when I_c varies from 5 to 10. This is because the belief output from LDPC decoder could be overconfident when I_c becomes large. Hence, I_c and I_e should be optimized to compromise between the BER performance and the computational complexity.

4.6 Conclusion

In this chapter, a low-complexity PBiGAMP-based iterative message passing receiver was pro-

posed for MFTN systems operating in frequency-selective fading channels. By inserting a few cyclic postfixes in the frequency domain and truncating the severe two-dimensional interferences, a segment-based frequency-domain received signal model was constructed in the form of a block circulant linear transition matrix. It was shown that the proposed model reduce the condition number of the ill-conditioned linear transition matrices, which can potentially lead to improved BER performance. Building on this model, the PBiGAMP-based parametric JCEE algorithm was developed for simultaneously estimating the modulated symbols and channel coefficients. For improving the robustness of the proposed JCEE algorithm to small perturbations, a refined JCEE algorithm was evolved by inserting a series of scaled identity matrices. The proposed JCEE algorithms can be readily decomposed into two FDE algorithms when the CSI is perfectly known. The simulation results verified the benefits of the proposed PBiGAMP-based receiver for MFTN systems operating in frequency-selective fading channels. Compared to its Nyquist-signaling counterpart, MFTN systems employing the proposed refined algorithms achieve about 39% higher transmission rate at the cost of 1.2 dB E_b/N_0 loss.

Chapter 5

Iterative Equalization for Index-Modulated MFTN Signaling

5.1 Introduction

The studies in Chapter 3 and Chapter 4 provide a pair of efficient ways to improve the demodulation performance of MFTN signaling, i.e., reducing the inherent interferences via the inactivated modulation units of IM and designing a series of powerful enough receivers. In Chapter 3, frequency-domain one-dimensional packing SEFDM signaling is combined with IM and its JCEE algorithm based on GMP-EP-VMP is further developed for improving the BER performance. Furthermore, a parametric message passing receiver has been designed for MFTN signaling in Chapter 4, which is able to approach the BER performance of Nyquist signaling.

Inspired by these studies, a novel index-modulated MFTN signaling is proposed in this chapter. One of the attractive motivations is that the inactivated subcarriers of IM are able to mitigate the two-dimensional coupling interferences of MFTN signaling[1], resulting in a remarkable BER performance gain. To deal with the remaining interferences, its low-complexity iterative equalization algorithms are also designed in frequency-selective fading channels.

Regards to the demodulation algorithms, the GMP and AMP-based algorithms have been exploited to design low-complexity iterative receivers for non-orthogonal multi-carrier signaling. Due to the constraints of the GMP algorithm, the messages passing between the factor nodes and the variable nodes need to be approximated as Gaussian distributions, resulting in a performance degradation. For example, the Gaussian approximation of the discrete *a priori* probabilities of the transmitted symbols leads to an additional BER performance loss. To enhance the accuracy of the Gaussian approximation, the EP rules has been employed for deriving the approximated Gaussian *a priori* distributions of the transmitted symbols in Chapter 3. As an evolutionary alternative solution, the AMP-based algorithm has also been exploited for

[1]As shown in Fig. 2.3, the ICIs and ISIs of MFTN signaling are imposed by the neighboring subcarriers and symbols, respectively. Hence, the inactivated subcarriers of zeros cannot interfere with the adjacent subcarriers.

designing iterative receivers of MFTN signaling in Chapter 4. The AMP-based algorithm circumvents the Gaussian approximation of the *a priori* distributions of the transmitted symbols, where the accurate discrete *a priori* probabilities can be used for updating messages. It has been verified that, under the same simulation configurations, the BER performance of MFTN signaling can be improved via utilizing the accurate discrete *a priori* distributions. However, AMP guarantees the convergence only when the equivalent channel matrix with the size approaching infinite obeys the independent and identically distributed zero-mean Gaussian distribution [49]. For non-orthogonal transmission systems, the equivalent channel matrix cannot satisfy the convergence conditions of AMP. Furthermore, time-frequency compression will lead to the ill-conditioning problem of MFTN signaling [154].

To improve the convergence of the AMP-based algorithm employing general linear transition matrices, the improved alternatives of AMP algorithm have been developed, such as the OAMP [51], damped AMP [49], UTAMP [155], and VAMP [52]. The damped AMP algorithm is simple and effective, except that the value of the damping coefficient lacks theoretical analysis. Based on the SVD of the general linear transition matrices, UTAMP was derived in the unitary transformation domain, guaranteeing its convergence for Gaussian variables. However, SVD has an excessive computational complexity. Moreover, VAMP was developed for relaxing the convergence condition of AMP. When the linear transition matrices are right-orthogonally invariant, the asymptotic behavior of VAMP can be described via a series of state evolution equations. Simulation results have demonstrated that the performance of VAMP is superior to that of AMP for an ill-conditioned matrix [52], [156]. Hence, VAMP-based algorithm is an efficient solution for tackling the ill-conditioning problem of non-orthogonal signaling.

In this chapter, an innovative index-modulated multi-carrier non-orthogonal transmission waveform is designed for achieving high spectral and energy efficiency. The inactivated subcarriers are exploited to alleviate the coupling of the two-dimensional self-interferences. Then, a pair of VAMP-based iterative equalization algorithms are developed in frequency-selective fading channels. The time-domain received signal model of MFTN-IM signaling is derived and then a VAMP-based TDE algorithm is developed by truncating the inherent two-dimensional interferences. To efficiently update the *a priori* probabilities of the transmitted symbols, an extended constellation set is employed for uniformly characterizing the activated and inactivated subcarriers. Since the VAMP-based TDE algorithm still suffers from a high computational complexity imposed by the inversion of a non-diagonal matrix,a VAMP-based FDE algorithm is further derived for simplifying the iterative equalization of MFTN-IM signaling. A subcarrier-based segment-wise frequency-domain received signal model is constructed for remarkably reducing the dimension of matrix operations. In this model, the equivalent channel matrix is reformulated as the product of a diagonal matrix and a normalized FFT matrix. Building on this, the ICIs and inter-segment eliminations are introduced for breaking dense short cycles in the factor graph model of FDE. As a result, the proposed VAMP-based FDE algorithm leads to an attractively low computational complexity.

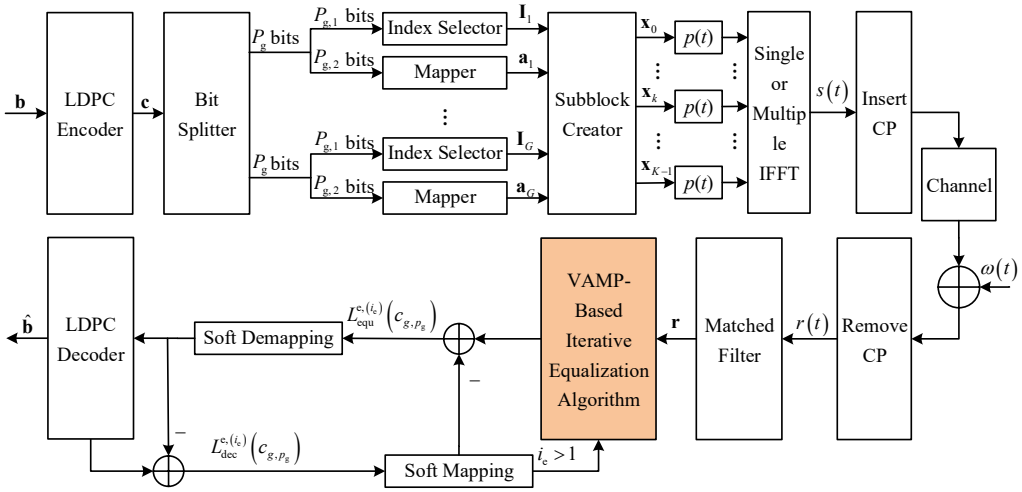


Figure 5.1: The transceiver structure of MFTN-IM signaling.

The rest of this chapter is organized as follows. In Section 5.2, the time-domain received signal model is derived for the novel non-orthogonal waveform. The proposed VAMP-based TDE and FDE algorithms are described in Section 5.3 and Section 5.4, respectively. Based on the proposed iterative equalization algorithm, the BER and NMSE performance of MFTN-IM signaling are evaluated and compared to the existing waveforms in Section 5.5. Finally, Section 5.6 provides the conclusions.

5.2 System Model

The LDPC-based transceiver structure of MFTN-IM signaling is depicted in Fig. 5.1. At the transmitter side, N_{b} input bits $\mathbf{b} = [b_0, \cdots, b_{N_{\text{b}}-1}]^T$ are fed into an LDPC encoder, which outputs N_{c} coded bits $\mathbf{c} = [c_0, \cdots, c_{N_{\text{c}}-1}]^T$. The coded bits are equally divided into G groups and each group contains $P_{\text{g}} = N_{\text{c}}/G$ coded bits, where the g group is represented as $\mathbf{c}_g = [c_{g,0}, \cdots, c_{g,p_{\text{g}}}, \cdots, c_{g,P_{\text{g}}-1}]^T$ and $c_{g,p_{\text{g}}}$ is the $(gP_{\text{g}} + p_{\text{g}} + 1)$-th element of $\mathbf{c}$. Considering a MFTN-IM system employing K subcarriers and N symbols in each subcarrier, the total number of the modulated symbols in an MFTN-IM symbol equals to $N_{\text{s}} = KN$. The P_{g} coded bits in each group are mapped as $K_{\text{g}} = K/G$ subcarriers in each MFTN-IM subblock. Only K_{a} out of K_{g} subcarriers are activated to transmit M-ary constellations, while the remaining inactivated subcarriers are set to zeros. The first $P_{\text{g},1} = \lfloor \log_2 \binom{K_{\text{g}}}{K_{\text{a}}} \rfloor$ coded bits in each group are used to select the indices of the activated subcarriers and other $P_{\text{g},2} = K_{\text{a}} \log_2 M$ coded bits are mapped onto the constellation set $\boldsymbol{\mathcal{S}}$. The activated index set and modulation symbol vector are denoted as $\mathbf{I}_g = \{I_{g,0}, I_{g,1}, \cdots, I_{g,K_{\text{a}}-1}\}$, $I_{g,k_{\text{a}}} \in \{0, \cdots, K_{\text{g}} - 1\}$ and $\mathbf{a}_g = [a_{g,0}, a_{g,1}, \cdots, a_{g,K_{\text{a}}-1}]^T$, $a_{g,k_{\text{a}}} \in \boldsymbol{\mathcal{S}}$, respectively. Accordingly, the g-th MFTN-IM subblock is expressed as $\mathbf{x}_g = [x_{g,0}, \cdots, x_{g,K_{\text{g}}-1}]^T$, where $x_{g,k_{\text{g}}} = a_{g,k_{\text{a}}}$ for $k_{\text{g}} = I_{g,k_{\text{a}}} \in \mathbf{I}_g$ and $x_{g,k_{\text{g}}} = 0$ for $k_{\text{g}} \notin \mathbf{I}_g$. The power of the signal constellation is normalized to unit average power, satisfying $\mathbb{E}\{\mathbf{a}_g^H \mathbf{a}_g\} = K_{\text{a}}$. Then, G subblocks are concatenated to generate the transmitted symbol $\mathbf{x} = [\mathbf{x}_0^T, \cdots, \mathbf{x}_{G-1}^T]^T$. After passing through a RRC shaped filter $p(t)$ with the

roll-off factor β and the time interval τT_0, the modulated sequences are transmitted via K non-orthogonal subcarriers, implemented using single or multiple IFFT modules [132]. The baseband transmitted MFTN-IM signal is expressed as

$$s(t) = \sqrt{K_{\mathrm{g}}/K_{\mathrm{a}}T_0} \sum_{k=0}^{K-1} \sum_{n=0}^{N-1} x_{k,n} p(t - n\tau T_0) e^{j2\pi k\nu F_0 t}, \tag{5.1}$$

where $\sqrt{K_{\mathrm{g}}/K_{\mathrm{a}}}$ denotes the normalized coefficient of signal power, $\tau, \nu \in (0, 1]$ are the time-domain and frequency-domain packing factors, T_0 denotes the time-domain symbol period, F_0 denotes the orthogonal subcarrier spacing, and $x_{k,n}$ is the n-th transmitted symbol of the k-th subcarrier.

When the length of cyclic prefixes is greater than that of the channel memory, the ISI imposed by channels can be ignored. Considering a multipath channel with L taps, the MFTN-IM received signal is given by

$$r(t) = \sum_{l=0}^{L-1} h_l s(t - \tau_l) + \omega(t), \tag{5.2}$$

where h_l and τ_l are the coefficient and delay of l-th channel tap, $\omega(t)$ is the AWGN process with zero mean and variance σ_0. After removing the cyclic prefixes at the receiver side, the output of the matched filter is represented as

$$\begin{aligned} r_{k_{\mathrm{r}},n_{\mathrm{r}}} &= \sqrt{K_{\mathrm{a}}/K_{\mathrm{g}}T_0} \int_{-\infty}^{\infty} r(t) p(t - n_{\mathrm{r}}\tau T_0) e^{-j2\pi k_{\mathrm{r}}\nu F_0 t} dt \\ &= \sum_{l=0}^{L-1} h_l \sum_{k_{\mathrm{t}}=0}^{K-1} \sum_{n_{\mathrm{t}}=0}^{N-1} x_{k_{\mathrm{t}},n_{\mathrm{t}}} e^{-j2\pi k_{\mathrm{t}} l\nu F_0 \tau T_0} \int_{-\infty}^{\infty} p(t - n_{\mathrm{r}}\tau T_0) \\ &\qquad \times p(t - (n_{\mathrm{t}} + l)\tau T_0) e^{-j2\pi(k_{\mathrm{r}} - k_{\mathrm{t}})\nu F_0 t} dt + \omega_{k_{\mathrm{r}},n_{\mathrm{r}}} \\ &= \sum_{l} h_l \sum_{k_{\mathrm{t}},n_{\mathrm{t}}} A_{\mathrm{p}}(\dot{n}_\Delta \tau T_0, k_\Delta \nu F_0) \psi_{k_\Delta,n_{\mathrm{r}}}^{k_{\mathrm{t}},l} x_{k_{\mathrm{t}},n_{\mathrm{t}}} + \omega_{k_{\mathrm{r}},n_{\mathrm{r}}}, \end{aligned} \tag{5.3}$$

where $\dot{n}_\Delta = n_{\mathrm{t}} - n_{\mathrm{r}} + l$, $k_\Delta = k_{\mathrm{t}} - k_{\mathrm{r}}$, n_{r} and k_{r} denote the time-domain and frequency-domain indices of the received signal, n_{t} and k_{t} denote the time-domain and frequency-domain indices of the transmitted signal, $A_{\mathrm{p}}(\tau T_0, \nu F_0) \triangleq \int_{-\infty}^{+\infty} p(t) p(t - \tau T_0) e^{j2\pi\nu F_0 t} dt$ is defined as the ambiguity function for characterizing the two-dimensional interferences[2], $\psi_{k_\Delta,n_{\mathrm{r}}}^{k_{\mathrm{t}},l} \triangleq \lambda_{k_{\mathrm{t}}}^{l} \theta_{k_\Delta}^{n_{\mathrm{r}}}$, $\lambda_{k_{\mathrm{t}}}^{l} \triangleq e^{-j2\pi k_{\mathrm{t}} l\nu F_0 \tau T_0}$, $\theta_{k_\Delta}^{n_{\mathrm{r}}} \triangleq e^{j2\pi k_\Delta n_{\mathrm{r}}\nu F_0 \tau T_0}$, $\omega_{k_{\mathrm{r}},n_{\mathrm{r}}} = \int_{-\infty}^{\infty} \omega(t) p(t - n_{\mathrm{r}}\tau T_0) e^{-j2\pi k_{\mathrm{r}}\nu F_0 t} dt$ denotes the colored noise process with an autocorrelation matrix $\mathbf{R}_\omega$, and the element of $\mathbf{R}_\omega$ is $\mathbb{E}\{\omega_{k_1,n_1} \omega_{k_2,n_2}^*\} =$

[2]For Nyquist signaling, $A_{\mathrm{p}}(\dot{n}_\Delta T_0, k_\Delta F_0) = 1$ for $\dot{n}_\Delta = 0$ and $k_\Delta = 0$, while $A_{\mathrm{p}}(\dot{n}_\Delta T_0, k_\Delta F_0) = 0$ for $\dot{n}_\Delta \neq 0$ or $k_\Delta \neq 0$. That means there is no inherent interference for Nyquist signaling. For MFTN-IM signaling, the ambiguity function satisfies $A_{\mathrm{p}}(\dot{n}_\Delta \tau T_0, k_\Delta \nu F_0) = 1$ for $\dot{n}_\Delta = 0$ and $k_\Delta = 0$, but usually does not equal to zero for $|\dot{n}_\Delta| \leq N_{\mathrm{I}}$ or $|k_\Delta| \leq K_{\mathrm{I}}$. It means that there exists ISIs and ICIs from the adjacent transmitted symbols and subcarriers. Similar to the definition in [153], the inherent interference energy of MFTN-IM signaling can be calculated as $E_{\mathrm{I}} = E_{\mathrm{s}} \sum_n \sum_k |A_{\mathrm{p}}(\dot{n}_\Delta \tau T_0, k_\Delta \nu F_0)|^2 - 1$, where E_{s} denotes the energy of the transmitted symbols.

$\sigma_0^2 A_{\mathrm{p}}\big[(n_1-n_2)\tau T_0,(k_1-k_2)\nu F_0\big]$.

Furthermore, the received signal model in (5.3) can be rewritten as a matrix form, i.e.,

$$\mathbf{r}=\mathbf{H}\mathbf{\Phi}\mathbf{x}+\boldsymbol{\omega}, \tag{5.4}$$

where $\mathbf{r}=[\mathbf{r}_0,\cdots,\mathbf{r}_{K-1}]^T$, $\mathbf{r}_k=[r_{k,0},\cdots,r_{k,N-1}]^T$, $\mathbf{H}$ is an $N_{\mathrm{s}}\times N_{\mathrm{s}}(L+1)$ channel matrix with the k-th row $[\mathbf{0}^T_{(k-1)(L+1)},\ \mathbf{h}^T,\ \mathbf{0}^T_{(N_{\mathrm{s}}-k)(L+1)}]$[3], $\mathbf{\Phi}$ denotes an $N_{\mathrm{s}}(L+1)\times N_{\mathrm{s}}$ interference matrix composing of $\phi^{(k_{\mathrm{t}},k_{\mathrm{r}})}_{n_{\mathrm{t}},n_{\mathrm{r}}-l}=A_{\mathrm{p}}((n_\Delta+l)\tau T_0,k_\Delta\nu F_0)\psi^{k_{\mathrm{t}},l}_{k_\Delta,n_{\mathrm{r}}}$, $\mathbf{x}=[\mathbf{x}_0,\cdots,\mathbf{x}_{K-1}]^T$ is an $N_{\mathrm{s}}\times 1$ transmitted symbol vector with $\mathbf{x}_k=[x_{k,0},\cdots,x_{k,N-1}]^T$.

5.3 Time-Domain Equalization Based on VAMP

In this section, the goal is to design an efficient receiver for the novel MFTN-IM signaling. Building on the time-domain received signal model, a vector-form factor graph is constructed by factorizing the marginal *a posteriori* probability density function of the transmitted symbols. Then, the VAMP algorithm is employed for deriving the parametric TDE algorithm.

5.3.1 Factor Graph Representation

Under the assumption of perfectly known CSI, the two-dimensional inherent interferences imposed by time-frequency packing and the ISIs results from a multipath channel can be combined into an equivalent channel matrix. Then, the time-domain received signal model is rewritten as

$$\mathbf{r}=\mathbf{G}\mathbf{x}+\boldsymbol{\omega}, \tag{5.5}$$

where each element of the equivalent channel matrix $\mathbf{G}$ is expressed as $g^{(k_{\mathrm{t}},k_{\mathrm{r}})}_{n_{\mathrm{t}},n_{\mathrm{r}}}=\sum_{l=0}^{L-1}h_l\phi^{(k_{\mathrm{t}},k_{\mathrm{r}})}_{n_{\mathrm{t}},n_{\mathrm{r}}-l}$.

Inspired by the derivations of VAMP in [52], the transmitted symbol vector is decomposed into two variables, i.e., $\mathbf{x}_1$ and $\mathbf{x}_2$, satisfying $\delta(\mathbf{x}_1-\mathbf{x}_2)$. According to Bayesian rules, the marginal *a posteriori* probability density function can be factorized as

$$p(\mathbf{x}|\mathbf{r})\propto p(\mathbf{x}_1)\delta(\mathbf{x}_1-\mathbf{x}_2)p(\mathbf{r}|\mathbf{x}_2). \tag{5.6}$$

where $p(\mathbf{r}|\mathbf{x}_2)\propto\mathcal{CN}(\mathbf{r};\mathbf{G}\mathbf{x}_2,\sigma_0^2\mathbf{I})$ is the likelihood function, $p(\mathbf{x}_1)$ denotes the *a priori* probability updated via the output LLR of the channel decoder. According to the factorization in (5.6), a cyclic-free vector factor graph can be constructed in Fig. 5.2. By introducing auxiliary variables $\mathbf{x}_1$ and $\mathbf{x}_2$, the vector factor graph is divided into two parts: denoising and LMMSE. The detailed derivations of message updating of the proposed TDE algorithm are as follows.

[3]Due to the limited length of channel memory, each row of the channel matrix contains several zero elements. That means that, for different symbols on the k-th subcarriers, the interferences imposed by the multipath channel only depend on adjacent L symbols, corresponding to non-zero elements in the k-th row of $\mathbf{H}$.

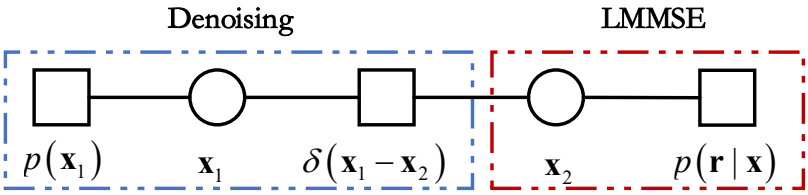


Figure 5.2: Vector factor graph of TDE for MFTN-IM signaling

5.3.2 Message Updating of VAMP-TDE

As shown in Fig. 5.1, the equalizer employs the soft information fed from the channel decoder (i.e., its output LLR) to update the *a priori* probability of the transmitted symbol vector. The iterations between the equalizer and the channel decoder are regarded as the external iterations, while the iterations of channel decoding are considered as the inner iterations. Assume that the output LLR of the channel decoder in the i_{e}-th external iteration is $L_{\mathrm{dec}}^{\mathrm{e},(i_{\mathrm{e}})}(c_{g,p_{\mathrm{g}}})$, the *a priori* probability of the p_{g}-th coded bit in the g-th MFTN-IM subblock is computed as

$$P^{(i_{\mathrm{e}})}(c_{g,p_{\mathrm{g}}}) = \frac{1}{2}\left[1+(-1)^{c_{g,p_{\mathrm{g}}}}\tanh\left(\frac{1}{2}L_{\mathrm{dec}}^{\mathrm{e},(i_{\mathrm{e}})}(c_{g,p_{\mathrm{g}}})\right)\right], \tag{5.7}$$

where $c_{g,p_{\mathrm{g}}} \in \{0,1\}$ and $p_{\mathrm{g}} \in \{0,\cdots,P_{\mathrm{g}}-1\}$.

Considering that the transmitted symbols contain the activated and inactivated subcarriers, where only the former is used to transmitted the M-ary constellations. To uniformly characterize the activated and inactivated subcarriers, this work introduces the extended constellation set $\tilde{\boldsymbol{\mathcal{S}}} = \{\boldsymbol{\mathcal{S}}, 0\}$[4] and then $\mathbf{x} \in \tilde{\boldsymbol{\mathcal{S}}}$. Building on this, the discrete *a priori* probability of the transmitted symbol can be calculated using $P^{(i_{\mathrm{e}})}(c_{g,p_{\mathrm{g}}})$ according to the activated pattern of IM and M-ary mapping rules. For the $m_1 \in \{0,\cdots,2^{P_{\mathrm{g},1}}-1\}$-th activated pattern of IM, the activated index set $\mathbf{I}_{m_1} = \{I_{m_1,0},\ldots,I_{m_1,K_{\mathrm{a}}-1}\}$ corresponds to the coded bit vector $\mathbf{c}_{m_1} = [c_{m_1,0},\cdots,c_{m_1,P_{\mathrm{g},1}-1}]^T$. Based on the constellation mapping rules, the $m_2 \in \{0,\cdots,2^{P_{\mathrm{g},2}}-1\}$-th modulated symbol $\mathbf{a}_{m_2} = [a_{m_2,0},\ldots,a_{m_2,K_{\mathrm{a}}-1}]$ corresponds to the coded bit vector $\mathbf{c}_{m_2} = [c_{m_2,0},\cdots,c_{m_2,P_{\mathrm{g},2}}-1]^T$. Therefore, the discrete *a priori* probability of the transmitted symbol $x_{g,k_{\mathrm{g}}}$ in the g-th MFTN-IM subblock is given by

$$P_{g,k_{\mathrm{g}},0}^{(i_{\mathrm{e}})} = \sum_{m_1,k_{\mathrm{g}}\notin\mathbf{I}_{m_1}}\left[\prod_{p_{\mathrm{g},1}=0}^{P_{\mathrm{g},1}-1} P^{(i_{\mathrm{e}})}(c_{g,p_{\mathrm{g},1}}=c_{m_1,p_{\mathrm{g},1}})\right], \tag{5.8}$$

$$P_{g,k_{\mathrm{g}},m}^{(i_{\mathrm{e}})} = \sum_{m_1,k_{\mathrm{g}}\in\mathbf{I}_{m_1}}\left[\prod_{p_{\mathrm{g},1}=0}^{P_{\mathrm{g},1}-1} P^{(i_{\mathrm{e}})}(c_{g,p_{\mathrm{g},1}}=c_{m_1,p_{\mathrm{g},1}})\prod_{p_{\mathrm{g},2}=P_{\mathrm{g},1}}^{P_{\mathrm{g}-1}} P^{(i_{\mathrm{e}})}(c_{g,p_{\mathrm{g},2}}=c_{m_2,(p_{\mathrm{g},2}-P_{\mathrm{g},1})})\right], \tag{5.9}$$

where $P_{g,k_{\mathrm{g}},0}^{(i_{\mathrm{e}})}$ and $P_{g,k_{\mathrm{g}},m}^{(i_{\mathrm{e}})}$ denote the *a priori* probabilities of $x_{g,k_{\mathrm{g}}} = 0$ and $x_{g,k_{\mathrm{g}}} = \boldsymbol{\mathcal{S}}_m$, $c_{g,p_{\mathrm{g},1}}$

[4]The element 0 represents the inactivated subcarrier. The set $\mathbf{S}$ contains the constellation points, corresponding to the activated subcarrier.

denotes the index bits for selecting the activated indices, and $c_{g,p_{\mathrm{g},2}}$ denotes the coded bits used for constellation mapping.

In the denoiser, assuming that the message $\mu_{\delta\to\mathbf{x}_1}(\mathbf{x}_1) \propto \mathcal{CN}(\mathbf{x}_1;\mathbf{r}_1(i),\gamma_1^{-1}(i)\mathbf{I}_{N_\mathrm{s}})$ passing from the factor node $\delta(\mathbf{x}_1-\mathbf{x}_2)$ to the variable node $\mathbf{x}_1$ in the i-th iteration is available, based on the sum-product algorithm, the belief of $\mathbf{x}_1$ is expressed as

$$b(\mathbf{x}_1) \propto p(\mathbf{x}_1)\mathcal{CN}(\mathbf{x}_1;\mathbf{r}_1(i),\gamma_1^{-1}(i)\mathbf{I}_{N_\mathrm{s}}) \propto \mathcal{CN}(\mathbf{x}_1;\hat{\mathbf{x}}_1(i),\eta_1^{-1}(i)\mathbf{I}_{N_\mathrm{s}}), \tag{5.10}$$

where the mean and variance vectors are given by

$$\hat{\mathbf{x}}_1(i) = \frac{\int \mathbf{x}_1 p(\mathbf{x}_1)\mathcal{CN}(\mathbf{x}_1;\mathbf{r}_1(i),\gamma_1^{-1}(i)\mathbf{I}_{N_\mathrm{s}})d\mathbf{x}_1}{\int p(\mathbf{x}_1)\mathcal{CN}(\mathbf{x}_1;\mathbf{r}_1(i),\gamma_1^{-1}(i)\mathbf{I}_{N_\mathrm{s}})d\mathbf{x}_1}, \tag{5.11}$$

$$\eta_1^{-1}(i) = \frac{\mathbf{1}_{N_\mathrm{s}}^T \int |\mathbf{x}_1-\hat{\mathbf{x}}_1(i)|^2 p(\mathbf{x}_1)\mathcal{CN}(\mathbf{x}_1;\mathbf{r}_1(i),\gamma_1^{-1}(i)\mathbf{I}_{N_\mathrm{s}})d\mathbf{x}_1}{N_\mathrm{s}\int p(\mathbf{x}_1)\mathcal{CN}(\mathbf{x}_1;\mathbf{r}_1(i),\gamma_1^{-1}(i)\mathbf{I}_{N_\mathrm{s}})d\mathbf{x}_1}. \tag{5.12}$$

Then, the message passing from the variable node $\mathbf{x}_1$ to the factor node $\delta(\mathbf{x}_1-\mathbf{x}_2)$ is calculated as

$$\begin{aligned}\mu_{\mathbf{x}_1\to\delta}(\mathbf{x}_1) &\propto \mathcal{CN}(\mathbf{x}_1;\hat{\mathbf{x}}_1(i),\eta_1^{-1}(i)\mathbf{I}_{N_\mathrm{s}})/\mathcal{CN}(\mathbf{x}_1;\mathbf{r}_1(i),\gamma_1^{-1}(i)\mathbf{I}_{N_\mathrm{s}}) \\ &\propto \mathcal{CN}(\mathbf{x}_1;\mathbf{r}_2(i),\gamma_2^{-1}(i)\mathbf{I}_{N_\mathrm{s}}).\end{aligned} \tag{5.13}$$

According to the derivations of the product of the Gaussian functions in [157], $\gamma_2(i)$ and $\mathbf{r}_2(i)$ are derived as

$$\gamma_2(i) = \eta_1(i) - \gamma_1(i), \tag{5.14}$$

$$\mathbf{r}_2(i) = (\eta_1(i)\hat{\mathbf{x}}_1(i) - \gamma_1(i)\mathbf{r}_1(i))/\gamma_2(i). \tag{5.15}$$

Since the message passing through factor node $\delta(\mathbf{x}_1–\mathbf{x}_2)$ remains unchange, the message passing from the factor node $\delta(\mathbf{x}_1–\mathbf{x}_2)$ to the variable node $\mathbf{x}_2$ satisfies $\mu_{\delta\to\mathbf{x}_2}(\mathbf{x}_2)\propto\mathcal{CN}(\mathbf{x}_2;\mathbf{r}_2(i),\gamma_2^{-1}(i)\mathbf{I}_{N_\mathrm{s}})$.

In the LMMSE estimator, assuming that the message $\mu_{\delta\to\mathbf{x}_2}(\mathbf{x}_2)$ passing from the factor node $\delta(\mathbf{x}_1-\mathbf{x}_2)$ to the variable node $\mathbf{x}_2$ is available, the belief of $\mathbf{x}_2$ is given by

$$\begin{aligned}b(\mathbf{x}_2) &\propto \mathcal{CN}(\mathbf{x}_2;\mathbf{r}_2(i),\gamma_2^{-1}(i)\mathbf{I}_{N_\mathrm{s}})\mathcal{CN}(\mathbf{r};\mathbf{G}\mathbf{x}_2,\sigma_0^2\mathbf{I}) \\ &\propto \mathcal{CN}(\mathbf{x}_2;\hat{\mathbf{x}}_2(i),\eta_2^{-1}(i)\mathbf{I}_{N_\mathrm{s}}),\end{aligned} \tag{5.16}$$

where, $p(\mathbf{r}|\mathbf{x}_2) \propto \mathcal{CN}(\mathbf{r};\mathbf{G}\mathbf{x}_2,\sigma_0^2\mathbf{I})$ is the likelihood function. The *a posteriori* mean and variance vectors of $\mathbf{x}_2$ are computed as

$$\hat{\mathbf{x}}_2(i) = (\frac{1}{\sigma_0^2}\mathbf{G}^H\mathbf{G}+\gamma_2(i)\mathbf{I}_{N_\mathrm{s}})^{-1}(\frac{1}{\sigma_0^2}\mathbf{G}^H\mathbf{r}+\gamma_2(i)\mathbf{r}_2(i)), \tag{5.17}$$

$$\eta_2^{-1}(i) = \frac{1}{N_\mathrm{s}}\mathrm{tr}\big((1/\sigma_0^2\mathbf{G}^H\mathbf{G}+\gamma_2(i)\mathbf{I}_{N_\mathrm{s}})^{-1}\big). \tag{5.18}$$

Similar to the derivations of (5.13), the message passing from the node $\mathbf{x}_2$ to the node $\delta(\mathbf{x}_1-\mathbf{x}_2)$ is given by

$$\begin{aligned}\mu_{\mathbf{x}_2\to\delta}(\mathbf{x}_2) &\propto \mathcal{CN}(\mathbf{x}_2;\hat{\mathbf{x}}_2(i),\eta_2^{-1}(i)\mathbf{I})/\mathcal{CN}(\mathbf{x}_2;\mathbf{r}_2(i),\gamma_2^{-1}(i)\mathbf{I}_{N_\mathrm{s}})\\ &\propto \mathcal{CN}(\mathbf{x}_2;\mathbf{r}_1(i+1),\gamma_1^{-1}(i+1)\mathbf{I}_{N_\mathrm{s}}).\end{aligned} \tag{5.19}$$

Moreover, the message passing from the factor node $\delta(\mathbf{x}_1-\mathbf{x}_2)$ to the variable node $\mathbf{x}_1$ satisfies $\mu_{\delta\to\mathbf{x}_1}(\mathbf{x}_1)\propto\mathcal{CN}(\mathbf{x}_1;\mathbf{r}_1(i+1),\gamma_1^{-1}(i+1)\mathbf{I}_{N_\mathrm{s}})$ with

$$\gamma_1(i+1)=\eta_2(i)-\gamma_2(i), \tag{5.20}$$

$$\mathbf{r}_1(i+1)=(\eta_2(i)\hat{\mathbf{x}}_2(i)-\gamma_2(i)\mathbf{r}_2(i))/\gamma_1(i). \tag{5.21}$$

According to the above-mentioned derivations, the proposed VAMP-TDE algorithm is summarized in **Algorithm** 7.

Algorithm 7 VAMP-TDE Algorithm for MFTN-IM Signaling

1: **Initialization**: The output LLR of the channel decoder is initialized as $L_{\mathrm{dec}}^{\mathrm{e},(1)}(c_{g,p_\mathrm{g}})=0$, where $g\in\{0,1,\cdots,G-1\}$ and $p_\mathrm{g}\in\{0,1,\cdots,P_\mathrm{g}-1\}$. Compute the *a priori* distribution of the transmitted symbol vector $\mathbf{x}$. The message passing from the factor node $\delta(\mathbf{x}_1-\mathbf{x}_2)$ to the variable node $\mathbf{x}_1$ is initialized as $\mu_{\delta\to\mathbf{x}_1}(\mathbf{x}_1)\propto\mathcal{CN}(\mathbf{x}_1;\mathbf{r}_1(1),\gamma_1^{-1}(1)\mathbf{I}_{N_\mathrm{s}})$, where $\mathbf{r}_1(1)=\mathbf{0}_{N_\mathrm{s}}$ and $\gamma_1(1)=0$.
2: **for** $i_\mathrm{e}=1$ to I_e **do**
3: **for** $i=1$ to I_in **do**
4: Compute the *a posteriori* mean vector $\hat{\mathbf{x}}_1(i)$ and variance $\eta_1^{-1}(i)$ of $\mathbf{x}_1$ according to (5.11) and (5.12);
5: Compute the message $\mu_{\delta\to\mathbf{x}_2}(\mathbf{x}_2)\propto\mathcal{CN}(\mathbf{x}_2;\mathbf{r}_2(i),\gamma_2^{-1}(i)\mathbf{I}_{N_\mathrm{s}})$ according to (5.14) and (5.15);
6: Compute the *a posteriori* mean vector $\hat{\mathbf{x}}_2(i)$ and variance $\eta_2^{-1}(i)$ of $\mathbf{x}_2$ according to (5.17) and (5.18);
7: Compute the message $\mu_{\delta\to\mathbf{x}_1}(\mathbf{x}_1)\propto\mathcal{CN}(\mathbf{x}_1;\mathbf{r}_1(i+1),\gamma_1^{-1}(i+1)\mathbf{I}_{N_\mathrm{s}})$ according to (5.20) and (5.21);
8: **end for**
9: Compute the output LLR of the equalizer according to the mean vector $\mathbf{r}_{k,q,1}(I_\mathrm{in}+1)$ and precision $\gamma_{k,q,1}^{-1}(I_\mathrm{in}+1)$ [88], and then feed then to the channel decoder;
10: Perform BCJR channel decoding and feed the output LLR of the channel decoder to the equalizer. Update the *a priori* probability of the transmitted symbol vector according to (5.7)-(5.9).
11: **end for**

5.4 Frequency-Domain Equalization Based on Interference Mitigation and VAMP

According to the derivations of VAMP-TDE algorithm, the calculations of the *a posteriori* mean vector $\hat{\mathbf{x}}_2(i)$ and variance $\eta_2^{-1}(i)$ in (5.17) and (5.18) perform the inversion of N_s matrix, resulting in a complexity order of $\mathcal{O}(N_\mathrm{s}^3)$. To simplify the computational complexity of the proposed iterative equalization algorithm, a VAMP-based FDE algorithm combined with interference mitigation is further developed through reconstructing a segment-wise frequency-domain received signal model on each subcarrier. In this model, the inherent interference matrix is decomposed into the sum of an ISI matrix and multiple ICI matrices. The ISI matrix can be further decomposed as the product of a diagonal matrix and discrete Fourier transform matrix. The diagonalized equivalent channel matrix can be obtained by transforming the received signal into the frequency domain, which circumvents the inversion of an N_s non-diagonal matrix. In addition, the estimates of the transmitted symbols are fully utilized to compensate the ICIs and the interferences induced by the neighboring segments. Finally, the message updating expressions of the proposed VAMP-FDE algorithm are derived in details.

5.4.1 Frequency-Domain Received Signal Model

Since the inherent interferences decrease with the increasing time-domain or frequency-domain interval, a truncated two-dimensional interference model, i.e., $A_\mathrm{p}\big[(n_\Delta+l)\tau T_0, k_\Delta \nu F_0\big]=0$ for $|n_\Delta+l|>N_\mathrm{I}$ or $|k_\Delta|>K_\mathrm{I}$, where N_I and K_I is used to denote the truncated length values of ISIs and ICIs, respectively. The transmitted symbols of the k_t-th subcarrier are spilt into L_q segments, i.e., $\mathbf{x}_{k_\mathrm{t},q}=[x_{k_\mathrm{t},qL_\mathrm{m}},\cdots,x_{k_\mathrm{t},(q+1)L_\mathrm{m}-1}]^T$, where L_m is the length of one segment, $q=0,\cdots,L_\mathrm{q}-1$, $N=L_\mathrm{q}L_\mathrm{m}$, $L_\mathrm{g}-1\le L_\mathrm{m}\le N$, and $L_\mathrm{g}=L+2N_\mathrm{I}$. The received signal vector of the k-th subcarrier in the q-th segment is expressed as

$$\mathbf{r}_{k_\mathrm{r},q}=\sum_{l=0}^{L-1}h_l\sum_{k_\mathrm{t}\in\mathcal{I}_{K_\mathrm{I}}^{k_\mathrm{r}}}\mathcal{D}(\boldsymbol{\psi}_{k_\Delta,q}^{k_\mathrm{t},l})(\mathbf{g}_{k_\Delta,l}*\mathbf{x}_{k_\mathrm{t},q})+\mathbf{z}_{k_\mathrm{r},q-1}^{\mathrm{tail}}+\mathbf{z}_{k_\mathrm{r},q+1}^{\mathrm{head}}+\boldsymbol{\omega}_{k_\mathrm{r},q},\tag{5.22}$$

where $\mathbf{r}_{k_\mathrm{r},q}=[r_{k_\mathrm{r},qL_\mathrm{m}},\cdots,r_{k_\mathrm{r},qL_\mathrm{m}+L_\mathrm{s}-1}]^T$, $L_\mathrm{s}=L_\mathrm{m}+L_\mathrm{g}-1$, h_l is the channel coefficient of the l-th tap, $\mathcal{I}_{K_\mathrm{I}}^{k_\mathrm{r}}=\{k_\mathrm{r}-K_\mathrm{I},k_\mathrm{r}-K_\mathrm{I}+1,\cdots,k_\mathrm{r}+K_\mathrm{I}\}$, $\boldsymbol{\psi}_{k_\Delta,q}^{k_\mathrm{t},l}=[\psi_{k_\Delta,qL_\mathrm{m}}^{k_\mathrm{t},l},\cdots,\psi_{k_\Delta,qL_\mathrm{m}+L_\mathrm{s}-1}^{k_\mathrm{t},l}]^T$, $\mathbf{g}_{k_\Delta,l}=[\mathbf{0}_l^T\ \ \mathbf{g}_{k_\Delta}^T\ \ \mathbf{0}_{(L-1-l)}^T]^T$ denotes the truncated interference with $\mathbf{g}_{k_\Delta}=[A_\mathrm{p}(N_\mathrm{I}\tau T_0,k_\Delta\nu F_0),\cdots,A_\mathrm{p}(-N_\mathrm{I}\tau T_0,k_\Delta\nu F_0)]^T$, $\boldsymbol{\omega}_{k_\mathrm{r},q}=[\omega_{k_\mathrm{r},qL_\mathrm{m}},\cdots,\omega_{k_\mathrm{r},qL_\mathrm{m}+L_\mathrm{s}-1}]^T$ denotes the truncated colored noise vector. Moreover, $\mathbf{z}_{k_\mathrm{r},q-1}^{\mathrm{tail}}$ and $\mathbf{z}_{k_\mathrm{r},q+1}^{\mathrm{head}}$ represent the interferences from the tail of the $(q-1)$-th segment and the header of the $(q+1)$-th segment, i.e.,

$$\mathbf{z}_{k_\mathrm{r},q-1}^{\mathrm{tail}}=\boldsymbol{\Xi}_\mathrm{t}\left[\sum_{l=0}^{L-1}h_l\sum_{k_\mathrm{t}\in\mathcal{I}_{K_\mathrm{I}}^{k_\mathrm{r}}}\mathcal{D}(\boldsymbol{\psi}_{k_\Delta,q-1}^{k_\mathrm{t},l})(\mathbf{g}_{k_\Delta,l}*\mathbf{x}_{k_\mathrm{t},q-1})\right],\tag{5.23}$$

$$\mathbf{z}_{k_\mathrm{r},q+1}^{\mathrm{head}} = \mathbf{\Xi}_\mathrm{h}\left[\sum_{l=0}^{L-1} h_l \sum_{k_\mathrm{t}\in\mathcal{I}_{K_\mathrm{I}}^{k_\mathrm{r}}} \mathcal{D}(\boldsymbol{\psi}_{k_\Delta,q+1}^{k_\mathrm{t},l})(\mathbf{g}_{k_\Delta,l} * \mathbf{x}_{k_\mathrm{t},q+1})\right], \tag{5.24}$$

where $\mathbf{\Xi}_\mathrm{t} = [\mathbf{0}_{(L_\mathrm{g}-1)\times L_\mathrm{m}}\ \mathbf{I}_{L_\mathrm{g}-1};\ \mathbf{0}_{L_\mathrm{m}\times L_\mathrm{m}}\ \mathbf{0}_{L_\mathrm{m}\times(L_\mathrm{g}-1)}]$, $\mathbf{\Xi}_\mathrm{h} = [\mathbf{0}_{L_\mathrm{m}\times(L_\mathrm{g}-1)}\ \mathbf{0}_{L_\mathrm{m}\times L_\mathrm{m}};\ \mathbf{I}_{L_\mathrm{g}-1}\ \mathbf{0}_{(L_\mathrm{g}-1)\times L_\mathrm{m}}]$, $\mathbf{z}_{k_\mathrm{r},-1}^{\mathrm{tail}} = \mathbf{z}_{k_\mathrm{r},L_\mathrm{q}}^{\mathrm{head}} = \mathbf{0}_{L_\mathrm{s}}$.

By inserting several zeros, the linear convolution in (5.22) is converted to cyclic convolution as

$$\mathbf{r}_{k_\mathrm{r},q} = \sum_{l=0}^{L-1} h_l \sum_{k_\mathrm{t}\in\mathcal{I}_{K_\mathrm{I}}^{k_\mathrm{r}}} \mathcal{D}(\boldsymbol{\psi}_{k_\Delta,q}^{k_\mathrm{t},l})(\mathbf{\Phi}_\mathrm{g}\mathbf{g}_{k_\Delta,l} \circledast \mathbf{\Phi}_\mathrm{m}\mathbf{x}_{k_\mathrm{t},q}) + \dot{\mathbf{z}}_{k_\mathrm{r},q}, \tag{5.25}$$

where $\mathbf{\Phi}_\mathrm{g} = [\mathbf{I}_{L_\mathrm{g}}\ \mathbf{0}_{L_\mathrm{g}\times(L_\mathrm{s}-L_\mathrm{g})}]^T$ is used to insert $(L_\mathrm{s}-L_\mathrm{g})$ zeros in $\mathbf{g}_{k_\Delta,l}$, $\mathbf{\Phi}_\mathrm{m} = [\mathbf{I}_{L_\mathrm{m}}\ \mathbf{0}_{L_\mathrm{m}\times(L_\mathrm{s}-L_\mathrm{m})}]^T$ is used to $(L_\mathrm{s}-L_\mathrm{m})$ zero elements in $\mathbf{x}_{k_\mathrm{t},q}$, and $\dot{\mathbf{z}}_{k_\mathrm{r},q} = \mathbf{z}_{k_\mathrm{r},q-1}^{\mathrm{tail}} + \mathbf{z}_{k_\mathrm{r},q+1}^{\mathrm{head}} + \boldsymbol{\omega}_{k_\mathrm{r},q}$. According to the properties of the cyclic convolution, (5.25) is rewritten as

$$\begin{aligned}
\mathbf{r}_{k_\mathrm{r},q} &= \sum_{l=0}^{L-1} h_l \sum_{k_\mathrm{t}\in\mathcal{I}_{K_\mathrm{I}}^{k_\mathrm{r}}} \mathcal{D}(\boldsymbol{\psi}_{k_\Delta,q}^{k_\mathrm{t},l})\mathbf{F}_{L_\mathrm{s}}^H\mathcal{D}(\breve{\mathbf{g}}_{k_\Delta,l})\mathbf{F}_{L_\mathrm{s}}\mathbf{\Phi}_\mathrm{m}\mathbf{x}_{k_\mathrm{t},q} + \dot{\mathbf{z}}_{k_\mathrm{r},q} \\
&= \sum_{l=0}^{L-1} h_l\lambda_{k_\mathrm{r}}^l\mathbf{F}_{L_\mathrm{s}}^H\mathcal{D}(\breve{\mathbf{g}}_{0,l})\mathbf{F}_{L_\mathrm{s}}\mathbf{\Phi}_\mathrm{m}\mathbf{x}_{k_\mathrm{r},q} + \mathbf{z}_{k_\mathrm{r},q}^{\mathrm{ici}} + \dot{\mathbf{z}}_{k_\mathrm{r},q} \\
&= \sum_{l=0}^{L-1} h_l\lambda_{k_\mathrm{r}}^l\mathbf{F}_{L_\mathrm{s}}^H\mathcal{D}(\breve{\mathbf{g}}_{0,l})\mathbf{F}_{L_\mathrm{s}}\mathbf{\Phi}_\mathrm{m}\mathbf{x}_{k_\mathrm{r},q} + \boldsymbol{\kappa}_{k_\mathrm{r},q} + \boldsymbol{\omega}_{k_\mathrm{r},q},
\end{aligned} \tag{5.26}$$

with

$$\mathbf{z}_{k_\mathrm{r},q}^{\mathrm{ici}} = \sum_{l=0}^{L-1} h_l \sum_{k_\mathrm{t}\in\mathcal{I}_{K_\mathrm{I}\backslash k_\mathrm{r}}} \lambda_{k_\mathrm{t}}^l\mathcal{D}(\boldsymbol{\theta}_{k_\Delta,q})\mathbf{F}_{L_\mathrm{s}}^H\mathcal{D}(\breve{\mathbf{g}}_{k_\Delta,l})\mathbf{F}_{L_\mathrm{s}}\mathbf{\Phi}_\mathrm{m}\mathbf{x}_{k_\mathrm{t},q}, \tag{5.27}$$

where $\breve{\mathbf{g}}_{k_\Delta,l} \triangleq \sqrt{L_\mathrm{s}}\mathbf{F}_{L_\mathrm{s}}\mathbf{\Phi}_\mathrm{g}\mathbf{g}_{k_\Delta,l}$, $\boldsymbol{\kappa}_{k_\mathrm{r},q} = \mathbf{z}_{k_\mathrm{r},q-1}^{\mathrm{tail}} + \mathbf{z}_{k_\mathrm{r},q+1}^{\mathrm{head}}$ denotes the interferences from the adjacent segments, $\mathcal{I}_{K_\mathrm{I}\backslash k_\mathrm{r}} = \{k_\mathrm{r}-K_\mathrm{I}, k_\mathrm{r}-K_\mathrm{I}+1, \cdots, k_\mathrm{r}-1, k_\mathrm{r}+1, \cdots, k_\mathrm{r}+K_\mathrm{I}\}$, $\boldsymbol{\theta}_{k_\Delta,q} = [\theta_{k_\Delta}^{qL_\mathrm{m}}, \cdots, \theta_{k_\Delta}^{qL_\mathrm{m}+L_\mathrm{s}-1}]^T$. Moreover, $\mathbf{\Theta}_{k,q}^{k_\Delta} \triangleq \sum_{l=0}^{L-1} h_l\lambda_k^l\mathcal{D}(\boldsymbol{\theta}_{k_\Delta,q})\mathbf{F}_{L_\mathrm{s}}^H\mathcal{D}(\breve{\mathbf{g}}_{k_\Delta,l})\mathbf{F}_{L_\mathrm{s}}\mathbf{\Phi}_\mathrm{m}$ denotes the equivalent ICI matrix in the q-th segment, $\mathbf{\Theta}_k^0 = \sum_{l=0}^{L-1} h_l\lambda_k^l\mathbf{F}_{L_\mathrm{s}}^H\mathcal{D}(\breve{\mathbf{g}}_{0,l})\mathbf{F}_{L_\mathrm{s}}\mathbf{\Phi}_\mathrm{m}$ denotes the ISI matrix independent of the subscript q.

After applying L_s-point FFT, the frequency-domain received symbol vector of the k_r-th subcarrier in the q-th segment is obtained as

$$\breve{\mathbf{r}}_{k_\mathrm{r},q} = \mathbf{F}_{L_\mathrm{s}}\mathbf{r}_{k_\mathrm{r},q} = \tilde{\mathbf{\Theta}}_{k_\mathrm{r}}^0\mathbf{x}_{k_\mathrm{r},q} + \breve{\boldsymbol{\kappa}}_{k_\mathrm{r},q} + \breve{\boldsymbol{\omega}}_{k_\mathrm{r},q}, \tag{5.28}$$

where $\tilde{\mathbf{\Theta}}_{k_\mathrm{r}}^0 = \sum_{l=0}^{L-1} h_l\lambda_{k_\mathrm{r}}^l\mathcal{D}(\breve{\mathbf{g}}_{0,l})\mathbf{F}_{L_\mathrm{s}}\mathbf{\Phi}_\mathrm{m} = \tilde{\mathbf{\Lambda}}_{k_\mathrm{r},0}\mathbf{F}_{L_\mathrm{s}}\mathbf{\Phi}_\mathrm{m}$ denotes the frequency-domain ISI ma-

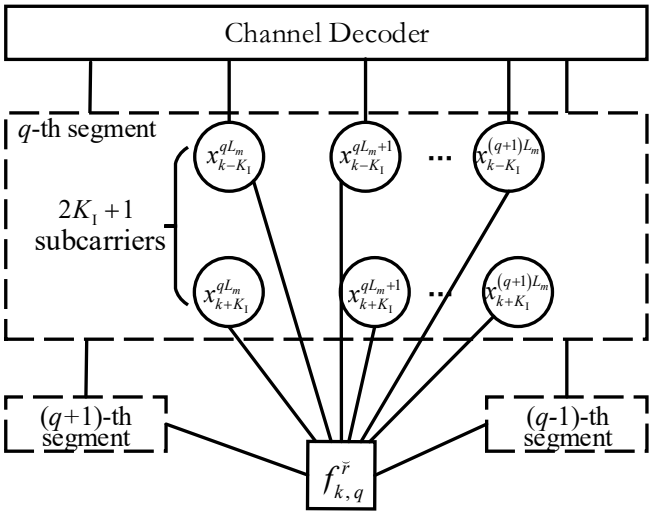


Figure 5.3: Factor graph model of FDE for MFTN-IM signaling

trix, $\tilde{\mathbf{\Lambda}}_{k_\mathrm{r},0} = \sum_{l=0}^{L-1} h_l \lambda_{k_\mathrm{r}}^l \mathcal{D}(\breve{\mathbf{g}}_{0,l})$, $\breve{\boldsymbol{\kappa}}_{k_\mathrm{r},q} = \mathbf{F}_{L_\mathrm{s}} \boldsymbol{\kappa}_{k_\mathrm{r},q}$ denotes the frequency-domain interference matrix, $\breve{\boldsymbol{\omega}}_{k_\mathrm{r},q} = \mathbf{F}_{L_\mathrm{s}} \boldsymbol{\omega}_{k_\mathrm{r},q}$ is the equivalent noise vector satisfying $\mathcal{CN}(\breve{\boldsymbol{\omega}}_{k_\mathrm{r},q}; 0, \gamma_{\breve{\omega}}^{-1})$ (referring to **Appendix** D).

5.4.2 Factor Graph Representation

According to the frequency-domain received signal model of MFTN-IM signaling in (5.28), under the assumption of perfectly known CSI, the marginal *a posteriori* probability density function is expressed as

$$p(\mathbf{x}_{k_\mathrm{r},q}|\breve{\mathbf{r}}_{k_\mathrm{r},q}) \propto p(\breve{\mathbf{r}}_{k_\mathrm{r},q}|\mathbf{x}_{k_\mathrm{r}-K_\mathrm{I},q}, \cdots, \mathbf{x}_{k_\mathrm{r}+K_\mathrm{I},q}, \breve{\boldsymbol{\kappa}}_{k_\mathrm{r},q}) \prod_{q' \in \mathcal{I}_1^q} \prod_{k \in \mathcal{I}_{K_\mathrm{I}}^{k_\mathrm{r}}} p(\mathbf{x}_{k,q'}), \tag{5.29}$$

where $p(\breve{\mathbf{r}}_{k_\mathrm{r},q}|\mathbf{x}_{k_\mathrm{r}-K_\mathrm{I},q}, \cdots, \mathbf{x}_{k_\mathrm{r}+K_\mathrm{I},q}, \breve{\boldsymbol{\kappa}}_{k_\mathrm{r},q})$ is the likelihood function, $p(\mathbf{x}_{k,q})$ denotes the *a poriori* probability density function of $\mathbf{x}_{k,q}$. Based on the factorization in (5.29), a scalar factor graph is constructed in Fig. 5.3[5]. The factor node $f_{k,q}^{\breve{r}}$ represents the likelihood function $p(\breve{\mathbf{r}}_{k,q}|\mathbf{x}_{k-K_\mathrm{I},q}, \cdots, \mathbf{x}_{k+K_\mathrm{I},q}, \breve{\boldsymbol{\kappa}}_{k,q})$. Observe that the factor model contains dense short cycles, easily resulting in the divergence of typical BP algorithm.

In the iterative receiver, assuming that the estimates $\hat{\mathbf{x}}_{k,q}(i-1)$ of the transmitted symbols in the $(i-1)$-th iteration is available, the frequency-domain interference estimates of the k_r-th

[5]For brevity, the subscript n of $x_{k,n}$ is replaced by the superscript in Fig. 5.3, while the following sections still exploit the subscript, i.e., $x_{k,n}$.

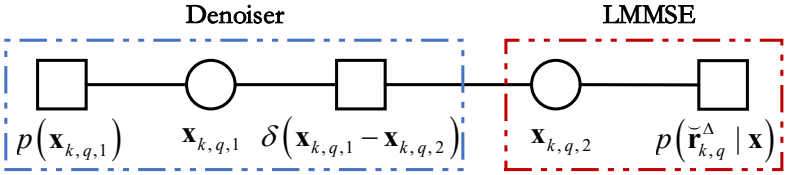


Figure 5.4: Vector factor graph model of FDE combined with interference mitigation for MFTN-IM signaling

subcarrier in the q-th segment is computed as

$$\begin{aligned}\hat{\breve{\boldsymbol{\kappa}}}_{k_{\mathrm{r}},q} &= \mathbf{F}_{L_{\mathrm{s}}}(\hat{\mathbf{z}}_{k_{\mathrm{r}},q}^{\mathrm{ici}}+\hat{\mathbf{z}}_{k_{\mathrm{r}},q-1}^{\mathrm{tail}}+\hat{\mathbf{z}}_{k_{\mathrm{r}},q+1}^{\mathrm{head}}) \\ &= \mathbf{F}_{L_{\mathrm{s}}}(\sum_{k\in\mathcal{I}_{K_{\mathrm{I}}\setminus k_{\mathrm{r}}}}\boldsymbol{\Theta}_{k,q}^{k_{\Delta}}\hat{\mathbf{x}}_{k,q}+\boldsymbol{\Xi}_{\mathrm{t}}\prod_{k\in\mathcal{I}_{K_{\mathrm{I}}}^{k_{\mathrm{r}}}}\boldsymbol{\Theta}_{k,q-1}^{k_{\Delta}}\hat{\mathbf{x}}_{k,q-1}+\boldsymbol{\Xi}_{\mathrm{h}}\prod_{k\in\mathcal{I}_{K_{\mathrm{I}}}^{k_{\mathrm{r}}}}\boldsymbol{\Theta}_{k,q+1}^{k_{\Delta}}\hat{\mathbf{x}}_{k,q+1}).\end{aligned} \tag{5.30}$$

The estimate $\hat{\breve{\boldsymbol{\kappa}}}_{k_{\mathrm{r}},q}$ is used to mitigate the frequency-domain interferences in (5.28) and then the received signal is given by

$$\breve{\mathbf{r}}_{k_{\mathrm{r}},q}^{\Delta}=\breve{\mathbf{r}}_{k_{\mathrm{r}},q}-\hat{\breve{\boldsymbol{\kappa}}}_{k_{\mathrm{r}},q}=\tilde{\boldsymbol{\Theta}}_{k_{\mathrm{r}}}^{0}\mathbf{x}_{k_{\mathrm{r}},q}+\breve{\boldsymbol{\kappa}}_{k_{\mathrm{r}},q}^{\Delta}+\breve{\boldsymbol{\omega}}_{k_{\mathrm{r}},q}. \tag{5.31}$$

The residual frequency-domain interference $\breve{\boldsymbol{\kappa}}_{k_{\mathrm{r}},q}^{\Delta}$ is ignored and $\mathbf{x}_{k_{\mathrm{r}},q}$ is decomposed into two variables $\mathbf{x}_{k_{\mathrm{r}},q,1}$ and $\mathbf{x}_{k_{\mathrm{r}},q,2}$, satisfying $\delta(\mathbf{x}_{k_{\mathrm{r}},q,1}-\mathbf{x}_{k_{\mathrm{r}},q,2})$. Then, the marginal *a posteriori* probability density function is reformulated as

$$p(\mathbf{x}_{k_{\mathrm{r}},q}|\breve{\mathbf{r}}_{k_{\mathrm{r}},q}^{\Delta})\propto p(\breve{\mathbf{r}}_{k_{\mathrm{r}},q}^{\Delta}|\mathbf{x}_{k_{\mathrm{r}},q})p(\mathbf{x}_{k_{\mathrm{r}},q,1})\delta(\mathbf{x}_{k_{\mathrm{r}},q,1}-\mathbf{x}_{k_{\mathrm{r}},q,2}). \tag{5.32}$$

According to (5.32), a cycle-free vector factor graph is constructed in Fig. 5.4. Similarly, the VAMP rules [52] is exploited to derive the message passing expressions between the variable nodes and the factor nodes.

5.4.3 Message Updating of VAMP-FDE

The *a priori* distribution of the transmitted symbol vector in the i_{e}-th external iteration can be updated according to (5.7)-(5.9). Similar to the message updating in (5.10)-(5.12), the marginal *a posteriori* distribution of $\mathbf{x}_{k,q,1}$ satisfies $b(\mathbf{x}_{k,q,1})\propto\mathcal{CN}(\mathbf{x}_{k,q,1};\hat{\mathbf{x}}_{k,q,1}(i),\eta_{k,q,1}^{-1}(i)\mathbf{I}_{L_{\mathrm{m}}})$ in the denoiser. Among them, the *a posteriori* mean vector and variance of $\mathbf{x}_{k,q,1}$ are derived as

$$\hat{\mathbf{x}}_{k,q,1}(i)=\frac{\int\mathbf{x}_{k,q,1}p(\mathbf{x}_{k,q,1})p^{\uparrow}(\mathbf{x}_{k,q,1})d\mathbf{x}_{k,q,1}}{\int p(\mathbf{x}_{k,q,1})p^{\uparrow}(\mathbf{x}_{k,q,1})d\mathbf{x}_{k,q,1}}, \tag{5.33}$$

$$\eta_{k,q,1}^{-1}(i)=\frac{\mathbf{1}_{L_{\mathrm{m}}}^{T}\int|\mathbf{x}_{k,q,1}-\hat{\mathbf{x}}_{k,q,1}(i)|^{2}p(\mathbf{x}_{k,q,1})p^{\uparrow}(\mathbf{x}_{k,q,1})d\mathbf{x}_{k,q,1}}{L_{\mathrm{m}}\int p(\mathbf{x}_{k,q,1})p^{\uparrow}(\mathbf{x}_{k,q,1})d\mathbf{x}_{k,q,1}}. \tag{5.34}$$

where $p^{\uparrow}(\mathbf{x}_{k,q,1}) = \mathcal{CN}(\mathbf{x}_{k,q,1}; \mathbf{r}_{k,q,1}(i), \gamma_{k,q,1}^{-1}(i)\mathbf{I}_{L_\mathrm{m}})$. Accordingly, the message passing from the factor node $\delta(\mathbf{x}_{k,q,1} - \mathbf{x}_{k,q,2})$ to the variable node $\mathbf{x}_{k,q,2}$ is updated as $\mu_{\delta \to \mathbf{x}_{k,q,2}}(\mathbf{x}_{k,q,2}) \propto \mathcal{CN}(\mathbf{x}_{k,q,2}; \mathbf{r}_{k,q,2}(i), \gamma_{k,q,2}^{-1}(i)\mathbf{I}_{L_\mathrm{m}})$. The precision $\gamma_{k,q,2}(i)$ and mean vector $\mathbf{r}_{k,q,2}(i)$ are calculated as

$$\gamma_{k,q,2}(i) = \eta_{k,q,1}(i) - \gamma_{k,q,1}(i), \tag{5.35}$$

$$\mathbf{r}_{k,q,2}(i) = (\eta_{k,q,1}(i)\hat{\mathbf{x}}_{k,q,1}(i) - \gamma_{k,q,1}(i)\mathbf{r}_{k,q,1}(i))/\gamma_{k,q,2}(i). \tag{5.36}$$

In the LMMSE estimator, the marginal *a posteriori* distribution is derived as

$$\begin{aligned} b(\mathbf{x}_2) &\propto \mathcal{CN}(\mathbf{x}_{k,q,2}; \mathbf{r}_{k,q,2}(i), \gamma_{k,q,2}^{-1}(i)\mathbf{I}_{L_\mathrm{m}})\mathcal{CN}(\breve{\mathbf{r}}_{k,q}^{\Delta}; \tilde{\mathbf{\Theta}}_k^0 \mathbf{x}_{k,q,2}, \gamma_{\breve{\omega}}^{-1}) \\ &\propto \mathcal{CN}(\mathbf{x}_{k,q,2}; \hat{\mathbf{x}}_{k,q,2}(i), \eta_{k,q,2}^{-1}(i)\mathbf{I}_{L_\mathrm{m}}), \end{aligned} \tag{5.37}$$

with

$$\hat{\mathbf{x}}_{k,q,2}(i) = \big(\gamma_{\breve{\omega}}(\tilde{\mathbf{\Theta}}_k^0)^H \tilde{\mathbf{\Theta}}_k^0 + \gamma_2(i)\mathbf{I}_{L_\mathrm{m}}\big)^{-1}\big(\gamma_{\breve{\omega}}(\tilde{\mathbf{\Theta}}_k^0)^H \breve{\mathbf{r}}_{k,q}^{\Delta} + \gamma_{k,q,2}(i)\mathbf{r}_{k,q,2}(i)\big), \tag{5.38}$$

$$\eta_{k,q,2}^{-1}(i) = \frac{1}{L_\mathrm{m}}\mathrm{tr}\big[\big(\gamma_{\breve{\omega}}(\tilde{\mathbf{\Theta}}_k^0)^H \tilde{\mathbf{\Theta}}_k^0 + \gamma_{k,q,2}(i)\mathbf{I}_{L_\mathrm{m}}\big)^{-1}\big]. \tag{5.39}$$

Then the matrix inversion operation in (5.38) and (5.39) can be simplified as

$$\begin{aligned} \mathbf{D}_{k,q,2}(i) &= \big(\gamma_{\breve{\omega}}(\tilde{\mathbf{\Theta}}_k^0)^H \tilde{\mathbf{\Theta}}_k^0 + \gamma_{k,q,2}(i)\mathbf{I}_{L_\mathrm{m}}\big)^{-1} \\ &= \big(\mathbf{\Phi}_\mathrm{m}^H \mathbf{F}_{L_\mathrm{s}}^H (\gamma_{\breve{\omega}}\tilde{\mathbf{\Lambda}}_{k,0}^H \tilde{\mathbf{\Lambda}}_{k,0} + \gamma_{k,q,2}(i)\mathbf{I}_{L_\mathrm{s}})\mathbf{F}_{L_\mathrm{s}}\mathbf{\Phi}_\mathrm{m}\big)^{-1} \\ &= \mathbf{\Phi}_\mathrm{m}^H \mathbf{F}_{L_\mathrm{s}}^H (\gamma_{\breve{\omega}}\tilde{\mathbf{\Lambda}}_{k,0}^H \tilde{\mathbf{\Lambda}}_{k,0} + \gamma_{k,q,2}(i)\mathbf{I}_{L_\mathrm{s}})^{-1}\mathbf{F}_{L_\mathrm{s}}\mathbf{\Phi}_\mathrm{m}. \end{aligned} \tag{5.40}$$

Hence, the *a posteriori* mean vector and variance of $\mathbf{x}_{k,q,2}$ are derived as

$$\hat{\mathbf{x}}_{k,q,2}(i) = \mathbf{D}_{k,q,2}(i)\big[\gamma_{\breve{\omega}}\mathbf{\Phi}_\mathrm{m}^H \mathbf{F}_{L_\mathrm{s}}^H \tilde{\mathbf{\Lambda}}_{k,0}^H \breve{\mathbf{r}}_{k,q}^{\Delta} + \gamma_{k,q,2}(i)\mathbf{r}_{k,q,2}(i)\big], \tag{5.41}$$

$$\eta_{k,q,2}^{-1}(i) = \frac{1}{L_\mathrm{m}}\mathrm{tr}(\mathbf{D}_{k,q,2}(i)). \tag{5.42}$$

Similarly, the message passing from the factor node $\delta(\mathbf{x}_{k,q,1} - \mathbf{x}_{k,q,2})$ to the variable node $\mathbf{x}_{k,q,1}$ is updated as $\mu_{\mathbf{x}_{k,q,1} \to \delta}(\mathbf{x}_{k,q,1}) \propto \mathcal{CN}(\mathbf{x}_{k,q,1}; \mathbf{r}_{k,q,1}(i+1), \gamma_{k,q,1}^{-1}(i+1)\mathbf{I}_{L_\mathrm{m}})$, where the precision and mean vector are calculated as

$$\gamma_{k,q,1}(i+1) = \eta_{k,q,2}(i) - \gamma_{k,q,2}(i), \tag{5.43}$$

$$\mathbf{r}_{k,q,1}(i+1) = (\eta_{k,q,2}(i)\hat{\mathbf{x}}_{k,q,2}(i) - \gamma_{k,q,2}(i)\mathbf{r}_{k,q,2}(i))/\gamma_{k,q,1}(i). \tag{5.44}$$

According to the aforementioned derivations, the proposed VAMP-based FDE combined with interference mitigation algorithm is summarized as **Algorithm** 8.

Algorithm 8 VAMP-FDE Algorithm Combined With Interference Mitigation for MFTN-IM Signaling

Initialization: The output LLR of the channel decoder is initialized as $L_{\mathrm{dec}}^{\mathrm{e},(1)}(c_{g,p_{\mathrm{g}}}) = 0$, where $g \in \{0, 1, \cdots, G-1\}$, $p_{\mathrm{g}} \in \{0, 1, \cdots, P_{\mathrm{g}}-1\}$. Compute the *a priori* distribution of the transmitted symbol vector $\mathbf{x}$. The message passing from the factor node $\delta(\mathbf{x}_{k,q,1} - \mathbf{x}_{k,q,2})$ to the variable node $\mathbf{x}_{k,q,1}$ is initialized as $\mathcal{CN}(\mathbf{x}_{k,q,1}; \mathbf{r}_{k,q,1}(1), \gamma_{k,q,1}^{-1}(1)\mathbf{I}_{L_{\mathrm{m}}})$, where $\mathbf{r}_{k,q,1}(1) = \mathbf{0}_{L_{\mathrm{m}}}$ and $\gamma_{k,q,1}(1) = 0$.
for $i_{\mathrm{e}} = 1$ to I_{e} **do**
  for $i = 1$ to I_{in} **do**
    for $q = 0$ to $L_{\mathrm{q}} - 1$ **do**
      for $k = 0$ to $K - 1$ **do**
        Compute the frequency-domain received signal using L_{s}-point FFT according to (5.28);
        Compute the frequency-domain interference estimate $\hat{\tilde{\boldsymbol{\kappa}}}_{k,q}$ according to (5.30);
        Mitigate the frequency-domain interferences according to (5.31);
        Compute the *a posterori* mean vector $\hat{\mathbf{x}}_{k,q,1}(i)$ and variance $\eta_{k,q,1}^{-1}(i)$ of $\mathbf{x}_{k,q,1}$ according to (5.33) and (5.34);
        Compute the message $\mu_{\delta \to \mathbf{x}_{k,q,2}}(\mathbf{x}_{k,q,2}) \propto \mathcal{CN}(\mathbf{x}_{k,q,2}; \mathbf{r}_{k,q,2}(i), \gamma_{k,q,2}^{-1}(i)\mathbf{I}_{L_{\mathrm{m}}})$ passing from the factor node $\delta(\mathbf{x}_{k,q,1} - \mathbf{x}_{k,q,2})$ to the variable node $\mathbf{x}_{k,q,2}$ according to (5.35) and (5.36);
        Compute the *a posterori* mean vector $\hat{\mathbf{x}}_{k,q,2}(i)$ and variance $\eta_{k,q,2}^{-1}(i)$ of $\mathbf{x}_{k,q,2}$ according to (5.41) and (5.42);
        Compute the message $\mu_{\delta \to \mathbf{x}_{k,q,1}}(\mathbf{x}_{k,q,1}) \propto \mathcal{CN}(\mathbf{x}_{k,q,1}; \mathbf{r}_{k,q,1}(i+1), \gamma_{k,q,1}^{-1}(i+1)\mathbf{I}_{L_{\mathrm{m}}})$ passing from the factor node $\delta(\mathbf{x}_{k,q,1} - \mathbf{x}_{k,q,2})$ to the variable node $\mathbf{x}_{k,q,1}$ according to (5.43) and (5.44);
      end for
    end for
  end for
  Compute the output LLR of the equalizer according to the mean vector $\mathbf{r}_{k,q,1}(I_{\mathrm{in}}+1)$ and variance $\gamma_{k,q,1}^{-1}(I_{\mathrm{in}}+1)$ [88], and then feed then to the channel decoder;
  Perform BCJR channel decoding and feed the output LLR of the channel decoder to the equalizer. Update the *a priori* probability of the transmitted symbol vector according to (5.7)-(5.9).
end for

5.5 Complexity Analysis and Simulation Results

5.5.1 Complexity Analysis

In this section, both of the proposed VAMP-TDE and VAMP-FDE algorithms are analyzed and then compared to the extended iterative equalization algorithms, which are summarized in TABLE 5.1. Since all algorithms employ the standard BCJR-based channel decoding algorithms, this section only discusses the computational complexity of the equalizer in each iteration.By introducing the extended constellation set, MMSE-TDE[152], GAMP-TDE[48], and GAMP-FDE[158] have been extended for MFTN-IM signaling.

The complexity of MMSE-TDE algorithm is dominated by the inversion of the equivalent channel matrix, having a complexity order of $\mathcal{O}(N_{\mathrm{s}}^3)$. For MFTN-IM signaling, the product of an $N_{\mathrm{s}} \times N_{\mathrm{s}}$ matrix and an N_{s} vector is calculated in the GAMP-TDE algorithm, resulting in a complexity order of $\mathcal{O}(N_{\mathrm{s}}^2)$. In [48], the complexity of GAMP-FDE depends on the complex multiplications and IFFT/FFT operations. The complexity of the former is $\mathcal{O}(L_{\mathrm{q}}K^2L_{\mathrm{s}}^2)$, while that of the latter is $\mathcal{O}((2L+3)L_{\mathrm{q}}KL_{\mathrm{s}}\log(KL_{\mathrm{s}}))$. In the proposed VAMP-TDE algorithm, the inversion of an $N_{\mathrm{s}} \times N_{\mathrm{s}}$ matrix is computed in (5.17) and (5.18), having a complexity order of $\mathcal{O}(N_{\mathrm{s}}^3)$. To reduce the computational complexity, the VAMP-FDE algorithm employs the proposed subcarrier-based segment-wise detection model. Through reconstructing the frequency-domain interference matrix, the inversion of a general matrix is simplified into the inversion of a diagonal matrix. For the detection of each subcarrier, only the complex multiplications of an $L_{\mathrm{s}} \times L_{\mathrm{s}}$ matrix and an L_{s} vector or of two L_{s} diagonal matrices are computed in the VAMP-FDE algorithm. Accordingly, the complexity is $\mathcal{O}(L_{\mathrm{s}})$. Moreover, (5.28) and (5.40)-(5.43) require four L_{s}-point IFFT/FFT operations in the VAMP-FDE algorithm, having a complexity order of $\mathcal{O}(4L_{\mathrm{s}}\log L_{\mathrm{s}})$.

Table 5.1: Complexity Analysis of Equalization of MFTN-IM Signaling

Algorithm	Complexity	
	Multiplication	IFFT/FFT Operations
MMSE-TDE	$\mathcal{O}(N_{\mathrm{s}}^3)$	NA
GAMP-TDE	$\mathcal{O}(N_{\mathrm{s}}^2)$	NA
VAMP-TDE	$\mathcal{O}(N_{\mathrm{s}}^3)$	NA
GAMP-FDE	$\mathcal{O}(L_{\mathrm{q}}K^2L_{\mathrm{s}}^2)$	$\mathcal{O}((2L+3)L_{\mathrm{q}}KL_{\mathrm{s}}\log(KL_{\mathrm{s}}))$
VAMP-FDE	$\mathcal{O}(L_{\mathrm{q}}KL_{\mathrm{s}})$	$\mathcal{O}(4L_{\mathrm{q}}KL_{\mathrm{s}}\log L_{\mathrm{s}})$

NA stands for "not applicable"

5.5.2 Simulation Results

To highlight the effectiveness of the novel MFTN-IM signaling, this section provides the BER performance comparison of different waveforms in the following. Furthermore, the proposed VAMP-based equalization algorithms for MFTN-IM signaling will be compared to the exist-

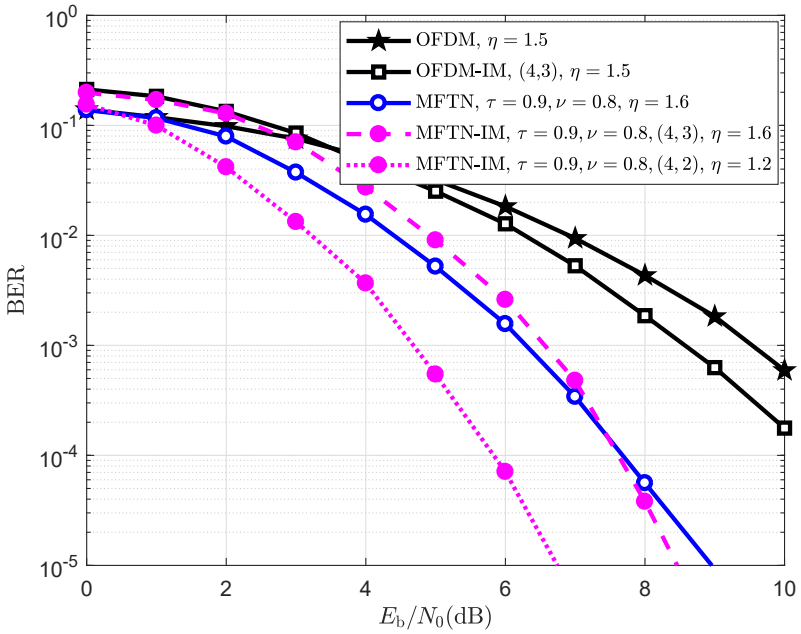


Figure 5.5: BER performance of different waveforms.

ing algorithms in terms of BER performance. The simulation configurations are described as follows.

The LDPC code has a length of $N_c = 4032$ and a code rate of $R_c = 3/4$; QPSK modulation is used with Gary mapping; the RRC pulse shaping has a roll-off factor of $\beta = 0.3$. The number of subcarriers is $K = 64$ (including one null DC subcarrier) and the number of symbols per subcarrier is $N = 512$. For each IM subblock, K_a out of K_g subcarriers are activated, which is represented as (K_g, K_a) in figure legends. In the subcarrier-based segment-wise detection model, the length of each segment is set to $L_m = 42$. The truncated lengths of the time-domain and frequency-domain interferences are $N_I = 12$ and $K_I = 1$, respectively. Considering a multipath channel having $L = 8$ taps, the coefficient of the l-th tap obeys the Gaussian distribution, i.e., $h_l \propto \mathcal{CN}(h_l; 0, 1/L)$[6]. In addition, the number of iterations between the equalizer and channel decoder is $I_e = 50$ and the maximum number of LDPC decoding iterations is $I_c = 5$.

The BER performance of the conceived MFTN-IM signaling is compared to those of OFDM[159], OFDM-IM[44], and MFTN[31] signaling in a multipath channel, as shown in Fig. 5.5. All MFTN-based schemes employ RRC shaping pulses, while OFDM signaling exploits the rectangular shaping pulse, i.e., $\beta = 0$. Two OFDM-based waveforms have the same spectral efficiency. Compared to OFDM signaling, OFDM-IM can obtain a significant BER performance gain in the high E_b/N_0 region. This is because the implicit transmission of OFDM-IM signaling can effectively circumvent the negative impact of frequency-selective properties of multipath channels on a portion of index bits. The conclusion is also verified in non-orthogonal systems.

[6]A quasi-static frequency-selective channel model is considered. The channel coefficients are fixed for each Monte Carlo simulation, while they vary according to the channel model for different Monte Carlo simulations.

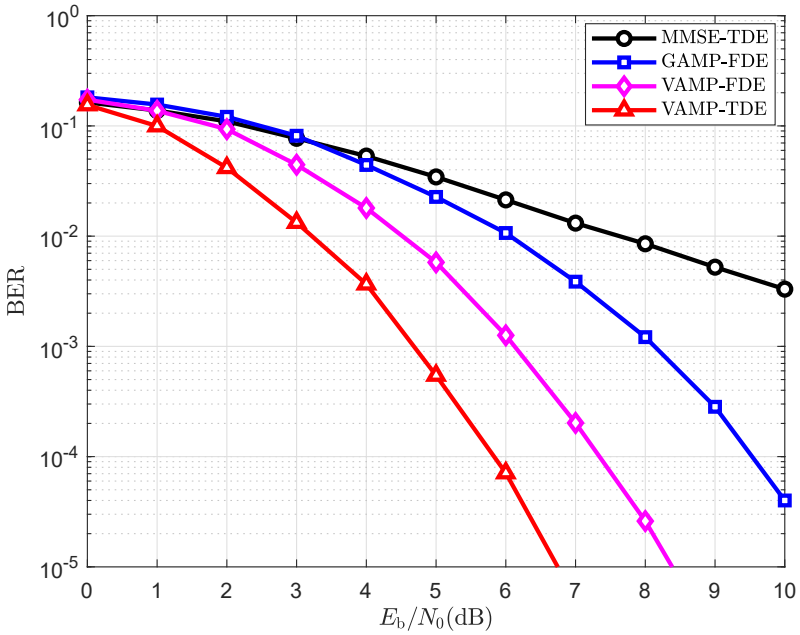


Figure 5.6: BER performance of different equalization algorithms for MFTN-IM signaling with $(K_g, K_a) = (4, 2)$.

Observe that MFTN-IM signaling with $(K_g, K_a) = (4, 3)$ can achieve about 0.5 dB E_b/N_0 gain at BER $= 10^{-5}$, compared to the MFTN counterpart with the same spectral efficiency. Due to time-frequency packing, MFTN-IM waveform with an appropriate configuration outperforms OFDM-IM waveform in terms of the spectral efficiency and BER performance. Moreover, the novel non-orthogonal waveform provides a more flexible transmission scheme. The BER performance of MFTN-IM signaling can be significantly improved at the cost of a certain spectral efficiency. When the number of the activated subcarriers further decreases, i.e., $(K_g, K_a) = (4, 2)$, the E_b/N_0 gain of MFTN-IM signaling increases up to 4 dB at BER $= 10^{-3}$, compared to OFDM-IM signaling.

In Fig. 5.6 and Fig. 5.7, the BER performance of MFTN-IM signaling is evaluated using different iterative equalization algorithms. The IM parameters are set to $(K_g, K_a) = (4, 2)$ and $(K_g, K_a) = (4, 3)$, respectively. Since the GAMP-FDE algorithm employs the segment-wise frequency-domain received signal model to improve the robustness of equalization to the small perturbations, it outperforms MMSE-TDE algorithm in terms of BER performance. It has been verified that the VAMP algorithm has better convergence than GAMP algorithm[52]. Therefore, the proposed VAMP-based equalization algorithms can further improve the BER performance of MFTN-IM signaling. To reduce the computational complexity, VAMP-FDE exploits the subcarrier-based segment-wise detection model and ignores the estimation accuracy of ICI and the interferences imposed by adjacent segments. Both of them lead to an additional BER performance loss. As shown in In Fig. 5.6, VAMP-FDE suffers from about 1.5 dB E_b/N_0 loss at BER $= 10^{-5}$ compared to VAMP-TDE. When the number of the activated subcarriers K_a increases, the interference suppression ability of the inactivated subcarriers

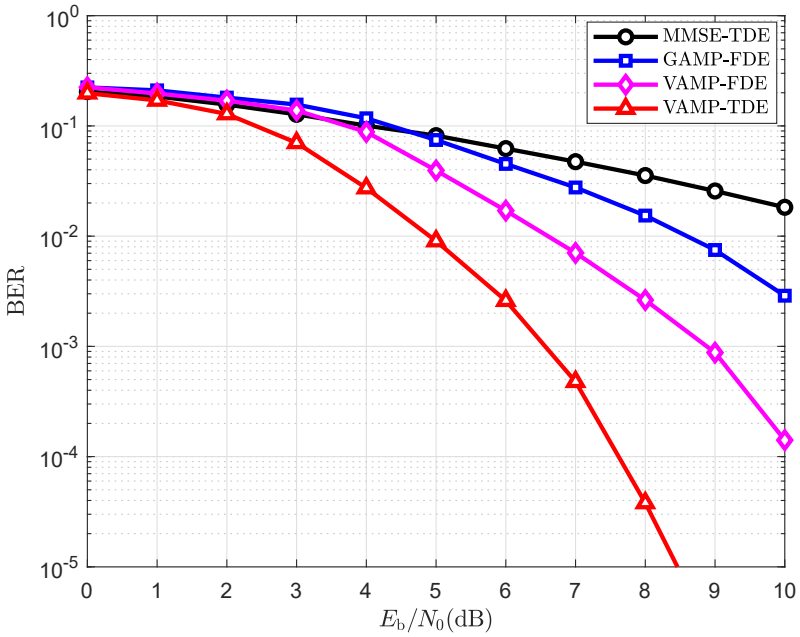


Figure 5.7: BER performance of different equalization algorithms for MFTN-IM signaling with $(K_g, K_a) = (4, 3)$.

is weakened. This results in a larger BER performance gap between VAMP-TDE and VAMP-FDE algorithms. In conclusion, the proposed VAMP-TDE algorithm has the advantage of BER performance, while the proposed VAMP-FDE algorithm can make a flexible compromise between BER performance and computational complexity.

The BER performance of MFTN-IM systems with various time-frequency packing factors is depicted in Fig. 5.8. The proposed VAMP-TDE algorithm has been employed and the IM parameters are $(K_g, K_a) = (4, 2)$. When the packing factor combination varies from $\tau = 1.0, \nu = 1.0$ to $\tau = 0.9, \nu = 0.8$, MFTN-IM signaling can increase the transmission rate by more than 39%. Regards to the demodulation performance, the E_b/N_0 loss of non-orthogonal waveform is only about 0.8 dB at BER = 10^{-5}. When the time-domain or frequency-domain packing factor further decreases, i.e., $\tau = 0.8, \nu = 0.8$ or $\tau = 0.9, \nu = 0.7$, the inherent interferences imposed by non-orthogonal transmission become severer, which results in more serious BER performance degradation. Compared to the counterpart with $\tau = 0.9, \nu = 0.8$, both of MFTN-IM systems with $\tau = 0.8, \nu = 0.8$ and $\tau = 0.9, \nu = 0.7$ suffer from 1.6 dB E_b/N_0 loss at BER = 10^{-5}. For a fixed spectral efficiency of MFTN-IM systems employing RRC shaping pulse, such as $\tau = 0.9, \nu = 0.7$ and $\tau = 0.7, \nu = 0.9$, the energy of the ISIs induced by the reduction of time-domain packing factor is much larger than that of the ICIs due to the frequency-domain compression. Hence, the MFTN-IM system with $\tau = 0.9, \nu = 0.7$ is superior to the case using $\tau = 0.7, \nu = 0.9$ in terms of BER performance. In practice, the BER performance of MFTN-IM signaling can be significantly improved through jointly optimizing the combination of the packing factors.

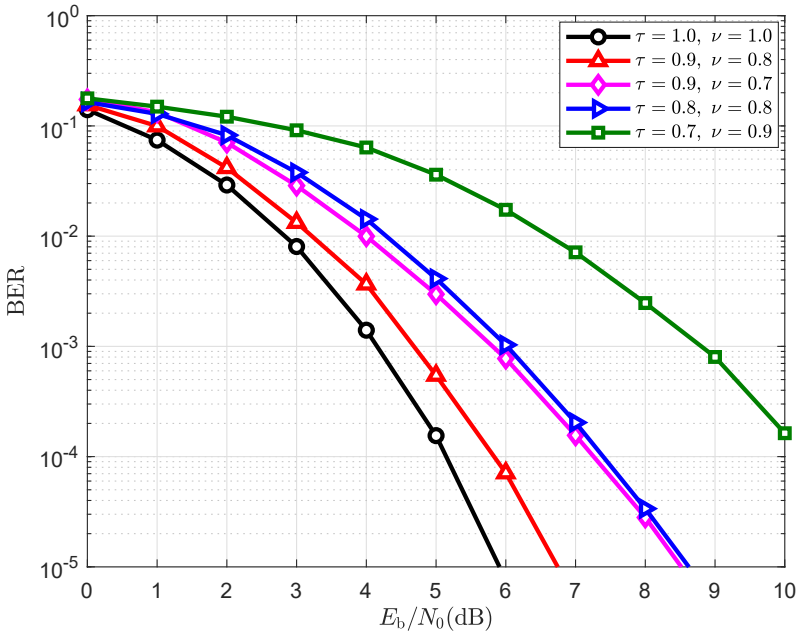


Figure 5.8: Impact of the packing factors on BER performance of MFTN-IM signaling.

For MFTN signaling, the spectral efficiency[7] can be continuously increased by selecting the channel coding rate and time-frequency packing factors. In addition, MFTN-IM signaling can also achieve a flexible compromise between spectral efficiency and BER performance by optimizing IM parameters, i.e., choosing a reasonable configuration of (K_g, K_a). Fig. 5.9 compares the BER performance of Nyquist signaling, MFTN signaling, and MFTN-IM signaling under the assumption of the same spectral efficiency. In the case of $\tau = 1.0, \nu = 1.0$, MFTN-based signaling is equivalent to Nyquist signaling, which is no longer affected by the two-dimensional inherent interferences. It is seen that MFTN-based signaling can achieve a better BER performance than Nyquist signaling by reducing the code rate R_c. For example, compared to the Nyquist-based counterpart, the E_b/N_0 gain of MFTN signaling is about 0.5 dB at BER = 10^{-5}. For MFTN-IM signaling, the reduction of the number of the activated subcarriers can also remarkably improve the BER performance. Compared to the case that two subcarriers are activated in each IM subblock, even if the time-frequency packing factors are decreased, the MFTN-IM scheme with only one activated subcarrier can also obtain about 2.1 dB E_b/N_0 gain at BER = 10^{-4}. This benefits from a large number of the inactivated subcarriers, which not only reduce the two-dimensional inherent interferences, but also improve the ability of MFTN-IM signaling to resist channel frequency-selective fading. Compared to the typical physical waveforms, MFTN-IM signaling can be flexibly designed in multiple dimensions to improve spectral efficiency and optimize demodulation performance. This is beneficial to adapt to complex transmission environment and meet heterogeneous communication requirements.

[7]The spectral efficiency of MFTN signaling is calculated as $\eta = R_c \log_2 M/[\tau\nu(1+\beta)]$. Moreover, the spectral efficiency of MFTN-IM signaling is computed as $\eta = R_c(K_a \log_2 M + \lfloor \log_2 \binom{K_g}{K_a} \rfloor)/[K_g\tau\nu(1+\beta)]$.

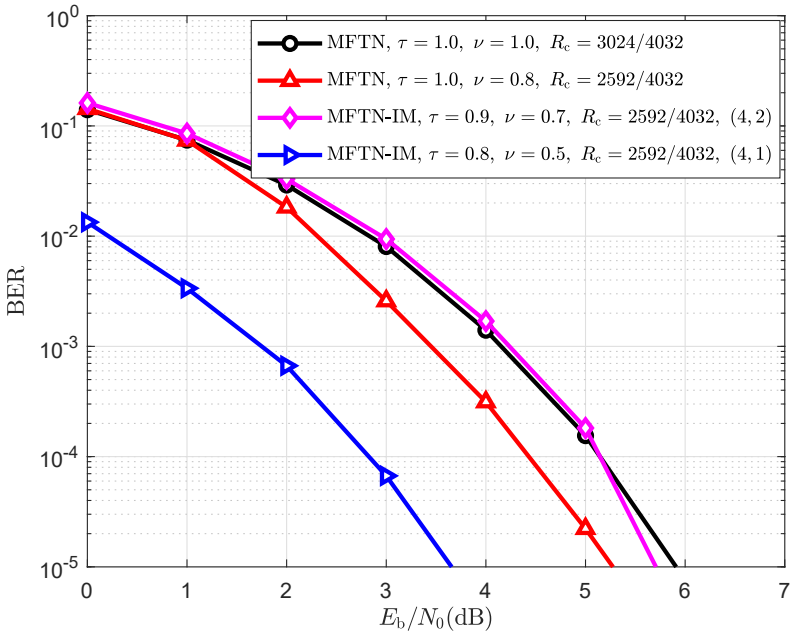


Figure 5.9: Impact of various combinations of packing factors and code rate on BER performance of MFTN-IM signaling.

5.6 Conclusion

In this paper, a novel combination of MFTN signaing and IM was designed for high spectral and energy efficiency. To fully benefit from the combination, a pair of VAMP-based iterative equalization algorithms were developed in the perfectly known CSI scenarios. Based on the time-domain received signal model, the VAMP-TDE algorithm was derived for mitigating the impact of the ill-conditioned problem on demodulation performance. To suppress the computationally heavy high-dimensional matrix inversion, a low-complexity VAMP-FDE algorithm was developed by reformulating a subcarrier-based segment-wise frequency-domain received signal model having low-dimensional matrices. In this model, the equivalent channel matrix in the frequency domain can be reconstructed as the product of a diagonal and a normalized DFT matrices. Consequently, the matrix inversion of the VAMP-based algorithm can be simplified into the inversion of a diagonal matrix, which significantly reduces the computational complexity of MFTN-IM receivers. Finally, the BER performance of the proposed VAMP-TDE and VAMP-FDE algorithms was evaluated in multipath channels and compared to those of the existing algorithms, for verifying the superiority of the novel schemes. Simulation results also demonstrated that the VAMP-TDE algorithm performed better with respect to BER performance, and the VAMP-FDE algorithm can make a flexible tradeoff between BER performance and computational complexity.

Chapter 6

Conclusions and Future Work

6.1 Summary of Outcomes

In this thesis, various low-complexity iterative receivers of non-orthogonal multi-carrier signaling have been comprehensively and systematically studied under the assumption of frequency-selective fading channel. In the framework of statistical signal processing and parameter estimation theory, this work proposed a hybrid message passing receiver for one-dimensional frequency-domain packing SEFDM signaling, a PBiGAMP-based frequency-domain iterative receiver for two-dimensional time-frequency packing MFTN signaling, and a pair of iterative equalization for index-modulated MFTN signaling. Specifically, the main contributions and innovative research results of this thesis are summarized as follows.

1. A joint channel estimation and equalization algorithm relying on hybrid message passing rules was proposed for SEFDM-IM signaling, for solving the low-complexity receiving problem of one-dimensional non-orthogonal multi-carrier signals over unknown frequency-selective fading channel. An extended constellation set was introduced for uniformly characterizing the activated and inactivated subcarriers. Based on the truncated interference model and the colored noise approximation using the CAR model, the received signal model was reformulated into a linear state space model and then the corresponding Forney-style factor graph was constructed. Through establishing the connection of multi-layer factor graph, the error propagation problem of channel estimation was overcome. To minimize the Gaussian approximation error of discrete *a priori* distribution, the EP algorithm was introduced for updating the forward messages of the transmitted symbols. According to GMP rules, the forward and backward message updating expressions were derived on factor graph. For the intractable inner product node, the VMP algorithm was exploited for deriving parametric message updating. Therefore, a JCEE algorithm based on GMP-EP-VMP was proposed. Simulation results showed that, compared to the Nyquist-based counterpart, SEFDM-IM signaling could improve the spectral efficiency up to 25% without BER performance loss.

2. A pair of PBiGAMP-based frequency-domain joint channel estimation and equalization algorithm were proposed for MFTN signals, for solving the low-complexity receiving problem of two-dimensional non-orthogonal multi-carrier signals over unknown frequency-selective fading channel. A segment-based frequency-domain received signal model with block circulant matrices was derived for reducing the condition number of the equivalent channel matrix, then alleviating the ill-conditioning problem of non-orthogonal multi-carrier signaling. To tackle the colored noise process imposed by non-orthogonal matched filter, a diagonalization method based on matrix decomposition was developed for the covariance matrix of the frequency-domain colored noise process. Then, a PBiGAMP-based frequency-domain JCEE algorithm was developed for solving the bilinear estimation problem of the transmitted symbols and channel coefficients. Since the module square operation of PBiGAMP may increase the condition number of the equivalent channel matrix, a refined frequency-domain JCEE algorithm was derived via introducing a series of scaled identity matrices. Simulation results demonstrated that the proposed frequency-domain JCEE algorithms could effectively recover the transmitted symbols and channel coefficients in high-speed mobile scenarios.

3. A novel index-modulated non-orthogonal waveform was proposed for simultaneously enhancing spectral efficiency and energy efficiency and then both VAMP-based TDE and FDE algorithms were developed for solving the symbol detection of MFTN-IM signaling in known frequency-selective fading channel. Relying on the extended constellation set including the inactivated subcarriers, the time-domain received symbol model of the novel MFTN-IM signaling was derived in frequency-selective fading channel. Then, its robust VAMP-based TDE algorithm was developed. To deal with the high computational complexity of TDE, a subcarrier-based segment-wise frequency-domain received signal model was constructed, significantly reducing the dimension of matrix operation for message updating. Building on this, a VAMP-based FDE algorithm was designed for simplifying the matrix inversion operation into the inversion of a diagonal matrix. Moreover, the computational complexity of iterative equalization decreases from $\mathcal{O}(N_{\mathrm{s}}^3)$ of TDE to $\mathcal{O}(L_{\mathrm{s}}), L_{\mathrm{s}} \ll N_{\mathrm{s}}$ of FDE. The effectiveness of two VAMP-based iterative equalization algorithms has been verified, and MFTN-IM signaling could perform better than Nyquist signaling in terms of BER performance.

6.2 Recommendations & Future Work

The research results in this thesis have made a breakthrough in the receiver design of non-orthogonal multi-carrier signaling, which provides a theoretical reference for future research. Building on the research in this thesis, further research can be carried out from the following three aspects:

1. Joint channel estimation and equalization algorithm of MFTN-IM signaling. Chapter 3.4 only discusses iterative equalization of MFTN-IM signaling under the assumption of known channel. However, CSI is usually obtained via channel estimation in practice. There-

fore, solving the joint channel estimation and equalization of MFTN-IM signaling in unknown channels is urgent. Inspired by the researches in Chapter 3.4, the bilinear VAMP algorithm may be used to design the joint channel estimation and equalization algorithm for MFTN-IM signals based on the proposed subcarrier-based segment-wise frequency-domain received signal model. The bilinear VAMP algorithm combines the expectation maximization (EM) estimation method with VAMP algorithm, where VAMP is used to estimate the transmitted signal and EM is used to estimate the unknown channel coefficients. However, when EM algorithm is used to estimate channel coefficients, the accuracy of channel estimation is ignored, which may lead to profound demodulation performance loss due to the error propagation. Therefore, it is of great significance to study robust and efficient joint channel estimation and equalization algorithm for the popularization and application of the novel non-orthogonal waveform.

2. Low-complexity receiver design of non-orthogonal multi-carrier signaling combined with dual-mode IM. In Chapter 3.2 and Chapter 3.4, the non-orthogonal multi-carrier waveform has been combined with single-mode IM, and then the corresponding low-complexity iterative receivers have been designed in frequency-selective fading channel. The inactivated subcarriers of single-mode IM can reduce the self-interference of non-orthogonal waveform, but limits its spectral efficiency improvement. In contrast, dual-mode IM can effectively solve the limited spectral efficiency of single-mode IM. The dual-mode IM not only explicitly transmits additional information bits, but also employs different modulation modes, instead of the inactivated subcarriers of zeros. Therefore, the combination of non-orthogonal multi-carrier signaling and dual-mode IM can further improve spectral efficiency. However, the non-orthogonal multi-carrier signaling based on dual-mode IM cannot reduce the self-interference by using the inactivated subcarrier, which increases the complexity of the receiver. In addition, the ISIs and ICIs introduced by time-frequency compression may significantly increase the detection difficulty of the two modulation modes in dual-mode IM. Therefore, how to design a low-complexity receiver for combining non-orthogonal multi-carrier signal and dual-mode IM, and how to design an efficient IM modulation mode detection method are challenging research issues.

3. Low-complexity receiver design of MFTN signaling in nonlinear channel. This paper only considers low-complexity receiver design for MFTN signaling in linear channel. Compared to single-carrier signaling, MFTN signaling suffers from a higher peak-to-average power ratio, which makes it vulnerable to nonlinear distortion induced by power amplifier. Therefore, designing a low-complexity receiver is urgent for MFTN signaling in nonlinear channel. A particle filter is an efficient method to solve nonlinear problems, at the cost of high computational complexity due to a large number of particles. An alternative solution is to approximate nonlinear channel to linear channel, and then design receivers based on the existing approaches for linear channel. Only a few studies have discussed the receiver design of single-carrier FTN signaling in nonlinear channel. For MFTN signaling, the nonlinear interferences imposed by channel are tightly coupled with the two-dimensional self-interference. This dramatically increases the complexity of its receiver. In conclusion, designing low-complexity

receivers of MFTN signaling in nonlinear channel is the key to achieving reliable transmission of non-orthogonal multi-carrier signaling in practical communication systems.

6.3 Concluding Remarks

In summary, this thesis developed a series of parametric message passing receivers for multi-carrier FTN signaling over frequency-selective fading channel, for solving the intractable channel estimation and symbol detection problem of spectrally efficient non-orthogonal multi-carrier waveforms. In addition to the satellite-ground transmission link, the proposed low-complexity receivers are also applicable to generic communication systems. The research results are hoped to provide a specific valuable reference for future high-speed wireless communications.

Bibliography

[1] W. Saad, M. Bennis, and M. Chen, "A vision of 6G wireless systems: Applications, trends, technologies, and open research problems," *IEEE Network*, vol. 34, no. 3, pp. 134–142, 2020.

[2] W. Jiang, B. Han, M. A. Habibi, and H. D. Schotten, "The road towards 6G: A comprehensive survey," *IEEE Open Journal of the Communications Society*, vol. 2, pp. 334–366, 2021.

[3] Z. Gao, L. Dai, D. Mi, Z. Wang, M. A. Imran, and M. Z. Shakir, "MmWave massive-MIMO-based wireless backhaul for the 5G ultra-dense network," *IEEE Wireless Communications*, vol. 22, no. 5, pp. 13–21, 2015.

[4] S. A. Busari, K. M. S. Huq, S. Mumtaz, L. Dai, and J. Rodriguez, "Millimeter-wave massive MIMO communication for future wireless systems: A survey," *IEEE Communications Surveys & Tutorials*, vol. 20, no. 2, pp. 836–869, 2018.

[5] M. A. Albreem, M. Juntti, and S. Shahabuddin, "Massive MIMO detection techniques: A survey," *IEEE Communications Surveys & Tutorials*, vol. 21, no. 4, pp. 3109–3132, 2019.

[6] E. Arikan, "Channel polarization: A method for constructing capacity-achieving codes for symmetric binary-input memoryless channels," *IEEE Transactions on Information Theory*, vol. 55, no. 7, pp. 3051–3073, 2009.

[7] I. Tal and A. Vardy, "How to construct polar codes," *IEEE Transactions on Information Theory*, vol. 59, no. 10, pp. 6562–6582, 2013.

[8] J. Dai, K. Niu, Z. Si, C. Dong, and J. Lin, "Polar-coded non-orthogonal multiple access," *IEEE Transactions on Signal Processing*, vol. 66, no. 5, pp. 1374–1389, 2018.

[9] T. Schmidl and D. Cox, "Robust frequency and timing synchronization for OFDM," *IEEE Transactions on Communications*, vol. 45, no. 12, pp. 1613–1621, 1997.

[10] C. Y. Wong, R. Cheng, K. Lataief, and R. Murch, "Multiuser OFDM with adaptive subcarrier, bit, and power allocation," *IEEE Journal on Selected Areas in Communications*, vol. 17, no. 10, pp. 1747–1758, 1999.

[11] B. Farhang-Boroujeny and H. Moradi, "OFDM inspired waveforms for 5G," *IEEE Communications Surveys & Tutorials*, vol. 18, no. 4, pp. 2474–2492, 2016.

[12] J. G. Andrews, S. Buzzi, W. Choi, S. V. Hanly, A. Lozano, A. C. K. Soong, and J. C. Zhang, "What will 5G be?" *IEEE Journal on Selected Areas in Communications*, vol. 32, no. 6, pp. 1065–1082, 2014.

[13] Alliance N, "5G white paper," *White Paper*, vol. 39, no. 3, pp. 1–125, 2015.

[14] M. Agiwal, A. Roy, and N. Saxena, "Next generation 5G wireless networks: A comprehensive survey," *IEEE Communications Surveys & Tutorials*, vol. 18, no. 3, pp. 1617–1655, 2016.

[15] L. Dong, H. Zhao, Y. Chen, D. Chen, T. Wang, L. Lu, B. Zhang, L. Hu, L. Gu, B. Li, H. Yang, H. Shen, T. Tian, Z. Luo, and K. Wei, "Introduction on IMT-2020 5G trials in china," *IEEE Journal on Selected Areas in Communications*, vol. 35, no. 8, pp. 1849–1866, 2017.

[16] X. Chen, D. W. K. Ng, W. Yu, E. G. Larsson, N. Al-Dhahir, and R. Schober, "Massive access for 5G and beyond," *IEEE Journal on Selected Areas in Communications*, vol. 39, no. 3, pp. 615–637, 2021.

[17] X. Liu, K.-Y. Lam, F. Li, J. Zhao, L. Wang, and T. S. Durrani, "Spectrum sharing for 6G integrated satellite-terrestrial communication networks based on NOMA and CR," *IEEE Network*, vol. 35, no. 4, pp. 28–34, 2021.

[18] M. Giordani and M. Zorzi, "Non-terrestrial networks in the 6G era: Challenges and opportunities," *IEEE Network*, vol. 35, no. 2, pp. 244–251, 2021.

[19] A. Kapovits, M.-I. Corici, I.-D. Gheorghe-Pop, A. Gavras, F. Burkhardt, T. Schlichter, and S. Covaci, "Satellite communications integration with terrestrial networks," *China Communications*, vol. 15, no. 8, pp. 22–38, 2018.

[20] G. Wang, S. Zhou, S. Zhang, Z. Niu, and X. Shen, "SFC-based service provisioning for reconfigurable space-air-ground integrated networks," *IEEE Journal on Selected Areas in Communications*, vol. 38, no. 7, pp. 1478–1489, 2020.

[21] S. Chen, S. Sun, and S. Kang, "System integration of terrestrial mobile communication and satellite communication - the trends, challenges and key technologies in B5G and 6G," *China Communications*, vol. 17, no. 12, pp. 156–171, 2020.

[22] T. Zhou, Y. Zhang, B. Zhang, H. Zeng, Z. Tan, X. Zhang, L. Wang, Z. Chen, J. Cao, K. Song, and Z. Yang, "Terahertz direct modulation techniques for high-speed communication systems," *China Communications*, vol. 18, no. 5, pp. 221–244, 2021.

[23] X. Lu, S. Venkatesh, and H. Saeidi, "A review on applications of integrated terahertz systems," *China Communications*, vol. 18, no. 5, pp. 175–201, 2021.

[24] Z. Chen, C. Han, Y. Wu, L. Li, C. Huang, Z. Zhang, G. Wang, and W. Tong, "Terahertz wireless communications for 2030 and beyond: A cutting-edge frontier," *IEEE Communications Magazine*, vol. 59, no. 11, pp. 66–72, 2021.

[25] M. S. Afaqui, E. Garcia-Villegas, and E. Lopez-Aguilera, "IEEE 802.11ax: Challenges and requirements for future high efficiency WiFi," *IEEE Wireless Communications*, vol. 24, no. 3, pp. 130–137, 2017.

[26] J. E. Mazo, "Faster-than-Nyquist signaling," *Bell System Technical Journal*, vol. 54, no. 8, pp. 1451–1462, 1975.

[27] T. Ishihara, S. Sugiura, and L. Hanzo, "The evolution of faster-than-Nyquist signaling," *IEEE Access*, vol. 9, pp. 86 535–86 564, 2021.

[28] J. B. Anderson, F. Rusek, and V. Öwall, "Faster-than-Nyquist signaling," *Proceedings of the IEEE*, vol. 101, no. 8, pp. 1817–1830, 2013.

[29] M. Rodrigues and I. Darwazeh, "A spectrally efficient frequency division multiplexing based communications system," in *8th International OFDM Workshop, Hamburg, Germany*, 2003, pp. 70–74.

[30] F. Rusek and J. B. Anderson, "The two dimensional Mazo limit," in *International Symposium on Information Theory*, 2005, pp. 970–974.

[31] ——, "Multistream faster than Nyquist signaling," *IEEE Transactions on Communications*, vol. 57, no. 5, pp. 1329–1340, 2009.

[32] Y. Ma, F. Tian, N. Wu, B. Li, and X. Ma, "A low-complexity receiver for multicarrier faster-than-Nyquist signaling over frequency selective channels," *IEEE Communications Letters*, vol. 24, no. 1, pp. 81–85, 2020.

[33] J. Zhou, Y. Qiao, Z. Yang, Q. Cheng, Q. Wang, M. Guo, and X. Tang, "Capacity limit for faster-than-Nyquist non-orthogonal frequency-division multiplexing signaling," *Scientific Reports*, vol. 7, no. 1, p. 3380, 2017.

[34] A. Barbieri, D. Fertonani, and G. Colavolpe, "Time-frequency packing for linear modulations: Spectral efficiency and practical detection schemes," *IEEE Transactions on Communications*, vol. 57, no. 10, pp. 2951–2959, 2009.

[35] S. Li, W. Yuan, J. Yuan, B. Bai, D. Wing Kwan Ng, and L. Hanzo, "Time-domain vs. frequency-domain equalization for FTN signaling," *IEEE Transactions on Vehicular Technology*, vol. 69, no. 8, pp. 9174–9179, 2020.

[36] E. Basar, "Index modulation techniques for 5G wireless networks," *IEEE Communications Magazine*, vol. 54, no. 7, pp. 168–175, 2016.

[37] E. Basar, M. Wen, R. Mesleh, M. Di Renzo, Y. Xiao, and H. Haas, "Index modulation techniques for next-generation wireless networks," *IEEE Access*, vol. 5, pp. 16 693–16 746, 2017.

[38] X. Cheng, M. Zhang, M. Wen, and L. Yang, "Index modulation for 5G: Striving to do more with less," *IEEE Wireless Communications*, vol. 25, no. 2, pp. 126–132, 2018.

[39] P. Yang, Y. Xiao, Y. L. Guan, M. Di Renzo, S. Li, and L. Hanzo, "Multidomain index modulation for vehicular and railway communications: A survey of novel techniques," *IEEE Vehicular Technology Magazine*, vol. 13, no. 3, pp. 124–134, 2018.

[40] T. Mao, W. Qi, Z. Wang, and C. Sheng, "Novel index modulation techniques: A survey," *IEEE Communications Surveys & Tutorials*, vol. 21, no. 1, pp. 315–348, 2019.

[41] N. Ishikawa, S. Sugiura, and L. Hanzo, "50 years of permutation, spatial and index modulation: From classic RF to visible light communications and data storage," *IEEE Communications Surveys & Tutorials*, vol. 20, no. 3, pp. 1905–1938, 2018.

[42] M. Wen, X. Cheng, L. Yang, Y. Li, X. Cheng, and F. Ji, "Index modulated OFDM for underwater acoustic communications," *IEEE Communications Magazine*, vol. 54, no. 5, pp. 132–137, 2016.

[43] N. Ishikawa, S. Sugiura, and L. Hanzo, "Subcarrier-index modulation aided OFDM - will it work?" *IEEE Access*, vol. 4, pp. 2580–2593, 2016.

[44] E. Başar, Ü. Aygölü, E. Panayırcı, and H. V. Poor, "Orthogonal frequency division multiplexing with index modulation," *IEEE Transactions on Signal Processing*, vol. 61, no. 22, pp. 5536–5549, 2013.

[45] F. Kschischang, B. Frey, and H.-A. Loeliger, "Factor graphs and the sum-product algorithm," *IEEE Transactions on Information Theory*, vol. 47, no. 2, pp. 498–519, 2001.

[46] H. A. Loeliger, "An introduction to factor graphs," *IEEE Signal Process. Mag.*, vol. 21, no. 1, pp. 28–41, 2004.

[47] H. Loeliger, J. Dauwels, J. Hu, S. Korl, L. Ping, and F. R. Kschischang, "The factor graph approach to model-based signal processing," *Proceedings of the IEEE*, vol. 95, no. 6, pp. 1295–1322, 2007.

[48] S. Rangan, "Generalized approximate message passing for estimation with random linear mixing," in *IEEE International Symposium on Information Theory Proceedings*, 2011, 2168–2172.

[49] S. Rangan, P. Schniter, A. K. Fletcher, and S. Sarkar, "On the convergence of approximate message passing with arbitrary matrices," *IEEE Transactions on Information Theory*, vol. 65, no. 9, pp. 5339–5351, 2019.

[50] Q. Guo and J. Xi, "Approximate message passing with unitary transformation," *arXiv preprint, arXiv:1504.04799*, 2015.

[51] J. Ma and L. Ping, "Orthogonal amp," *IEEE Access*, vol. 5, pp. 2020–2033, 2017.

[52] S. Rangan, P. Schniter, and A. K. Fletcher, "Vector approximate message passing," *IEEE Transactions on Information Theory*, vol. 65, no. 10, pp. 6664–6684, 2019.

[53] A. Liveris and C. Georghiades, "Exploiting faster-than-Nyquist signaling," *IEEE Transactions on Communications*, vol. 51, no. 9, pp. 1502–1511, 2003.

[54] F. Rusek and J. B. Anderson, "Constrained capacities for faster-than-Nyquist signaling," *IEEE Transactions on Information Theory*, vol. 55, no. 2, pp. 764–775, 2009.

[55] Q. Li, F.-K. Gong, P.-Y. Song, and S.-H. Zhai, "Pre-equalized interference cancellation for faster-than-Nyquist signaling," *IEEE Access*, vol. 7, pp. 77 868–77 876, 2019.

[56] Q. Li, F.-K. Gong, P.-Y. Song, G. Li, and S.-H. Zhai, "Beyond DVB-S2X: Faster-than-Nyquist signaling with linear precoding," *IEEE Transactions on Broadcasting*, vol. 66, no. 3, pp. 620–629, 2020.

[57] S. B. Makarov, M. Liu, A. S. Ovsyannikova, S. V. Zavjalov, I. I. Lavrenyuk, W. Xue, and J. Qi, "Optimizing the shape of faster-than-Nyquist (FTN) signals with the constraint on energy concentration in the occupied frequency bandwidth," *IEEE Access*, vol. 8, pp. 130 082–130 093, 2020.

[58] M. El Hefnawy and H. Taoka, "Overview of faster-than-Nyquist for future mobile communication systems," in *IEEE 77th Vehicular Technology Conference (VTC Spring)*, 2013, pp. 1–5.

[59] Q. Shi, N. Wu, X. Ma, and H. Wang, "Frequency-domain joint channel estimation and decoding for faster-than-Nyquist signaling," *IEEE Transactions on Communications*, vol. 66, no. 2, pp. 781–795, 2018.

[60] W. Yuan, N. Wu, Q. Guo, D. W. K. Ng, J. Yuan, and L. Hanzo, "Iterative joint channel estimation, user activity tracking, and data detection for FTN-NOMA systems supporting random access," *IEEE Transactions on Communications*, vol. 68, no. 5, pp. 2963–2977, 2020.

[61] J. Liu, W. Liu, X. Hou, Y. Kishiyama, L. Chen, and T. Asai, "Enhanced non-orthogonal waveform (eNOW) for 5G evolution and 6G," in *26th IEEE Asia-Pacific Conference on Communications (APCC)*, 2021, pp. 56–61.

[62] Y.-J. Zhu, W.-Y. Wang, and G. Xin, "Faster-than-Nyquist signal design for multiuser multicell indoor visible light communications," *IEEE Photonics Journal*, vol. 8, no. 1, pp. 1–12, 2016.

[63] M. Jana, A. Medra, L. Lampe, and J. Mitra, "Pre-equalized faster-than-Nyquist transmission," *IEEE Transactions on Communications*, vol. 65, no. 10, pp. 4406–4418, 2017.

[64] S. Liang, Z. Jiang, L. Qiao, X. Lu, and N. Chi, "Faster-than-Nyquist precoded CAP modulation visible light communication system based on nonlinear weighted look-up table predistortion," *IEEE Photonics Journal*, vol. 10, no. 1, pp. 1–9, 2018.

[65] M. Jana, L. Lampe, and J. Mitra, "Design of time-frequency packed WDM superchannel transmission systems," *Journal of Lightwave Technology*, vol. 38, no. 24, pp. 6719–6731, 2020.

[66] G. Ku and J. M. Walsh, "Resource allocation and link adaptation in LTE and LTE advanced: A tutorial," *IEEE Communications Surveys & Tutorials*, vol. 17, no. 3, pp. 1605–1633, 2015.

[67] M. Jia, Z. Yin, Q. Guo, G. Liu, and X. Gu, "Downlink design for spectrum efficient IoT network," *IEEE Internet of Things Journal*, vol. 5, no. 5, pp. 3397–3404, 2018.

[68] T. Xu and I. Darwazeh, "Transmission experiment of bandwidth compressed carrier aggregation in a realistic fading channel," *IEEE Transactions on Vehicular Technology*, vol. 66, no. 5, pp. 4087–4097, 2017.

[69] T. Xu and I. Darwazeh, "Nyquist-SEFDM: Pulse shaped multicarrier communication with sub-carrier spacing below the symbol rate," in *10th International Symposium on Communication Systems, Networks and Digital Signal Processing (CSNDSP)*, 2016, pp. 1–6.

[70] A. G. A. Gelgor and V. P. Nguyen, "The design and performance of SEFDM with the Sinc-to-RRC modification of subcarriers spectrums," in *International Conference on Advanced Technologies for Communications (ATC)*, 2016, pp. 65–69.

[71] I. Darwazeh, T. Xu, T. Gui, Y. Bao, and Z. Li, "Optical SEFDM system; bandwidth saving using non-orthogonal sub-carriers," *IEEE Photonics Technology Letters*, vol. 26, no. 4, pp. 352–355, 2014.

[72] Y. Wang, Y. Zhou, T. Gui, K. Zhong, X. Zhou, L. Wang, A. P. T. Lau, C. Lu, and N. Chi, "Efficient MMSE-SQRD-based MIMO decoder for SEFDM-based 2.4-Gb/s-spectrum-compressed WDM VLC system," *IEEE Photonics Journal*, vol. 8, no. 4, pp. 1–9, 2016.

[73] H. Ghannam and I. Darwazeh, "SEFDM over satellite systems with advanced interference cancellation," *IET Communications*, vol. 12, no. 1, pp. 59–66, 2018.

[74] F. Rusek and J. B. Anderson, "Serial and parallel concatenations based on faster than Nyquist signaling," in *EEE International Symposium on Information Theory*, 2006, pp. 1993–1997.

[75] ——, "Non binary and precoded faster than Nyquist signaling," *IEEE Transactions on Communications*, vol. 56, no. 5, pp. 808–817, 2008.

[76] A. Prlja, J. B. Anderson, and F. Rusek, "Receivers for faster-than-Nyquist signaling with and without turbo equalization," in *IEEE International Symposium on Information Theory*, 2008, pp. 464–468.

[77] J. B. Anderson, A. Prlja, and F. Rusek, "New reduced state space BCJR algorithms for the ISI channel," in *IEEE International Symposium on Information Theory*, 2009, pp. 889–893.

[78] J. B. Anderson and A. Prlja, "Turbo equalization and an M-BCJR algorithm for strongly narrowband intersymbol interference," in *IEEE International Symposium On Information Theory & Its Applications*, 2010, pp. 261–266.

[79] A. Prlja and J. B. Anderson, "Reduced-complexity receivers for strongly narrowband intersymbol interference introduced by faster-than-Nyquist signaling," *IEEE Transactions on Communications*, vol. 60, no. 9, pp. 2591–2601, 2012.

[80] S. Li, B. Bai, J. Zhou, P. Chen, and Z. Yu, "Reduced-complexity equalization for faster-than-Nyquist signaling: New methods based on ungerboeck observation model," *IEEE Transactions on Communications*, vol. 66, no. 3, pp. 1190–1204, 2018.

[81] S. Sugiura, "Frequency-domain equalization of faster-than-Nyquist signaling," *IEEE Wireless Communications Letters*, vol. 2, no. 5, pp. 555–558, 2013.

[82] S. Sugiura and L. Hanzo, "Frequency-domain-equalization-aided iterative detection of faster-than-Nyquist signaling," *IEEE Transactions on Vehicular Technology*, vol. 64, no. 5, pp. 2122–2128, 2015.

[83] T. Ishihara and S. Sugiura, "Frequency-domain equalization aided iterative detection of faster-than-Nyquist signaling with noise whitening," in *IEEE International Conference on Communications (ICC)*, 2016, pp. 1–6.

[84] ——, "Iterative frequency-domain joint channel estimation and data detection of faster-than-Nyquist signaling," *IEEE Transactions on Vehicular Technology*, vol. 16, no. 9, pp. 6221–6231, 2017.

[85] P. Şen, T. Aktaş, and A. Ö. Yilmaz, "A low-complexity graph-based LMMSE receiver designed for colored noise induced by FTN-signaling," in *IEEE Wireless Communications and Networking Conference (WCNC)*, 2014, pp. 642–647.

[86] W. Yuan, N. Wu, H. Wang, and J. Kuang, "Variational inference-based frequency-domain equalization for faster-than-Nyquist signaling in doubly selective channels," *IEEE Signal Processing Letters*, vol. 23, no. 9, pp. 1270–1274, 2016.

[87] N. Wu, W. Yuan, H. Wang, Q. Shi, and J. Kuang, "Frequency-domain iterative message passing receiver for faster-than-Nyquist signaling in doubly selective channels," *IEEE Wireless Communications Letters*, vol. 5, no. 6, pp. 584–587, 2016.

[88] N. Wu, W. Yuan, Q. Guo, and J. Kuang, "A hybrid BP-EP-VMP approach to joint channel estimation and decoding for FTN signaling over frequency selective fading channels," *IEEE Access*, vol. 5, pp. 6849–6858, 2017.

[89] T. Yu, M. Zhao, J. Zhong, J. Zhang, and P. Xiao, "Low-complexity graph-based turbo equalisation for single-carrier and multi-carrier FTN signalling," *IET Signal Processing*, vol. 11, no. 7, pp. 838–845, 2017.

[90] X. Wen, W. Yuan, D. Yang, N. Wu, and J. Kuang, "Low complexity message passing receiver for faster-than-Nyquist signaling in nonlinear channels," *IEEE Access*, vol. 6, pp. 68 233–68 241, 2018.

[91] W. Yuan, N. Wu, A. Zhang, X. Huang, Y. Li, and L. Hanzo, "Iterative receiver design for FTN signaling aided sparse code multiple access," *IEEE Transactions on Wireless Communications*, vol. 19, no. 2, pp. 915–928, 2020.

[92] G. Forney, "Maximum-likelihood sequence estimation of digital sequences in the presence of intersymbol interference," *IEEE Transactions on Information Theory*, vol. 18, no. 3, pp. 363–378, 1972.

[93] G. Ungerboeck, "Adaptive maximum-likelihood receiver for carrier-modulated data-transmission systems," *IEEE Transactions on Communications*, vol. 22, no. 5, pp. 624–636, 1974.

[94] R. Laroia, S. Tretter, and N. Farvardin, "A simple and effective precoding scheme for noise whitening on intersymbol interference channels," *IEEE Transactions on Communications*, vol. 41, no. 10, pp. 1460–1463, 1993.

[95] S. Li, J. Yuan, B. Bai, and N. Benvenuto, "Code-based channel shortening for faster-than-Nyquist signaling: Reduced-complexity detection and code design," *IEEE Transactions on Communications*, vol. 68, no. 7, pp. 3996–4011, 2020.

[96] M. Opper and D. Saad, *Advanced Mean Field Methods: Theory and Practice*. MIT press, Cambridge, MA, USA, 2001.

[97] S. Katsura and M. Takizawa, "Bethe lattice and the Bethe approximation," *Progress Theoretical Phys.*, vol. 51, no. 1, pp. 82–99, 1974.

[98] M. J. Wainwright and M. I. Jordan, "Graphical models, exponential families, and variational inference," *Foundations and Trends in Machine Learning*, vol. 1, no. 1/2, 1–305, 2008.

[99] Q. Guo, D. Huang, S. Nordholm, J. Xi, and Y. Yu, "Iterative frequency domain equalization with generalized approximate message passing," *IEEE Signal Processing Letters*, vol. 20, no. 6, pp. 559–562, 2013.

[100] I. Kanaras, A. Chorti, M. R. D. Rodrigues and I. Darwazeh, "Spectrally efficient FDM signals: Bandwidth gain at the expense of receiver complexity," in *IEEE International Conference on Communications*, 2009, pp. 1–6.

[101] I. Kanaras, A. Chorti, M. R. D. Rodrigues, and I. Darwazeh, "A combined MMSE-ML detection for a spectrally efficient non orthogonal FDM signal," in *5th International Conference on Broadband Communications, Networks and Systems*, 2008, pp. 421–425.

[102] S. Isam, I. Kanaras, and I. Darwazeh, "A truncated SVD approach for fixed complexity spectrally efficient FDM receivers," in *IEEE Wireless Communications and Networking Conference*, 2011, pp. 1584–1589.

[103] T. Xu, R. C. Grammenos, F. Marvasti, and I. Darwazeh, "An improved fixed sphere decoder employing soft decision for the detection of non-orthogonal signals," *IEEE Communications Letters*, vol. 17, no. 10, pp. 1964–1967, 2013.

[104] Y. Feng, Y. Ma, Z. Li, C. Yan, and N. Wu, "Low-complexity factor graph-based iterative detection for RRC-SEFDM signals," in *10th International Conference on Wireless Communications and Signal Processing (WCSP)*, 2018, pp. 1–6.

[105] T. Xu and I. Darwazeh, "A soft detector for spectrally efficient systems with non-orthogonal overlapped sub-carriers," *IEEE Communications Letters*, vol. 18, no. 10, pp. 1847–1850, 2014.

[106] K. Park, H. Kim, A. Lee, D. Kang, and W. Oh, "Iterative frequency-domain inter-carrier interference cancellation for coded SEFDM," *Electronics Letters*, vol. 53, no. 19, pp. 1333–1335, 2017.

[107] B. Yu, H. Zhang, X. Hong, and C. Guo, "Channel equalization and data detection for SEFDM over frequency selective fading channels," *IET Communications*, vol. 12, no. 18, pp. 2315–2323, 2018.

[108] A. Chorti, I. Kanaras, M. R. Rodrigues, and I. Darwazeh, "Joint channel equalization and detection of spectrally efficient FDM signals," in *21st Annual IEEE International Symposium on Personal, Indoor and Mobile Radio Communications*, 2010, pp. 177–182.

[109] S. Isam and I. Darwazeh, "Robust channel estimation for spectrally efficient FDM system," in *19th International Conference on Telecommunications (ICT)*, 2012, pp. 1–6.

[110] H. Ghannam and I. Darwazeh, "Robust channel estimation methods for spectrally efficient FDM systems," in *IEEE 87th Vehicular Technology Conference (VTC Spring)*, 2018, pp. 1–6.

[111] P. N. Whatmough, M. R. Perrett, S. Isam, and I. Darwazeh, "VLSI architecture for a reconfigurable spectrally efficient FDM baseband transmitter," *IEEE Transactions on Circuits and Systems I: Regular Papers*, vol. 59, no. 5, pp. 1107–1118, 2012.

[112] H. Ghannam, D. Nopchinda, M. Gavell, H. Zirath, and I. Darwazeh, "Experimental demonstration of spectrally efficient frequency division multiplexing transmissions at

E-band," *IEEE Transactions on Microwave Theory and Techniques*, vol. 67, no. 5, pp. 1911–1923, 2019.

[113] M. Jana, L. Lampe, and J. Mitra, "Precoded time-frequency-packed multicarrier faster-than-Nyquist transmission," in *IEEE 20th International Workshop on Signal Processing Advances in Wireless Communications (SPAWC)*, 2019, pp. 1–5.

[114] S. Yang, F. Luo, and L. Yang, "16QAM spectral efficiency frequency division multiplexing transmission with Tomlinson–Harashima precoding for intensity modulation and direct detection optical links," *Optical and Quantum Electronics*, vol. 52, no. 9, pp. 1–14, 2020.

[115] L. Bahl, J. Cocke, F. Jelinek, and J. Raviv, "Optimal decoding of linear codes for minimizing symbol error rate," *IEEE Transactions on Information Theory*, vol. 20, no. 2, pp. 284–287, 1974.

[116] S. Peng, A. Liu, X. Liu, K. Wang, and X. Liang, "MMSE turbo equalization and detection for multicarrier faster-than-Nyquist signaling," *IEEE Transactions on Vehicular Technology*, vol. 67, no. 3, pp. 2267–2275, 2018.

[117] M. Jana, L. Lampe, and J. Mitra, "Interference cancellation for time-frequency packed super-Nyquist WDM systems," *IEEE Photonics Technology Letters*, vol. 30, no. 24, pp. 2099–2102, 2018.

[118] B. Cai, A. Liu, X. Tong, and F. Cheng, "Training sequences design for channel estimation in FTN system using discrete Fourier transform techniques," *IET Communications*, vol. 11, no. 17, pp. 2561–2565, 2017.

[119] Q. Li, M. Wen, B. Clerckx, S. Mumtaz, A. Al-Dulaimi, and R. Q. Hu, "Subcarrier index modulation for future wireless networks: Principles, applications, and challenges," *IEEE Wireless Communications*, vol. 27, no. 3, pp. 118–125, 2020.

[120] T. Ishihara and S. Sugiura, "Faster-than-Nyquist signaling with index modulation," *IEEE Wireless Communications Letters*, vol. 6, no. 5, pp. 630–633, 2017.

[121] P. Chaki, T. Ishihara, and S. Sugiura, "Eigenvalue decomposition precoded faster-than-Nyquist transmission of index modulated symbols," in *IEEE International Symposium on Information Theory (ISIT)*, 2021, pp. 3279–3284.

[122] S. Li, N. Wu, Q. Shi, and Q. Guo, "FTN signaling-aided space-time multi-mode index modulation systems with a GMP-based receiver," *IEEE Access*, vol. 7, pp. 162 898–162 912, 2019.

[123] H. Liu, L. Liu, and P. Wang, "Spectrally efficient nonorthogonal frequency division multiplexing with index modulation," in *17th International Conference on Parallel and Distributed Computing, Applications and Technologies (PDCAT)*, 2016, pp. 290–293.

[124] M. Nakao and S. Sugiura, "Spectrally efficient frequency division multiplexing with index-modulated non-orthogonal subcarriers," *IEEE Wireless Communications Letters*, vol. 8, no. 1, pp. 233–236, 2019.

[125] V. W. S. Wong, R. Schober, D. W. K. Ng, and L.-C. Wang, *Key Technologies for 5G Wireless Systems*. Cambridge University Press, 2017.

[126] L. Dai, B. Wang, Z. Ding, Z. Wang, S. Chen, and L. Hanzo, "A survey of non-orthogonal multiple access for 5G," *IEEE Communications Surveys & Tutorials*, vol. 20, no. 3, pp. 2294–2323, 2018.

[127] Y. Liu, Z. Qin, M. Elkashlan, Z. Ding, A. Nallanathan, and L. Hanzo, "Nonorthogonal multiple access for 5G and beyond," *Proceedings of the IEEE*, vol. 105, no. 12, pp. 2347–2381, 2017.

[128] P. Banelli, S. Buzzi, G. Colavolpe, A. Modenini, F. Rusek, and A. Ugolini, "Modulation formats and waveforms for 5G networks: Who will be the heir of OFDM?: An overview of alternative modulation schemes for improved spectral efficiency," *IEEE Signal Processing Magazine*, vol. 31, no. 6, pp. 80–93, 2014.

[129] G. Wunder, P. Jung, M. Kasparick, T. Wild, F. Schaich, Y. Chen, S. T. Brink, I. Gaspar, N. Michailow, A. Festag, L. Mendes, N. Cassiau, D. Ktenas, M. Dryjanski, S. Pietrzyk, B. Eged, P. Vago, and F. Wiedmann, "5GNOW: Non-orthogonal, asynchronous waveforms for future mobile applications," *IEEE Communications Magazine*, vol. 52, no. 2, pp. 97–105, 2014.

[130] I. Kanaras, A. Chorti, M. R. D. Rodrigues, and I. Darwazeh, "A fast constrained sphere decoder for ill conditioned communication systems," *IEEE Communications Letters*, vol. 14, no. 11, pp. 999–1001, 2010.

[131] T. van Erven and P. Harremos, "Rényi divergence and Kullback-Leibler divergence," *IEEE Transactions on Information Theory*, vol. 60, no. 7, pp. 3797–3820,

[132] S. Isam and I. Darwazeh, "Simple DSP-IDFT techniques for generating spectrally efficient FDM signals," in *7th International Symposium on Communication Systems, Networks & Digital Signal Processing (CSNDSP)*, 2010, pp. 20–24.

[133] S. I. A. Ahmed, "Spectrally efficient FDM communication signals and transceivers: Design, mathematical modelling and system optimization," Ph.D. dissertation, University College London (University of London), 2011.

[134] I. Sekita, T. Kurita, and N. Otsu, "Complex autoregressive model for shape recognition," *IEEE Transactions on Pattern Analysis and Machine Intelligence*, vol. 14, no. 4, pp. 489–496, 1992.

[135] Q. Guo and L. Ping, "LMMSE turbo equalization based on factor graphs," *IEEE Journal on Selected Areas in Communications*, vol. 26, no. 2, pp. 311–319, 2008.

[136] J. Céspedes, P. M. Olmos, M. Sánchez-Fernández, and F. Perez-Cruz, "Expectation propagation detection for high-order high-dimensional MIMO systems," *IEEE Transactions on Communications*, vol. 62, no. 8, pp. 2840–2849, 2014.

[137] W. Yuan, N. Wu, Q. Guo, Y. Li, C. Xing, and J. Kuang, "Iterative receivers for downlink MIMO-SCMA: Message passing and distributed cooperative detection," *IEEE Transactions on Wireless Communications*, vol. 17, no. 5, pp. 3444–3458, 2018.

[138] M. Senst and G. Ascheid, "How the framework of expectation propagation yields an iterative IC-LMMSE MIMO receiver," in *IEEE Global Telecommunications Conference - GLOBECOM 2011*, 2011, pp. 1–6.

[139] N. Wu, W. Yuan, Q. Guo, and J. Kuang, "A hybrid BP-EP-VMP approach to joint channel estimation and decoding for FTN signaling over frequency selective fading channels," *IEEE Access*, vol. 5, pp. 6849–6858, 2017.

[140] Z. Hu, F. Chen, M. Wen, F. Ji, and H. Yu, "Low-complexity LLR calculation for OFDM with index modulation," *IEEE Wireless Communications Letters*, vol. 7, no. 4, pp. 618–621, 2018.

[141] J. Winn and C. M. Bishop, "Variational message passing," *J. Mach. Learn. Res.*, vol. 6, pp. 661–694, 2005.

[142] J Dauwels, "On variational message passing on factor graphs," in *IEEE International Symposium on Information Theory*, 2007, pp. 2546–2550.

[143] E. Panayirci, M. T. Altabbaa, M. Uysal, and H. V. Poor, "Sparse channel estimation for OFDM-based underwater acoustic systems in Rician fading with a new OMP-MAP algorithm," *IEEE Transactions on Signal Processing*, vol. 67, no. 6, pp. 1550–1565, 2019.

[144] A. Piemontese, A. Modenini, G. Colavolpe, and N. S. Alagha, "Improving the spectral efficiency of nonlinear satellite systems through time-frequency packing and advanced receiver processing," *IEEE Transactions on Communications*, vol. 61, no. 8, pp. 3404–3412, 2013.

[145] G. Colavolpe and T. Foggi, "Time-frequency packing for high-capacity coherent optical links," *IEEE Transactions on Communications*, vol. 62, no. 8, pp. 2986–2995, 2014.

[146] M. Secondini, T. Foggi, F. Fresi, G. Meloni, F. Cavaliere, G. Colavolpe, E. Forestieri, L. Potí, R. Sabella, and G. Prati, "Optical time-frequency packing: Principles, design, implementation, and experimental demonstration," *Journal of Lightwave Technology*, vol. 33, no. 17, pp. 3558–3570, 2015.

[147] J. T. Parker and P. Schniter, "Parametric bilinear generalized approximate message passing," *IEEE Journal of Selected Topics in Signal Processing*, vol. 10, no. 4, 1–14, 2016.

[148] Kim H J, Choi K, Lee H B, Jung H K, and Hahn S Y, "A new algorithm for solving ill conditioned linear systems," *IEEE Transactions on Magnetics*, vol. 32, no. 3, pp. 1373–1376, 1996.

[149] T. Piotrowski and I. Yamada, "MV-PURE estimator: Minimum-variance pseudo-unbiased reduced-rank estimator for linearly constrained ill-conditioned inverse problems," *IEEE Transactions on Signal Processing*, vol. 56, no. 8, pp. 3408–3423, 2008.

[150] L. Liu, Y. Li, C. Huang, C. Yuen, and Y. L. Guan, "A new insight into GAMP and AMP," *IEEE Transactions on Vehicular Technology*, vol. 68, no. 8, pp. 8264–8269, 2019.

[151] C. Huang, L. Liu, C. Yuen, and S. Sun, "Iterative channel estimation using LSE and sparse message passing for mmWave MIMO systems," *IEEE Transactions on Signal Processing*, vol. 67, no. 1, pp. 245–259, 2019.

[152] M. Tuchler, A. C. Singer, and R. Koetter, "Minimum mean squared error equalization using a priori information," *IEEE Transactions on Signal Processing*, vol. 50, no. 3, pp. 673–683, 2002.

[153] S. Peng, A. Liu, X. Tong, and K. Wang, "On Max-SIR time-frequency packing for multicarrier faster-than-Nyquist signaling," *IEEE Communications Letters*, vol. 21, no. 10, pp. 2142–2145, 2017.

[154] Y. Ma, N. Wu, J. A. Zhang, B. Li, and L. Hanzo, "Parametric bilinear iterative generalized approximate message passing reception of ftn multi-carrier signaling," *IEEE Transactions on Communications*, vol. 69, no. 12, pp. 8443–8458, 2021.

[155] M. Luo, Q. Guo, M. Jin, Y. C. Eldar, D. Huang, and X. Meng, "Unitary approximate message passing for sparse bayesian learning," *IEEE Transactions on Signal Processing*, vol. 69, pp. 6023–6039, 2021.

[156] S. Sarkar, A. K. Fletcher, S. Rangan, and P. Schniter, "Bilinear recovery using adaptive vector-AMP," *IEEE Transactions on Signal Processing*, vol. 67, no. 13, pp. 3383–3396, 2019.

[157] Q. Guo and D. D. Huang, "A concise representation for the soft-in softout LMMSE detector," *IEEE Communications Letters*, vol. 15, no. 5, 566–568, 2011.

[158] Y. Ma, N. Wu, J. A. Zhang, B. Li, and L. Hanzo, "Generalized approximate message passing equalization for multi-carrier faster-than-Nyquist signaling," *IEEE Transactions on Vehicular Technology*, vol. 71, no. 3, pp. 3309–3314, 2022.

[159] B. Farhang-Boroujeny, "OFDM versus filter bank multicarrier," *IEEE Signal Processing Magazine*, vol. 28, no. 3, pp. 92–112, 2011.

[160] A. M. Mathai, *A handbook of generalized special functions for statistical and physical sciences*. Oxford University Press, USA, 1993.

[161] P. J. Davis, *Circulant Matrices*. John Wieley & Sons, Inc, 1979.

Appendix A

Derivations of (3.41) and (3.42)

In contrast to the elementary or multiplication nodes, the extraordinary inner product node lacks explicit Gaussian message updating rules on Forney-style factor graph. Note that the inner product constraint is equivalent to a dot product of the corresponding independent vectors $\breve{\mathbf{h}}_q^{\tilde{l}}$ and $\breve{\mathbf{x}}_q^{\tilde{l}}$, while the inner elements are also assumed to be independent. According to BP rules [60], [91], the forward messages of the m-th element of vector $\breve{\mathbf{s}}_q^{\tilde{l}}$ is expressed as

$$\begin{aligned}\overrightarrow{\mu}(s_m) &\propto \int \delta(s_m - \tilde{h}_m x_m)\overrightarrow{\mu}(x_m)\overrightarrow{\mu}(\tilde{h}_m)dx_m d\tilde{h}_m \\ &\propto \frac{1}{|\tilde{h}_m|}\int \mathcal{CN}\big(s_m/\tilde{h}_m; \overrightarrow{m}_{x_m}(i), \overrightarrow{v}_{x_q}(i)\big)\mathcal{CN}\big(\tilde{h}_q; \overrightarrow{m}_{\tilde{h}_m}(i), \overrightarrow{v}_{\tilde{h}_m}(i)\big)d\tilde{h}_m. \end{aligned} \tag{A.1}$$

However, it is hard to derive an analytical Gaussian expression for the above equation. To obtain the approximated Gaussian messages of $\breve{\mathbf{s}}_q^{\tilde{l}}$, according to the moment matching method [136], the first-order and second-order moments of variables $\breve{\mathbf{s}}_q^{\tilde{l}}$ are calculated. Based on the Mellin transform [160], it is easy to derive that the nth-order moment of the product of two statistically independent random variables is equal to the product of two nth-order moments of the corresponding independent random variables, i.e.,

$$\mathbb{E}\{(x_m h_m)^n\} = \mathbb{E}\{x_m^n\}\mathbb{E}\{h_m^n\}. \tag{A.2}$$

Based on the *a priori* probabilities obtained from the channel decoder and channel estimator, the approximated forward mean vector and covariance matrix of variables $\breve{\mathbf{s}}_q^{\tilde{l}}$ are given by

$$\overrightarrow{\mathbf{m}}_{\breve{\mathbf{s}}_q^{\tilde{l}}}(i) = \overrightarrow{\mathbf{m}}_{\breve{\mathbf{x}}_q^{\tilde{l}}}(i) \odot \overrightarrow{\mathbf{m}}_{\breve{\mathbf{h}}_q^{\tilde{l}}}(i), \tag{A.3}$$

$$\begin{aligned}\overrightarrow{\mathbf{V}}_{\breve{\mathbf{s}}_q^{\tilde{l}}}(i) = &\left[\mathcal{D}\big(\overrightarrow{\mathbf{m}}_{\breve{\mathbf{x}}_q^{\tilde{l}}}(i) \odot \overrightarrow{\mathbf{m}}_{\breve{\mathbf{x}}_q^{\tilde{l}}}(i)\big) + \overrightarrow{\mathbf{V}}_{\breve{\mathbf{x}}_q^{\tilde{l}}}(i)\right] \\ &\times \left[\mathcal{D}\big(\overrightarrow{\mathbf{m}}_{\breve{\mathbf{h}}_q^{\tilde{l}}}(i) \odot \overrightarrow{\mathbf{m}}_{\breve{\mathbf{h}}_q^{\tilde{l}}}(i)\big) + \overrightarrow{\mathbf{V}}_{\breve{\mathbf{h}}_q^{\tilde{l}}}(i)\right] - \mathcal{D}\big(\overrightarrow{\mathbf{m}}_{\breve{\mathbf{s}}_q^{\tilde{l}}}(i) \odot \overrightarrow{\mathbf{m}}_{\breve{\mathbf{s}}_q^{\tilde{l}}}(i)\big).\end{aligned} \tag{A.4}$$

Appendix B

Derivations of (4.12)

According to Theorem 5.6.2 in [161], assuming that an $mn \times mn$ block circulant matrix $\mathbf{A}$ consists of m^2 $n \times n$ matrices and the first n rows are represented as $\mathbf{A}_{[1:n,:]} = [\mathbf{A}_1,\ \mathbf{A}_2,\ \cdots,\ \mathbf{A}_m]$, the matrix $\mathbf{A}$ satisfies

$$\mathbf{A} = \sum_{k=0}^{m-1} (\mathbf{\Pi}_m^k \otimes \mathbf{A}_{k+1}), \tag{B.1}$$

where $\mathbf{\Pi}_m^k$ is $m \times m$ circulant permutation matrix with the first row $(\mathbf{\Pi}_m^k)_{[1,:]} = \boldsymbol{\lambda}_{\mathbf{\Pi}_m^k} = [\mathbf{0}_k^T,\ 1,\ \mathbf{0}_{(m-k-1)}^T]$, and $\mathbf{A}_k$ is an $n \times n$ arbitrary matrix.

Hence, the matrix $\bar{\mathbf{G}}_{q,l}$ of (4.14) is decomposed into

$$\bar{\mathbf{G}}_{q,l} = \mathbf{\Pi}_K^{K_\mathrm{I}} \otimes \mathcal{D}(\breve{\mathbf{g}}_{0,l}). \tag{B.2}$$

Since $\mathbf{\Pi}_K^{K_\mathrm{I}}$ is a circulant matrix, it can be diagonalized by the normalized discrete Fourier transform matrix. The above equation can be rewritten as

$$\begin{aligned}
\bar{\mathbf{G}}_{q,l} &= \big(\mathbf{F}_K^H \mathbf{\Lambda}_{\mathbf{\Pi}_K^{K_\mathrm{I}}} \mathbf{F}_K\big) \otimes \big[\mathbf{I}_{L_\mathrm{s}}^H \big(\mathbf{I}_{L_\mathrm{s}} \mathcal{D}(\breve{\mathbf{g}}_{0,l}) \mathbf{I}_{L_\mathrm{s}}^H\big) \mathbf{I}_{L_\mathrm{s}}\big] \\
&= (\mathbf{F}_K \otimes \mathbf{I}_{L_\mathrm{s}})^H \big[\mathbf{\Lambda}_{\mathbf{\Pi}_K^{K_\mathrm{I}}} \otimes \mathcal{D}(\breve{\mathbf{g}}_{0,l})\big] (\mathbf{F}_K \otimes \mathbf{I}_{L_\mathrm{s}}) \\
&= (\mathbf{F}_K \otimes \mathbf{I}_{L_\mathrm{s}})^H \mathbf{\Lambda}_{q,l} (\mathbf{F}_K \otimes \mathbf{I}_{L_\mathrm{s}}),
\end{aligned} \tag{B.3}$$

where $\mathbf{\Lambda}_{q,l} = \mathbf{\Lambda}_{\mathbf{\Pi}_K^{K_\mathrm{I}}} \otimes \mathcal{D}(\breve{\mathbf{g}}_{0,l})$ is a KL_s diagonal matrix with $\mathbf{\Lambda}_{\mathbf{\Pi}_K^{K_\mathrm{I}}} = \mathcal{D}\big(\sqrt{K} \mathbf{F}_K^H \boldsymbol{\lambda}_{\mathbf{\Pi}_m^{K_\mathrm{I}}}^H\big)$.

Appendix C

Derivations of the distribution of the equivalent noise in (4.14)

In (4.14), the colored noise term is given by

$$\breve{\boldsymbol{\varpi}}_q = \breve{\boldsymbol{\kappa}}_q + \breve{\boldsymbol{\omega}}_q = \left(\mathbf{F}_K \otimes \mathbf{F}_{L_\mathrm{s}}\right)\left[\mathbf{z}_q^{\mathrm{ici}} + (\mathbf{I}_K \otimes \boldsymbol{\Xi}_\mathrm{t})\mathbf{z}_{q-1} + (\mathbf{I}_K \otimes \boldsymbol{\Xi}_\mathrm{h})\mathbf{z}_{q+1} + \boldsymbol{\omega}_q\right], \tag{C.1}$$

where $\mathbf{z}_q$ denotes the noiseless measurement vector in the q-th segment and $\boldsymbol{\omega}_q$ contains the zero mean colored noise samples. Hence, the mean vector of the colored noise $\breve{\boldsymbol{\varpi}}_q$ is derived as

$$\hat{\boldsymbol{\kappa}}_q(i) = \left(\mathbf{F}_K \otimes \mathbf{F}_{L_\mathrm{s}}\right)\left[\hat{\mathbf{z}}_q^{\mathrm{ici}}(i) + (\mathbf{I}_K \otimes \boldsymbol{\Xi}_\mathrm{t})\hat{\mathbf{z}}_{q-1}(i) + (\mathbf{I}_K \otimes \boldsymbol{\Xi}_\mathrm{h})\hat{\mathbf{z}}_{q+1}(i)\right], \tag{C.2}$$

where $\hat{\mathbf{z}}_q(i) = \left(\mathbf{F}_K \otimes \mathbf{F}_{L_\mathrm{s}}\right)^H \sum_{l=0}^{L-1} h_{q,l}\breve{\mathbf{G}}_{q,l}\hat{\mathbf{x}}_q(i) + \hat{\mathbf{z}}_q^{\mathrm{ici}}(i)$ is the estimate of the noiseless measurement vector in the q-th segment, $\hat{\mathbf{x}}_q(i)$ is the estimate of the transmitted symbol vector in the q-th segment, $\hat{\mathbf{z}}_q^{\mathrm{ici}}(i) = [(\hat{\mathbf{z}}_{0,q}^{\mathrm{ici}}(i))^T, \cdots, (\hat{\mathbf{z}}_{K-1,q}^{\mathrm{ici}}(i))^T]^T$ is the ICI estimate of the ICI in the q-th segment, and

$$\hat{\mathbf{z}}_{k_\mathrm{r},q}^{\mathrm{ici}}(i) = \sum_{l=0}^{L-1} h_{q,l} \sum_{k_\mathrm{t} \in \mathcal{I}_{K_\mathrm{I}} \backslash k_\mathrm{r}} \lambda_{k_\mathrm{t}}^l \mathcal{D}(\boldsymbol{\theta}_{k_\Delta,q})\mathbf{F}_{L_\mathrm{s}}^H \mathcal{D}(\breve{\mathbf{g}}_{k_\Delta,l})\mathbf{F}_{L_\mathrm{s}} \boldsymbol{\Phi}_\mathrm{m} \hat{\mathbf{x}}_{k_\mathrm{t},q}(i). \tag{C.3}$$

Moreover, the covariance matrix $\mathbf{R}_{\breve{\boldsymbol{\varpi}}_q}(i)$ of the frequency-domain equivalent noise vector $\breve{\boldsymbol{\varpi}}_q$ contains the covariance matrix $\mathbf{R}_{\breve{\boldsymbol{\omega}}_q}$ of the frequency-domain colored noise process and the variance vector $\boldsymbol{\nu}_{\boldsymbol{\kappa}_q}(i)$ of the equivalent interference in each iteration. Among them, the covariance matrix $\mathbf{R}_{\breve{\boldsymbol{\omega}}_q}$ of the frequency-domain colored noise process is expressed as

$$\begin{aligned} \mathbf{R}_{\breve{\boldsymbol{\omega}}_q} &= (\mathbf{F}_K \otimes \mathbf{F}_{L_\mathrm{s}})\mathbf{R}_{\boldsymbol{\omega}_q}(\mathbf{F}_K \otimes \mathbf{F}_{L_\mathrm{s}})^H \\ &= (\mathbf{F}_K \otimes \mathbf{F}_{L_\mathrm{s}})(\ddot{\mathbf{R}}_{\boldsymbol{\omega}_q} - \dot{\mathbf{R}}_{\boldsymbol{\omega}_q})(\mathbf{F}_K \otimes \mathbf{F}_{L_\mathrm{s}})^H, \end{aligned} \tag{C.4}$$

where $\mathbf{R}_{\boldsymbol{\omega}_q}$ denotes the covariance matrix of the time-domain colored noise process $\boldsymbol{\omega}_q$, $\ddot{\mathbf{R}}_{\boldsymbol{\omega}_q}$ is

a $KL_{\rm s} \times KL_{\rm s}$ block circulant matrix having K^2 $L_{\rm s}$ circulant matrices, and $\dot{\mathbf{R}}_{\boldsymbol{\omega}_q}$ is $KL_{\rm s} \times KL_{\rm s}$ block circulant matrix having K^2 $L_{\rm s}$ Toeplitz matrices. Specifically, the first $L_{\rm s}$ rows of $\ddot{\mathbf{R}}_{\boldsymbol{\omega}_q}$ is given by

$$(\ddot{\mathbf{R}}_{\boldsymbol{\omega}_q})_{[1:L_{\rm s},:]} = [\mathcal{D}(\boldsymbol{\theta}_{-K_{\rm I},q})\ddot{\boldsymbol{\Theta}}_{-K_{\rm I}},\ \cdots,\ \mathcal{D}(\boldsymbol{\theta}_{K_{\rm I},q})\ddot{\boldsymbol{\Theta}}_{K_{\rm I}},\ \mathbf{0}_{L_{\rm s}\times(K-2K_{\rm I}-1)L_{\rm s}}], \tag{C.5}$$

where $\boldsymbol{\theta}_{k_\Delta,q} = [\theta_{k_\Delta}^{qL_{\rm m}}, \cdots, \theta_{k_\Delta}^{qL_{\rm m}+L_{\rm s}-1}]^T$, $\ddot{\boldsymbol{\Theta}}_{k_\Delta}$ is an $L_{\rm s}\times L_{\rm s}$ circulant matrix with the first row vector $(\ddot{\boldsymbol{\Theta}}_{k_\Delta})_{[1,:]} = [A_{\rm p}(0,k_\Delta), \cdots, A_{\rm p}(N_{\rm I}\tau T_0, k_\Delta), 0, \cdots, 0, A_{\rm p}(-N_{\rm I}\tau T_0, k_\Delta), \cdots, A_{\rm p}(-\tau T_0, k_\Delta)]$. Similarly, the first $L_{\rm s}$ rows of $\dot{\mathbf{R}}_{\boldsymbol{\omega}_q}$ is expressed as

$$(\dot{\mathbf{R}}_{\boldsymbol{\omega}_q})_{[1:L_{\rm s},:]} = [\mathcal{D}(\boldsymbol{\theta}_{-K_{\rm I},q})\dot{\boldsymbol{\Theta}}_{-K_{\rm I}},\ \cdots,\ \mathcal{D}(\boldsymbol{\theta}_{K_{\rm I},q})\dot{\boldsymbol{\Theta}}_{K_{\rm I}},\ \mathbf{0}_{L_{\rm s}\times(K-2K_{\rm I}-1)L_{\rm s}}], \tag{C.6}$$

where $\dot{\boldsymbol{\Theta}}_{k_\Delta}$ is an $L_{\rm s}\times L_{\rm s}$ Toeplitz matrices with the first row vector $(\dot{\boldsymbol{\Theta}}_{k_\Delta})_{[1,:]} = [0, \cdots, 0, A_{\rm p}(-N_{\rm I}\tau T_0, k_\Delta), \cdots, A_{\rm p}(-\tau T_0, k_\Delta)]$ and the first column vector $(\dot{\boldsymbol{\Theta}}_{k_\Delta})_{[:,1]} = [0, \cdots, 0, A_{\rm p}(N_{\rm I}\tau T_0, k_\Delta), \cdots, A_{\rm p}(\tau T_0, k_\Delta)]^T$.

According to the properties of block circulant matrices in [161], the block circulant matrix can be diagonalized via two-dimensional FFT operations. Hence, (C.4) is rewritten as

$$\mathbf{R}_{\breve{\boldsymbol{\omega}}_q} = \ddot{\boldsymbol{\Lambda}}_{\boldsymbol{\omega}_q} - \dot{\boldsymbol{\Upsilon}}_{\boldsymbol{\omega}_q} \approx \ddot{\boldsymbol{\Lambda}}_{\boldsymbol{\omega}_q} - \mathcal{D}(\dot{\boldsymbol{\Upsilon}}_{\boldsymbol{\omega}_q}), \tag{C.7}$$

where $\ddot{\boldsymbol{\Lambda}}_{\boldsymbol{\omega}_q} = (\mathbf{F}_K \otimes \mathbf{F}_{L_{\rm s}})\ddot{\mathbf{R}}_{\boldsymbol{\omega}}(\mathbf{F}_K \otimes \mathbf{F}_{L_{\rm s}})^H$ is a $KL_{\rm s}$ diagonal matrix, $\dot{\boldsymbol{\Upsilon}}_{\boldsymbol{\omega},q} = (\mathbf{F}_K \otimes \mathbf{F}_{L_{\rm s}})\dot{\mathbf{R}}_{\boldsymbol{\omega}}(\mathbf{F}_K \otimes \mathbf{F}_{L_{\rm s}})^H$ is $KL_{\rm s}\times KL_{\rm s}$ block diagonal matrix. Through appropriately selecting the time-frequency packing factors, the approximation error of (C.7) can be controlled [59].

Assuming that the average *a posteriori* variance of the transmitted symbol vector is $\bar{\nu}_q^x(i)$, the variance vector of the equivalent interference is $\boldsymbol{\nu}_q^{\rm int}(i) = [\nu_{0,q}^{\rm int}(i), \cdots, \nu_{K-1,q}^{\rm int}(i)]^T$ and $\nu_{k,q}^{\rm int}(i)$, which satisfies

$$\begin{aligned}\nu_{k,q}^{\rm int}(i) = \frac{1}{L_{\rm s}} \sum_{k_{\rm t}\in\mathcal{I}_{K_{\rm I}\backslash k}} \mathbf{1}_{L_{\rm s}}^T \left[\sum_{l=0}^{L-1} \hat{h}_{q,l}(i)\lambda_{k_{\rm t}}^l \mathcal{D}(\breve{\mathbf{g}}_{k_\Delta,l})\right]\left[\sum_{l=0}^{L-1} \hat{h}_{q,l}(i)\lambda_{k_{\rm t}}^l \mathcal{D}(\breve{\mathbf{g}}_{k_\Delta,l})\right]^H \mathbf{1}_{L_{\rm s}}\bar{\nu}_q^x(i) \\ + \frac{1}{L_{\rm s}}\left[\sum_{l=0}^{L-1} l|\hat{h}_{q-1,l}|^2\bar{\nu}_{q-1}^x(i) + \sum_{l=0}^{L-1}(L-1-l)|\hat{h}_{q+1,l}|^2\bar{\nu}_{q+1}^x(i)\right],\end{aligned} \tag{C.8}$$

where the first term represents the variance of the ICIs within one segment and the second term represents the variance of the ICIs between different segments.

According to the above derivations, the covariance matrix of the frequency-domain equivalent noise process in the q-th segment is approximated as

$$\boldsymbol{\nu}_q^{\breve{\boldsymbol{\varpi}}}(i) = \mathbf{R}_{\breve{\boldsymbol{\omega}}_q}\mathbf{1}_{KL_{\rm s}} + \boldsymbol{\nu}_q^{\rm int}(i). \tag{C.9}$$

In conclusion, the distribution of frequency-domain equivalent noise process in the i-th iteration obeys $\breve{\boldsymbol{\varpi}}_q \sim \mathcal{CN}\big[\breve{\boldsymbol{\varpi}}_q; \hat{\boldsymbol{\kappa}}_q(i), \mathcal{D}(\boldsymbol{\nu}_q^{\breve{\boldsymbol{\varpi}}}(i))\big]$.

Appendix D

Derivations of the distribution of the frequency-domain equivalent noise in (5.28)

In (5.28), the covariance matrix of the frequency-domain equivalent noise $\breve{\boldsymbol{\omega}}_{k_\mathrm{r},q}$ is expressed as

$$\mathbf{R}_{\breve{\boldsymbol{\omega}}_{k_\mathrm{r},q}} = \mathbf{F}_{L_\mathrm{s}} \mathbf{R}_{\boldsymbol{\omega}_{k_\mathrm{r},q}} \mathbf{F}_{L_\mathrm{s}}^H = \mathbf{F}_{L_\mathrm{s}} (\ddot{\mathbf{R}}_{\boldsymbol{\omega}_{k_\mathrm{r},q}} - \dot{\mathbf{R}}_{\boldsymbol{\omega}_{k_\mathrm{r},q}}) \mathbf{F}_{L_\mathrm{s}}^H, \tag{D.1}$$

where $\mathbf{R}_{\boldsymbol{\omega}_{k_\mathrm{r},q}}$ denotes the covariance matrix of the time-domain colored noise process $\boldsymbol{\omega}_{k_\mathrm{r},q}$. $\ddot{\mathbf{R}}_{\boldsymbol{\omega}_q}$ is an $L_\mathrm{s}\times L_\mathrm{s}$ circulant matrix with the first row vector $(\ddot{\mathbf{R}}_{\boldsymbol{\omega}_q})_{[1,:]} = [A_\mathrm{p}(0,0), \cdots, A_\mathrm{p}(N_\mathrm{I}\tau T_0, 0), 0, \cdots, A_\mathrm{p}(-\tau T_0, 0)]$. $\dot{\mathbf{R}}_{\boldsymbol{\omega}_{k_\mathrm{r},q}}$ is an $L_\mathrm{s}\times L_\mathrm{s}$ Toeplitz matrix, where the first row vector is $(\dot{\mathbf{R}}_{\boldsymbol{\omega}_{k_\mathrm{r},q}})_{[1,:]} = [0, \cdots, 0, A_\mathrm{p}(-N_\mathrm{I}\tau T_0, 0), \cdots, A_\mathrm{p}(-\tau T_0, 0)]$ and the first column vector is $(\dot{\mathbf{R}}_{\boldsymbol{\omega}_{k_\mathrm{r},q}})_{[:,1]} = [0, \cdots, 0, A_\mathrm{p}(N_\mathrm{I}\tau T_0, 0), \cdots, A_\mathrm{p}(\tau T_0, 0)]^T$.

According to the properties of the circulant matrices [161], (D.1) is simplified as

$$\mathbf{R}_{\breve{\boldsymbol{\omega}}_{k_\mathrm{r},q}} = \ddot{\boldsymbol{\Lambda}}_{\boldsymbol{\omega}_q} - \dot{\boldsymbol{\Upsilon}}_{\boldsymbol{\omega}} \approx \ddot{\boldsymbol{\Lambda}}_{\boldsymbol{\omega}} - \mathcal{D}(\dot{\boldsymbol{\Upsilon}}_{\boldsymbol{\omega}}), \tag{D.2}$$

where $\ddot{\boldsymbol{\Lambda}}_{\boldsymbol{\omega}} = \mathbf{F}_{L_\mathrm{s}} \ddot{\mathbf{R}}_{\boldsymbol{\omega}} \mathbf{F}_{L_\mathrm{s}}^H$ is an L_s diagonal matrix, $\dot{\boldsymbol{\Upsilon}}_{\boldsymbol{\omega}} = \mathbf{F}_{L_\mathrm{s}} \dot{\mathbf{R}}_{\boldsymbol{\omega}} \mathbf{F}_{L_\mathrm{s}}^H$ is an L_s diagonal matrix. Observe that the covariance matrix of (D.2) is independent of the subscript k_r and q. Hence, the frequency-domain colored noise $\breve{\boldsymbol{\omega}}_{k_\mathrm{r},q}$ obeys the Gaussian distribution $\mathcal{CN}(\breve{\boldsymbol{\omega}}_{k_\mathrm{r},q}; 0, \gamma_{\breve{\omega}}^{-1})$, where $\gamma_{\breve{\omega}}$ is inversely proportional to the average value of the main diagonal elements of $\mathbf{R}_{\breve{\boldsymbol{\omega}}_{k_\mathrm{r},q}}$.